Characterising Heterogeneity of Glioblastoma using Multi-parametric Magnetic Resonance Imaging

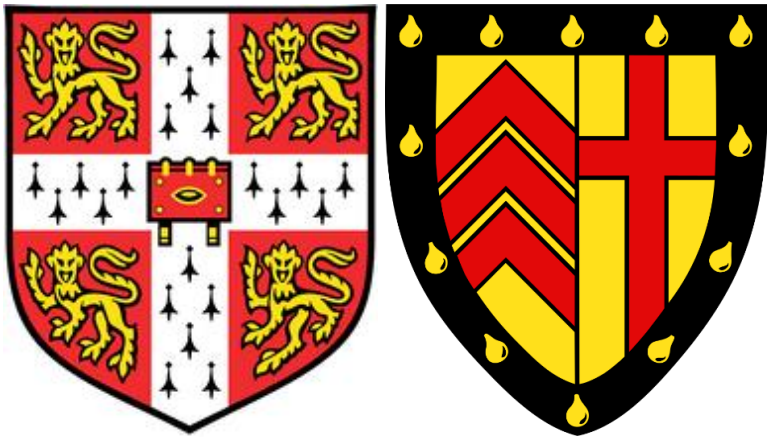

Chao Li

Cambridge Brain Tumour Imaging Laboratory,

Division of Neurosurgery, Department of Clinical Neurosciences

University of Cambridge

This dissertation is submitted for the degree of

Doctor of Philosophy

Clare College

August 2018

I would like to dedicate this thesis to my loving families …

Declaration

I hereby declare that except where specific reference is made to the work of others, the contents of this dissertation are original and have not been submitted in whole or in part for consideration for any other degree or qualification in this, or any other University. This dissertation is the result of my own work and includes nothing which is the outcome of work done in collaboration, except where specifically indicated in the text. This dissertation contains less than 60,000 words including appendices, bibliography, footnotes, tables and equations and has less than 150 figures.

Chao Li

August 2018

Contents

Acknowledgements

Firstly, I would like to express my sincere gratitude to my PhD supervisor, Mr Stephen Price, for his guidance to my PhD projects, for his motivation during my research. He not only offered me the opportunity of studying in Cambridge, but also showed me into the career path as an academic clinician. His great patience and guidance have helped me to overcome the difficulties throughout my research. He has created such an excellent research environment as a group leader, with his immense knowledge and encouragement. The door to Mr Price's office is always open to me whenever I have difficulties or need discussion, by which he steered me to the right direction in my PhD study.

I would like to thank my second supervisor, Dr Florian Markowetz, for his generous support and guidance. He opened the door for me of learning bioinformatics techniques, which broaden my horizons from various perspectives. He also kindly gave me access to the research facilities and resources in Cancer Research UK Cambridge Institute, which allows me to have the opportunities of exploring the broader topic of cancer research. The CI group meeting and lectures are insightful and energetic, during which I can learn plenty of world-class research tools and ideas.

The Cambridge Brain Tumour Imaging Laboratory:

Dr Timothy Larkin was a senior member before I joined the lab. Although I have not had the chance to meet him in person, he had helped the lab to set up the pipeline of image processing using FSL and MATLAB functions, which we are still using in our research. I would like to thank Dr Natalie Boonzaier, a senior PhD student who graduated in 2016, for her great help in collecting and maintaining the patient database, for providing her tumour masks for the inter-rater reliability test. She kept helping me after she left for London. I would like to thank Dr Jiun-Lin Yan, who arrived a year before me as a senior PhD student, for his time and efforts in setting up the general methodology of image processing. He is always ready to help and discuss, which inspired me for research ideas. In addition to the help in research, he is such a

good friend in helping me to settle down in Cambridge, as well as a neurosurgeon colleague for communication. I wish to thank Mr Bart van Dijken, a visiting PhD student from the University of Groningen, Netherlands, for his help in database correction and discussion. I wish to thank Dr Rohitashwa Sinha, a neurosurgeon registrar and a fellow PhD student, for his help in data collection and discussion. I would like to thank Dr Rory Piper, an academic foundation trainee, for his help in progression analysis. I also wish to thank Dr Roushanak Rahmat, a post-doc of the lab, for her valuable discussion.

Cancer Research UK Cambridge Institute:

I would thank Dr Mary McLean for her helpful advice on the sequence protocols of chemical shift imaging and the analysis of spectra, as well as the great help in data collection. I wish to thank Dr Turid Torheim, a post-doc of Markowetz Lab, for her feedback and discussion. Her valuable questions and comments have helped me to validate and clarify my research. She also kindly helped me to establish the experimental pipeline. I also wish to thank Dr Andrew Holding, a senior research associate in Markowetz Lab and Ms Amy Cullen, a research assistant of Markowetz Lab, for their help in establishing tissue processing protocols, with great patience and kindness. I wish to thank Dr Mireia Crispin-Ortuzar for her insightful discussion and comments.

The Department of Clinical Neurosciences, the Division of Neurosurgery, the Wolfson Brain Imaging Centre and the Department of Oncology:

I wish to thank Professor Michael Coleman, Dr Ruma Raha-Chowdhury Dr Adrian Carpenter, Dr Emmanuel Stamatakis, and Mrs Shannon Tinley-Browne, for organising seminars and lectures, and for the considerate guidance during the PhD study. I would also like to thank Mr Colin Watts and Dr Raj Jena who provided me with precious suggestions for my projects. I wish to also thank all the radiologists, radiographers, and research nurses involved in sequence development and patient scanning.

The Department of Radiology and EPSRC Centre for mathematical and statistical analysis of multimodal clinical imaging:

I would like to thank Dr Tomasz Matys for his help in patient recruitment, data retrieval and annotation. I wish to thank Professor John Aston and Professor Carola-Bibiane Schönlieb for their guidance in mathematical modelling. I would like to thank Dr Yuan Huang, Dr Pan Liu, Dr Jingjing Zou, Dr Jianmin Yuan and Mr Shuo Wang for their technical help and supports.

The funding bodies:

I would like to take this opportunity to thank The Cambridge Trust and the China Scholarship Council for providing funding for my PhD study in Cambridge. I would like to thank the British Neuro-Oncology Society for funding my Conference attendance. I wish to express my appreciation to the EG Fearnsides Trust and ISMRM who funded my attendance for 2018 ISMRM conference in Paris. I would like to thank Clare College for funding my research.

I would like to finally express my sincerest gratitude to the patients who participated in the study. Their voluntary time and efforts for the scanning have provided researchers and clinicians with precious information for finding the chance to combat this disease.

Abstract

A better understanding of tumour heterogeneity is central for accurate diagnosis, targeted therapy and personalised treatment of glioblastoma patients. This thesis aims to investigate whether pre-operative multi-parametric magnetic resonance imaging (MRI) can provide a useful tool for evaluating inter-tumoural and intra-tumoural heterogeneity of glioblastoma.

For this purpose, we explored: 1) the utilities of habitat imaging in combining multi-parametric MRI for identifying invasive sub-regions (I & II); 2) the significance of integrating multi-parametric MRI, and extracting modality inter-dependence for patient stratification (III & IV); 3) the value of advanced physiological MRI and radiomics approach in predicting epigenetic phenotypes (V). The following observations were made:

I. Using a joint histogram analysis method, habitats with different diffusivity patterns were identified. A non-enhancing sub-region with decreased isotropic diffusion and increased anisotropic diffusion was associated with progression-free survival (PFS, hazard ratio [HR] = 1.08, $P < 0.001$) and overall survival (OS, HR = 1.36, $P < 0.001$) in multivariate models.

II. Using a thresholding method, two low perfusion compartments were identified, which displayed hypoxic and pro-inflammatory microenvironment. Higher lactate in the low perfusion compartment with restricted diffusion was associated with a worse survival (PFS: HR = 2.995, $P = 0.047$; OS: HR = 4.974, $P = 0.005$).

III. Using an unsupervised multi-view feature selection and late integration method, two patient subgroups were identified, which demonstrated distinct OS ($P = 0.007$) and PFS ($P < 0.001$). Features selected by this approach showed significantly incremental prognostic value for 12-month OS ($P = 0.049$) and PFS ($P = 0.022$) than clinical factors.

IV. Using a method of unsupervised clustering via copula transform and discrete feature extraction, three patient subgroups were identified. The subtype demonstrating high inter-

dependency of diffusion and perfusion displayed higher lactate than the other two subtypes (P = 0.016 and P = 0.044, respectively). Both subtypes of low and high inter-dependency showed worse PFS compared to the intermediate subtype (P = 0.046 and P = 0.009, respectively).

V. Using a radiomics approach, advanced physiological images showed better performance than structural images for predicting O6-methylguanine-DNA methyltransferase (MGMT) methylation status. For predicting 12-month PFS, the model of radiomic features and clinical factors outperformed the model of MGMT methylation and clinical factors (P = 0.010).

In summary, pre-operative multi-parametric MRI shows potential for the non-invasive evaluation of glioblastoma heterogeneity, which could provide crucial information for patient care.

Abbreviations

5-ALA	5-aminolevulinic acid
ADC	Apparent diffusion coefficient
AUC	Area under the curve
BBB	Blood-brain barrier
BET	Brain extraction tool
CCRT	Concomitant chemo-radiotherapy
CE	Contrast-enhancing/contrast enhancement
Cho	Choline
Cr	Creatine
CSI	Chemical shift imaging
CT	Computed tomography
DICOM	Digital imaging and communications in medicine
DCE-MRI	Dynamic contrast enhanced MRI
DSC-MRI	Dynamic susceptibility contrast MRI
DTI	Diffusion tensor imaging
DWI	Diffusion-weighted imaging
EES	Extravascular extracellular space
EGFR	Epidermal growth factor receptor
EOR	Extent of resection
EPI	Echo-planar imaging

FA	Fractional anisotropy
FDT	FMRIB's diffusion toolbox
FLAIR	Fluid-attenuated inversion recovery
FLIRT	FMRIB's linear image registration tool
FOV	Field of view
FSL	FMRIB software library
GLCM	Grey level co-occurrence matrix
GLRLM	Grey level run-length matrix
GLSZM	Grey level size-zone matrix
Glx	Glutamine and glutamate
GTR	Gross total resection
IDH	Isocitrate dehydrogenase
KPS	Karnofsky performance score
Lac	Lactate
Lip	Lipids
LASSO	Least absolute shrinkage and selection operator
LOOCV	Leave-one-out cross-validation
MD	Mean diffusivity
MGLSZM	Multiple grey level size-zone matrix
MGMT	O6-methylguanine-DNA methyltransferase
mIns	Myo-Inositol
ML9	Macromolecule and lipid at 0.9 ppm
MRI	Magnetic resonance imaging
MRS	Magnetic resonance spectroscopy
MVDA	Multi-View Biological Data Analysis

MTT	Mid-transit time
NAA	N-acetyl aspartate
NAWM	Normal-appearing white matter
NB	Naïve Bayes
NE	Non-enhancing
NF1	neurofibromatosis type 1
NIFTI	Neuroimaging Informatics Technology Initiative
NGS	next-generation sequencing
NIHR	National Institute of Health and Research
NN	Neural Network
OS	Overall survival
PCA	Principal component analysis
PCh	Phosphocholine
PDGFR	Platelet derived growth factor receptor
PET	Positron emission tomography
PFS	Progression-free survival
ppm	Parts per million
PTEN	Phosphatase and tensin homolog deleted on chromosome 10
PWI	Perfusion-weighted imaging
RANO	Response assessment in Neuro-oncology
rCBF	Relative cerebral blood flow
rCBV	relative cerebral blood volume
RF	random forest
ROC	Receiver operator characteristic
ROI	Region of interest

SD	Standard deviation
STR	Subtotal resection
SVM	support vector machine
TCGA	the Cancer Genome Atlas
TE	Echo time
TERT	Telomerase reverse transcriptase
TP53	Tumour protein p53
TR	Repetition time
TTP	Time to Peak
TMZ	Temozolomide
VASARI	Visually Accessible Rembrandt Images
WBIC	Wolfson Brain Imaging Centre
WHO	World Health Organisation

“*千里之行，始于足下*”

–老子

“*A journey of a thousand miles begins with a single step*.”

-Laozi

Chapter 1 Glioblastoma Heterogeneity: A Multifaceted View

1.1 Overview

Glioblastoma is the commonest primary malignant tumour in the central nervous system of adults. Although the overall age-standardised incidence is only 4.64/100,000 patient-years (Brodbelt et al., 2015), it is one of the leading cancer-related death causes in young adults, with a recently reported rising incidence (Johnson, 2012). Over the last decade, the standard first-line management of this disease has been accepted as maximal safe surgical resection followed by concomitant and adjuvant temozolomide (TMZ) chemoradiotherapy, which has been shown to improve patient outcomes. However, the survival of most glioblastoma patients remains low. The median overall survival (OS) of optimally managed patients is only 12-15 months (Hegi et al., 2005a, Ricard et al., 2012).

Glioblastoma is characterised by its diffuse infiltration into the surrounding normal brain tissue, which renders a total surgical resection impossible. Moreover, the high proliferation and resistance to adjuvant therapies often cause current treatment strategies to be ineffective. In addition, the heterogeneity of glioblastoma can further challenge diagnosis, prognosis determination and treatment planning. Thus, these tumours are associated with a high tendency of local recurrence and high mortality rate.

1.2 Heterogeneous nature of glioblastoma

Glioblastomas are highly heterogeneous tumours by nature. The heterogeneity of this disease was initially described according to its microscopic manifestation, such as, the various extent

of necrosis and haemorrhage. Other histological observations indicating heterogeneity include cellular pleomorphism and variations in microvascularization (Louis et al., 2016). For recent decades, however, it has been noticed that under the same histological diagnosis of glioblastoma, patients may have distinct clinical outcomes (Verhaak et al., 2010), suggesting that multiple phenotypes may exist under the same disease entity. With further knowledge, tumour heterogeneity is found not limited to histological level. Actually, tumour heterogeneity is a multifaceted research field, which involves multiple aspects of knowledge, including genomics, mathematics, radiology, and clinical oncology.

There are two levels of tumour heterogeneity that exist. The heterogeneity of glioblastoma can be found not only among patients but also within an individual tumour. Many tumour sub-populations can exist in the same tumour, which may result from the tumour clonal evolution and constitute a complex tumour system (Burrell et al., 2013). Therefore, for clarity, the tumour heterogeneity among patients is termed as inter-tumoural heterogeneity, whilst heterogeneity observed within individual tumours is known as intra-tumoural heterogeneity (Figure 1.1).

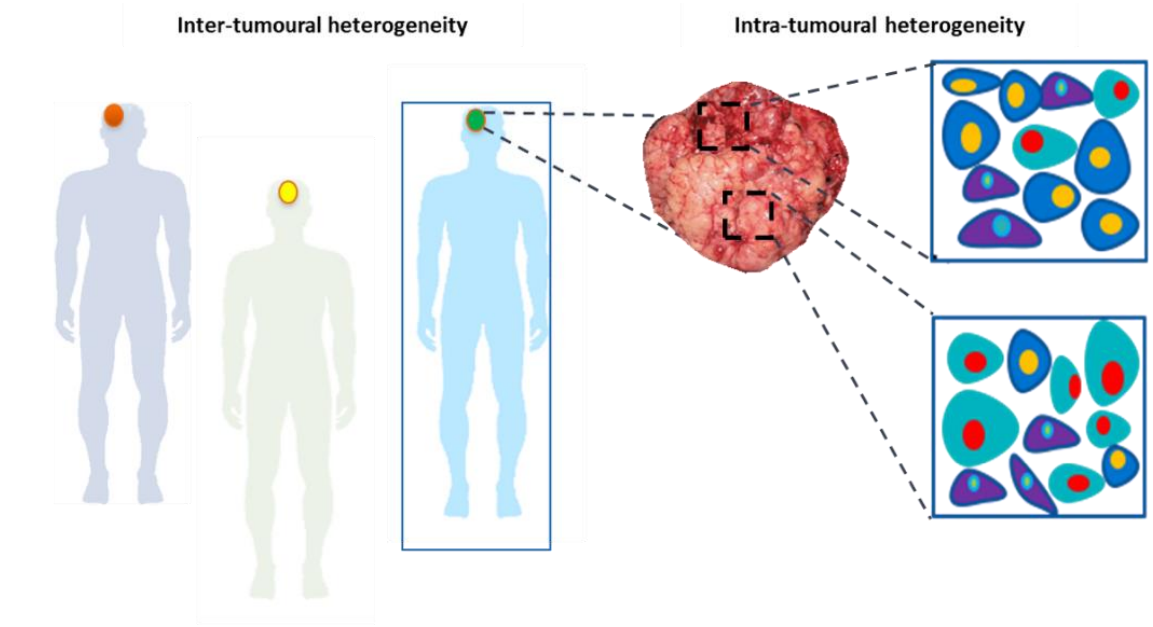

Figure 1.1 Inter-tumoural and intra-tumoural heterogeneity. Inter-tumoural heterogeneity refers to the variations among patients, whereas intra-tumoural heterogeneity refers to the spatial variations existing in the same tumour. Sub-populations of tumour cells may co-exist in the same tumour, which may result from the tumour evolution.

1.3 Significance

It has been established that heterogeneity is one of the hallmarks of tumourigenesis (Greaves and Maley, 2012). There is a pressing but unmet need for a better understanding of tumour heterogeneity, which is of particular importance for the personalised treatment of glioblastoma.

Firstly, given the diverse treatment response of patients, an accurate assessment of inter-tumoural heterogeneity of glioblastoma holds promise for outcome improvement, with the potential of more precise diagnosis and therapeutic stratification for patients.

Secondly, as it is accepted that some intra-tumoural clones/sub-regions have advantages in migration, invasion, and treatment resistance, and therefore would be particularly responsible for treatment failure. Identifying these invasive clones/sub-regions before treatment and further understanding how they influence tumour invasiveness may lead to future treatment targets.

Last but not least, as a result of the selective stress in tumour evolution, heterogeneity may in reverse facilitate the emergence of novel mutations, and thus lead to adaptable clones (Yan et al., 2014). Although currently a wide range of therapeutic strategies, including immunotherapy and gene therapy, are under development or in the clinical trial, their efficacy and safety need further evaluation. Knowledge about tumour heterogeneity would help the development of new therapeutic strategies and clinical assessment techniques.

1.4 Histology

In the past century, histology assessment is the gold standard for the diagnosis of glioblastoma. Glioblastomas were diagnosed mainly based on their microscopic histological appearances and the cellular morphology observed on tumour tissue sections. The common histological features include necrosis, microvascular proliferation, mitoses, pseudopalisades, thromboses, and haemorrhages (Louis et al., 2016, Habberstad et al., 2012). Among these histopathological criteria, necrosis and microvascular proliferation are central to the microscopic diagnosis, which was found to be consistently co-existing in a retrospective study of 200 primary glioblastoma patients (Habberstad et al., 2012).

The past decade witnessed substantial advances in the identification of disease-related genetic alterations. Efforts have been made to improve the traditional histopathological paradigm using molecular genetic classification. As a step forward, the '2016 WHO Classification of Tumours of the Central Nervous System' has incorporated isocitrate dehydrogenase (IDH) mutations into the classification of glioblastoma (Louis et al., 2016). The significance of this version of WHO classification is not only to provide a novel classification for more accurate determination of diagnosis and prognosis, but also to mark the first attempt of combining molecular markers into the clinically applicable guideline (Figure 1.2).

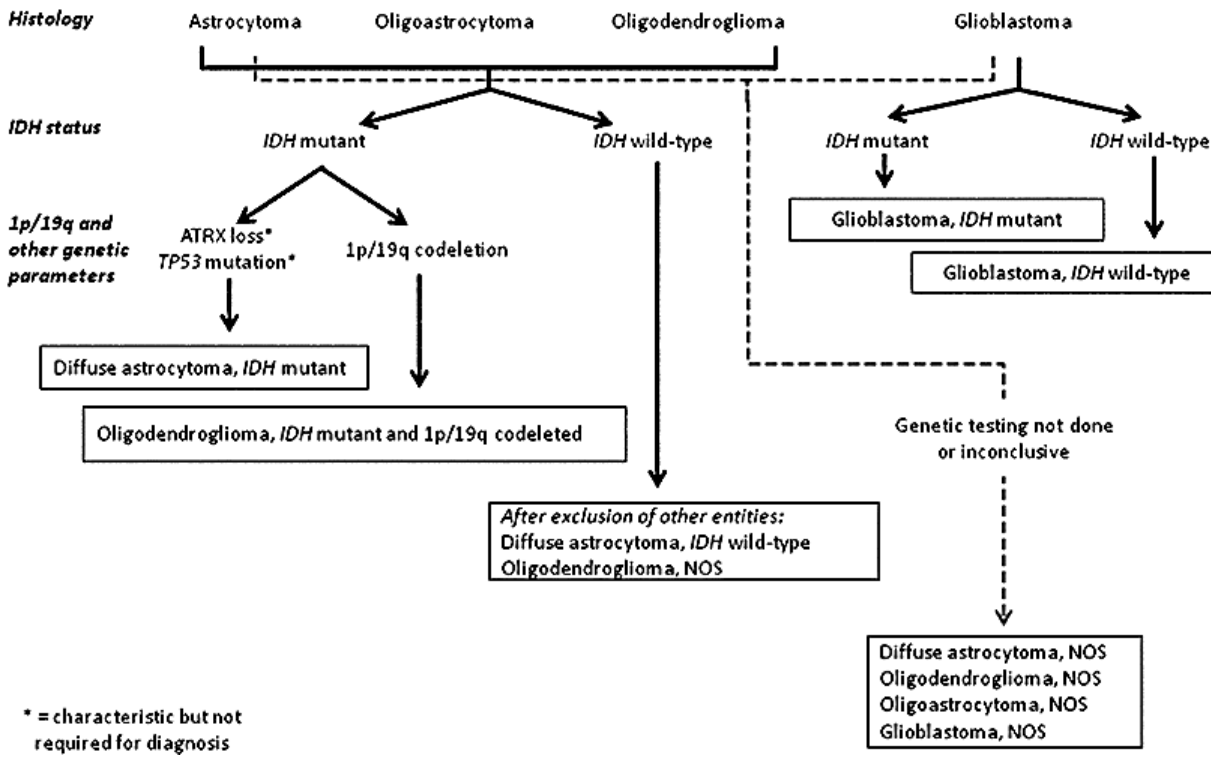

Figure 1.2 2016 WHO classification of the diffuse gliomas (Louis et al., 2016)

1.5 Molecular markers

In the last decades, knowledge of glioblastoma heterogeneity has accumulated from the genetic profiling of patients. Several genetic and epigenetic markers are reported to add diagnostic

and/or prognostic values, including IDH mutations, O^6-methylguanine-DNA methyltransferase (MGMT) promoter methylation status, epidermal growth factor receptor (EGFR) mutations, tumour protein p53 (TP53) mutations, telomerase reverse transcriptase (TERT) promoter mutations. Here is a brief introduction to two markers that are relevant in this thesis.

1.5.1 IDH mutations

IDH mutations are among one of the most frequently mutated metabolic genes identified in human cancers, although exactly how the aberrant enzymatic activity modulates cellular transformation is still unclear (Ye et al., 2013).

IDH mutations are considered as one of the driver mutations of gliomas, with diagnostic and prognostic significance. The Cancer Genome Atlas (TCGA) project reported that 12% glioblastomas have IDH-1 mutations, which are more likely to occur in young patients (Parsons et al., 2008a). In secondary glioblastomas, the mutations are associated with a better survival (Parsons et al., 2008a). By contrast, only 5-8% primary glioblastomas were reported to have IDH mutations (Yen et al., 2010). In a retrospective study including 404 patients with grade II-IV gliomas, multivariate survival analysis showed that IDH-1 mutation was a favourable prognostic marker, independent of other clinical factors (Sanson et al., 2009). However, whether the prognostic value of IDH mutations is from the gene function per se or arises from the better treatment response still needs further investigation (Sanson et al., 2009, Cohen et al., 2013).

Due to the diagnostic and prognostic values of IDH mutations in glioblastoma, the 2016 WHO classification separated glioblastoma into three subtypes: IDH-wildtype, IDH-mutant, and NOS. The diagnosis of NOS is reserved for the circumstances in which the evaluation cannot be performed. A comparison of the clinical characteristics of IDH-wildtype and IDH-mutant glioblastomas is in Table 1.1 (adapted from (Louis et al., 2016)).

Table 1.1 Characteristics of IDH-wildtype and IDH-mutant glioblastoma

	IDH-wildtype	IDH-mutant
Precursor lesion	Not identifiable; develops *de novo*	Diffuse astrocytoma; Anaplastic astrocytoma
Proportion of glioblastoma	~90%	~10%
Median age at diagnosis	~62 years	~44 years
Male to female ratio	1.42:1	1.05:1
Median length of clinical history	4 months	15 months
Median overall survival		
Surgery + radiotherapy	9.9 months	24 months
Surgery + chemoradiotherapy	15 months	31 months
Location	Supratentorial	Preferentially frontal
Necrosis	Extensive	Limited

1.5.2 MGMT promoter methylation status

The gene of MGMT contains five exons and a CpG island. In normal conditions, most of the CpG sites within the island are unmethylated. The gene function of MGMT is central in maintaining genomic integrity, by encoding a DNA repair protein, which can reduce the DNA damage caused by TMZ (Pegg, 1990). The methylated MGMT promoter can lead to a better sensitivity to TMZ, by silencing the MGMT expression (Hegi et al., 2008, Hegi et al., 2005a).

A methylated MGMT promoter was found in about 40% of primary glioblastoma, and over 70% of secondary glioblastoma (Riemenschneider et al., 2010, Weller et al., 2010). The MGMT promoter methylation status is reported to be an independent prognostic marker for glioblastoma patients (Boots-Sprenger et al., 2013). After chemoradiotherapy, 49% methylated glioblastoma cases survived for more than 2 years. In comparison, only 15% unmethylated glioblastoma cases can survive longer than 2 years (Hegi et al., 2005a).

1.6 Genomics

With the advancement of next-generation sequencing (NGS) technique, large-scale data were generated through genomics, epigenomics, transcriptomics and proteomics analysis. Genomics can promote the understanding of tumour heterogeneity, by depicting the complicated genetic signatures of glioblastoma (Brennan et al., 2013). Multiple distinct molecular subtypes have been identified, characterised by the alterations of PDGFRA, IDH-1, EGFR and NF1. These four subtypes, namely proneural, neural, classical and mesenchymal subtypes, are derived from the transcriptional signatures (Verhaak et al., 2010). The distinct patient survivals of these four subtypes suggest that they may represent different entities, even under the same histological diagnosis of glioblastoma (Ye et al., 2012, Bhat et al., 2013).

This classification scheme, however, did not distinguish the transcriptomes of tumour cells and non-malignant cells. A recent revisit of this scheme using glioblastoma-specific mRNA revealed that three tumour-intrinsic subtypes robustly exist: classical, proneural, and mesenchymal (Wang et al., 2017). The exclusion of neural subtype is possibly due to the contamination of non-malignant cells in original samples. Further, using paired samples from primary and recurrent tumours, this study found that these transcriptional subtypes were consistent in only 55% samples, highlighting the plasticity of this classification. The shift between subtypes was postulated to be mediated by the interaction between tumour cells with microenvironmental cues (Wang et al., 2017).

Above evidence have established the existence of inter-tumour heterogeneity of glioblastoma. As we mentioned above, remarkable intra-tumour heterogeneity exists within individual glioblastoma. It was thus speculated that multiple subtypes may co-exist within a single tumour. To address this hypothesis, a fluorescence guided multisampling approach was developed in a previous study (Sottoriva et al., 2013a), by which multiple spatially separated tumour samples were collected through surgical resections. The results confirmed the existence of multiple subtypes within the same tumour. Further, with the phylogeny of these sample fragments reconstructed, it was revealed that the intra-tumoural heterogeneity may arise from the clonal evolution during the disease progression, which may impact patient treatment and thus have clinical significance (Sottoriva et al., 2013a).

1.7 Mathematical models

It has been a challenge to evaluate glioblastoma heterogeneity with quantitative methods. As a useful tool for hypothesis testing in understanding the biological process, mathematical modelling shows potential in this regard. To simulate the evolution of a complex tumour system, many mathematical models have been proposed. The different aspects of tumour behaviours, i.e., the growth rate of tumour cells, tumour cellularity, angiogenesis, are considered in sophisticated models (McDougall et al., 2006, Frieboes et al., 2006, Swanson et al., 2003). More recently, with a spatial model of tumour evolution, how short-range dispersal and cell turnover can affect intra-tumour heterogeneity was simulated (Waclaw et al., 2015). These models exhibit potential in providing theoretical models for tumour heterogeneity study.

Medical images have the unique advantage of providing global information of a tumour. Thus, it would be possible to infer the microscopic tumour growth, invasion and evolution using multi-parametric and multi-temporal imaging. Considering that glioma exhibits high abilities of proliferation and migration, a mathematical approach was developed to quantify net proliferation rate (ρ) and net diffusion factor (D), using T1-weighted and T2-weighted images to calculate patient-specific metrics (Swanson et al., 2008). The invasiveness metrics from this approach has shown correlates with patient clinical outcomes and tumour extent of resection (Baldock et al., 2014).

Other studies have incorporated advanced imaging modalities into the mathematical model to reflect the physiological information of tumour growth (Hormuth et al., 2015). With the advantages of diffusion imaging in reflecting the white matter tract pathology, a model using diffusion tensor imaging was proposed (Jbabdi et al., 2005). This study was based on the hypothesis that tumour infiltration may preferentially spread along white matter tracts (Jbabdi et al., 2005).

1.8 Magnetic resonance imaging

1.8.1 Advantages of the imaging approach

Imaging approach plays an important role in the assessment of glioblastoma heterogeneity and clinical patient management. It would provide indispensable tools for the assessment of tumour heterogeneity. Compared to the aforementioned methods, imaging approach has several advantages in evaluating tumour heterogeneity.

One of the advantages is that imaging is non-invasive or minimally invasive in the acquisition. Therefore, it can be performed repeatedly at different time points, with lower risks than invasive procedures, which can significantly facilitate the temporal evaluation of tumour growth and invasion. Another advantage is that tumour imaging can profile an entire tumour *in vivo*. Although histological and genetic assessments can determine tumour malignancy, they are based on a fraction of tumour samples obtained via surgery or biopsy, which is prone to sampling errors. In comparison, the spatial information from imaging is not limited by the tumour tissue obtained.

Magnetic resonance imaging (MRI) is by far the most widely used imaging technique for glioblastoma (Sorensen, 2006, Kuzucan et al., 2012). The excellent ability of MRI in visualising soft tissue offers the advantage of reflecting brain structure. Further, multiple MRI sequences have been developed to target different tumour properties, which provide crucial complementary information for tumour grading, malignant assessment, diagnosis determination and treatment response prediction.

Current clinical evaluation of glioblastoma is primarily based on anatomical MRI sequences, including post-contrast T1-weighted imaging, T2-weighted imaging, T2 fluid-attenuated inversion recovery (FLAIR). Among these MRI sequences, post-contrast T1-weighted imaging is the most widely used. A typical presentation of glioblastoma on post-contrast T1-weighted imaging is a contrast-enhancing mass lesion with the central non-enhancing sub-regions (commonly considered as ‘necrosis’), and peritumoural oedema surrounding the contrast-enhancing lesion. These radiographical manifestations suggest that glioblastoma is highly heterogeneous in terms of morphological appearances.

T2-weighted FLAIR shows hyperintensity surrounding the contrast-enhancing tumour core. Compared to T2-weighted images, T2-weighted FLAIR provides the advantages of cerebrospinal fluid (CSF) suppression. Normally, the non-enhancing peritumoural areas visualised on T2-weighted FLAIR images are considered to represent a tumour region outside of the tumour core visualised on contrast-enhancing images, which may include both oedematous and infiltrative regions (Villanueva-Meyer et al., 2017).

1.8.2 Limitations of conventional MRI

Although widely used in clinical practice, conventional MRI sequences are considered to bear several limitations.

Firstly, the enhancement on post-contrast T1-weighed imaging is used to provide references for tumour grading. However, evidence shows that this enhancement does not necessarily correlate with tumour malignancy. Some glioblastomas may not demonstrate enhancement, whereas some low-grade glioma or other tumour types may be contrast-enhancing (Pouratian et al., 2007).

Secondly, the enhancement can facilitate the delineation of tumour margin, based on the process of contrast agent passing through the brain blood barrier (BBB). This leakage of the BBB, however, is not specific in delineating the tumour invasion area (White et al., 2005). It is known that current surgical resection based on conventional post-contrast T1-weighted imaging fails to resect the tumour effectively, due to the highly infiltrative growth of glioblastoma (Neira et al., 2017). This failure suggests that the invasive margin of glioblastoma is well beyond the region visualised on post-contrast T1-weighted images (Price et al., 2006).

Other MRI sequences may complement the information of post-contrast T1-weighted imaging. Among them, T2-weighted sequences are especially sensitive to oedematous tissue. With the advantages of T2-weighted imaging, T2-weighted fluid-attenuated inversion recovery (FLAIR) sequence adds the advantage of suppressing cerebrospinal fluid signal. Therefore, T2-weighted and T2-weighted FLAIR sequences are widely used to investigate white matter abnormalities and localise tumours. The Response Assessment in Neuro-Oncology (RANO) Working Group suggests combining these techniques into clinical assessment, to compensate

for the limitations of T1-weighted imaging (Wen et al., 2010). These sequences, however, are still considered to be non-specific for differentiating tumour infiltration from tumour-associated oedema and delayed radiation white matter change (Wen et al., 2010). Previous evidence showed that FLAIR is non-specific in managing tumour with stroke patients (Green et al., 2002, Price et al., 2011).

Another limitation of conventional imaging is in its weakness of differentiating pseudoprogression with true progression. Pseudoprogression was recognised long ago, but the incidence was reported to be increasing since temozolomide (TMZ) chemoradiotherapy was accepted as the standard of care. The possible explanation is that the increased sensitivity to the TMZ chemoradiotherapy may cause a higher extent of treatment-related necrosis (Bach and Jordan, 2005). In a cohort study which investigated 208 newly-diagnosed glioblastoma patients treated with the Stupp protocol of TMZ concomitant and adjuvant chemoradiotherapy, pseudoprogression was observed in 30% patients and significantly associated with MGMT methylation status (Brandes et al., 2008). Since pseudoprogression is almost indistinguishable from true progression on conventional imaging, the diagnosis of pseudoprogression is recommended to be made according to a retrospective review and should incorporate imaging and clinical parameters (Wen et al., 2010).

To summarize, although magnetic resonance imaging has unique advantages in investigating tumour heterogeneity non-invasively, it bears many limitations in reflecting tumour physiology. There is a clinical demand for the improvement of imaging techniques. Further, new post-processing techniques are in pressing demand to integrate multiple imaging techniques for precise patient management.

Pre-clinical and clinical physiological imaging sequences have shown their potentials in compensating the limitations of conventional sequences (van Dijken et al., 2017). These physiological sequences are considered to be more specific in reflecting tumour physiology. Integrating the multiple imaging modalities may potentially provide a more comprehensive measurement for tumour heterogeneity. Following is the introduction of the techniques of advanced imaging and data analysis that will be used in this thesis.

1.8.3 Perfusion imaging

Perfusion refers to the biological process in which blood supply is delivered to the organ/tissue through the capillary bed. The measurement of tissue perfusion is crucial to determine the physiological state of the organ/tissue.

The utility of quantitative perfusion MRI in oncology is based on the commonly observed associations between tumour malignancy and angiogenesis (Figure 1.3). As the tumours progress, there is a frequent observation of mismatched energy demand and blood supply. This mismatch may create a hypoxic tumour microenvironment, which may lead to the activations of angiogenic factors that modulate the formation of new blood vessels (Wesseling et al., 1997, Hanahan and Weinberg, 2011a). This tumour-related neovasculature, however, is marked by the aberrant vascular structure, which is inefficient in delivering blood supply and may lead to the failure of BBB (Hanahan and Weinberg, 2011a).

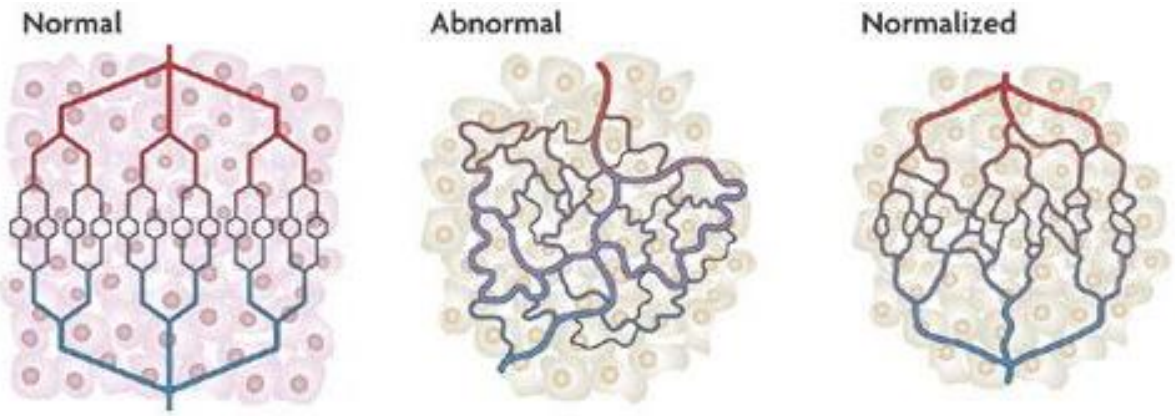

Figure 1.3 Abnormal Vasculature of Tumours. The dilated and tortuous tumour vasculature is characterised by increased permeability and higher interstitial pressure compared with normal. After anti-angiogenesis therapy, the vascular permeability decreased and vasculature is improved (Ellis and Hicklin, 2008).

Perfusion MRI includes the imaging techniques with or without exogenous contrast agent. The most commonly-used in oncological imaging are those with exogenous contrast agent, i.e., dynamic susceptibility contrast (DSC) MRI and dynamic contrast-enhanced (DCE) MRI. With the diffusable tracers, the wash-in and wash-out kinetics can be detected to reflect tissue perfusion (Detre et al., 1992). Using these techniques, contrast-enhancing images are

dynamically acquired in every a few seconds, during and after the contrast agent administered intravenously. Thus, the signal change in this process is detected to reflect the hemodynamics. Imaging biomarkers representing microvasculature characteristics are thus calculated from the model fitting of the dynamics.

1.8.3.1 Dynamic susceptibility contrast MRI

The contrast agent in the blood vessels can lead to different susceptibility between the vessel and the tissue (Rosen et al., 1990). DSC imaging measures the amount of contrast agent which remains in the tumour vessels during the first pass of the bolus passing through the capillary bed. By detecting T2* signal intensity reduction in this process, a concentration-time curve of the contrast agent can be fitted (Paulson and Schmainda, 2008). This technique allows for the calculation of several imaging biomarkers from the curve, including the relative cerebral blood volume (rCBV), the time to peak (TTP), mean transit time (MTT) and cerebral blood flow (CBF) (Figure 1.4).

Among the above biomarkers, rCBV is the most widely used and has been intensively documented in the literature. Normally, the blood volume in a given amount of tissue can be calculated from the concentration-time curve, using the area under the curve (Petrella and Provenzale, 2000). However, the absolute value of CBV can be affected by a number of factors, including the injection time and amount of the contrast agent, the cardiac output of the subjects. In addition, the capillary permeability of different subjects can be various, which can significantly influence the blood volume calculation (Petrella and Provenzale, 2000). Therefore, the CBV value is normally expressed as a relative value (rCBV) to the intra-subject control (the contralateral whiter matter is normally used).

Previous studies showed that rCBV is associated with tumour angiogenesis and proliferation, and may predict tumour grading and patient outcomes (Law et al., 2008, Santarosa et al., 2016). A recent study of 288 glioma patients explored the correlations between the imaging phenotype with the genotype. The results demonstrated that rCBV can indicate IDH mutation status, which was associated with the hypoxia-initiated angiogenesis (Kickingereder et al., 2015). In a retrospective pilot study of recurrent glioblastoma who received angiogenic-inhibiting chemotherapy, rCBV maps were derived from DSC perfusion imaging. The hyperperfusion

volume of rCBV, defined as the volume of tumour sub-regions with higher rCBV value than a predetermined threshold, was found to show a correlation with time to progression of patients (Sawlani et al., 2010). Another study, using a series of image features extracted from pre-treatment DSC-MRI, identified a subgroup of patients with poor clinical outcomes. Angiogenesis and hypoxia pathways were enriched in this subgroup, which may potentially benefit from antiangiogenic therapies (Liu et al., 2016).

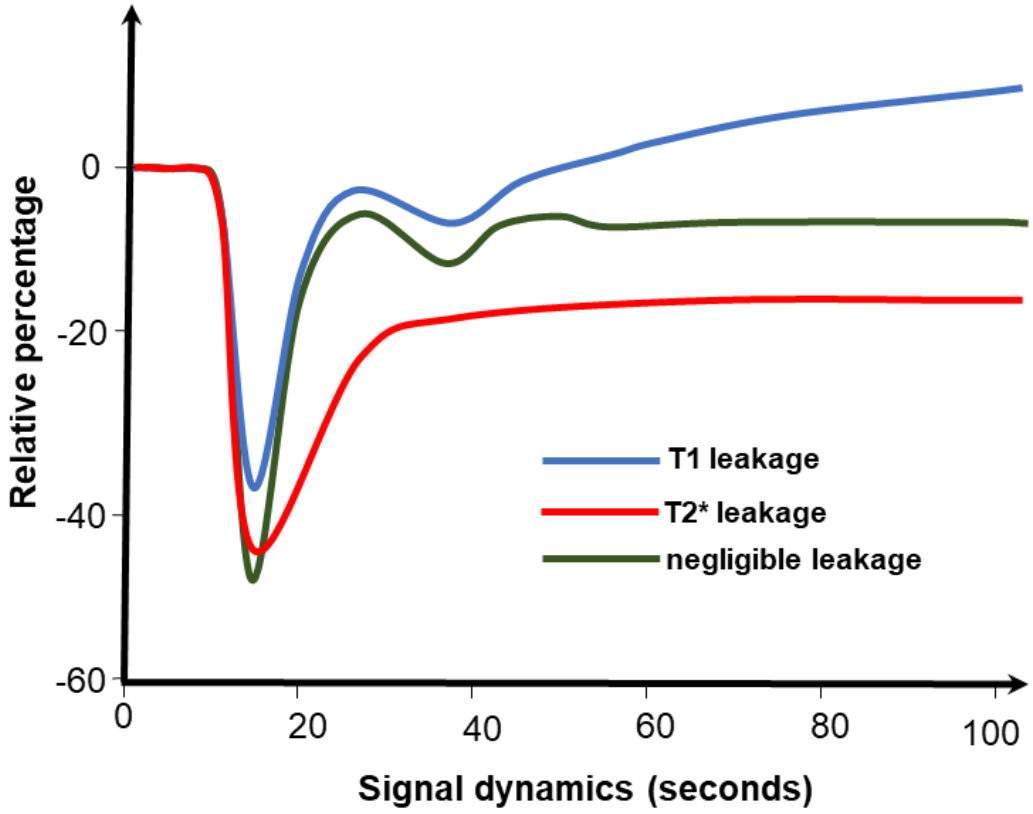

Figure 1.4 Signal intensity-time curve of DSC. DSC imaging measures the amount of contrast agent which remains in the tumour vessels during the contrast agent passing through the capillary bed, by detecting T2* signal intensity reduction in this process. The significant contrast leakage caused by the disrupted blood-brain barrier in glioblastoma may confound the assumption of the modelling. Therefore, a leakage correction is required for the DSC data analysis. The leakage can display different patterns, as shown above (adapted from (Goo and Ra, 2017)). The T1-dominant (increases above baseline) and T2*-dominant (fails to return to baseline) patterns can be related to different tumour characteristics (Plaza et al., 2013).

Although DSC-MRI provides diagnostic and prognostic values in the above studies, the application of DSC-MRI is restricted by the challenges in its post-processing data analysis (Paulson and Schmainda, 2008). One of these challenges is caused by the permeability of the tumour-related neovasculature, which is often observed in solid tumours as above mentioned. This permeability leads to the leakage of the contrast agent into the extravascular extracellular space (EES), which may complicate the curve fitting of the T2* signal intensity reduction. Thus, it is crucial to compensate for the leakage effect in the post-processing (Paulson and Schmainda, 2008). A preload of contrast agent and post-processing leakage correction algorithms are recommended. A recent study using a single-dose and low-flip-angle method was reported to provide comparable measurement to the double-dose method (Kathleen M Schmainda, 2018).

Since above perfusion biomarkers can be computed at a voxel by voxel basis, previous studies showed that the spatial heterogeneity of angiogenesis within gliomas can be characterised using the DSC-derived parameters (Lupo et al., 2005).

1.8.3.2 Dynamic contrast-enhanced MRI

Although DCE-MRI is not used in this thesis, it is widely used in cancer imaging research and should be briefly introduced. The T1-weighted technique measures the relaxivity effects of the paramagnetic contrast agent, which may cause a shortening of T1 relaxation time and lead to higher signals on T1-weighted images (Petrella and Provenzale, 2000). DCE-MRI can detect the T1-weighted signal increase, during the process of contrast agent passing through from the intravascular space into EES. The signal intensity-time curve can be estimated after injecting the contrast agent. As the images are dynamically acquired every a few seconds, this curve can reflect the kinetics of contrast agent efflux, which is an overall effect of the tissue perfusion, permeability of blood vessels and the volume of EES (Essig et al., 2013). This curve is then converted into a time-concentration curve, for the calculation of imaging biomarkers. As the relaxivity effects are normally stronger than the susceptibility effects, DCE-MRI requires a smaller dose of contrast agent in the acquisition, compared to DSC-MRI (Petrella and Provenzale, 2000).

The differences in the mechanisms of contrast enhancement result in different analysis methods between DCE-MRI and DSC-MRI. To interpret the curve of DCE-MRI, pharmacokinetic models are developed considering two compartments: blood plasma and EES. Parameters can be calculated from the compartment-based pharmacokinetic models (Asselin et al., 2012, Tofts and Kermode, 1991), including contrast transfer coefficient (K^{trans}), fractional blood plasma volume (v_p), and the volume of EES (v_e). Among these markers, K^{trans} is most-frequently used, which reflects the combined effects of blood flow and microvascular permeability. Due to the dilated and tortuous tumour vasculature, tumours usually demonstrate significantly higher permeability than normal tissue. As the anti-angiogenic therapy is considered to reduce neovasculature and permeability, K^{trans} is reported to be useful in treatment response (Sorensen et al., 2009).

1.8.4 Diffusion imaging

Diffusion imaging is used to measure the mobility of water molecules in brain tissue, based on the flux of protons in water (Sabatke and Burge, 2002). Normally, the water molecules move in Brownian motion resulting from their thermal energy. Thus, water molecules conform to a Gaussian distribution in brain tissue, provided there is no barrier restricting their movement. In brain tissue, however, the movement of these water molecules displays as the interaction with the microstructure including fibres, cellular structures or macromolecules. By detecting water molecule movement, diffusion imaging can quantify the overall diffusivity of water molecules observed at voxel levels using statistical models, which thus would provide information to the brain microstructure (Le Bihan et al., 2001). Therefore, diffusion imaging has potentials in measuring the highly heterogeneous microstructure in glioblastoma, which is influenced by the tumour cellular proliferation and destruction. MRI is the only imaging method that detects diffusion so far.

Diffusion imaging has evolved into several techniques, among which the simplest is diffusion weighted imaging, from which apparent diffusion coefficient (ADC) can be calculated. Diffusion weighted imaging (DWI) is acquired through a spin-echo planar sequence. After two gradient field applied, the movement of protons is sensitised, leading to the signal loss due to dephasing, which can be detected and the degree of diffusion is thus calculated. The higher

degree of diffusion, the greater signal loss. Diffusion gradients are characterised by b-value (s/mm^2), defined as:

$$b = \gamma^2 G^2 \delta^2 (\Delta - \delta/3)$$

where γ represents the gyromagnetic ratio and diffusion gradient is characterised by G (amplitude), Δ (duration) and δ (interval) (Huisman, 2010). The most commonly used b-values are 0 and 1000 s/mm^2 (Huisman, 2010).

Therefore, after gradient application, the diffusion coefficient can be calculated as:

$$\frac{S}{S_0} = e^{-bD}$$

where S_0 is the signal before applying the gradient, while S is the signal after the gradient. The diffusion coefficient D can thus be calculated from each voxel in the images. To interpret the resultant images, ADC is calculated with the assumption that diffusion is unrestricted, which is a three-dimensional isotropic Gaussian distribution model, using the following equation:

$$\mathrm{ADC} = D = -b\ln(\frac{S}{S_0})$$

In real biological tissue, the microscopic diffusion process is a much more complicated process than the simple equation described above, which is measured at the macroscopic voxel level (Le Bihan, 2013). Additionally, the diffusion measured at voxel level has integrated the effects of both microscopic diffusion and microvascular perfusion (Le Bihan et al., 1988). Therefore, it has been suggested that ADC represents the 'apparent' diffusion coefficient, instead of the 'true' diffusion coefficient represented by D.

The value of ADC is well documented in previous literature. It is reported to have a negative correlation with tumour cellularity in a meta-analysis of 729 patients (Chen et al., 2013a). One previous study, using the post-mortem human brain with meningioma, compared ADC value with cellularity at a voxel-by-voxel basis. The result showed that ADC values below a threshold of 0.929×10^{-3} mm^2/s in the peritumoural FLAIR hyperintense region could indicate higher cellularity than other peritumoural FLAIR hyperintense regions (LaViolette et al., 2014). This

study however also found that the necrotic regions with extremely restricted diffusion had lower ADC values than hypercellularity area (LaViolette et al., 2014). Besides the correlation with tumour cellularity, the significance of ADC in patient survival prediction was also reported by previous studies. In a retrospective study, higher pre-treatment ADC histogram features can be used to stratify bevacizumab-treated recurrent glioblastoma patients according to the 6-month progression-free survival (Pope et al., 2009). Another retrospective study of 112 patients also reported incremental prognostic values from ADC histogram features over MGMT methylation status (Choi et al., 2016).

Although the above studies suggested the clinical utility of ADC in the determination of tumour malignancy, ADC values should be treated with caution, considering that other factors may influence its value. For example, vasogenic oedema may demonstrate an increase in ADC where protons accumulate, while cytotoxic oedema shows a decrease in ADC because of the loss function of Na/K-ATPase leading to water accumulating inside cells. One recent study reported the non-linear relation between ADC values with levels of lactate and lipids as measured by MR spectroscopy, suggesting the need to better elucidate the physiological meaning of this imaging marker (Gadda et al., 2017).

Diffusion, however, is intrinsically a three-dimensional process. Hence, there is a need to address the directionality in diffusion measurement. The brain microstructure is established to be fibrillary, which means the neuronal tissue is normally organised in bundles (Hagmann et al., 2006). This structural pattern thus constrains the movement of water molecules. As a result, the diffusion of the water molecules is not isotropic. Since the diffusion parallel to the white matter tracts is faster than the perpendicular direction, this anisotropy of the diffusion can be used to indicate the overall direction of the white matter tract (Le Bihan et al., 2001). By applying gradients along three orthogonal directions (Dxx, Dyy, Dzz) and average the three images, the average directionality of diffusion can be calculated.

The assumption of isotropic Gaussian distribution is too simplistic to reflect the fibrillary brain microstructure. With the assumption of anisotropic Gaussian distribution, a diffusion tensor can be resulted from the model fitting, in the form of a 3×3 matrix that characterises the

diffusion in three-dimensional space. The eigenvectors and eigenvalues ($\lambda_1 \geq \lambda_2 \geq \lambda_3$) of the tensor can be calculated from the following tensor:

$$D = \begin{bmatrix} D_{xx} & D_{xy} & D_{xz} \\ D_{xy} & D_{yy} & D_{yz} \\ D_{xz} & D_{yz} & D_{zz} \end{bmatrix}$$

With this method, the tensor is decomposed into three eigenvalues which describe the size of axes, and three eigenvectors which describe their directions (Figure 1.5). It is of note that the assumption that the water molecules conform to Gaussian diffusion is not sufficient to reflect the complicated brain structure, including the fibre cross and merge, which means multiple fibres orientations may exist in one single voxel. This is particularly important for the study of brain structure connectivity. Therefore, more complicated tensor distribution functions were proposed to better model the model the diffusion process (Leow et al., 2009, Zhan et al., 2009, Nir et al., 2017).

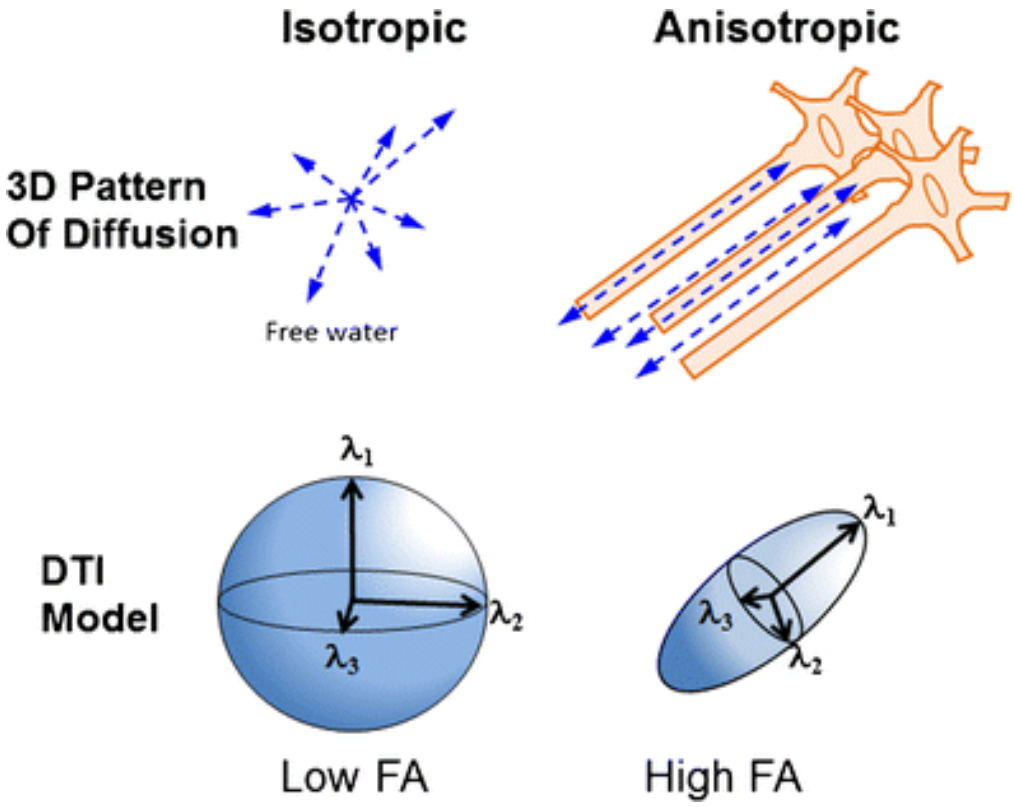

Figure 1.5 Tensor Decomposition of Diffusion Imaging (Vorona and Berman, 2015).

The tensor is usually represented as an ellipsoid, with three principle orthogonal axes corresponding to the eigenvectors. The eigenvector corresponding to the largest eigenvalue (λ_1) represents the principal diffusion direction. If the eigenvalues are similar to each other, the diffusion is isotropic; if the eigenvalues are distinct with each other, the diffusion is anisotropic. From the eigenvalues, mean diffusivity (MD) is therefore calculated as:

$$MD = \frac{\lambda_1 + \lambda_2 + \lambda_3}{3}$$

With each eigenvalue compared to the mean value of all eigenvalues (D), the fractional anisotropy (FA) and the relative anisotropy (RA) are respectively calculated as:

$$FA = \sqrt{\frac{3}{2}} \sqrt{\frac{(\lambda_1 - D)^2 + (\lambda_2 - D)^2 + (\lambda_3 - D)^2}{{\lambda_1}^2 + {\lambda_2}^2 + {\lambda_3}^2}}$$

$$RA = \sqrt{\frac{(\lambda_1 - D)^2 + (\lambda_2 - D)^2 + (\lambda_3 - D)^2}{3D}}$$

where

$$D = \frac{\lambda_1 + \lambda_2 + \lambda_3}{3}$$

According to the equation, FA measures the ratio of the anisotropic component to the full tensor. RA represents the ratio of the anisotropic component to the isotropic component. Despite the improvement for better characterisation of the magnitude of diffusion, these scalars are affected by both isotropic and anisotropic components, as described in the equations. Therefore, various studies have reported that it is insensitive to detect the changes after stroke (Green et al., 2002), and fails to differentiate the peritumoural region of infiltrating and non-infiltrating regions in brain metastases (Lu et al., 2003).

To improve above scalars, a tensor decomposition technique was proposed (Pena et al., 2006a). Based on this method, a decomposition of p:q was proposed to describe the tensor with an isotropic component (p) and anisotropic component (q). The values are calculated with the equations below:

$$p = \sqrt{3}\,D = \frac{\lambda_1 + \lambda_2 + \lambda_3}{\sqrt{3}}$$

$$q = \sqrt{(\lambda_1 - D)^2 + (\lambda_2 - D)^2 + (\lambda_3 - D)^2}$$

These indices are considered sensitive to the subtle disruption of white matter tracts caused by tumour infiltration. Using 35 glioma patients and seven normal volunteers, one previous study showed that the p:q decomposition can characterise tissue signature of the brain. An increase in the isotropic component (p) may indicate tumour infiltration and a reduction in the anisotropic component (q) indicates fibre disruption (Price et al., 2004). In a subsequent image-guided biopsy study, this decomposition technique achieved a sensitivity of 98% and specificity of 81% in differentiating gross tumour with tumour infiltration, while T2 is non-specific in comparison (Price et al., 2006).

This decomposition also demonstrates advantages in the graphical representation of the tensor (Pena et al., 2006a). In a follow-up study of glioma patients, three DTI patterns can be identified, according to the comparison of p and q maps, with one map superimposed to the other map (Price et al., 2007). This technique can predict patterns of tumour recurrence (Price et al., 2007) and patient progression-free survival (Mohsen et al., 2013). Later it was reported that IDH-1 mutation was significantly associated with a minimally invasive phenotype determined by this technique (Price et al., 2017).

To summarise, diffusion imaging provides crucial information about tumour microstructure. To better interpret the diffusion tensor, different decomposition techniques of full tensor into scalar maps were proposed. The isotropic and anisotropic components revealed using the decomposition could be a useful tool to depict the tumour microstructure changes caused by tumour invasion and infiltration, thus would provide information for measurement of tumour heterogeneity and patient stratification.

1.8.5 Magnetic resonance spectroscopy

Magnetic resonance spectroscopy (MRS) is an important *in vivo* method that detects the metabolites. Proton nuclei (^{1}H) signals are commonly used for measurement due to the abundance of protons in human tissues (Raschke et al., 2015b). MRS is based on the chemical

shift properties of the atom, which means the interaction between the electric shell of the ^{1}H nucleus with surrounding molecules may cause the altered spin frequency of the atom when experiencing altered external magnetic field (B_0) (Bertholdo et al., 2013). The corresponding change can be detected through the chemical shift imaging (CSI) and expressed as parts per million (ppm). Although not quantitative, this technique shows potential in reflecting the metabolite profiles and metabolic state according to the spectra peaks attributed to the metabolites.

Single voxel and multi-voxel techniques can be applied for MRS acquisition. The typical spatial resolution of MRS is between 1-10 cm^3, whereas the typical achievable resolution of MRI is 1-10 mm^3 (Blüml, 2013). Although currently the spatial resolution of CSI still needs further improvement, the biochemical and metabolic information that CSI confers can provide extra information to the anatomical information of conventional MRI (Soares and Law, 2009b).

The amount of metabolites that are measurable by MRS partially depends on the echo time (TE). Generally, short TE (i.e. 30 ms) can facilitate the measurement of more metabolite compared to long TE (i.e. 136 ms) (Howe et al., 2003). A short TE, however, may cause a water shoulder that brings difficulties in measurement, which may be compensated using an intra-subject normalisation. Another challenge posed by shorter acquisition time is that the resolution of CSI is low, compared to structural images.

A series of metabolites can be quantified using MRS technique and have clinical significance, including N-acetylaspartate (NAA), choline (Cho), creatine (Cr), myo-inositol (mIns), glutamate + glutamine (Glx), lactate (Lac), lipids (Lip) and macromolecule (MM). A description of the peak resonance and significance of the metabolites is in Table 1.2.

Table 1.2 Significance of the metabolites of MRS

Metabolites	Peak resonance (ppm)	Significance
Choline (Cho)	3.2	Marker of cell membrane turnover
Creatine/phosphocreatine (Cr)	3.0	Marker of cellular energetic metabolism
N-acetylaspartate (NAA)	2.0	Neuronal marker
Glutamate + Glutamine (Glx)	2.1 - 2.6	Excitatory neurotransmitter
Lipids (Lip)	0.9 – 1.4	Tissue damage/destruction
Lactate (Lac)	1.3	Marker of anaerobic glycolysis
Myo-inositol (mIns)	3.5	Potential glial marker
Macromolecule	0.87-3.8	Marker of amino acids of cytosolic proteins

Creatine (including signals from creatine and phosphocreatine) is a component of cell membrane and a marker of cellular energetic metabolism, which is relatively constant in the healthy brain. Therefore, it is normally used as a reference metabolite, providing an intra-subject normalisation (Lowry et al., 1983). However, the normalisation to Cr is prone to the variability of this metabolite caused by the pathological change, i.e., the oedema effect caused by tumour infiltration, as well as the regional variation caused by receive coil sensitivity. To compensate these biases, previous studies proposed to use the Cr in the same voxel as a normalisation (Price et al, 2016).

Choline is a precursor of acetylcholine and a marker of the cell membrane. Several choline-containing compounds exist in tissue, including choline, phosphocholine (PCh), and glycerophosphocholine, among which PCh is associated with cellular proliferation (Bulik et al., 2013a), which can be observed in malignant cell dividing, gliosis or inflammation, and thus is considered as non-specific (Bertholdo et al., 2013).

N-acetylaspartate (NAA) is the acetylated derivative of aspartate acid, which is produced in the mitochondria of neurons. Thus, NAA is considered as a neuronal marker. A decline of this

marker indicates the loss or dysfunction of neurons (Howe et al., 2003), which may be caused by the tumour destructive growth in glioblastoma.

The common pattern of metabolic changes in glioblastoma is an elevation in Cho level and a decrease in NAA level (Soares and Law, 2009a). Specifically, NAA may display significant decline when neurons are destructed during glioblastoma progression (Figure 1.6). At the same time, Cho may be elevated in glioblastoma due to cell proliferation. Therefore, the Cho/NAA ratio may be used as an indicator of tumour-related abnormality (Norska and Barker, 2010). In a previous study, a Cho-NAA index (CNI) was proposed to better interpret the tumour-related abnormality, integrating these two spectral peaks (McKnight et al., 2001). A linear regression of the choline versus NAA was performed to calculate the proposed CNI. Using histopathological validation from image-guided biopsy, a CNI threshold of 2.5 was shown to distinguish tumour tissue from other non-tumour tissue, with a sensitivity 90% and a specificity of 86% (McKnight et al., 2002).

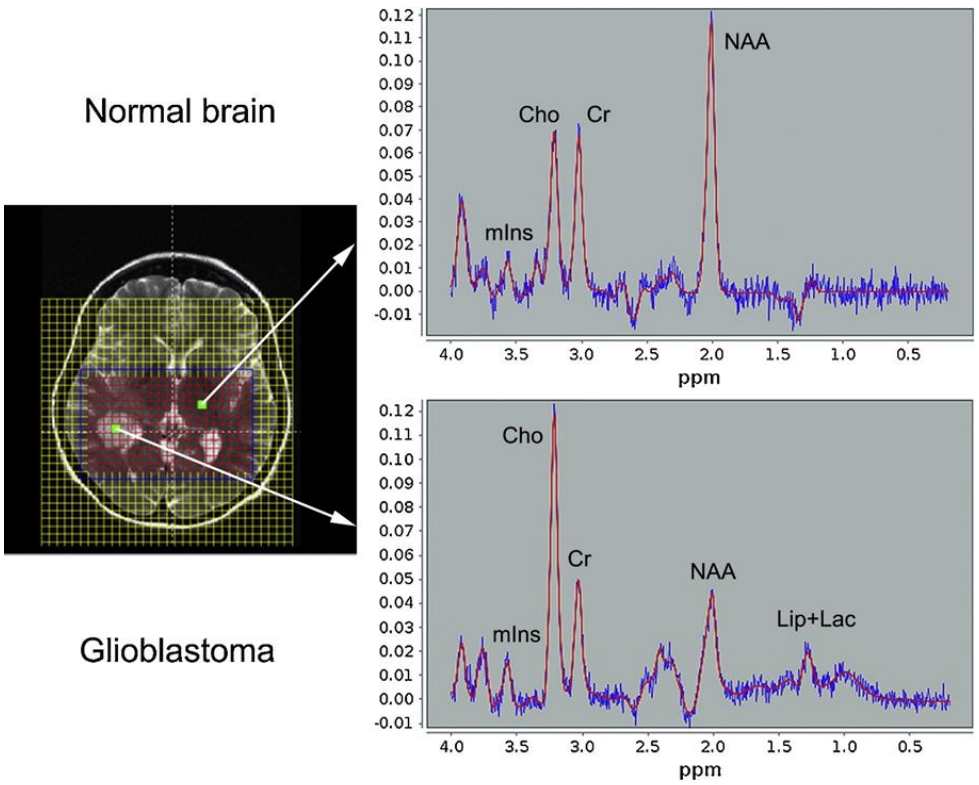

Figure 1.6 Single voxel spectroscopy of normal brain and glioblastoma (Bulik et al., 2013b).

Other metabolites can also be measured by MRS. In the normal brain, myo-inositol is a potential glial marker that is associated with glial proliferation (Soares and Law, 2009b). Glutamate is the major excitatory neurotransmitters in the brain. Since glutamate and glutamine are difficult to differentiate in spectroscopy, they are normally measured as Glx (Yahya et al., 2008). Lactate is a marker of anaerobic glycolysis that is associated with hypoxia or ischemia, whereas lipids may indicate the tissue damage which may be caused by anaerobic glycolysis (Moller-Hartmann et al., 2002). Previously, Glx and lactate + lipids were reported to be helpful in distinguishing high-grade and low-grade gliomas (Chawla et al., 2007).

Although not fully understood, most macromolecule (MM) peaks may be attributed to the amino acids of cytosolic proteins (Povazan et al., 2015). The MM peaks in the range 0.9-4.0 ppm overlap with other metabolite peaks, which poses significant challenges for evaluating the concentration of MM (Opstad et al., 2008, Povazan et al., 2015). As the lipids peak at 0.9 ppm is very difficult to separate with the MM peak at 0.87 ppm, they are normally expressed as a single measure (ML9) (Opstad et al., 2004, Opstad et al., 2008). Using an MM + lipids profiles, glioblastoma was reported to be differentiated from brain metastases with a specificity and sensitivity of 80% (Opstad et al., 2004).

The significance of MRS techniques in assessing tumour histology subtypes, malignancy grades and treatment response has been demonstrated in previous studies (Padhani and Miles, 2010, Howe et al., 2003, Julia-Sape et al., 2015). Using a tissue type basis set, the proportions of tumour tissue can be decomposed from the ^{1}H spectra in grade II and grade IV glioma patients, which would potentially be used to estimate tumour extent and delineation (Raschke et al., 2015a), suggesting the potential of this technique in tumour heterogeneity study. Furthermore, attempts have been made to integrate MRS technique into clinical practices. Incorporating with structural MRI, ^{1}H MRS has shown values in radiation and surgical planning (Norska and Barker, 2010).

Because of the heterogeneous cellular structure and metabolic status, glioblastoma normally displays highly heterogeneous metabolic patterns. This metabolic heterogeneity can be observed not only among patients, but also within each individual tumour. For example, in some tumour regions, due to the lack of blood supply, glioblastoma tends to undergo cell death because of hypoxia and displays higher proportions of necrosis. Thus, in these regions, a higher

level of Lac and Lip is frequently observed (Bulik et al., 2013b). Therefore, multi-voxel MRS will complement other MRI modalities in the evaluation of tumour heterogeneity, by providing important metabolic information.

1.9 Tumour habitat imaging

Although emerging advanced imaging techniques are developed, traditional imaging interpretation fails to address intra-tumoural heterogeneity comprehensively. Until recently, medical images are mainly qualitatively assessed by clinicians in common practice. Quantitative assessment of some imaging markers normally relies on the averaged values within the regions of interest. As such, the spatial information carried by tumour imaging may not be considered, which significantly limits the characterisation of tumour heterogeneity. Therefore, there is a rising clinical demand for developing quantitative imaging interpretation approach, which can be leveraged to address spatial and temporal tumour heterogeneity. The following sections will focus on the emerging post-processing analytic methods that show potential in the measurement of spatial tumour heterogeneity.

As discussed above, heterogeneity of glioblastoma may be caused by the intra-tumoural evolutional dynamics (Sottoriva et al., 2013a). Moreover, tumour microenvironment may also exhibit heterogeneity in microanatomy, constituents and metabolism (Lathia et al., 2011). In tumour biology, specialised compartments in the microenvironment are termed as tumour niches, which can not only harbour distinct tumour clones, but also facilitate clonal interaction and tumour evolution (Hambardzumyan and Bergers, 2015b). Multiple tumour niches exist within individual glioblastoma, including perivascular niche, hypoxic niche, and invasive niche (Hambardzumyan and Bergers, 2015a). These niches may display diversity in their biological characteristics and functional behaviours. Particularly, in the hypoxic niche, stem-like tumour cells may arise, mediated by hypoxia-inducible factors (HIF). These stem-like tumour cells are known to be resistant to treatment to other differentiated cells and may later contribute to tumour progression and aggressiveness (Hambardzumyan and Bergers, 2015a, Barcellos-Hoff et al., 2013, Plaks et al., 2015).

Tumour habitat imaging is a rising field that attempts to identify tumour sub-regions using multiple imaging modalities (Figure 1.7). The hypothesis of this approach is based on the different properties revealed by multiple imaging sequences. Thus, the combinations of high or low values of these sequences can reveal multiple tumour habitats with distinct traits, which were reported to be associated with signalling pathway, molecular subtype and patient survival of in glioblastoma patients (Dextraze et al., 2017, Lee et al., 2015).

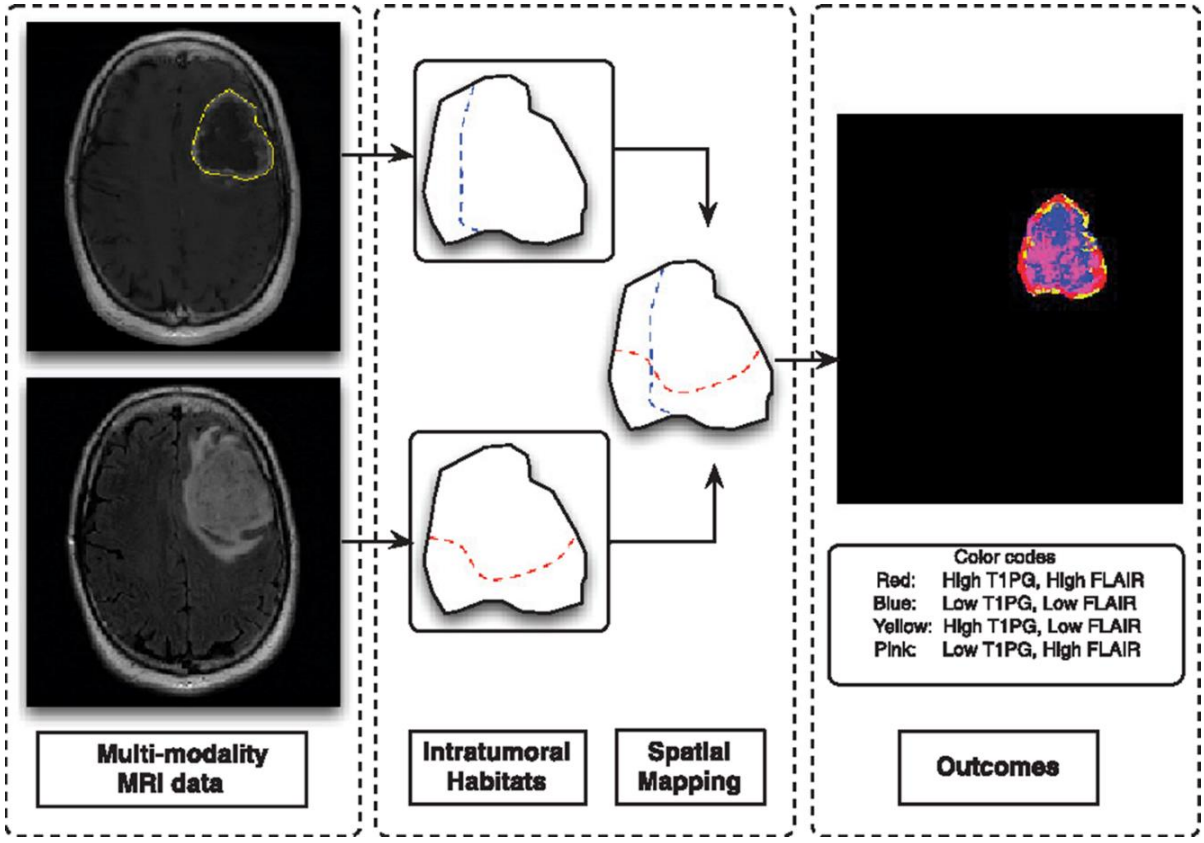

Figure 1.7 A case example of tumour habitats in glioblastoma. Four tumour habitats are identified by combining post-contrast T1-weighted and FLAIR images (Zhou et al., 2014).

In glioblastoma, angiogenesis often results in aberrant microvasculature in solid tumours, which is typically inefficient in resource delivery and may induce perfusion heterogeneity (Gillies et al., 1999). Additionally, significant variation of tumour cellularity can be observed within solid tumours. High or low cell densities can exist in either sufficiently or poorly perfused sub-regions, causing spatial variation in the tumour microenvironment (Gatenby et al., 2013). As we discussed above, perfusion imaging can measure the tumour vascularity,

which has been shown to be correlated to cellular proliferation in high-grade gliomas (Price et al., 2011). Diffusion weighted imaging provides information about the tissue microstructure (Kalpathy-Cranner et al., 2014), by measuring microscopic diffusivity of water molecules. Therefore, integrating physiological imaging may lead to a better characterisation of intra-tumoural habitats. Using this approach, the invasive tumour sub-regions in the non-enhancing region has been reported to be associated with patient survival (Boonzaier et al., 2017b).

1.10 Radiomics and radiogenomics

1.10.1 Definition and advantages

In the last decade, advances in image processing and computer vision have been achieved, which allows radiomics becoming a rapidly-developing area. Radiomics refers to an approach which can firstly extract high-throughput quantitative imaging features from subjects/regions of interest, and later use these features for tumour characterisation (Aerts et al., 2014b). These high throughput quantitative imaging features include those describing tumour shape, size, volume, intensity and texture characteristics (Aerts et al., 2014b, Kuo and Jamshidi, 2014). A large number of features allows for a more comprehensive measurement of tumours. Recent evidence showed that these imaging features carry important information that is correlated with clinical outcomes and molecular phenotypes (Li et al., 2016, Aerts et al., 2014a, Lao et al., 2017, Zhang et al., 2017, Grossmann et al., 2017). Thus, radiomics has great potentials in addressing glioblastoma heterogeneity, which would provide valuable significances for patient management (Limkin et al., 2017, Verma et al., 2017, Lambin et al., 2017). Below is an introduction of radiomics workflow and challenges.

1.10.2 Workflow

The workflow of radiomics involves a series of techniques, including feature extraction, feature selection, machine learning and model validation.

1.10.2.1 Tumour segmentation

Accurate segmentation of tumour regions of interest (ROIs) is central for the entire workflow. Segmentation includes both manual segmentation and automatic/semi-automatic segmentation. Although manual segmentation is commonly performed by experienced clinicians, it is a best practice to evaluate the consistency of the annotation, to avoid the inter-rater variability. Automatic or semi-automatic segmentation is more reproducible than manual segmentation, though the accuracy still needs further improvement, compared to clinical experts' annotation. Considerable efforts have been made to develop automatic algorithms to segment tumour regions accurately, trained by the ground truth annotated by clinical experts (Jones et al., 2015a, Petersen et al., 2017, Perkuhn et al., 2018).

1.10.2.2 Feature extraction

In general, two main radiomics feature sets can be extracted from the segmented tumour regions: semantic features and agnostic features (Gillies et al., 2016). Both semantic and agnostic radiomic features can be derived from multi-modality MRIs.

Semantic features

Semantic features are those descriptors used in clinical diagnosis or traditional imaging study. Normally these features are manually scored by clinicians using lexicons or guidelines from the radiology community. These features may be challenged by their reproducibility due to the inter-rater variability.

Visually Accessible Rembrandt Images (VASARI) Research Project, a standardised feature assessment system, was developed by TCGA radiology working group (https://wiki.nci.nih.gov/display/CIP/VASARI/). The VASARI lexicon consists of 30 features that describe tumour characteristics (Mazurowski et al., 2013). The assessment is based on T1-weighted, T2-weighted and FLAIR images. A set of features, such as tumour location, tumour size, the proportion of necrosis/enhancing tumour/oedema, are manually scored by clinicians. This feature set has been reported to predict survival and molecular subtype (Nicolasjilwan et al., 2015, Gevaert et al., 2015).

Agnostic features

Agnostic features are those computational metrics extracted from medical images with mathematical or statistical algorithms. Quantitative imaging features are automatically computed in high-throughput from the pre-defined ROIs. The most commonly-used features include intensity histogram, texture, and tumour shape/size features.

- **Intensity histogram features**

Voxel intensities within a tumour can be acquired voxel by voxel from the grey-level images. The intensity distribution of these voxels thus is described as a series of first-order statistics, including maximum, minimum, standard deviation, mean, median, nth centiles, skewness and kurtosis. The utility of rCBV histogram features in glioma grading and survival prediction has been previously reported (Emblem et al., 2008). Another study reported that pre-treatment ADC histogram features can predict response to treatment response to bevacizumab in recurrent glioblastoma (Pope et al., 2009). Therefore, histogram features have potentials in reflecting glioblastoma heterogeneity.

- **Texture features**

Texture analysis is a method complementary to histogram analysis in assessing tumour heterogeneity. A variety of mathematical or statistical methods are used to measure the relationship of pixel groups in medical images. Therefore, texture features can provide a series of measures reflecting the spatial distribution of voxel groups (Davnall et al., 2012). Previously, texture features have been used to distinguish spatial heterogeneity caused by regional oedema, vascularization, and necrosis (Ryu et al., 2014). In a retrospective of 79 glioblastoma patients, texture features from the pre-operative post-contrast T1-weighted images were reported to be robust predictors of patient survival (Molina et al., 2016).

Several types of texture metrics are commonly used: grey level co-occurrence matrix (GLCM), grey level run-length matrix (GLRLM), grey level size-zone matrix (GLSZM), and multiple grey level size-zone matrix (MGLSZM). Among them, the grey level co-occurrence features

are the most widely used feature set, which counts the voxel pairs of certain voxel values in different directions (Haralick et al., 1973). The features extracted using this method include homogeneity, variance, contest, energy and entropy, which can potentially quantify tumour heterogeneity (Haralick et al., 1973).

- **Shape features**

Shape features are developed to describe the geometrical properties of a tumour quantitatively. These features can be extracted from the 2D or 3D tumour volumetric structural images. The usefulness of shape features can be supported by the observation that the growth/invasion patterns lead to morphological variations of tumours and can be captured by shape-based features (Itakura et al., 2015). Shape features are reported to be associated with the disease stage and tumour invasiveness (Aerts et al., 2014b). The most commonly-used descriptors include tumour area, tumour perimeter, compactness, roughness, sphericity, curvature (Xu et al., 2012, Yap et al., 2013).

1.10.2.3 Machine learning model

After high-throughput features have been extracted, the feature interpretation is crucial for the following analysis. Machine learning algorithms are statistical methods that can be applied to imaging features for pattern recognition and endpoint prediction (i.e., clinical outcomes, molecular markers or histological subtypes) (Wang and Summers, 2012). Commonly-used machine learning algorithms include supervised learning and unsupervised learning (Zhou et al., 2018).

Supervised learning involves a training phase in which the algorithms are trained by ground truth or prior knowledge to tune the parameters of predictive models. According to the outputs, supervised learning methods typically include regression (outputs are continuous variables) and classification (outputs are classified as labels) (Wang and Summers, 2012). Random forest (RF) and support vector machine (SVM) are among the most popular supervised learning algorithms (Statnikov et al., 2008). In contrast, unsupervised learning helps to explore features purely based on the data structure without known outputs. The most common task for

unsupervised learning method is clustering. Popular unsupervised learning technique includes *k*-means, which aims to separate observations into k clusters, with all observations in each cluster have the nearest mean (Jain, 2010). To select the optimal model parameters and reduce the bias of feature/model selection, cross-validation procedure is recommended.

As discussed above, high-throughput radiomic features can be extracted from the radiographic images. However, a large feature number compared to the patient number may cause overfitting. Therefore, in the model selection stage, it is crucial to perform feature ranking and selection, which is an essential step before final model construction. An effective feature selection procedure can reduce feature redundancy and noise, providing the capability of selecting the most robust and informative imaging biomarkers for clinical decision making.

1.10.2.4 Independent validation

After the optimal models are tuned in the above process, there is a crucial need to validate the predictive model using another independent cohort. The purpose is to reduce the randomness of the model selection process. To test the generalization of the predictive model, the optimal independent validation cohort is from another research centre, preferably using a prospective clinical trial design.

1.10.3 Radiogenomics

Radiogenomics, which is an approach of establishing the associations between radiomics features with genomics features of diseases. Multiple benefits could be achieved through this association: firstly, the biological validation of imaging phenotypes revealed by radiomics approach could potentially be achieved (Gevaert et al., 2014). Secondly, by building the models predicting genetic markers/phenotypes, imaging features could be used as non-invasive surrogates for the genetic markers, which rely on the tissue obtained via the invasive procedure. Thirdly, since only a limited amount of samples can be taken from each individual patient, sub-regional imaging features may potentially be used to reflect the spatial tumour evolution and identify the hallmark driver mutations, by establishing the association between imaging

features and genomic features from multiple regional tissues, obtained through image-guided biopsy.

As such, radiogenomics approach can potentially provide a useful tool for intra-tumoural heterogeneity, since the imaging features are not limited to the sample(s) taken. In addition, it can facilitate longitudinal patient management in disease monitoring, and benefit patient evaluation by reducing the risk of invasive procedures. Further, by integrating clinical characteristics from large patient cohorts into the radiogenomics model, and the efficacy of radiomics/radiogenomics models can be significantly enhanced (Itakura et al., 2015, Aerts et al., 2014b).

1.10.4 Challenges and opportunities

1.10.4.1 Model reproducibility

There are several possible reasons that may significantly affect the reproducibility of imaging features. Firstly, the imaging acquisition and reconstruction may have an impact on the acquired images, as the downstream analysis is typically based on the assumption that all data are in the standard intensity distribution. However, since most radiomics studies are using retrospective cohorts, the imaging protocol of each individual patient can be various. Secondly, the radiomics process involves multiple procedures which may cause errors, including segmentation variability, model testing and parameter tuning. The significant findings may be generated by random in the pipeline. Thirdly, since a large number of features can be extracted from the radiomics pipeline, overfitting can be caused in the evaluation of imaging features and thus the predictive models constructed using these features.

There are several strategies which can potentially solve these challenges. Firstly, it is crucial to perform imaging normalisation or standardisation in the pre-processing step of the radiomics pipeline, to reduce the impact of heterogeneous imaging data generated from different scanners or protocols. Several normalisation techniques have been advanced to solve this challenge (Shinohara et al., 2014). A recent study evaluating the intensity normalization techniques in multiple sclerosis patients. The results showed that the decile based piece-wise linear normalization can provide a combination of better tissue discrimination and reasonable

computational cost (Shah et al., 2011). Developing effective methods with the consideration of glioblastoma heterogeneity is further needed.

Secondly, to reduce the randomness of in the radiomics pipeline. The experimental design is crucial for the validation of radiomics pipeline. For tumour segmentation, it is of significance to include the inter-rater variability test if manual or semi-automatic segmentation methods are adopted, as discussed above. For a rigorous model construction, separating the patients into a development, test and validation set is desirable for the study design. A cross-validation is recommended for each phase of model development, test and validation, in the evaluation of the model performance. Also, pseudo-randomization achieved by permutation test can also help to reduce selection randomness and improve reproducibility. A standardisation of the pipeline is still in crucial need for best practice.

Thirdly, to reduce the risk of overfitting, it is important to reduce the feature dimensionality and select the optimal features, as we mentioned above. Importantly, increasing the number of subjects would be helpful to improve the robustness of the model. To meet this demand, it has become the consensus from the community to establish imaging repository for data exchange or multiple centre collaboration.

1.10.4.2 Clinical validation

Most current radiomics/radiogenomics study are using retrospective cohorts, which limits the reliability of their clinical translational power. With the emergence of multiple omics, a large number of datasets is being generated and sophisticated research tools are being developed. The efficacy of these tools, however, should be tested and validated with the guidance of clinical criteria, including clinical prior knowledge. Further, to validate the clinical utilities of imaging biomarkers, it is crucial to test the models/features by considering the clinical hypothesis. As tumours are a complex evolving system, a clinical hypothesis-driven experimental design may have the potential to address clinical critical issues and meet clinical demands.

Therefore, future directions with clinical perspective consideration are crucial. Firstly, multiple disciplinary collaboration is demanded to further translate the radiomics approach into clinical

practice. This involves but not limited to 1) developing imaging modality or biomarkers with more specific tumour biology targeting; 2) exploiting statistical algorithms of feature extraction and analysis with a more clinically relevant hypothesis; 3) designing more disease or organ-specific analytic tools. Secondly, clinical trials involving standardised imaging setting, therapeutic regimen and outcome measure would be crucial, which would, therefore, facilitate the validation of imaging biomarkers with more clinical relevance. Thirdly, a prospective and longitudinal study design would be required for the clinical validation of radiomics approach, which would be critical to investigate the efficacy of radiomics features or predictive models.

1.11 Summary

Heterogeneity is one of the fundamental traits of glioblastoma, which poses a significant challenge to patient stratification. Understanding the mechanism of tumour heterogeneity is central for accurate diagnosis, targeted therapy and personalised treatment.

In past decades, advances in molecular biology have been achieved for a better understanding of glioblastoma heterogeneity. Most of the molecular markers, however, are based on invasive approach, which may increase the risks of patients and be prone to sampling error. There is a pressing but unmet need for the development of a non-invasive approach that could be used to measure tumour heterogeneity for disease monitoring and patient management.

Although widely used in clinical practice, conventional MRI bears the limitation of non-specificity in reflecting tumour physiology. Multiple advanced physiological MRI modalities have been developed, including perfusion and diffusion MRI, and MR spectroscopy. The imaging parameters that are generated from these quantitative advanced MRI can be used to measure tumour vascularity, cellularity and metabolism, respectively. Multi-parametric MRI shows great potentials in providing a more comprehensive measure of tumour heterogeneity non-invasively.

Tumour habitat imaging is a method that could be used for the identification of intra-tumoural habitats with different imaging characteristics. Radiomics is a rapidly developing research area, which can convert the medical images into high-throughput minable imaging features for

tumour characterisation. These approaches have shown diagnostic and prognostic values in various types of cancer, and thus would provide useful tools for heterogeneity evaluating and outcome prediction.

Currently, many attempts have been made to examine the utilities of habitat imaging and radiomics in the measurement of tumour heterogeneity and patient stratification. Most of the studies, however, are using conventional imaging techniques. Further studies are needed to investigate whether habitat imaging and radiomics are useful in evaluating inter-tumoural and intra-tumoural heterogeneity of glioblastoma, based on the pre-operative multi-parametric MRI.

Chapter 2 Hypothesis

2.1 General hypothesis

Pre-treatment multi-parametric MRI could be useful in revealing inter-tumoural and intra-tumoural heterogeneity in glioblastoma patients non-invasively. Such findings could provide biomarkers for patient survival prediction and future personalised treatment.

2.2 Hypotheses Tested

1. Glioblastoma may display an extensive intra-tumoural heterogeneous diffusion pattern. Particularly, tumour infiltration may be facilitated by white matter tracts and cause disruption. As discussed in Section 1.8.4, DTI is sensitive in detecting tumour infiltration by detecting water mobility, which can be decomposed into isotropic and anisotropic components. We hypothesised that a joint histogram analysis of isotropic and anisotropic diffusion components could differentiate tumour regions into sub-regions with different diffusion patterns, which may be useful for a better understanding of intra-tumoural heterogeneity of tumour infiltration. (Chapter 4)
2. As discussed in Section 1.9, intra-tumoural habitats can be revealed by multi-parametric MRI. Previous evidence showed that adaptive and resistant clones may exist in the low perfusion sub-regions, which cause treatment failure. As discussed Section 1.8, perfusion imaging can quantify tumour perfusion, whereas diffusion can reflect cellular structure by measuring water mobility. We hypothesised that two low perfusion compartments could be visualised and quantified using multi-parametric quantitative MRI. They both have lower perfusion but with different diffusivity. The tumour habitats identified using this approach may display different properties that could correlate with patient prognosis. (Chapter 5)

3. Multi-parametric MRI can not only reveal the intra-tumoural habitats, but also provides crucial information about inter-tumoural heterogeneity to reflect interpatient variation. With multiple imaging modalities developed, an effective method to integrate these modalities is lacking. We hypothesised that a multi-view feature selection and machine learning approach could effectively integrate histogram features from quantitative multi-parametric MRI. The selected imaging features using this approach may offer incremental values in survival prediction. (Chapter 6)
4. As we discussed in Section 1.8, multiple imaging modalities provide complementary information regarding tumour biology. Limited studies have addressed the overall inter-dependence between perfusion and diffusion imaging, which may help understand the tumour invasiveness. We hypothesised that the inter-dependence of perfusion and diffusion imaging can be characterised, which would provide useful information for evaluating tumour microenvironment. The imaging phenotypes revealed by this approach could be of prognostic value. (Chapter 7)
5. As discussed in Section 1.10, radiomics is can characterise a tumour using a large number of features extracted from the images. This approach has shown potential to predict the tumour genetic markers. As epigenetic change is crucial for tumour progression and may be impacted by tumour microenvironment, we hypothesised that using radiomics approach, physiological MRIs may provide improved accuracy than conventional structural MRIs, for the prediction of MGMT promoter methylation status. The predictive models constructed using the selected radiomic features could improve the prognostic performance. (Chapter 8)

We will test above hypotheses using a cohort which has been prospectively recruited for pre-operative multi-parametric MRI scanning. The imaging protocol included structural imaging (T1-weighted, T2-weighted, and FLAIR), perfusion, diffusion and MR spectroscopy. This cohort has been treated and followed up in Addenbrooke's Hospital. With available patient treatment response and outcome measures, this cohort would facilitate the hypothesis testing regarding tumour heterogeneity.

The details of patient recruitment and imaging protocol are detailed in Chapter 3. The general imaging processing pipeline is also detailed in Chapter 3, including brain extraction, DTI, DSC and spectroscopy processing, image co-registration, tumour segmentation, feature extraction and machine learning algorithms are introduced. The clinical details of the patients, including treatment regimen, evaluation of molecular markers, the extent of resection, post-operative response and progression are also introduced in Chapter 3.

In Chapter 4-8, multiple post-processing analytic techniques were applied to test the usefulness of tumour habitat imaging (Chapter 4-5), modality integration (Chapter 6), modality inter-dependence (Chapter 7) and radiomics (Chapter 8) in revealing intra-tumoural and inter-tumoural heterogeneity. In Chapter 9, a summary of the general limitations of this thesis and future directions are discussed.

Chapter 3 General Methods

3.1 Patient population

This study was approved by the local Institutional Review Board (ethics reference No.: 10/H0308/23). Acquisition of patients' data was granted by the NIHR funded "Magnetic Resonance Imaging to Characterise Invasive Phenotypes in Cerebral Gliomas" study (ISRCTN62033854). Informed written consent was obtained from all patients. Patient characteristics are demonstrated in Appendix A.

We included two patient cohorts in this thesis using the same inclusion and exclusion criteria. The main cohort was used in Chapters 4-7. In Chapter 8, we included another validation cohort to validate the radiomics model developed from the primary development cohort. The scanning parameters of the validation cohort are different from the primary development cohort.

3.1.1 Inclusion and exclusion criteria

Inclusion:

- Radiological diagnosis of supratentorial glioblastoma
- Age ≥ 18 years and ≤ 75 years
- Pre-operative World Health Organization performance status 0-1 (Karnofsky performance score ≥ 70)
- Suitable for craniotomy or biopsy
- Likely to receive concomitant chemoradiotherapy

Exclusion:

- Previous history of cranial surgery or cranial radiotherapy/chemotherapy
- Unsuitable for contrast-enhanced MRI scan

- Unconfirmed post-operative pathological diagnosis of GBM
- Pregnancy or plan for pregnancy
- Allergic to aminolevulinic acid or suffering from porphyria

3.1.2 Treatment and response evaluation

3.1.2.1 Treatment

To achieve maximal safe resection, surgery was performed with the guidance of neuro-navigation (StealthStation, Medtronic, Fridley, MN, USA) and 5-aminolevulinic acid fluorescence (5-ALA, Medac, Stirling, UK). The extent of resection was assessed according to the post-operative MRI scans acquired within 72 hours, and was classified as complete resection, partial resection of enhancing tumour or biopsy (Vogelbaum et al., 2012).

Concomitant temozolomide chemoradiotherapy (CCRT) and adjuvant chemotherapy (Stupp regimen) (Stupp et al., 2009) was performed after surgery as soon as possible, given patients' conditions were stable. During radiotherapy, concomitant TMZ chemotherapy was administered with a dose of 75mg/m^2/day, adjusted if patients' body weight changed. After radiotherapy, TMZ chemotherapy was continued for six circles, with the dose of 150-200mg/m^2/day for 5 days followed by a 28-day break. Other patients received short-course radiotherapy or best supportive care.

3.1.2.2 Evaluation of treatment response

Treatment response was evaluated according to the Response Assessment in Neuro-Oncology criteria (Wen et al., 2010), which incorporates clinical and radiological changes to identify progression. Pseudoprogression was suspected where new contrast enhancement appeared within first the 12 weeks after completing chemoradiotherapy. In such cases, treatment was continued and pseudoprogression was identified if later response occurred. As a result, in some cases, true progression was determined retrospectively.

In Chapter 4, to evaluate the progression volume in a subset of patients, available follow-up post-contrast T1-weighted images were collected by Dr Jiun-Lin Yan. The progression was determined on post-contrast T1-weighted images, excluding pseudoprogression according to above criteria. A volumetric analysis of the tumour progression was calculated after imaging co-registration, using a previously proposed approach (van der Hoorn et al., 2016).

For survival analysis of patients, relevant covariates, including IDH-1 mutation, MGMT promoter methylation status (assessments of IDH-1 mutation and MGMT methylation are detailed in Section 3.2), sex, age, the extent of resection and contrast-enhancing tumour volume, were accounted. Patients who were alive at the last known follow-up were censored. Following instances occurred in this patient cohort due to uncontrollable reasons: 1) some patients were lost in follow-up; 2) in some patients, MGMT promoter methylation status was missing.

3.2 Assessment of molecular markers

3.2.1 IDH-1 mutation

IDH-1 R132H mutation was firstly determined via immunohistochemistry. After the paraffin was removed and a heat-induced antigen retrieval was performed, IDH-1 R132H mutation-specific antibody (Dianova, Hamburg, Germany) was applied at a 1:20 dilution on slices. A secondary antibody avidin-based detection system was used. In patients for whom IDH-1 R132H mutation was not detected by immunohistochemistry, tumour DNA was extracted from tumour-rich tissue and sequenced for other rare IDH mutation in codon 132 of the IDH-1 gene and codon 172 of the IDH2 gene using the targeted next-generation sequencing (Ion AmpliSeq Cancer Hotspot Panel v2 and Ion PGM System, Thermo Fisher Scientific, Waltham, MA, USA).

3.2.2 MGMT promoter methylation status

MGMT promoter methylation status was evaluated as follows: DNA was extracted from the dissected neoplastic cell-rich tissue and was bisulphite-converted using the EpiTect Bisulphite

Kit (Qiagen, Hilden, Germany). Pyrosequencing of four CpG sites (CpGs 76-79) in exon 1 of the MGMT gene was performed using the CE-Marked therascreen MGMT Pyro Kit on a Pyromark Q24 System (Qiagen, Hilden, Germany). A cut-off of 10% mean methylation for the four CpG sites was used to determine tumours as either methylated or unmethylated, based on the previously published data (Collins et al., 2014, Dunn et al., 2009a).

3.3 MRI acquisition

Two patient cohorts were included in this thesis using different scanning protocols. All MRI sequences of the developmental cohort were performed at a 3-Tesla Siemens Magnetron MRI system (Siemens Healthcare, Munich, Germany) at Wolfson Brain Imaging Centre (WBIC) at Addenbrooke's Hospital, Cambridge, UK. All MRI sequences of the validation cohort were performed at a 3T system (MR750, GE Healthcare, Waukesha, WI) in Magnetic Resonance Imaging and Spectroscopy Unit (MRIS), Department of Radiology, University of Cambridge.

3.3.1 Pre-operative sequences

- Anatomical sequences: pre-contrast T1-weighted, post-contrast 3D T1-weighted imaging, T2-weighted, Fluid-attenuated inversion recovery (FLAIR)
- Diffusion Tensor Imaging (DTI) sequence
- Perfusion-weighted sequence: Dynamic Susceptibility Contrast (DSC) imaging
- MR spectroscopy (chemical shift imaging, CSI)

3.3.2 Imaging parameters

3.3.2.1 Structural imaging

1. Axial precontrast T1-weighted sequence (T1W): TR/TE 500/8.6ms; flip angle 90°; FOV 240 × 240 mm; slice thickness: 4 mm; slice gap: 1mm; voxel size 0.75 × 0.75 × 5 m.
2. Post-contrast T1-weighted imaging (T1C) was acquired after intravenous injection of 9 mL gadobutrol (Gadovist, 1.0 mmol/mL; Bayer, Leverkusen, Germany) followed by

a 20-mL saline flush. Scanning parameter: TR/TE/TI 2300/2.98/900 ms; flip angle 9°; FOV 256 × 240 mm; slice thickness: 1 mm; no slice gap; voxel size 1.0 × 1.0 × 1.0 mm.

3. T2-weighted sequence (T2W): TR/TE 4840-5470/114 ms; refocusing pulse flip angle 150°; FOV 220 x 165 mm; 23-26 slices; 0.5 mm slice gap; voxel size of 0.7 × 0.7 × 5.0 mm.
4. T2-weighted fluid attenuated inversion recovery (FLAIR): TR/TE/TI 7840-8420/95/2500 ms; refocusing pulse flip angle 150°; FOV 250 × 200 mm; 27 slices; 1 mm slice gap; voxel size of 0.78 × 0.78 × 4.0 mm.

3.3.2.2 Physiological imaging

1. Diffusion tensor imaging (DTI) was acquired using a single-shot echo-planar sequence. The setting is: TR/TE 8300/98 ms; flip angle 90°; FOV 192 × 192 mm; 63 slices; no slice gap; voxel size 2.0 × 2.0 × 2.0 mm; 12 directions; b values: 350, 650, 1000, 1300, and 1600 sec/mm^2; scanning time: 9 minutes 26 seconds.
2. Dynamic susceptibility contrast-enhancement (DSC): TR/TE 1500/30 ms; flip angle 90°; FOV 192 × 192 mm; 19 slices; slice gap 1.5 mm; voxel size of 2.0 × 2.0 × 5.0 mm;) with 9 mL gadobutrol (Gadovist 1.0 mmol/mL) followed by a 20 mL saline flush.

3.3.2.3 Chemical shift imaging

Multi-voxel 2D ^{1}H-MRS chemical shift imaging utilized a semi-LASER sequence (TR/TE 2000/30-35 ms; flip angle 90°; FOV 160 × 160 mm; voxel size 10 × 10 × 15-20 mm). PRESS excitation was selected to encompass a grid of 8 rows × 8 columns on T2-weighted images.

3.3.2.4 Imaging protocol of validation cohort

Axial T1-weighted imaging: TR/TE/TI: 8.2/3.2/450ms; slice thickness: 1mm; flip angle 12°; FOV 100 × 100 mm;), after intravenous injection of 9 mL gadobutrol (Gadovist,1.0

mmol/mL; Bayer, Leverkusen, Germany), post-contrast T1-weighted imaging was acquired; Axial T2-weighted imaging: TR/TE/TI: 5226/8ms; flip angle 111°; FOV 100 × 100 mm; slice thickness: 6mm; FLAIR: TR/TE/TI: 8000/125/2158 ms; flip angle 111°; FOV 80 × 80 mm; slice thickness: 7mm; DTI: TR/TE 8000/88ms; flip angle 90°; FOV 100 × 100 mm; slice thickness: 3mm; 64 directions; b values 1000 sec/mm2; DSC: TR/TE 2000/17 ms; flip angle 60°; FOV 100 ×100 mm; slice thickness: 6mm, with 9 mL gadobutrol followed by a 20 mL saline flush.

3.4 MRI processing

After imaging acquisition, all images were anonymised and stored in the WBIC server. Data were firstly retrieved from the server and processed in a standardized pipeline for each subject, as shown in Figure 3.1.

All images are converted from Digital Imaging and Communications in Medicine (DICOM) format to Neuroimaging Informatics Technology Initiative (NIFTI) format for further analysis. The process of downloading and sorting was routinely performed using the Shell functions in WBIC server.

Different modalities were analysed separately using an in-house pipeline. For anatomical images, the brain extraction was performed to strip the skull for further co-registration in FSL (FMRIB Software Library) v5.0.8 (Smith et al., 2004, Jenkinson et al., 2012). For perfusion imaging, leakage correction was performed in NordicICE (NordicNeuroLab, Bergen, Norway), before calculating perfusion markers. For diffusion tensor imaging, a standard processing pipeline was followed, according to the manual of FMRIB's Diffusion Toolbox (FDT) (Jellison et al., 2004).

After processing of all imaging modalities, co-registration was performed by using T2-weighted images as reference. Subsequently, regions of interest (ROI) were either manually delineated or automatically generated using algorithms on relevant modalities, according to the research questions addressed in each separate study.

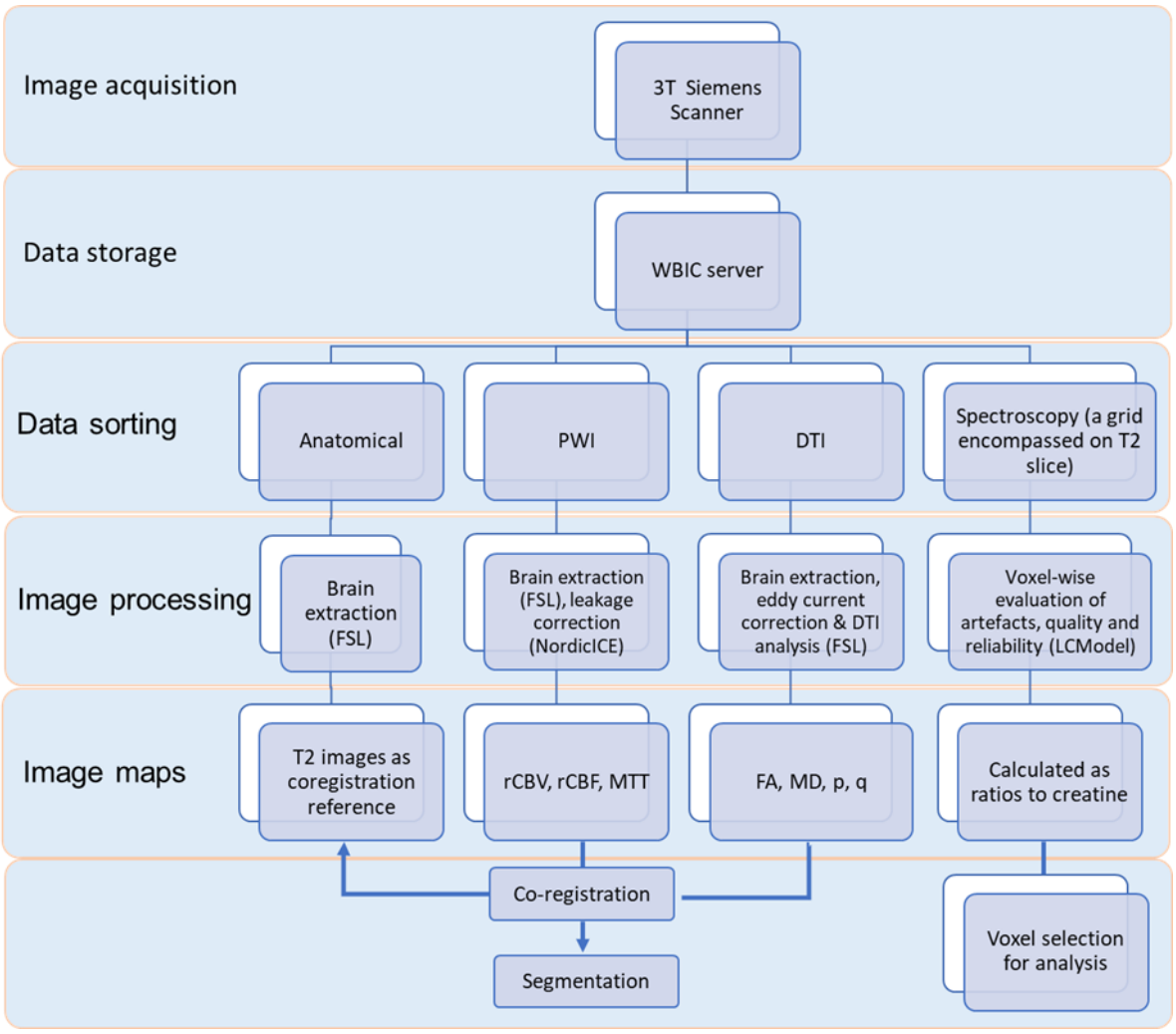

Figure 3.1 Overview of the image processing pipeline

3.4.1 Brain extraction

Prior to the processing pipeline, the skull-stripping of all images was performed using the function 'bet' in FSL. This process was firstly done automatically, which can generate a binary brain mask (Figure 3.2). This mask was then manually corrected slice by slice. The raw images with the skull were then multiplied by the corrected binary mask, using the function 'fslmaths' in FSL.

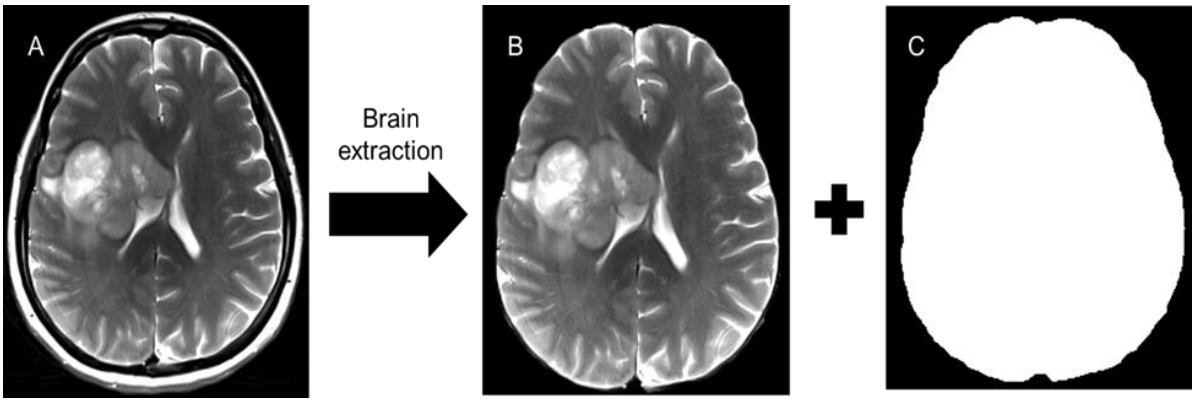

Figure 3.2 A demonstration of brain extraction. After brain extraction, the skull is stripped from the T2-weighted images (A). The brain map (B) and brain mask (C) are generated.

3.4.2 DTI processing

3.4.2.1 Eddy current correction

Eddy current was caused by the strong magnetic field gradients flanked by short ramp times in diffusion-weighted echo-planar imaging (EPI). The eddy current can induce stretches and shears in the diffusion weighted images, which may cause significant image distortions and artefacts (Bodammer et al., 2004). Therefore, eddy current correction is crucial for the tensor measure and must be performed before the following DTI analysis. This process was done by using the function 'eddy_correct' in FDT. A new function 'eddy' has been released in the new version for better distortion correction.

3.4.2.2 Diffusion tensor analysis

Diffusion tensor was generated from the images using the function of 'dtifit'. The default output parameters of this process include a series of parameters (https://fsl.fmrib.ox.ac.uk/fsl/fslwiki/FDT/UserGuide), including FA, L1, L2, L3, MD, MO, SO, V1, V2 and V3. The detailed description of these parameters can be found the Table 3.1 and demonstrated in Figure 3.3.

Table 3.1 Outputs of DTI analysis

Output	Description
V1, V2, V3	1st, 2nd, and 3rd eigenvectors
L1, L2, L3 $(\lambda_1, \lambda_2, \lambda_3)$	1st, 2nd, and 3rd eigenvalues
MD	mean diffusivity
FA	fractional anisotropy
MO	mode of the anisotropy (oblate ~ -1; isotropic ~ 0; prolate ~ 1)
S0	raw T2 signal with no diffusion weighting (b0 images)

With the function of 'fslmaths' built-in FSL, DTI-p and -q were calculated from the outputs of FDT, according to below equations (Pena et al., 2006a). DTI-p and -q maps are generated. For clinical utility, ADC maps were derived directly from the scanner using b-values 0-1000 sec/mm^2.

$$p = \sqrt{3}\, MD$$

$$q = \sqrt[2]{(\lambda_1 - MD)^2 + (\lambda_2 - MD)^2 + (\lambda_3 - MD)^2}$$

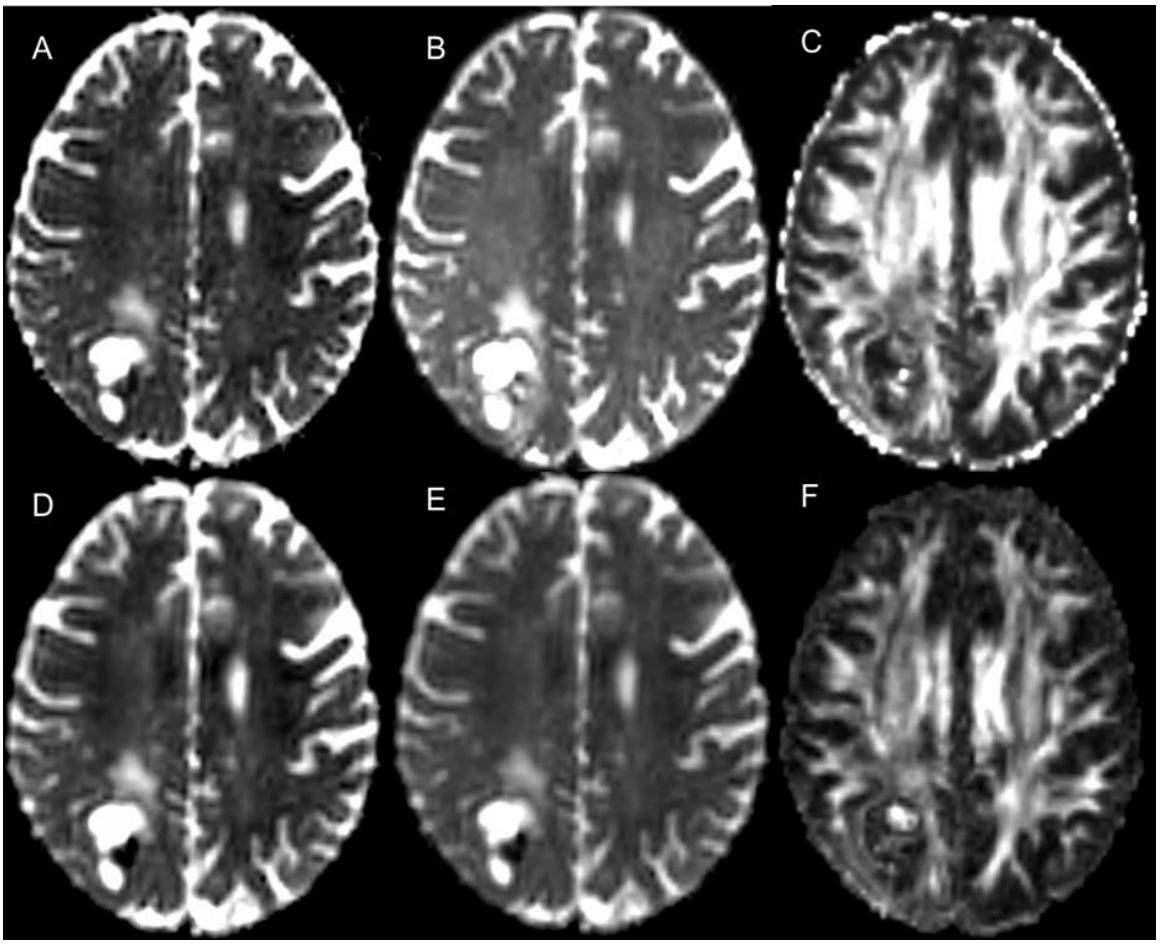

Figure 3.3 A demonstration of resultant images from DTI analysis. The ADC map is directly calculated from the scanner and brain extraction is performed in FSL using 'bet' function (A). The tensor analysis is performed in FDT, which generates a series of outputs, including b0 map (B), FA (C) and MD map (D). DTI-p (D) and DTI-q (E) were then calculated using 'fslmaths' function in FSL according to the definition equation.

3.4.3 DSC image processing

DSC data was processed using the module of perfusion analysis in NordicICE. Brain extraction was firstly applied for further co-registration.

The pre-bolus baseline images were automatically detected and defined as the entire period before the first pass. Spatial or temporal smoothing is not applied to reduce potential confounders (Hu et al., 2015). The artery input function was defined using automatic detection.

Contrast agent leakage correction was then applied, with Gamma variate function enabled (Figure 3.4).

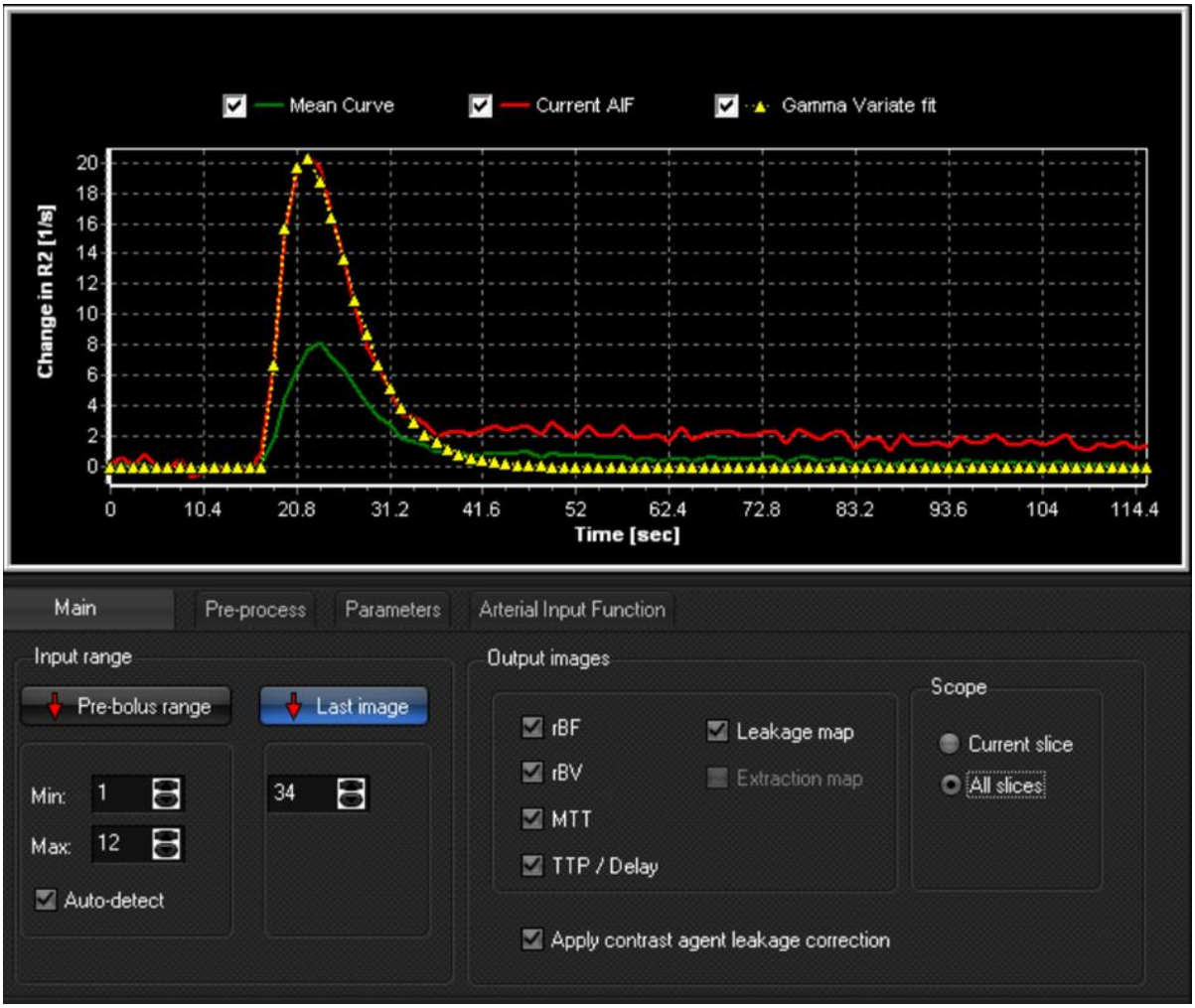

Figure 3.4 Perfusion analysis and leakage correction using NordicICE

After processing, the value of relative cerebral blood volume (rCBV), relative cerebral blood flow (rCBF), time to peak (TTP) and mean transit time (MTT) were calculated and parametric maps were produced. A demonstration of the raw perfusion weighted image and perfusion-weighted markers is in Figure 3.5.

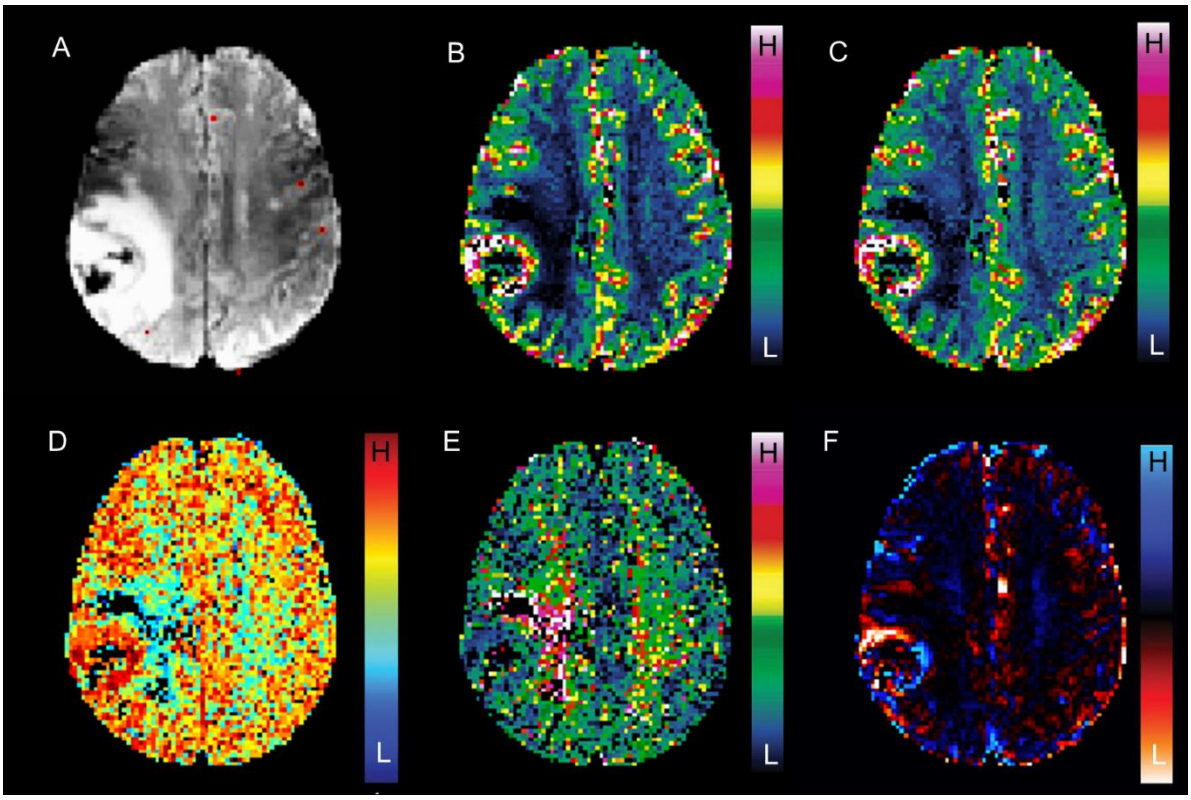

Figure 3.5 An illustration of the perfusion weighted images and perfusion markers derived after leakage correction. A: raw perfusion weighted image. B-F: leakage-corrected maps with NordicICE. B: rCBV; C: rCBF; D: MTT; E: delay map; F: leakage map.

3.4.4 MRS processing

Multi-voxel MR spectroscopy data were acquired using the T2-weighted slices for spectroscopy planning in scanning (Figure 3.6), which were visually selected by experienced neuro-radiologists. A grid of 8 rows × 8 columns were then superimposed to the selected T2 slice for voxels analysis. An example of the superimposed grid on T2-space slice is shown in Figure 3.6. The voxels for analysis are from 5 to 12 (rows and columns).

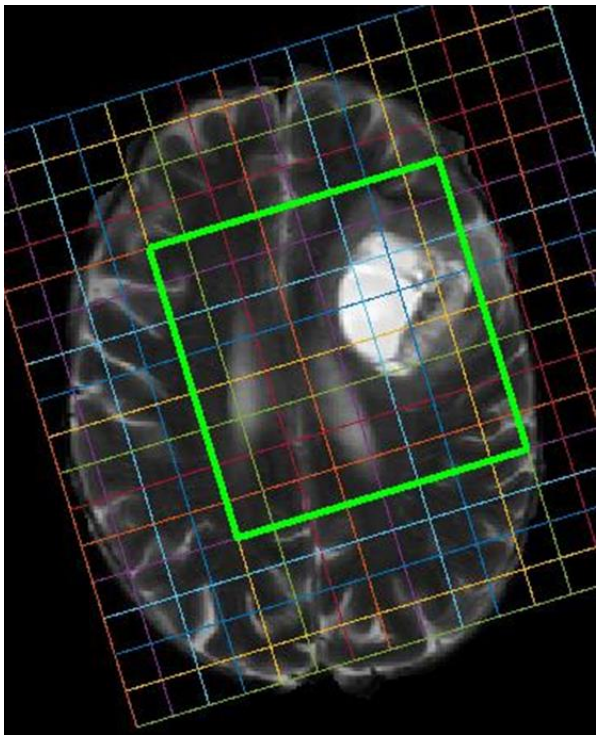

Figure 3.6 A grid is superimposed on the selected T2-weighted image.

The acquired MRS data from the multiple voxels in the grid were then processed using LC Model (Provencher, Oakville, Ontario) using default setting (Provencher, 2001, Raschke et al., 2015b). All relevant spectra from MRS voxels of interest were visually assessed for artefacts using previously published criteria (Kreis, 2004). The LC Model processing was performed by Dr Natalie R Boonzaier, a previous lab member.

The values of the Cramer-Rao lower bounds indicated by the LC Model program were used to evaluate the quality and reliability of MRS data and measured concentration values. The Cramer-Rao lower bounds values standard deviation (SD) greater than 20% were discarded (Price et al., 2016). For each grid, the peak size of metabolites was calculated and then normalised by the value of total creatine (Cr) of in the same voxel, to avoid the dilution effect caused by tumour-associated oedema (Wijnen et al., 2012). Therefore, the final concentrations of metabolites were expressed as a ratio to creatine (Cr). The selection and normalisation were performed by using an in-house MATLAB script written by Dr Timothy Larkin, a previous senior member of Cambridge Brain Tumour Imaging Laboratory. It is of note that the

normalisation using Cr is limited by the regional and individual variability, as well as the spatial variations caused by the sensitivity of receive coil.

3.4.5 Imaging co-registration

3.4.5.1 Pre-operative images

Image co-registration was performed in FSL. Since all pre-operative MRIs were acquired at the same time point, their co-registration was performed using FMRIB's linear image registration tool (FLIRT) functions (Jenkinson et al., 2002). As the spectroscopy has been planned on T2-weighted images, all the other pre-operative images were co-registered to T2-weighted images, using 12 degrees of freedom with affine transformation (Chapter 5- 8). In Chapter 4, to investigate the tenor decomposed components specifically, anatomical images were co-registered to DTI B0 images with an affine transformation using FLIRT.

- **Co-registration to T2 images**

In Chapter 5-8, all images were co-registered to T2 images, as CSI was planned on the T2 slices. The co-registration scheme is as follows: FLAIR images were firstly co-registered to T2-weighted images. Before co-registering to T2-weighted images, the pre-contrast and post-contrast T1-weighted images were co-registered to FLAIR images. The respective transformation matrix in co-registration was saved. Considering the contrast effect of T1-weighted imaging and FLAIR are similar, this procedure may lead to a better co-registration quality than direct co-registering T1-weighted images to T2-weighted images. Next, the function 'convert_xfm' was used to concatenate the two transformation matrices (T1-weighted to FLAIR, and FLAIR to T2-weighted), to create a new transformation matrix that was applied to co-register T1-weighted images to T2-weighted images.

For the co-registration of diffusion imaging, b0 image was firstly co-registered to T2-weighted images, with the transformation matrix saved. This matrix was later applied to ADC, MD, FA, p and q maps, after the DTI analysis pipeline was performed. Similarly, the co-registration of perfusion weighted imaging to T2-weighted images was firstly performed. The transformation matrix was then applied to co-register rCBV, rCBF and MTT to T2-weighted images.

- **Co-registration to DTI images**

In Chapter 4, to investigate the effects of directional diffusivity to tumour infiltration, the raw tensor was firstly decomposed and the b0 images were firstly derived. To avoid the potential distortion of co-registration to the raw tensor. The co-registration to b0 images was performed, which transformed T2-weighted, T1-weighted, FLAIR, perfusion-weighted images to tensor space using FLIRT, with the transformation matrix.

3.4.5.2 Progression images

In Chapter 4, to evaluate the effects of different diffusion patterns to tumour progression rate, tumour progression was analysed in a subset of 57 patients with available follow-up images in the development cohort. The progression data were collected by Dr Jiun-Lin Yan. The true progression was determined by the multi-disciplinary team in Neuro-Oncology clinic, with the consideration of both radiological and clinical measurement. For the co-registration between progression images with pre-operative images, a two-stage non-linear semi-automatic co-registration tool was applied, which was developed by previous lab members, Dr Anouk van der Hoorn and Dr Jiun-Lin Yan (van der Hoorn et al., 2016). Briefly, this coregistration method firstly calculated the transformation matrix between the pre-operative lesion and tumour cavity on progression images. The matrix was then applied to the brain parenchyma using the non-linear coregistration tool of FMRIB's non-linear image registration tool (FNIRT) functions in FSL. Quality of the co-registration was visually inspected by the Dr Jiun-Lin Yan, Dr Anouk van der Hoorn and Dr Natalie R Boonzaier.

3.4.6 Tumour segmentation

3.4.6.1 Manual segmentation

To delineate the tumour margin on the conventional imaging, a manual segmentation was performed on the post-contrast T1-weighted images and FLAIR images slice by slice, using an open source software 3D Slicer v4.6.2 (Surgical Planning Laboratory, Brigham and Women's Hospital, Boston, MA, USA; www.slicer.org), a medical image computing platform (Fedorov et al., 2012).

1. Contrast-enhancing (CE)-ROI

The contrast-enhancing (CE) lesion on T1-weighted images was defined as all the area within the contrast-enhancing margin. The segmented volume is considered as the tumour core, which is associated with the leakage caused by neovasculature (Figure 3.7: right).

2. FLAIR-ROI

The FLAIR abnormality delineates the diffuse tumour invasion and oedema regions, as demonstrated as the hyperintense signals on T2-weighted FLAIR image (Figure 3.7: left).

To reduce the variability of the manual segmentation, the inter-rater reliability testing was performed by Dr Natalie R Boonzaier, a researcher with > 4 years of brain tumour image analysis experience and reviewed by Dr Tomasz Matys, a neuroradiologist with > 8 years of experience. Inter-rater reliability testing of regions of interest (ROIs) showed excellent agreement between the raters, with Dice scores (mean ± standard deviation [SD]) of 0.85 ± 0.10 and 0.86 ± 0.10 for contrast-enhancing and FLAIR ROIs respectively.

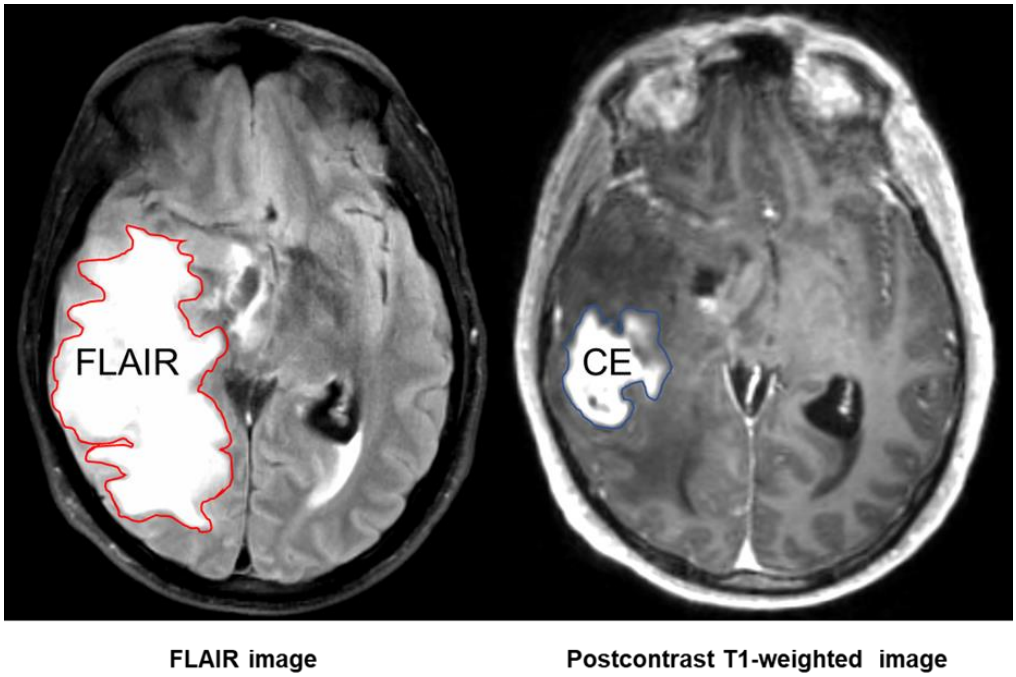

Figure 3.7 Tumour are manually delineated on FLAIR and post-contrast T1-weighted images respectively and two tumour ROIs are obtained.

3. Non-enhancing (NE)-ROI

The non-enhancing (NE)-ROI, defined as the FLAIR abnormalities outside of contrast enhancement, were obtained in MATLAB (MathWorks, Natick, MA, USA) by a Boolean subtraction on contrast-enhancing and FLAIR ROIs. This ROI is considered to delineate the infiltrative regions outside of CE region (Figure 3.8).

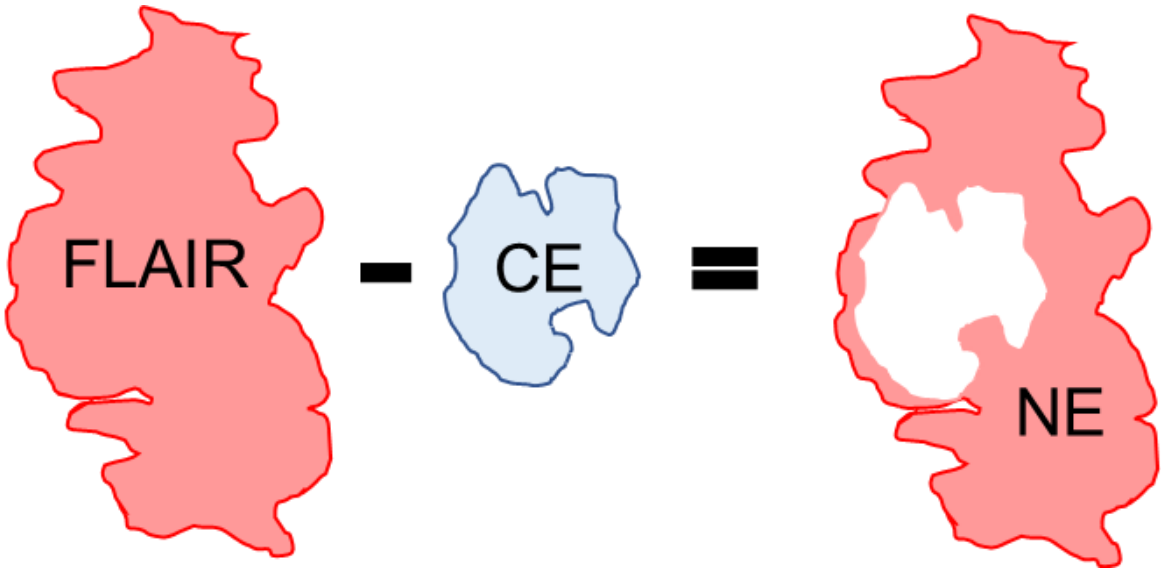

Figure 3.8 Non-enhancing region is obtained from FLAIR and post-contrast T1-weighted images using Boolean subtraction in MATALB.

4. Normal-appearing white matter

A region of 10mm in diameter from the contralateral normal-appearing white matter was manually reviewed and determined. It is typically located in the white matter which has the longest distance from the tumour location and has no perceivable abnormalities. This procedure has provided fair controls in the previous publication (Boonzaier et al., 2017b).

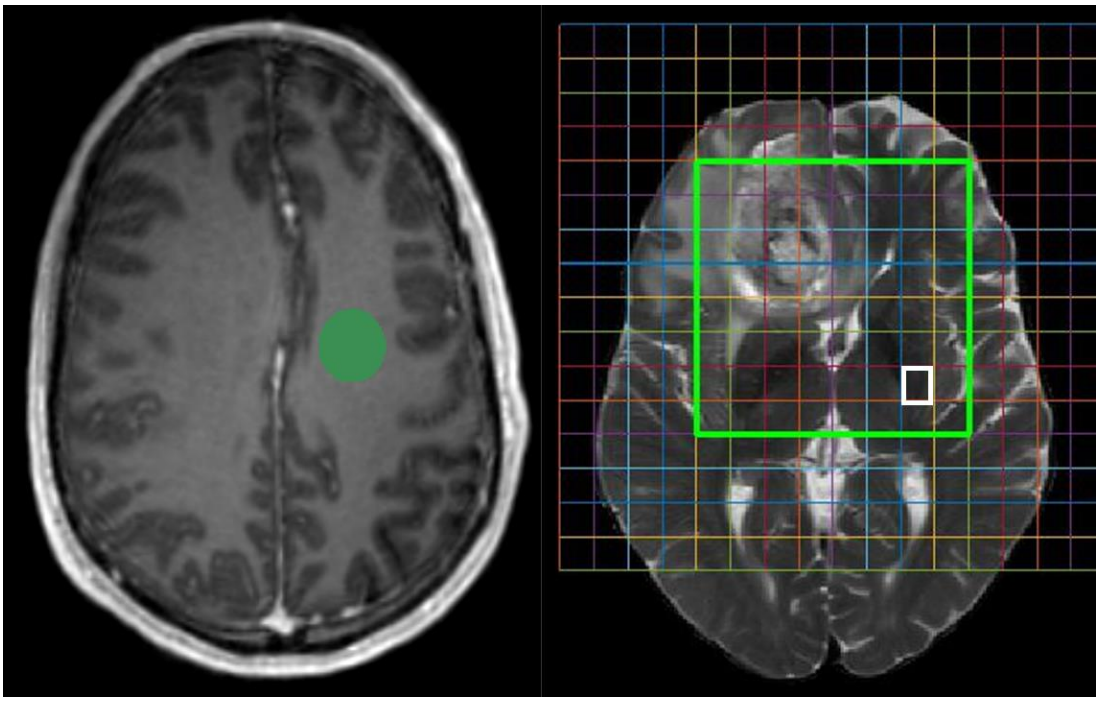

Figure 3.9 Normal-appearing white matter (green) on structural images (left) and the normal control grid (white) for CSI analysis (right)

3.4.6.2 Hypothesis-driven segmentation (tumour habitats)

Spatial habitats were identified using the combinations of high or low pixel values of multi-parametric physiological imaging sequences. This selection of the combinations was determined according to the relevant clinical hypotheses. For example, to interpret the habitats with different diffusion properties, multiple combinations of isotropic and anisotropic components of DTI were used, with a joint histogram method (Chapter 4). To reveal the low perfusion compartments with different diffusivity, subsets of ADC and rCBV values were used, with a thresholding method (Chapter 5).

3.4.7 Image analysis

3.4.7.1 Volumetric analysis

The raw volumes of the ROIs were calculated in FSL using the function 'fslstats'. To reduce the bias, all masks have been binarized before used for further analysis. The proportional volumes were calculated as a ratio of ROI in the contrast-enhancing volume or FLAIR volume.

3.4.7.2 Feature extraction

1. **Univariate and joint histogram features**

Histogram analysis was performed using the Statistics and Machine Learning Toolbox of MATLAB. Each voxel of DTI-p and -q in tumour ROIs was normalized by dividing it by the mean value in the contralateral normal-appearing white matter. The univariate histograms were constructed with the normalized voxels using 100 bins. Histogram features, i.e., mean, median, standard deviation, kurtosis, skewness, were then calculated from the histogram (Chapter 4 & 6). In Chapter 4, we also proposed a joint histogram analysis, to characterise the joint distribution of DTI components for the identification of multiple intra-tumoural infiltrative habitats. The methods are detailed in Chapter 4.

2. **Radiomic features**

Radiomic features were extracted automatically in MATLAB v2017b (MathWorks, Natick, MA), using open-source codes available in Github (Echegaray et al., 2017). The extracted image features include following feature sets: shape features, margin features, intensity features and grey-level co-occurrence matrix (GLCM) texture features. The methods and descriptions of feature sets are detailed in Chapter 8.

3.4.7.3 Machine learning

1. **Unsupervised learning**

A supervised learning method, the Multi-View Biological Data Analysis (MVDA), was used in unsupervised clustering of patients (Chapter 6). This method was implemented in R and available from GitHub (https://github.com/angy89/MVDA). The details of this approach are in Chapter 6.

2. Supervised learning

To select the optimal predictive models for MGMT methylation status, four supervised learning methods were compared in Chapter 8, including support vector machines, random forest, naïve Bayes, and neural network.

Support vector machines (SVM) can transform features into a higher dimensional space and calculate a maximal margin hyperplane to separate data into different classes. We used a Gaussian radial basis function kernel-based SVM algorithm implanted in R Package 'kernlab'.

Random forest (RF) is a classification scheme that uses an ensemble of decision trees. The individual decision tree is constructed with random subsets of training sets and features, and then applied to test sets for classification. We used random forest algorithm implanted in R Package 'ranger'.

Naïve Bayes (NB) algorithm calculates the posterior distributions of the unknown parameters in the joint model of the observed data and the unknown parameters, based on Bayes' theorem. We used the Naïve Bayes algorithm implanted in R Package 'naivebayes'.

Neural network (NN) is based on a collection of artificial neurons. Each artificial neuron can process inputs and pass the outputs to the connected artificial neurons. The weight of the artificial neurons and connections are trained and applied to the testing set. We used a feed-forward neural network with a single hidden layer implanted in Package 'nnet'.

3.4.7.4 Multi-voxel MRS analysis

Since the spatial resolution between CSI and other MRI modalities are significantly different, it is challenging to measure the metabolic state of ROIs in T2-space. Voxels from T2-weighted MRIs were projected onto CSI space according to their coordinates using MATLAB. Thus, the metabolic status in each voxel could be matched to the voxels in the physiological images,

which were co-registered to T2-weighted images. The proportion of T2-space tumour voxels occupying each MRS voxel was calculated, and MRS voxels were selected according to the threshold defined in subsequent studies for further analyses. The projection of T2 space voxels to CSI space is demonstrated in Figure 3.10. A case example with the demonstration of spectra is demonstrated in Figure 3.11.

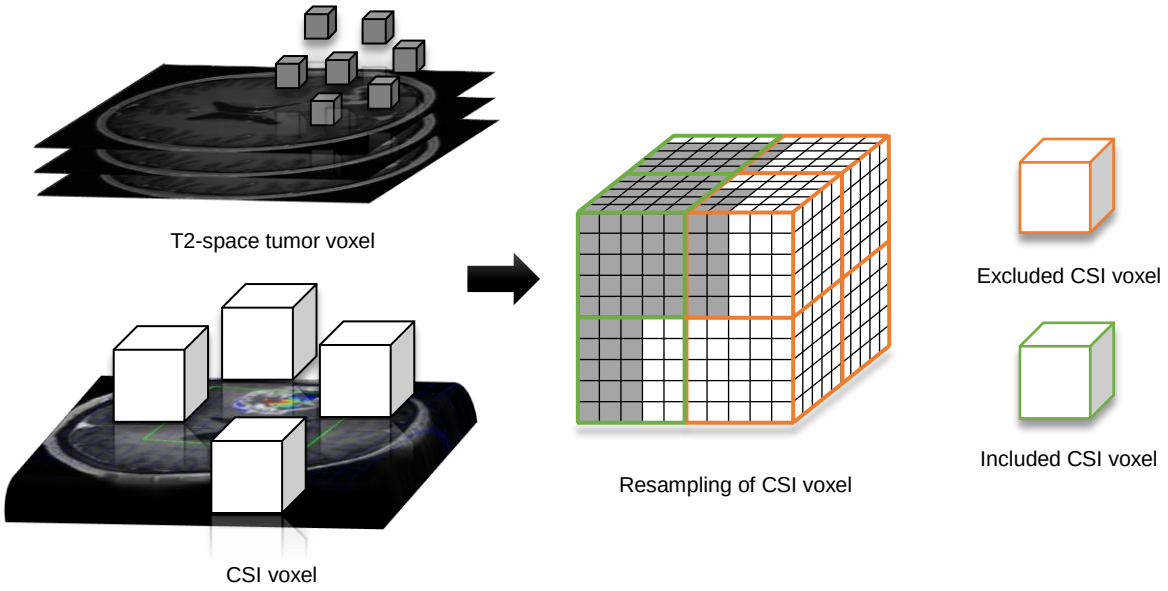

Figure 3.10 An illustration of projecting T2 space voxel into CSI voxels. As the CSI was planned on T2-weighted images, the T2-space tumour voxels (grey cubes) can be projected to CSI voxels (white cubes) according to their coordinates. After projection, the proportion of T2-space tumour voxels in CSI voxels can be calculated. A threshold can be used as the inclusion criteria. In this example, a threshold of 50% is used. Since only in the green CSI voxels, T2-space tumour voxels occupy more than 50%. Thus, only the green CSI voxels are included for further analysis, whereas orange voxels are excluded.

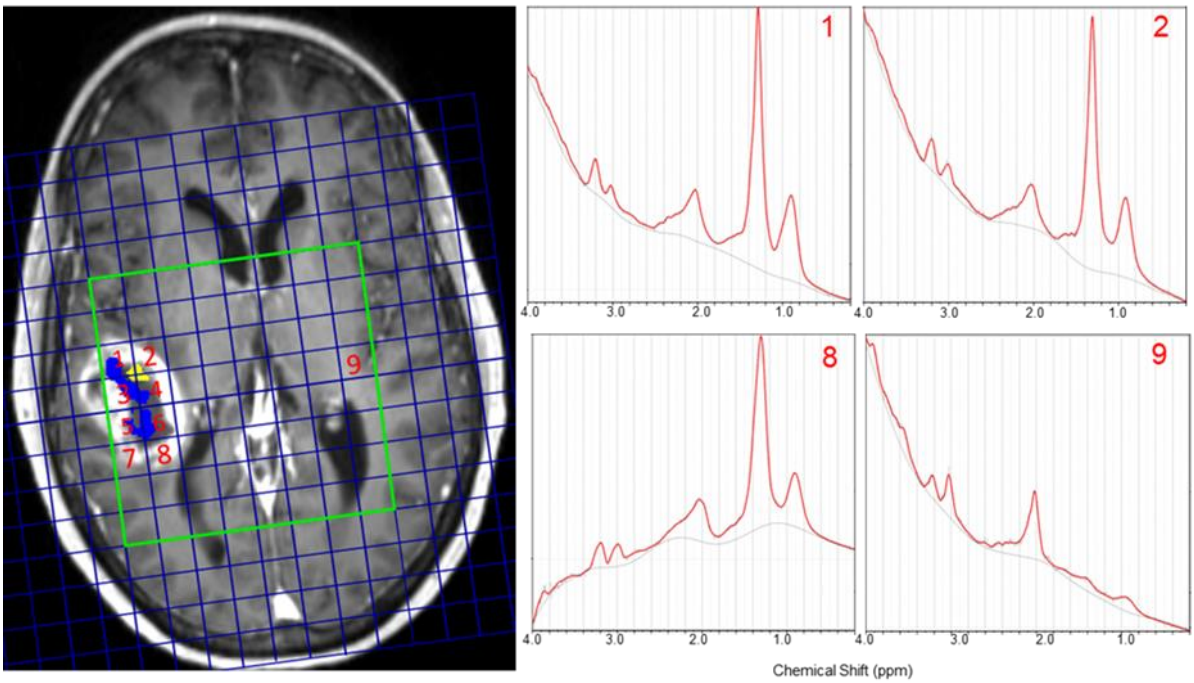

Figure 3.11 Illustration of multiple voxel MRS analysis. Left: the selection criteria. The T2-space pixels were projected to CSI space according to their coordinates. The proportion of T2-space tumour pixels occupying each CSI voxel was calculated. A criterion was applied that only those CSI voxels were included when the proportion of tumour voxels are over 50%. In this case, grid 1-8 met the criteria. The proportion of the tumour voxels in the ROI was taken as the weight of each CSI voxel in the ROI. The summed weighted value was used as the final metabolic value of two compartments. Right: Example spectra of two compartments, abnormal control (CEC) and normal control (NAWM).

Other imaging analysis methods are specified and detailed in relative chapters (Chapter 4-8) respectively.

Chapter 4 Intra-tumoural Heterogeneity of Glioblastoma Infiltration Revealed by Joint Histogram Analysis of Diffusion Tensor Imaging

4.1 Abstract

Background

Glioblastoma is a heterogeneous disease characterized by its infiltrative growth, rendering complete resection impossible. Diffusion tensor imaging (DTI) shows potential in detecting tumour infiltration by reflecting microstructure disruption.

Objective

We aimed to explore the heterogeneity of glioblastoma infiltration using a joint histogram analysis of DTI, to investigate the incremental prognostic value of infiltrative patterns over clinical factors, and to identify specific sub-regions for targeted therapy.

Methods

A total of 115 primary glioblastoma patients were prospectively recruited for surgery and pre-operative MRI. The joint histograms of decomposed anisotropic and isotropic components of DTI were constructed in both contrast-enhancing and non-enhancing tumour regions. Patient survival was analysed with joint histogram features and relevant clinical factors. The incremental prognostic values of histogram features were assessed using receiver operating

characteristic curve analysis. The correlation between the proportion of diffusion patterns and tumour progression rate was tested using Pearson correlation.

Results

We found that joint histogram features were associated with patient survival and improved survival model performance. Specifically, the proportion of non-enhancing tumour sub-region with decreased isotropic diffusion and increased anisotropic diffusion was correlated with tumour progression rate ($P = 0.010$, $r = 0.35$), affected progression-free survival (hazard ratio = 1.08, $P < 0.001$) and overall survival (hazard ratio = 1.36, $P < 0.001$) in multivariate models.

Conclusion

Joint histogram features of DTI showed incremental prognostic values over clinical factors for glioblastoma patients. The non-enhancing tumour sub-region with decreased isotropic diffusion and increased anisotropic diffusion may indicate a more infiltrative habitat and potential treatment target.

4.2 Introduction

As we discussed in Chapter 1, glioblastoma is characterised by its extensive heterogeneity in the tumour clonal composition (Sottoriva et al., 2013b, Verhaak et al., 2010). It is recognized that glioblastoma is also heterogeneous in its infiltrative pattern. Migratory clones within a tumour may result in a more infiltrative phenotype, which may be especially responsible for treatment failure (Giese et al., 2003). A previous study showed that the migratory phenotype of a subset of cells can predict tumour recurrence (Smith et al., 2016). Understanding the intra-tumoural heterogeneity of glioblastoma infiltration is of clinical significance for targeted surgery and radiotherapy.

Magnetic resonance imaging (MRI) has unique advantages in understanding spatial structural variations within glioblastoma. Current clinical management is primarily based on structural sequences, among which the post-contrast T1-weighted imaging is most widely-used. This approach, however, provides limited quantitative information about tumour infiltration, as stated in section 1.8.2. Other sequences, such as fluid attenuated inversion recovery (FLAIR), although integrated into clinical assessment (Wen et al., 2010), is still considered to be non-specific for differentiating tumour infiltration from oedema and delayed radiation white matter change (Price et al., 2006).

As discussed in Section 1.8.4, diffusion tensor imaging (DTI) is a method that measures the magnitude and direction of water molecule movement and has been shown to be sensitive in detecting tumour infiltration (Price et al., 2017). Glioblastoma cells may preferentially migrate along white matter tracts and cause disruption (Hambardzumyan and Bergers, 2015b). The diffusion of water molecules in the tumour and the peritumoural brain is consequently altered. By decomposing the tensor into isotropic (DTI-p) and anisotropic (DTI-q) components, the directional diffusion can be measured (Pena et al., 2006a). This approach has been found useful in predicting tumour progression and patient survival (Price et al., 2007, Mohsen et al., 2013). It remains to be discovered, however, whether integrating these components can offer a more comprehensive measure of tumour infiltration. Furthermore, molecular biomarkers, such as isocitrate dehydrogenase (IDH) mutations(Parsons et al., 2008b) and oxygen 6–methylguanine-DNA methyltransferase (MGMT) promoter methylation (Hegi et al., 2005a),

are reported to be of diagnostic and prognostic significance for glioblastoma. One previous study has shown that IDH mutant glioblastoma is less invasive determined by DTI maps (Price et al., 2017). Whether the DTI markers, particularly DTI-p and -q, can provide additional prognostic value to molecular markers is unclear.

The purpose of this study was to explore the heterogeneity of glioblastoma infiltration using joint histogram analysis of DTI, to investigate the incremental prognostic value of infiltrative patterns over clinical factors, and to identify specific sub-regions that may be suitable for targeted therapy. The hypothesis was that joint histogram analysis of diffusion parameters can differentiate anatomically-defined regions into sub-regions with different diffusion patterns of prognostic value.

4.3 Methods

4.3.1 Study design

We prospectively and preoperatively recruited patients with an initial radiological diagnosis of supratentorial primary glioblastoma from July 2010 to August 2015. The inclusion and exclusion criteria are in Section 3.1.1. This study was approved by the local institutional review board. Signed informed consent was obtained from all patients. Patient treatment is detailed in Section 3.1.2.1. Assessment of IDH-1 mutation and MGMT methylation status are described in 3.2.

4.3.2 Pre-operative MRI acquisition

A 3-Tesla MRI system (Magnetron Trio; Siemens Healthcare, Erlangen, Germany) was used. Pre-operative DTI, post-contrast T1-weighted imaging, T2-weighted imaging and T2-weighted FLAIR were acquired for all the subjects pre-operatively. Sequence details are provided in 3.3.2.2. All patient underwent MRI within 72hrs postoperatively.

4.3.3 Image processing

DTI was processed with FSL v5.0.8, as described in Section 3.4.2. DTI-p and -q were calculated using previously described equations (Pena et al., 2006a). Anatomical images were co-registered to DTI with an affine transformation, using FLIRT (Jenkinson et al., 2002). Tumour ROIs were manually drawn as described in 3.4.6.1.

4.3.4 Histogram analysis

Histogram analysis was performed in the Statistics and Machine Learning Toolbox of MATLAB. Contrast-enhancing and non-enhancing ROIs were analysed independently. A demonstration of histogram analysis is shown in Figure 4.1. Each voxel of DTI-p and -q in tumour ROIs was normalized by dividing it by the mean value in the contralateral normal-appearing white matter as discussed in Section 3.4.6, which has been used in previous studies as a robust normalisation technique (Boonzaier et al., 2017b, Yan et al., 2017). The univariate histograms of DTI-p and -q were constructed with the normalized voxels using 100 bins (Figure 4.1. A & B). The mean, median, 25th and 75th percentile of the histogram were calculated.

The joint histogram was constructed with the x-axis and y-axis representing the normalized DTI-p and -q values respectively, using 50 × 50 bins on both axes (Fig 4.1. C). Each voxel within the tumour was assigned to a corresponding bin in the 3D space, according to the DTI-p and -q values they carried. Since the voxel values were normalized as above, the coordinator point ($p = 1$, $q = 1$) was designated to represent the diffusion pattern in the contralateral normal-appearing white matter, which was calculated as the mean value of DTI-p and DTI-q in the regions of interest, as described above. Thus, four voxel groups describing the co-occurrence distribution of DTI-p and -q abnormality were obtained (Fig 1. D), namely:

I. Voxel Group I (decreased DTI-p/decreased DTI-q, $p\downarrow/q\downarrow$)
II. Voxel Group II (decreased DTI-p/increased DTI-q, $p\downarrow/q\uparrow$)
III. Voxel Group III (increased DTI-p/increased DTI-q, $p\uparrow/q\uparrow$)
IV. Voxel Group IV (increased DTI-p/decreased DTI-q, $p\uparrow/q\downarrow$)

The proportion of each voxel group in the ROI was used as joint histogram features, obtained from both contrast-enhancing and non-enhancing tumour regions, providing eight features per patient.

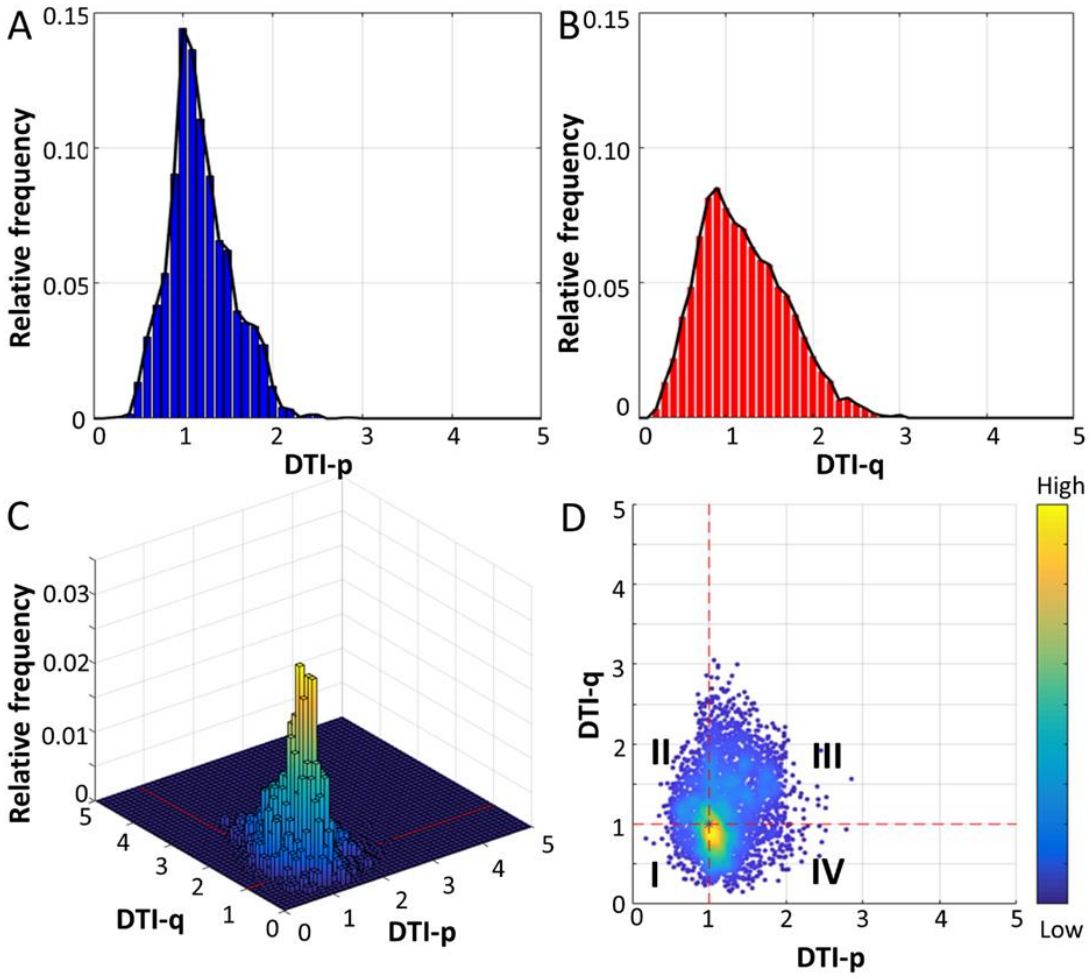

Figure 4.1 Illustration of the univariate and joint histogram analysis. Univariate histograms of DTI-p (A) and -q (B) were constructed using 100 bins. The joint histogram was constructed with x- and y-axis representing DTI-p and -q values using 50 × 50 bins. The bin height of the joint histogram represented the relative frequency of voxels falling into a specific DTI-p and -q range (C). Four voxel groups of DTI-p and -q abnormalities were obtained (D): I. Voxel Group I (decreased DTI-p/decreased DTI-q); II. Voxel Group II (decreased DTI-p/increased DTI-q); III. Voxel Group III (increased DTI-p/increased DTI-q); IV. Voxel Group IV (increased DTI-p/decreased DTI-q).

4.3.5 Evaluation of treatment response and tumour progression

The extent of resection and treatment response were assessed as described in 3.1.2. The time to tumour progression was defined as the period between surgery date and the date of first post-contrast T1-weighted images that showed progression (as determined by a consultant neuroradiologist). Available progression images were reviewed with the collaboration of Dr Jiun-Lin Yan and Dr Rory J Piper. A two-stage semiautomatic co-registration between the progression images and pre-operative post-contrast T1-weighted images was performed using a previously reported tool (van der Hoorn et al., 2016, Yan et al., 2017). This coregistration method firstly calculated the transformation matrix between the pre-operative lesion and tumour cavity on progression images. The matrix was then applied to the brain parenchyma using FNIRT in FSL. After coregistration, the progression tumour volume was calculated using FSL function of fslmaths. The progression rate was defined as progression volume normalized by time to progression.

4.3.6 Statistical analysis

All statistical analyses were performed in RStudio v3.2.3 (Rstudio, Boston, MA, USA). Histogram features or tumour volume were assessed using Wilcoxon signed rank test. Survival was evaluated in patients who have received concurrent TMZ chemoradiotherapy followed by adjuvant TMZ post-operatively. Cox proportional hazards regression was performed, accounting for relevant covariates, including IDH-1 mutation, MGMT methylation, sex, age, the extent of resection and contrast-enhancing tumour volume. Patients who were alive at the last known follow-up were censored. For Kaplan-Meier analysis, continuous variables were dichotomized using optimal cutoff values, calculated by the R Package “survminer” (https://cran.r-project.org/web/packages/survminer/). Logistic regression models were used to test prognostic values of covariates for 12-, and 18-month OS and PFS. The baseline models were firstly constructed using all above relevant clinical covariates. Specific histogram features were then added one by one into the baseline model to assess their incremental prognostic value, by comparing the area under the receiver operator characteristics curve (AUC) using one-way ANOVA. To select prognostic variables, multivariate Cox regression was performed, using forward and backward stepwise procedures. The forward procedure started from the

model containing only one covariate and add one covariate in each step, whereas the backward procedure initiated from the model containing all covariates and delete one covariate in each step. For each step, the model was evaluated using the Akaike Information Criterion (AIC). The final models were constructed using the covariates selected by this procedure. Correlations between variables were tested using the Pearson correlation test. The hypothesis of no effect was rejected at a two-sided level of 0.05.

4.4 Results

4.4.1 Patients

We prospectively recruited 136 patients into the study. After surgery, 115 (84.6%) histologically confirmed glioblastoma patients (mean age 59.3 years, range 22 - 76 years, 87 males) were included. A flowchart of patient recruitment is demonstrated in Figure 4.2. Clinical characteristic of 115 included patients is summarized in Table 4.1.

Of the 115 patients, 84 (73.0 %) patients received concurrent temozolomide (TMZ) chemoradiotherapy followed by adjuvant TMZ, post-operatively. Other patients received a short-course radiotherapy (17.4%, 20/115) or best supportive care (9.6%, 11/115), due to their poor post-operative performance status. Survival data were available for 80 of 84 (95.2%) patients that were treated with CCRT and 4 (4.8%) patients were lost to follow up.

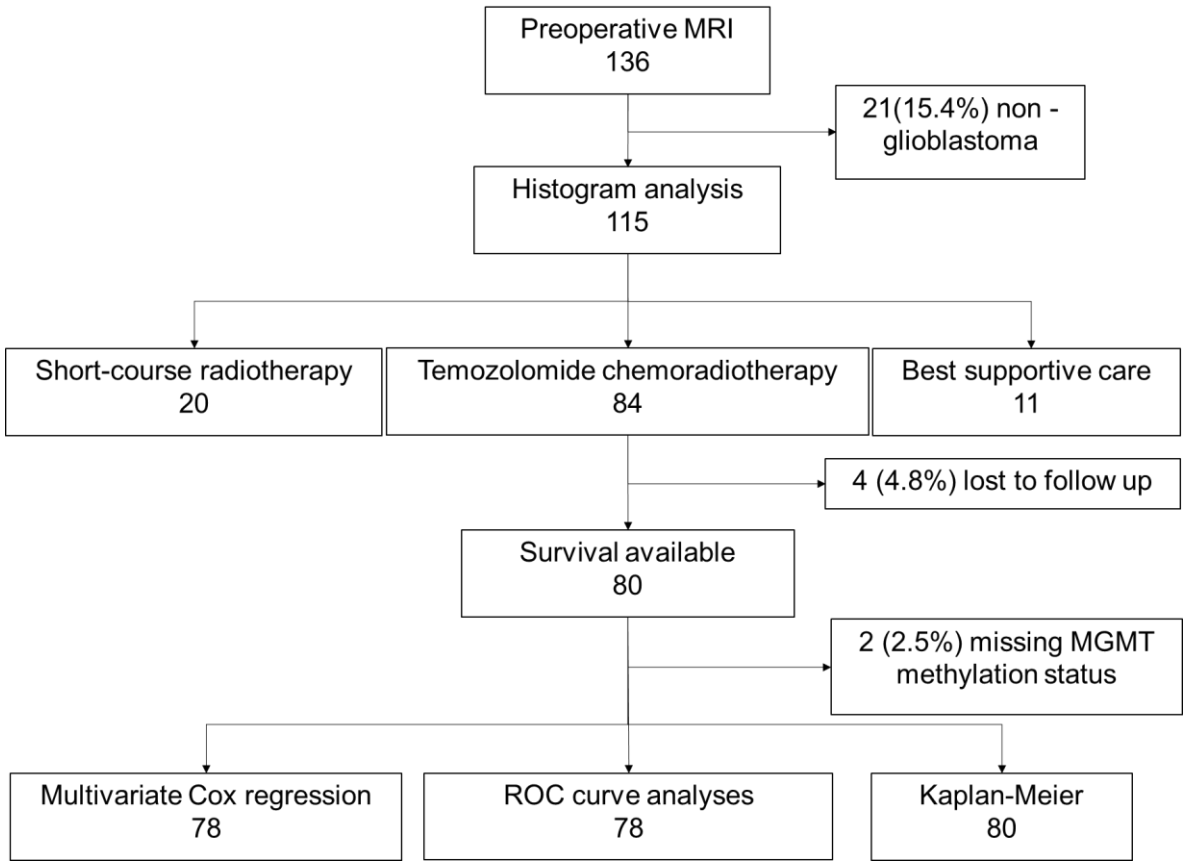

Figure 4.2 Flowchart showing how patients were excluded. A total of 136 patients with a radiological diagnosis of glioblastoma were prospectively recruited and underwent surgery. Twenty-one patients were excluded because of non-glioblastoma pathology diagnosis. Histogram analysis was performed on the pre-operative MRIs of 115 glioblastoma patients. Among these patients, 84 patients received concurrent temozolomide (TMZ) chemoradiotherapy followed by adjuvant TMZ after surgery. Four patients were lost to follow up. Since MGMT methylation status was missing in two patients, multivariate Cox regression and receiver operator characteristics curve analyses were performed on 78 patients. Twenty-seven patients who were alive at the last known follow-up or died of other disease were censored.

Table 4.1 Clinical characteristics

Variables	Patient Number
Age at diagnosis	
<60	40
≥60	75
Sex	
Male	87
Female	28
Extent of resection (of enhancing tumour)	
Complete resection	77
Partial resection	32
Biopsy	6
MGMT-methylation status*	
Methylated	48
Unmethylated	63
IDH-1 mutation status	
Mutant	7
Wild-type	108
Tumour volumes(cm3) #	
Contrast-enhancing	53.6 ± 33.8
Non-enhancing	62.5 ± 44.0
Survival (days)	
Median OS (range)	424 (52 -1376)
Median PFS (range)	262 (25-1130)

*MGMT-methylation status unavailable for 4 patients; #mean ± SD of original data. SD: standard deviation; MGMT: O-6-methylguanine-DNA methyltransferase; IDH-1: Isocitrate dehydrogenase 1; cm: centimeter; OS: overall survival; PFS: progression-free survival.

4.4.2 Diffusion signatures of contrast-enhancing and non-enhancing regions

The diffusion signatures of ROIs are demonstrated in Table 4.2. For univariate histogram features, both contrast-enhancing and non-enhancing regions displayed increased DTI-p (all values greater than 1). A decreased DTI-q (all values less than 1) was consistently observed in the contrast-enhancing region, whereas non-enhancing regions displayed increased mean and 75th percentile of DTI-q. In accordance with the univariate histogram, joint histogram analysis showed that Voxel Group IV (increased DTI-p/decreased DTI-q, p↑/q↓) accounted for the largest proportion in tumours.

Table 4.2 Histogram features

Variables	contrast-enhanced region	non-enhancing region	*P* value
	Mean ± SD	Mean ± SD	
DTI-p histogram features			
25th percentile	1.18 ± 0.23	1.11 ± 0.15	**< 0.001**
Median	1.47 ± 0.38	1.32 ± 0.23	**0.001**
Mean	1.57 ± 0.36	1.37 ± 0.22	**< 0.001**
75th percentile	1.90 ± 0.60	1.59 ± 0.30	**< 0.001**
DTI-q histogram features			
25th percentile	0.42 ± 0.14	0.71± 0.18	**< 0.001**
Median	0.65 ± 0.19	0.95 ± 0.23	**< 0.001**
Mean	0.71 ± 0.19	1.01 ± 0.24	**< 0.001**
75th percentile	0.93 ± 0.24	1.24 ± 0.29	**< 0.001**
DTI Joint histogram features (%)			
Voxel Group I	8.50 ± 10.37	5.49 ± 6.17	**< 0.001**
Voxel Group II	3.83 ± 4.92	7.27 ± 8.07	**< 0.001**
Voxel Group III	20.78 ± 13.65	40.33 ± 18.97	**< 0.001**
Voxel Group IV	66.90 ± 16.28	46.92 ± 20.40	**< 0.001**

DTI: diffusion tensor imaging; p: isotropic component; q: anisotropic component; SD: standard deviation; Voxel Group I: decreased DTI-p, decreased DTI-q (p↓/q↓,); Voxel Group II: decreased DTI-p, increased DTI-q (p↓/q↑); Voxel Group III: increased DTI-p, increased DTI-q (p↑/q↑); Voxel Group IV: increased DTI-p, decreased DTI-q (p↑/q↓).

4.4.3 Multivariate survival analysis

The multivariate survival model of PFS and OS were fitted in 78 patients for whom all relevant covariates were available (Table 4.3). Five joint histogram features were significantly associated with survivals. Specifically, higher proportions of Voxel Group II (p↓/q↑), in both contrast-enhancing and non-enhancing regions, were associated with worse survival (in contrast-enhancing region, PFS: HR = 1.06, P = 0.036; OS: HR = 1.09, P = 0.004; in non-enhancing region, PFS: HR = 1.08, P < 0.001; OS: HR = 1.11, P < 0.001). The Kaplan-Meier curves are demonstrated in Figure 4.3, with P values from the Log-rank test.

Table 4.3 Cox multivariate modelling of survivals

Variables	Progression-free survival*			Overall survival*		
	HR	**95%CI**	***P* value**	**HR**	**95%CI**	***P* value**
Contrast-enhancing region						
Voxel Group I	1.02	0.990-1.049	0.205	1.03	1.000-1.064	0.049
Voxel Group II	1.06	1.004-1.128	0.036	1.09	1.028-1.156	0.004
Voxel Group III	1.01	0.989-1.025	0.449	1.01	0.988-1.028	0.432
Voxel Group IV	0.98	0.968-1.001	0.061	0.98	0.960-0.996	0.015
Non-enhancing region						
Voxel Group I	1.02	0.975-1.057	0.463	0.997	0.947-1.049	0.904
Voxel Group II	1.08	1.041-1.128	<0.001	1.11	1.064-1.165	<0.001
Voxel Group III	1.01	0.996-1.026	0.145	1.01	0.997-1.026	0.116
Voxel Group IV	0.98	0.969-0.996	0.014	0.98	0.969-0.997	0.015

*Cox models accounted for each histogram feature and all covariates of sex, age, extent of resection, IDH-1 mutation status, MGMT methylation status and contrast-enhancing tumour volume. MGMT: O-6-methylguanine-DNA methyltransferase; IDH-1: Isocitrate dehydrogenase 1; HR: hazard ratio; CI: confidence interval; Voxel Group I: decreased DTI-p, decreased DTI-q (p↓/q↓); Voxel Group II: decreased DTI-p, increased DTI-q (p↓/q↑); Voxel Group III: increased DTI-p, increased DTI-q (p↑/q↑); Voxel Group IV: increased DTI-p, decreased DTI-q (p↑/q↓).

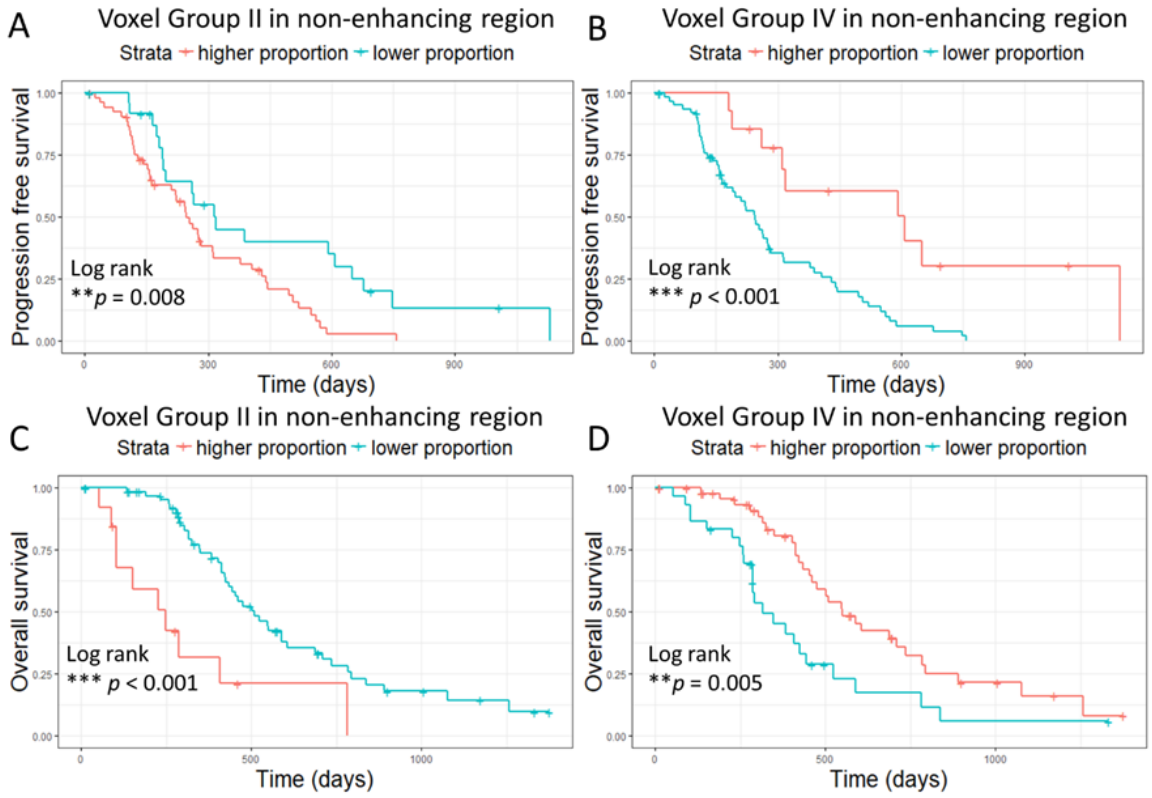

Figure 4.3 Kaplan-Meier plots of survival analysis. The proportions of voxel groups were dichotomized using optimal cutoff values calculated in R. Log-rank test showed higher proportion of Voxel Group II in non-enhancing tumour region was associated with worse PFS ($P = 0.008$, cut off value 2.3%) (A) and worse OS ($P < 0.001$, cut off value 12.8%) (C). Lower proportion of Voxel Group IV in non-enhancing tumour region was associated with worse PFS ($P < 0.001$, cut off value 65.9%) (B) and worse OS ($P = 0.005$, cut off value 36.9%) (D).

4.4.4 Incremental Prognostic Value of Joint Histogram Features

The results of model comparisons are shown in Table 4.4. Six joint histogram features significantly improved the model (each $P < 0.05$): Voxel group I (p↓/q↓), Voxel group II (p↓/q↑), Voxel group IV (p↑/q↓) in the contrast-enhancing region, and Voxel group II (p↓/q↑), Voxel group III (p↑/q↑), Voxel group IV (p↑/q↓) in the non-enhancing region. Particularly, Voxel Group II (p↓/q↑) in the non-enhancing region significantly improved the 12-month and 18-month survival models.

Table 4.4 Model Comparisons

Model	12 month AUC	95% CI	*P* value	18 month AUC	95% CI	*P* value
Progression-free survival						
baseline*	0.77	0.65-0.88		0.75	0.61-0.88	
Contrast-enhancing region						
+Voxel Group I	0.81	0.71-0.92	0.038	0.78	0.65-0.92	0.424
+Voxel Group II	0.80	0.70-0.91	0.153	0.86	0.76-0.96	0.003
+Voxel Group III	0.77	0.66-0.88	0.916	0.79	0.66-0.91	0.229
+Voxel Group IV	0.81	0.70-0.91	0.077	0.81	0.68-0.93	0.044
Non-enhancing region						
+Voxel Group I	0.76	0.65-0.88	0.792	0.76	0.63-0.89	0.763
+Voxel Group II	0.80	0.70-0.91	0.096	0.86	0.74-0.97	0.017
+Voxel Group III	0.80	0.69-0.91	0.372	0.83	0.71-0.95	0.023
+Voxel Group IV	0.80	0.70-0.91	0.154	0.83	0.71-0.95	0.011
Overall survival						
baseline*	0.81	0.70-0.93		0.71	0.58-0.83	
Contrast-enhancing region						
+Voxel Group I	0.82	0.69-0.95	0.070	0.75	0.63-0.87	0.091
+Voxel Group II	0.84	0.73-0.96	0.063	0.77	0.65-0.88	0.075
+Voxel Group III	0.81	0.70-0.93	0.746	0.73	0.60-0.85	0.443
+Voxel Group IV	0.84	0.72-0.95	0.164	0.77	0.65-0.88	0.035
Non-enhancing region						
+Voxel Group I	0.81	0.70-0.93	0.942	0.71	0.58-0.83	0.952
+Voxel Group II	0.84	0.72-0.96	0.015	0.78	0.66-0.89	0.022
+Voxel Group III	0.84	0.74-0.94	0.109	0.74	0.61-0.86	0.196
+Voxel Group IV	0.85	0.75-0.95	0.019	0.76	0.64-0.88	0.053

*Baseline models were built using sex, age, extent of resection, IDH-1 mutation status, MGMT methylation status and contrast-enhancing tumour volume. MGMT: O-6-methylguanine-DNA methyltransferase; IDH-1: Isocitrate dehydrogenase 1; AUC: area under receiver operator characteristics curve; HR: hazard ratio; CI: confidence interval; DTI: diffusion tensor imaging; Voxel Group I: decreased DTI-p, decreased DTI-q (p↓/q↓,); Voxel Group II: decreased DTI-p, increased DTI-q (p↓/q↑); Voxel Group III: increased DTI-p, increased DTI-q (p↑/q↑); Voxel Group IV: increased DTI-p, decreased DTI-q (p↑/q↓).

4.4.5 Stepwise Multivariate Cox Model Selection

All clinical factors and histogram features that significantly improved AUC were tested (Table 4.5). Significant prognostic variables for both PFS and OS included the extent of resection, MGMT methylation status and Voxel Group II (p↓/q↑) in the non-enhancing region. Specifically, Voxel Group II (p↓/q↑) in the non-enhancing region contributed to a worse PFS (HR 1.08, $P < 0.001$) and worse OS (HR 1.36, $P < 0.001$), and displayed a higher HR than other voxel groups.

Table 4.5 Stepwise Cox multivariate modelling of survivals

Variables	Progression-free survival*			Overall survival*		
	HR	95%CI	*P* value	HR	95%CI	*P* value
Sex	1.58	0.90-2.77	0.109	/	/	/
Age	/	/	/	/	/	/
Extent of resection	3.25	1.67-6.34	0.001	2.13	1.12-4.06	0.022
IDH-1 mutation status	/	/	/	/	/	/
MGMT methylation status	0.50	0.29-0.86	0.013	0.51	0.27-0.97	0.040
Contrast-enhancing volume	/	/	/	1.02	1.01-1.03	0.001
Voxel Group I (contrast-enhancing region)	/	/	/	1.06	1.02-1.11	0.006
Voxel Group II (contrast-enhancing region)	/	/	/	/	/	/
Voxel Group IV (contrast-enhancing region)	/	/	/	/	/	/
Voxel Group II (non-enhancing region)	1.08	1.04-1.13	<0.001	1.36	1.16-1.59	<0.001
Voxel Group III (non-enhancing region)	/	/	/	1.19	1.05-1.34	0.005
Voxel Group IV (non-enhancing region)	/	/	/	1.18	1.05-1.32	0.005

*All clinical factors and joint histogram features that showed incremental prognostic values in model comparisons were included into selection. Final models were built only using the covariates selected by the stepwise procedure. HR: hazard ratio; CI: confidence interval; IDH-1: Isocitrate dehydrogenase 1; MGMT: O-6-methylguanine-DNA methyltransferase; Voxel Group I: decreased DTI-p, decreased DTI-q (p↓/q↓); Voxel Group II: decreased DTI-p, increased DTI-q (p↓/q↑); Voxel Group III: increased DTI-p, increased DTI-q (p↑/q↑); Voxel Group IV: increased DTI-p, decreased DTI-q (p↑/q↓).

4.4.6 Correlations with tumour progression rate

The correlation with tumour progression rate was tested in 57 patients who had progression and available MR images at progression. The progression volume (mean ± SD) outside of the resection cavity was 14.3 ± 22.0 cm^3. The progression rate (mean ± SD) was 0.003 ± 0.013 cm^3/day. The results indicated that Voxel Group II (p↓/q↑) in the non-enhancing region had a significant positive correlation (P = 0.010, r = 0.35) with the progression rate, whereas Voxel Group IV (p↑/q↓) in the non-enhancing region (P = 0.040, r = -0.28) showed a negative correlation. No significant correlations were found from other voxel groups. Two examples of pre-operative and progression images, as well as the annotated sub-regions of Voxel Group II and Voxel Group IV in the non-enhancing region, are demonstrated in Figure 4.4 & Figure 4.5.

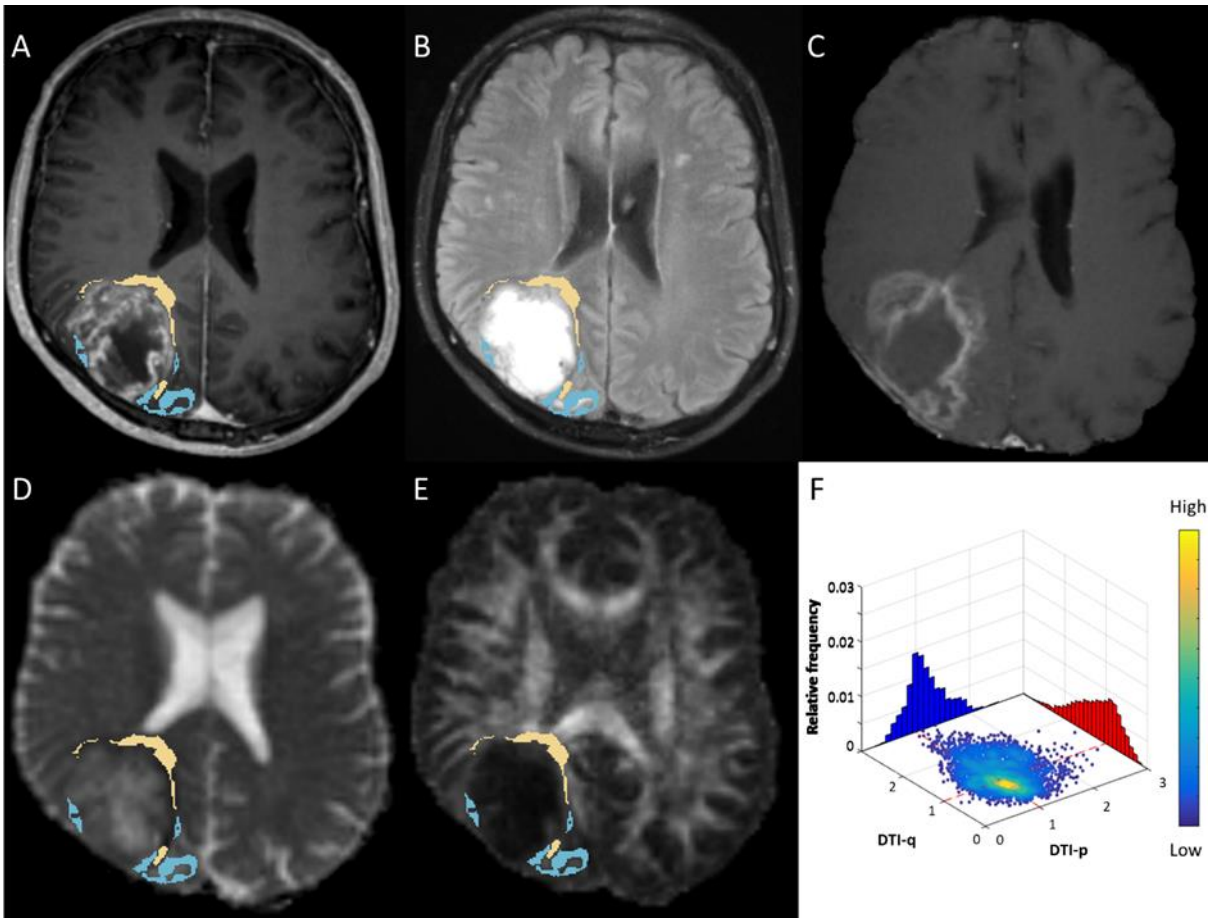

Figure 4.4 The Voxel Group II (yellow) and Voxel Group IV (blue) of non-enhancing in case 1. The 63-year-old man was radiologically diagnosed with primary glioblastoma (A & B). Volumetric analysis of pre-operative MRI showed contrast-enhancing tumour volume was 83.6 cm^3. The patient received tumour resection with the guidance of neuro-navigation and 5-aminolevulinic acid fluorescence with the aim of maximal resection, but only subtotal resection was achieved according to 72h post-operative MRI. The pathological assessment confirmed this was an MGMT-methylated glioblastoma and IDH mutation was negative. The patient received concomitant and adjuvant temozolomide chemoradiotherapy. The progression-free survival was 47 days and overall survival was 104 days. The post-contrast T1-weighted imaging showed the progression was around the resection cavity (C). Joint histogram analysis of pre-operative DTI-p (D) and DTI-q (E) maps showed Voxel Group II (yellow) occupied 15.5% in the non-enhancing tumour and Voxel Group IV (blue) occupied 28.2% of the non-enhancing tumour (F).

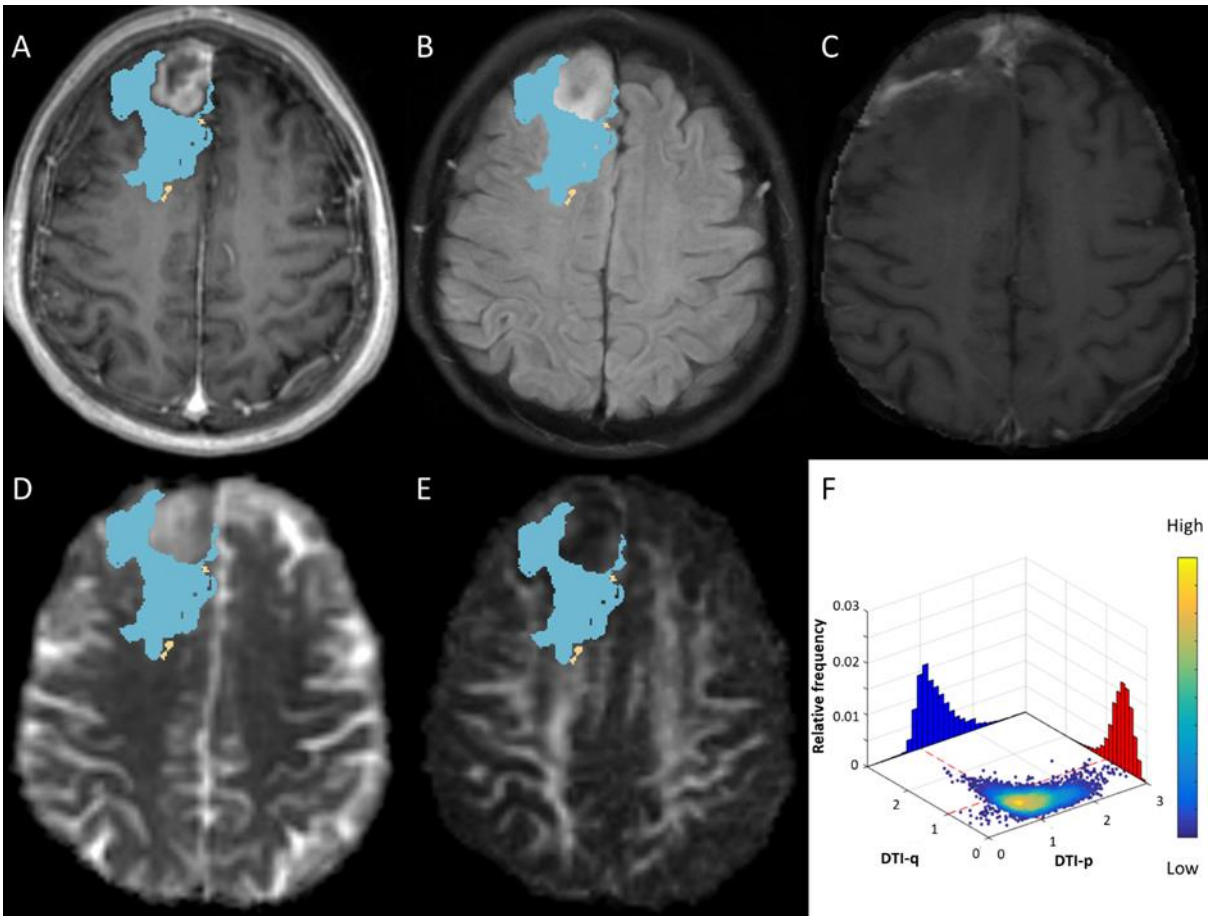

Figure 4.5 The Voxel Group II (yellow) and Voxel Group IV (blue) of non-enhancing in case 2. The 65-year-old man was radiologically diagnosed with primary glioblastoma (A & B). Volumetric analysis showed contrast-enhancing tumour volume was 37.4 cm3. Gross total resection was achieved in this patient with the guidance of neuro-navigation and 5-aminolevulinic acid fluorescence. The pathological assessment confirmed an MGMT-methylated glioblastoma and IDH mutation was negative. The patient received concomitant and adjuvant temozolomide chemoradiotherapy. The progression-free survival was 1006 days and the patient was alive in the last follow-up. Post-contrast T1-weighted imaging showed a minor progression around the resection cavity (C). Joint histogram analysis of pre-operative DTI-p (D) and DTI-q (E) maps showed Voxel Group II (yellow) occupied 2.3% of the non-enhancing tumour and Voxel Group IV (blue) occupied 81.5% of the non-enhancing tumour (F).

4.5 Discussion

In this study, we found that joint histogram analysis using DTI-p and -q can reflect the heterogeneity of glioblastoma infiltration. The histogram features obtained using this method can improve the prognostic value of IDH-1 mutation and MGMT promoter methylation status. The non-enhancing sub-region with decreased DTI-p and increased DTI-q may indicate a more infiltrative tumour habitat.

Previous studies have shown that DTI has potential in studying white matter pathology and is useful in detecting tumour infiltration (Zhang, 2010, Price et al., 2004, Sternberg et al., 2014). Using stereotactic biopsies, DTI-p and -q is demonstrated to distinguish the gross tumour and peritumoural region (Price et al., 2006). As the only in vivo method of describing brain microstructure, it confers additional information for surgical stratification (Potgieser et al., 2014, Jones et al., 2015b). However, the interpretation of the tensor is challenging due to its high dimensionality (Sternberg et al., 2014). Substantial efforts have been made to simplify the tensor into scalar measures. Among these markers, fractional anisotropy (FA) and mean diffusivity (MD) are commonly used (Pena et al., 2006a). Since FA can be affected by both anisotropic and isotropic components (according to its definition equation), its utility is inconsistent. An enhanced visualization and quantification of tensor imaging was subsequently advanced by decomposing the raw tensor into isotropic (p) and anisotropic (q) components (Pena et al., 2006a). This technique has shown its utility in detecting the subtle change caused by tumour invasion and predicting progression (Price et al., 2017). Consistent with previous studies (Price et al., 2006). Our univariate results showed increased DTI-p and decreased DTI-q can be found in the majority of the tumour area. Additionally, the non-enhancing tumour may display increased DTI-q, which was not observed in the contrast-enhancing region and may characterize the infiltrative region.

Previous studies have shown that histogram features extracted from DTI can characterize tumour heterogeneity and carry diagnostic values (Wagner et al., 2016). Every intra-tumoural voxel bears both isotropic and anisotropic diffusion information. Neither DTI-p nor DTI-q is sufficient to reflect the full tensor. This rationalizes the joint histogram analysis approach of this study. It has been previously suggested to combine DTI measures with structural images

(Bammer, 2003), which is why the joint histogram analysis was performed in tumour regions identified on anatomical images. The results showed the Voxel Group IV (p↑/q↓) had the largest proportion in both contrast-enhancing and non-enhancing tumour regions. In this sub-region, the brain microstructure is destroyed, resulting in more isotropic diffusion. There is a reduction in numbers of axons that facilitate tumour cell infiltration. The displacement and compression of fibres may also mean the 'fast track' to infiltrate is diminished and, thus, decreased anisotropic diffusion is observed. The significantly higher proportion of this diffusion pattern in the bulk tumour than the infiltrated tumour may suggest more substantial fibre damage.

More diffusion patterns can be revealed by this approach. Particularly, the higher proportion of Voxel Group II (p↓/q↑) in non-enhancing regions showed increased hazard ratio in both OS and PFS models. Since the decreased DTI-p is thought to reflect the elevated cell density and increased DTI-q may indicate intact fibres which may facilitate the tumour migration, this sub-region may represent a migratory tumour habitat. Though the proportion s relatively low, the significant association with patient survival and tumour progression may indicate its invasiveness. As shown in the case examples, some locations of this sub-region are in the vicinity of the surgical cavity. Our findings may allow for better targeting of radiotherapy in these sub-regions. Histological correlation of these findings is required.

The joint histogram features found in our study showed clinical significance, with incremental prognostic values when integrated with clinical factors. Particularly, in the model of overall survival, contrast-enhancing tumour volume had a smaller HR than all the voxel groups identified. The IDH-1 mutation did not show its prognostic value in this cohort, possibly due to the limited patient numbers. As the more infiltrative sub-region identified, targeted resection and radiation therapy can perhaps be achieved, which may reduce the radiation damage to the normal brain and enhance the efficacy of treatment.

There are some limitations in our study. Firstly, the patient population reported is from a single centre and the results were not validated by another cohort. However, since imaging setting may significantly impact the calculation of DTI-based metrics, this single centre study can reduce the confounder from the imaging setting and facilitate hypothesis test. Secondly,

although our current study did not have biological validation, previous studies have validated the histological correlates of DTI-p and DTI-q by image-guided biopsies (Price et al., 2006). This current study aimed to use DTI joint histogram analysis as a surrogate to investigate glioblastoma infiltration. The findings of this study need further validation using the tumour tissue biopsied from the invasive sub-regions identified.

4.6 Conclusion

We used a joint histogram analysis of DTI-p and -q to investigate glioblastoma infiltration. The results showed that this method may help to better understand the heterogeneity of tumour infiltration and offer incremental prognostic values over clinical factors; the non-enhancing region with decreased DTI-p and increased DTI-q may be able to define an infiltrative sub-region responsible for tumour progression. This finding may be useful for targeted surgery and radiation therapy.

Chapter 5 Low Perfusion Compartments in Glioblastoma Quantified by Advanced Magnetic Resonance Imaging and Correlated with Patient Survival

5.1 Abstract

Background

Glioblastoma exhibits profound intra-tumoural heterogeneity in blood perfusion, which may cause inconsistent therapy response. Particularly, low perfusion may create hypoxic microenvironment and induce resistant clones. Thus, developing validated imaging approaches that define low perfusion compartments is crucial for clinical management.

Methods

A total of 112 newly-diagnosed supratentorial glioblastoma patients were prospectively recruited for maximal safe resection. Preoperative MRI included anatomical, dynamic susceptibility contrast (DSC), diffusion tensor imaging (DTI) and chemical shift imaging (CSI). The apparent diffusion coefficient (ADC) and relative cerebral blood volume (rCBV) were calculated from DTI and DSC respectively. Using thresholding methods, two low perfusion compartments (ADC_H-$rCBV_L$ and ADC_L-$rCBV_L$) were identified. Volumetric analysis was performed. Lactate and macromolecule/lipid levels were determined from multi-voxel spectroscopy. Progression-free survival (PFS) and overall survival (OS) were analysed using Kaplan-Meier and multivariate Cox regression analyses.

Results

Two compartments displayed higher lactate and macromolecule/lipid levels than normal controls (each $P < 0.001$), suggesting hypoxic and pro-inflammatory microenvironment. The proportional volume of ADC_L-$rCBV_L$ compartment was associated with a larger infiltration area ($P < 0.001$, rho = 0.42). Lower lactate in this compartment was associated with a less invasive phenotype visualized on DTI. Multivariate Cox regression showed higher lactate level in the ADC_L-$rCBV_L$ compartment was associated with a worse survival (PFS: HR = 2.995, $P = 0.047$; OS: HR = 4.974, $P = 0.005$).

Conclusions

The ADC_L-$rCBV_L$ compartment represents a treatment resistant sub-region associated with glioblastoma invasiveness. This approach was based on clinically available imaging modalities and could thus provide crucial pre-treatment information for clinical decision making.

5.2 Introduction

Chapter 4 has shown that diffusion imaging can provide a useful tool to reveal the intra-tumoural infiltrative habitat. In this Chapter, we investigate the prognostic values of the intra-tumoural habitats revealed by multi-parametric MRI.

In a study performed by the previous group member, Dr Natalie R Boonzaier, tumour habitats that were highly perfused with restricted diffusion were identified and found to be correlated with tumour invasiveness(Boonzaier et al., 2017a). This finding is supported by the commonly observed angiogenesis and elevated perfusion of glioblastoma, associated with a more invasive phenotype (Hanahan and Weinberg, 2011b), as stated in Section 1.8.3. However, a potent angiogenesis inhibitor failed to demonstrate consistent benefits in clinical trials of *de novo* glioblastoma (Chinot et al., 2014). A possible explanation is the profound intra-tumoural perfusion heterogeneity in glioblastomas, which is due to the aberrant microvasculature and inefficient nutrient delivery. This heterogeneity can give rise to regions within tumours where the demand and supply of nutrients are mismatched (Komar et al., 2009). Consequently, the sufficiently perfused sub-regions may hold the advantages for progression and proliferation, whereas the insufficiently perfused sub-regions may have a hypoxic microenvironment (Gillies et al., 1999), which may preferentially induce adaptive and resistant clones in the low perfusion sub-regions (Pistollato et al., 2010). It is therefore important to understand the function of low perfusion sub-regions and evaluate their effects on treatment resistance.

Current clinical practice infers the low perfusion regions as the non-enhancing regions within contrast enhancement on post-contrast images, which can lead to non-specific results using the conventional weighted images (O'Connor et al., 2008, O'Connor et al., 2015), as discussed in Section 1.8.2. Multiparametric imaging may allow for a more comprehensive evaluation of tumour physiology, compared to the morphological heterogeneity seen with structural MRIs.

Here we sought to quantify the low perfusion compartments in glioblastoma using multi-parametric physiological magnetic resonance imaging (MRI). The relative cerebral blood volume (rCBV) calculated from perfusion weighted imaging measures tumour vascularity (Liu et al., 2016). The apparent diffusion coefficient (ADC) calculated from diffusion imaging

provides information about tumour microstructure by measuring the movement of water molecules (Pope et al., 2012). Thus, the two low perfusion compartments we visualized have distinct properties: one compartment with restricted diffusivity that may represent cellular sub-regions adapting to hypoxic acidic conditions (Gatenby et al., 2013), and one compartment with increased diffusivity that may represent necrotic sub-regions with diminishing cellular structure. We studied the metabolic signatures in each compartment using MR spectroscopy and the impact it has on patient survival. Using multivariate survival analysis, we demonstrate that the volume and lactate level of these two compartments are clinically important.

5.3 Methods

5.3.1 Patient cohort

Patients with a radiological diagnosis of primary supratentorial glioblastoma suitable for maximal safe surgical resection were prospectively recruited from July 2010 to April 2015. The inclusion and exclusion criteria are in Section 3.1.1. This study was approved by the local institutional review board. Signed informed consent was obtained from all patients. Patient treatment is detailed in Section 3.1.2.1. Assessment of IDH-1 R132H Mutation and MGMT Methylation Status are described in 3.2. The patient included in this study was summarized in Figure 5.1.

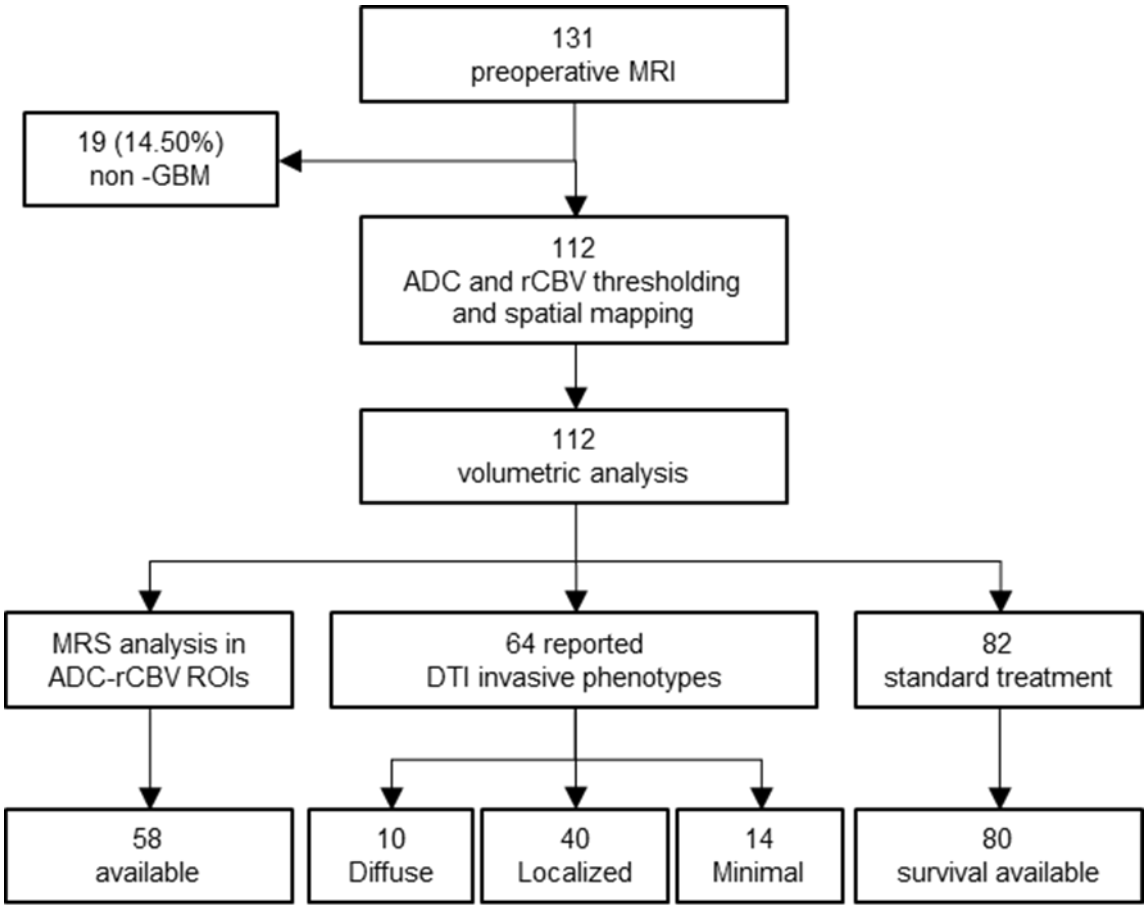

Figure 5.1 Flow diagram of the study design and patient recruitment. Nineteen patients were excluded due to pathological non-glioblastoma diagnosis. Due to the criteria of multiple voxel selection, patients with missing Lac/Cr and ML9/Cr data were excluded in MRS analysis. DTI invasive phenotypes were correlated with the 64 patients overlapping with a previously reported cohort. Patient survival was reviewed retrospectively to exclude pseudoprogression and was only analysed in those who received standard chemoradiotherapy.

5.3.2 MRI acquisition

Pre-operative MRI sequences in this study included: post-contrast T1-weighted, T2-weighted, T2-weighted fluid attenuated inversion recovery (FLAIR), dynamic susceptibility contrast-enhancement (DSC), diffusion tensor imaging (DTI) with inline ADC calculation, and multi-voxel 2D 1H-MRS chemical shift imaging (CSI). Sequence details are provided in 3.3.2.2. All

patient underwent MRI within 72hrs postoperatively as a clinical routine scanning to evaluate extent of resection.

5.3.3 Image processing

For each subject, all images were co-registered to T2-weighted images with an affine transformation, using the linear image registration tool (FLIRT) functions (Jenkinson et al., 2002) in FSL v5.0.0 (Oxford, UK) (Smith et al., 2004).

DTI was processed as described in Section 3.4.2 (Behrens et al., 2003). The decomposition into isotropic (p) and anisotropic (q) components was performed as previously described (Pena et al., 2006b). DSC was processed as described in Section 3.4.3. The relative cerebral blood volume (rCBV), mean transit time (MTT) and relative cerebral blood flow (rCBF) maps were calculated. CSI data were processed as described in 3.4.4.

5.3.4 Regions of interest and volumetric analysis

Conventional tumour regions of interest (ROIs) were manually drawn as described in 3.4.6.1. ADC-rCBV ROIs were further generated using quartile values in Matlab (v2016a, The MathWorks, Inc., Natick MA). The procedure is illustrated in Figure 5.2. Firstly, ADC and rCBV values were obtained from each voxel within the contrast-enhancing (CE) ROI and pooled together as described previously (Boonzaier et al., 2017a). The lowest quartile of the pooled rCBV values ($rCBV_L$) was interpreted as low perfusion regions. Then the first quartile (ADC_L) and last quartile (ADC_H) of ADC map were respectively overlaid on $rCBV_L$ maps. Finally, two intersections of ADC_L-$rCBV_L$ and ADC_H-$rCBV_L$ ROIs were obtained. Other regions within CE outside the two ADC-rCBV ROIs were taken as abnormal controls (CE control, CEC). Raw volumes of ROIs were calculated in FSL (Smith et al., 2004). Proportional volumes (%) of two ADC-rCBV ROIs were calculated as the ratio of the raw volumes to CE volume.

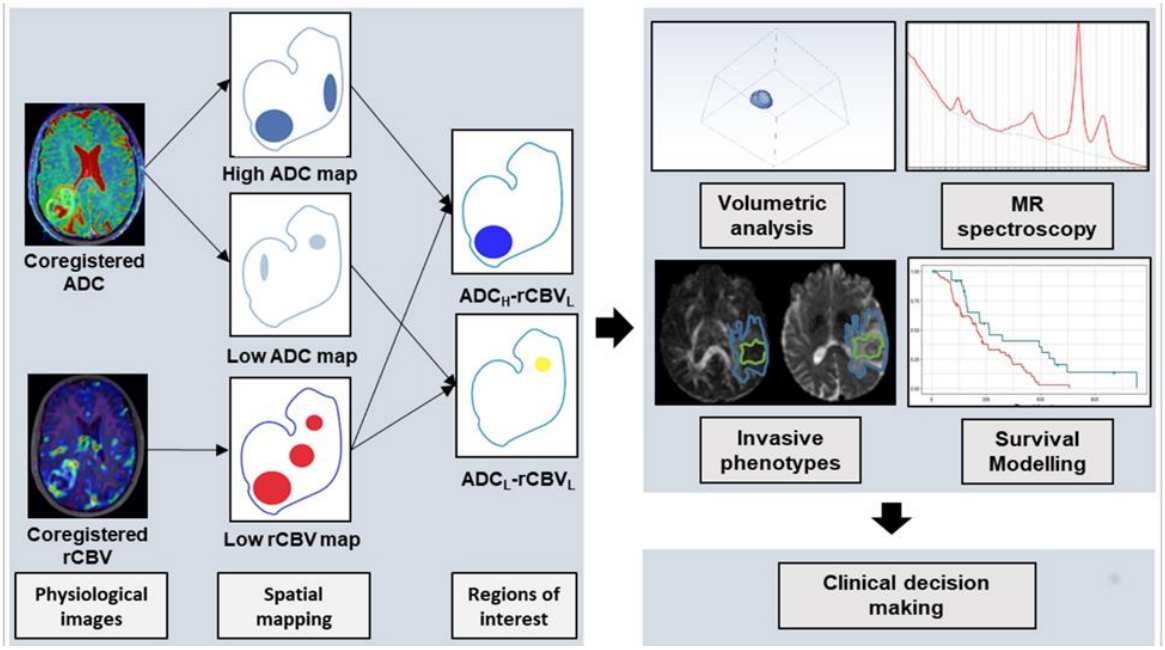

Figure 5.2 Illustration of the pipeline to identify two ADC-rCBV compartments. Both ADC and rCBV maps are co-registered to the T2 weighted images and tumour regions are segmented manually. Low perfusion tumour regions are partitioned using a quartile threshold. Similarly, two ADC sub-regions are partitioned using high and low ADC quartile thresholds respectively. The spatial overlap between the thresholded rCBV and ADC maps defined two compartments ADC$_H$-rCBV$_L$ and ADC$_L$-rCBV$_L$. MR volumetric and metabolic analyses of both compartments are performed and interrogated in invasive phenotype and patient survival analysis models.

5.3.5 Multi-voxel MRS processing

Only those MRS voxels that were completely within the delineated tumour were included in further analyses. The weight of each MRS voxel was taken as the proportion of the ADC-rCBV compartments in that MRS voxel. The sum weighted value was used as the final metabolic value. This method provides an objective method for MRS voxel selection (Figure 5.3).

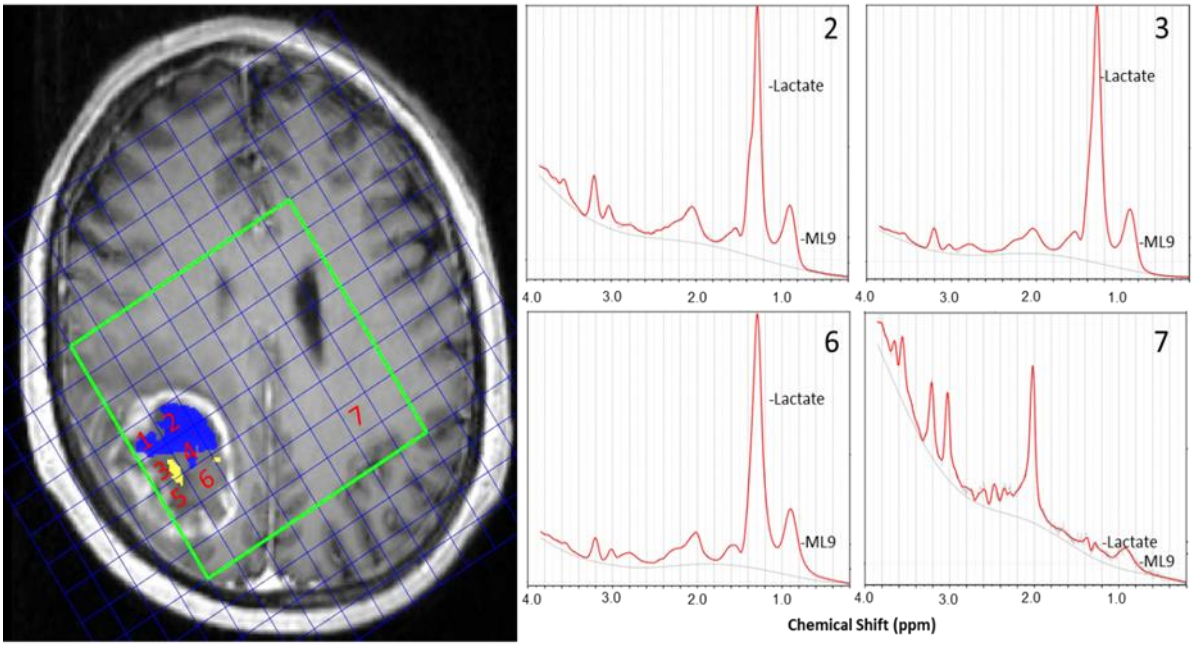

Figure 5.3 Illustration of multiple voxel MRS analysis. Left: the selection criteria. The T2-space pixels are projected to MRS space according to their coordinates. The proportion of T2-space tumour pixels occupying each MRS voxel is calculated. A criterion is applied that only those MRS voxels are included when this voxel is completely within the delineated tumour. In this case, grid 1-6 met the criteria. A weighted average metabolite content for each region is calculated from the metabolite content of each voxel within it weighted by that voxel's percentage of (ADC_H-$rCBV_L$ [blue]: grid 1,2 and 4 are counted; ADC_L-$rCBV_L$ [yellow], grid 3 and 5 are counted; abnormal control [CEC]: grid 1-6 are counted). Right: Example spectra of ROIs. Each spectrum corresponds to the grids on the left. Grid 2: lactate/Cr ratio 13.2, ML9/Cr ratio: 10.4; grid 3: lactate/Cr ratio 28.4, ML9/Cr ratio: 22.7; grid 6: lactate/Cr ratio 8.9, ML9/Cr ratio: 16.6; grid 7 (NAWM): lactate/Cr ratio 0.37, ML9:1.36.

5.3.6 DTI invasive phenotypes

We investigated DTI invasive phenotypes of 64 patients which overlap with a previously reported cohort and have been correlated to isocitrate dehydrogenase (IDH) mutation status (Price et al., 2017). Three invasive phenotypes were classified using previously described criteria (Price et al., 2007) based on the decomposition of diffusion tensor into isotropic (p) and anisotropic components (q). This approach classified glioblastoma into three phenotypes: (a) diffuse invasive phenotype, where the p abnormality is larger than the q abnormality in all directions; (b) localised invasive phenotype, where p abnormality exceeds the q abnormality in

one particular direction; and (c) minimal invasive phenotype: where p abnormality is similar to the q abnormality (Figure 5.4). Previous studies showed this approach can predict tumour recurrence pattern (Price et al., 2007).

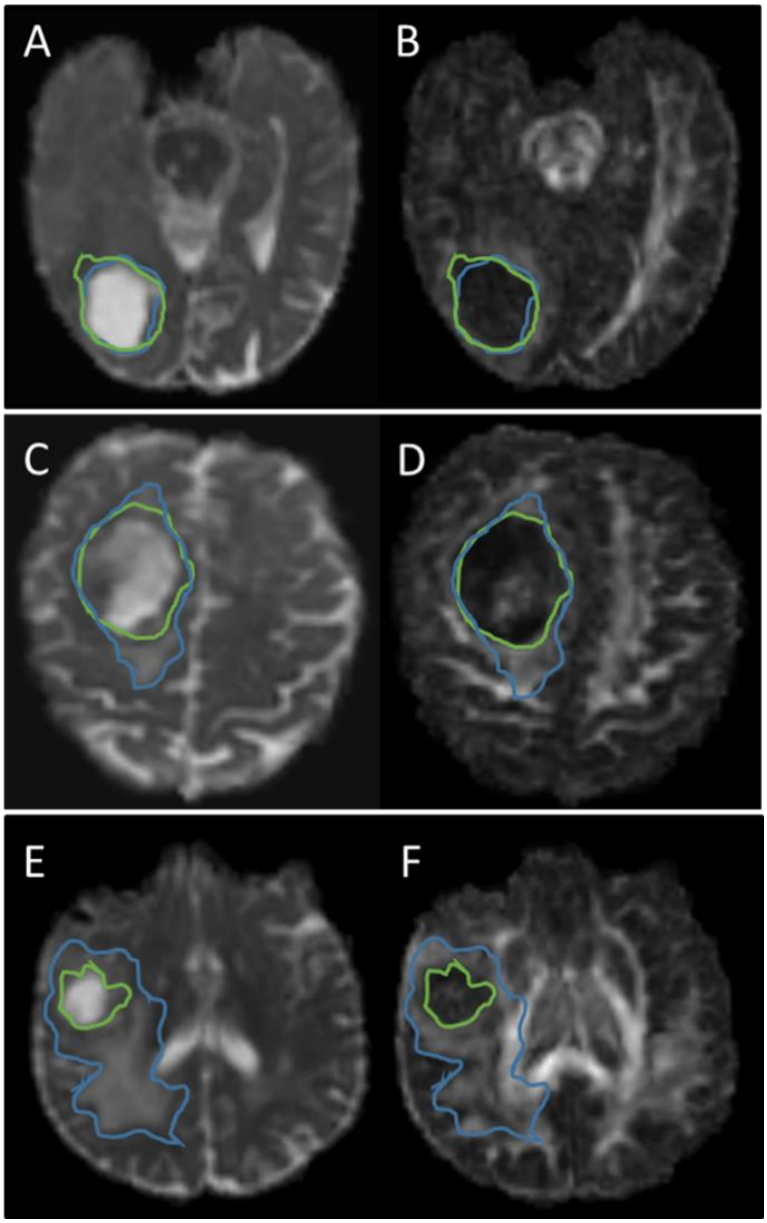

Figure 5.4 Examples of DTI invasive phenotypes. (A), (C), (E): DTI-p maps with abnormality outlined by the blue line; (B), (D), (F): DTI-q maps with abnormality outlined by the green line. All the delineation were manually performed by clinical experts. (A) & (B) show a minimal invasive phenotype. The isotropic abnormality is similar to the anisotropic abnormality. (C) & (D) show a localised invasive phenotype. The isotropic abnormality is larger than the anisotropic abnormality in one direction. (E) & (F) show a diffuse

invasive phenotype. The isotropic abnormality is larger than the anisotropic abnormality in more than one direction.

5.3.7 Statistical analysis

All analyses were performed with RStudio v3.2.3. Continuous variables were tested with Welch Two Sample t-test. MRS data or tumour volume, were compared with Wilcoxon rank sum test or Kruskal-Wallis rank sum test (multiple comparisons), using Benjamin-Hochberg procedure for controlling the false discovery rate in multiple comparisons. Spearman rank correlation was used to model the relation between the volume of two ADC-rCBV ROIs and the volume of CE and FLAIR ROIs. Kaplan-Meier using log-rank test and Cox proportional hazards regression analyses were performed to evaluate patient survival. For the Kaplan-Meier analysis, the volumes of ROIs and MRS variables were dichotomized using the function of 'surv_cutpoint' in R Package "survminer". Patients who were alive at the last known follow-up were censored. Multivariate Cox regression with forward and backward stepwise procedures was performed, accounting for relevant covariates, including IDH-1 mutation, MGMT methylation, sex, age, the extent of resection and contrast-enhancing tumour volume. The forward procedure started from the model with one covariate. The backward procedure initiated from the model including all covariates. For each step, the Akaike Information Criterion (AIC) was used to evaluate the model performance. The final multivariate model was constructed using the covariates selected by the stepwise procedures. The hypothesis of no effect was rejected at a two-sided level of 0.05.

5.4 Results

5.4.1 Patients

After surgery, 19 (14.5%) patients were excluded due to non-glioblastoma pathological diagnosis and 112 patients (mean age 59.4 years, range 22-76, 84 males; Overview: Table 5.1) were included. Among them, 82 (73.2%) patients received a standard dose of radiotherapy plus temozolomide concomitant and adjuvant chemotherapy post-operatively. Eighty of 112

(71.4%) patients had survival data available. The median progression-free survival (PFS) of these patients was 265 days (range 25-1130 days) and overall survival was 455 days (range 52-1376 days).

Table 5.1 Patient clinical characteristics and ROI volumes

Variables	Patient number	CE		FLAIR		ADC_H-$rCBV_L$		ADC_L-$rCBV_L$	
		Mean ± SD (cm^3)	*P*	Mean ±SD (cm^3)	*P*	Mean ± SD (cm^3)	*P*	Mean ± SD (cm^3)	*P*
Age at diagnosis									
<60	38	41.9±24.0	0.022	101.4±55.4	0.143	4.3±3.7	0.020	1.9±1.6	0.224
≥60	74	58.6±35.7		119.5±63.8		6.3±4.8		2.5±2.4	
Sex									
Male	84	54.5±34.1	0.323	115.2±62.8	0.675	5.8±4.6	0.657	2.4±2.3	0.328
Female	28	48.5±30.0		107.7±57.8		5.4±4.4		1.9±1.8	
Extent of resection									
Complete	75	45.8±26.0	0.006	106.0±58.0	0.062	4.8±3.9	0.002	2.1±1.8	0.685
Partial	37	67.4±40.8		128.3±66.1		7.5±5.2		2.6±2.8	
MGMT-methylation status*									
Methylated	48	48.4±32.7	0.154	105.4±66.3	0.161	4.8±4.1	0.099	2.2±2.4	0.282
Unmethylated	60	55.8±32.1		121.1±57.9		6.1±4.5		2.4±2.0	
IDH-1 mutation status									
Mutant	7	54.6±35.4	0.895	102.2±69.1	0.471	5.8±4.9	0.843	2.2±1.7	0.787
Wild-type	105	52.9±33.1		114.1±61.2		5.6±4.6		2.3±2.2	

*MGMT-methylation status unavailable for 4 patients. CE: Contrast-enhancing; cm: centimetres; FLAIR: fluid attenuated inversion recovery; ADC_L-$rCBV_L$: region of low-ADC and low-rCBV; ADC_H-$rCBV_L$: region of high-ADC and low-rCBV; IDH-1: Isocitrate dehydrogenase1; MGMT: O-6-methylguanine-DNA methyltransferase; SD: Standard deviation.

5.4.2 Multiparametric MRI identifies two low perfusion compartments

The volumes of ROIs for patient subgroups are compared in Table 5.1. The ADC_H-$rCBV_L$ compartment (volume 5.7 ± 4.6 cm^3) was generally larger than the ADC_L-$rCBV_L$ compartment (volume 2.3 ± 2.2 cm^3) ($P < 0.001$). Completely resected tumours had smaller CE volume (*P*

= 0.006) and smaller ADC_H-$rCBV_L$ compartment ($P = 0.002$). Figure 5.5 (A, D) shows the two compartments for two cases.

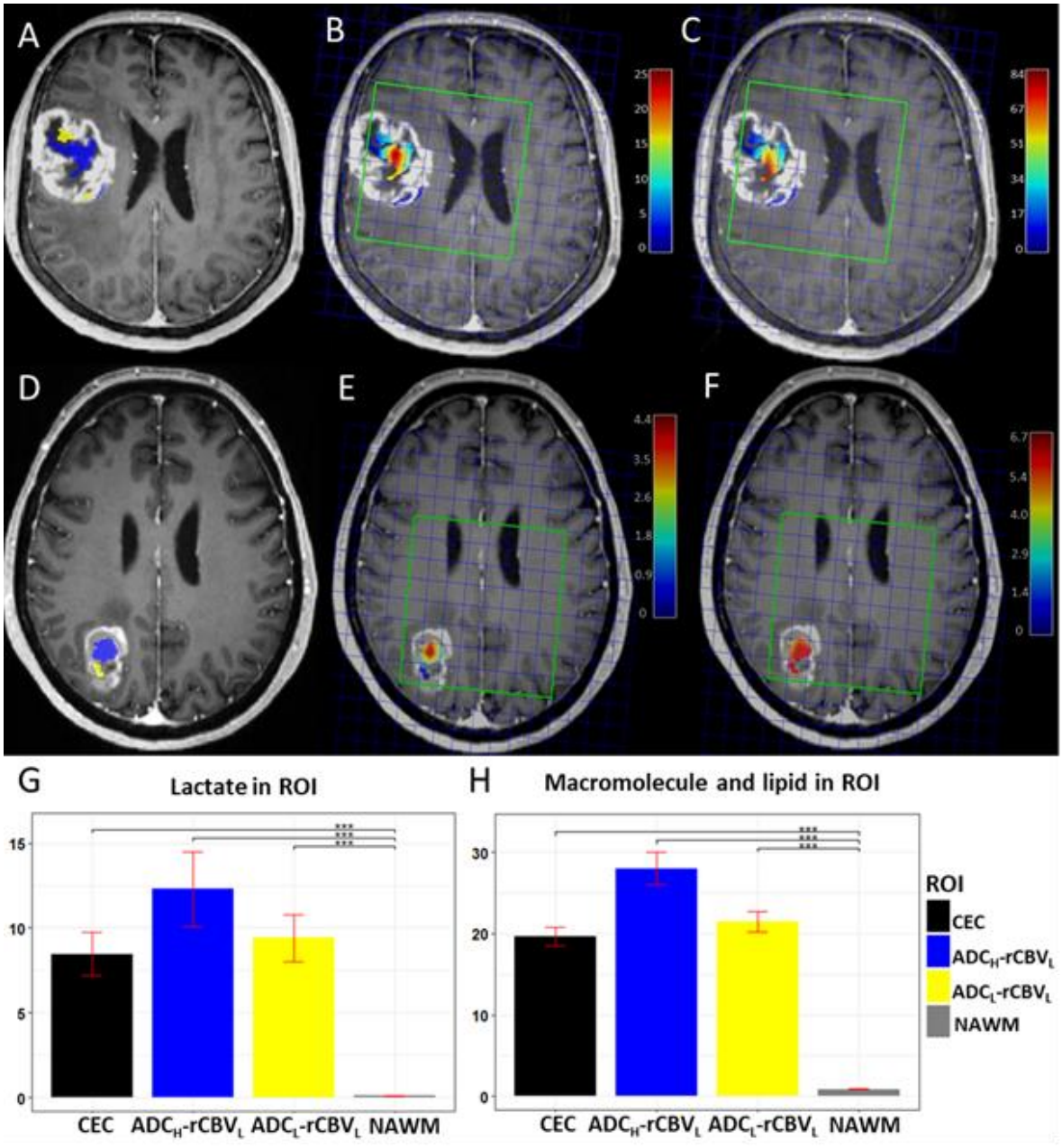

Figure 5.5 Two hypoxic compartments and MRS characteristics. Case 1: A-C; Case 2: D-F. A & D show the location of ADC_L-$rCBV_L$ (yellow) and ADC_H-$rCBV_L$ (blue) compartments. B & E demonstrate the Lac/Cr ratios of the two compartments. C & F demonstrate the ML9/Cr ratios in the two compartments. The colour

bar shows the level of metabolites (red: high, blue: low). Note that case 1 shows greater tumour volume and higher lactate level. G & H demonstrate the MRS characteristics of the compartments over the patient cohort. Yellow: ADC_L-$rCBV_L$; blue: ADC_H-$rCBV_L$; black: contrast-enhancing control (CEC); grey: normal-appearing white matter (NAWM). G: mean Lac/Cr level; H: mean ML9/Cr. ***: $P < 0.001$.

5.4.3 Low perfusion compartments displayed hypoxic and pro-inflammatory metabolic signatures

The ADC_H-$rCBV_L$ compartment showed a significantly higher lactate/creatine (Lac/Cr) ratio than NAWM ($P < 0.001$), as well as an increased ML9/Cr ratio compared to NAWM ($P < 0.001$). Similarly, the ADC_L-$rCBV_L$ compartment displayed higher Lac/Cr ratio and ML9/Cr ratio than NAWM (both $P < 0.001$). Although not significant, the Lac/Cr and ML9/Cr ratios in the ADC_H-$rCBV_L$ compartment were higher than the ADC_L-$rCBV_L$ compartment (Table 5.2). Figure 5.5 shows overlays between the rCBV-ADC compartments in two example cases and the metabolite levels of the two compartments.

Table 5.2 Metabolic characteristics measured by MRS.

Lac/Cr					
	Descriptive		**ADC_L-$rCBV_L$**	**CEC**	**NAWM**
ROI	Mean ± SD	95% CI	*P*	*P*	*P*
ADC_H-$rCBV_L$	12.3±15.4	7.9-16.7	0.427	0.411	< 0.001
ADC_L-$rCBV_L$	9.4±9.8	6.6-12.2	/	0.407	< 0.001
CEC	8.5±8.9	5.9-11.0	/	/	< 0.001
NAWM	0.10±0.28	0.02-0.17	/	/	/
ML9/Cr					
	Descriptive		**ADC_L-$rCBV_L$**	**CEC**	**NAWM**
ROI	Mean ± SD	95% CI	*P*	*P*	*P*
ADC_H-$rCBV_L$	28.0±71.6	9.2-46.9	0.650	0.529	< 0.001
ADC_L-$rCBV_L$	21.5±31.2	13.3-29.7	/	0.492	< 0.001
CEC	19.7±29.3	12.0-27.4	/	/	< 0.001
NAWM	0.87±0.68	0.70-1.05	/	/	/

ROI: region of interest; ADC_L-$rCBV_L$: ROI of low-ADC and low-rCBV; ADC_H-$rCBV_L$: ROI of high-ADC and low-rCBV; CEC: contrast enhancement control; NAWM: normal appearing white matter; Lac: lactate; ML9: Macromolecule and lipid at 0.9ppm; Cr: creatine; CI: confidence interval.

5.4.4 Low perfusion compartments exhibited diverse effects on tumour invasion

The contrast-enhancing (CE) tumour volume was significantly correlated with the Lac/Cr ratio in the ADC_L-$rCBV_L$ ($P = 0.018$, rho = 0.34). Interestingly, the volume of tumour infiltration beyond contrast enhancement, which was delineated on FLAIR images and normalised by CE volume, showed a moderate positive correlation with the proportional volume of the ADC_L-$rCBV_L$ compartment ($P < 0.001$, rho = 0.42) and a negative correlation with the proportional volume of the ADC_H-$rCBV_L$ compartment ($P < 0.001$, rho = -0.32).

5.4.5 The ADC_L-$rCBV_L$ compartment of minimally invasive tumours is less hypoxic

The minimally invasive phenotype displayed a lower volume of ADC_L-$rCBV_L$ compartment than the localised ($P = 0.031$) and diffuse phenotype (not significant), and a higher volume of ADC_H-$rCBV_L$ compartment than the localised ($P = 0.024$) and diffuse phenotype (not significant), suggesting the effects of the two low perfusion compartments to tumour invasiveness were different. Of note, the minimally invasive phenotype displayed lower Lac/Cr ratio compared to the localised ($P = 0.027$) and diffuse phenotype ($P = 0.044$), indicating that the ADC_L-$rCBV_L$ compartment experienced less hypoxic stress in the minimally invasive tumours. A full comparison between the three invasive phenotypes can be found in Table 5.3.

Table 5.3 Comparison of the three DTI invasive phenotypes.

		Diffuse	Localised	Minimal	Comparisons		
		10 (15.6%)	40 (62.5%)	14 (21.9%)	Localised-Diffuse	Minimal-Diffuse	Minimal-Localised
ROI	**Variable**	**Mean ± SD**	**Mean ± SD**	**Mean ± SD**	***P* value**	***P* value**	***P* value**
CE	Volume (cm^3)	53.8±35.0	39.7±16.0	52.7±36.2	0.388	0.406	0.390
FLAIR	Volume (cm^3)	116.7±57.3	82.0±31.5	85.2±68.4	0.067	0.062	0.490
ADC_H-$rCBV_L$	Volume#	0.10±0.04	0.08±0.03	0.12±0.04	0.036	0.140	0.024
ADC_L-$rCBV_L$	Volume#	0.04±0.03	0.06±0.03	0.03±0.02	0.080	0.104	0.031
ADC_H-$rCBV_L$	Lac/Cr	12.9±20.3	12.9±12.3	3.5±3.8	0.206	0.182	0.190
ADC_L-$rCBV_L$	Lac/Cr	9.0±9.1	10.0±8.9	1.8±2.3	0.407	0.044	0.027
CEC	Lac/Cr	8.8±9.2	8.8±7.6	2.7±2.7	0.218	0.080	0.073

*raw volumes; #proportional volumes; ROI: region of interest; CE: contrast enhancement; cm: centimeters; FLAIR: fluid attenuated inversion recovery; ADC_L-$rCBV_L$: ROI of low-ADC and low-rCBV; ADC_H-$rCBV_L$: ROI of high-ADC and low-rCBV; CEC: contrast enhancement control; Lac: lactate; Cr: creatine; SD: Standard deviation.

5.4.6 Low perfusion compartments exhibited diversity in treatment response

First, we used multivariate Cox regression to analyse all relevant clinical covariates. The results showed that extent of resection (EOR) (PFS: hazard ratio [HR] = 2.825, $P = 0.003$; OS: HR = 2.063, $P = 0.024$), CE tumour volume (OS: HR = 2.311, $P < 0.001$) and FLAIR tumour volume (OS: HR = 0.653, $P = 0.031$) were significantly associated with survivals.

Next, we included the volumes of two compartments and their Lac/Cr ratios into the survival models. The results using stepwise procedure showed that higher volumes of the two compartments were associated with better PFS (ADC_H-$rCBV_L$: HR = 0.102, P = 0.049; ADC_L-$rCBV_L$: HR = 0.184, P = 0.033), whilst the higher Lac/Cr ratio in the two compartments was associated with worse PFS (ADC_H-$rCBV_L$: HR = 6.562, P = 0.002; ADC_L-$rCBV_L$: HR = 2.995, P = 0.047). Further, the higher Lac/Cr ratio in the ADC_L-$rCBV_L$ compartment was also associated with worse OS (HR = 4.974, P = 0.005). In contrast, the Lac/Cr ratio in the contrast-enhancing control regions was associated with better survivals (PFS: HR = 0.053, P = 0.001; OS: HR = 0.090, P = 0.007). The results of the Cox proportional hazards models are described in Table 5.4 and the Kaplan-Meier curves using log-rank test are shown in Figure 5.6.

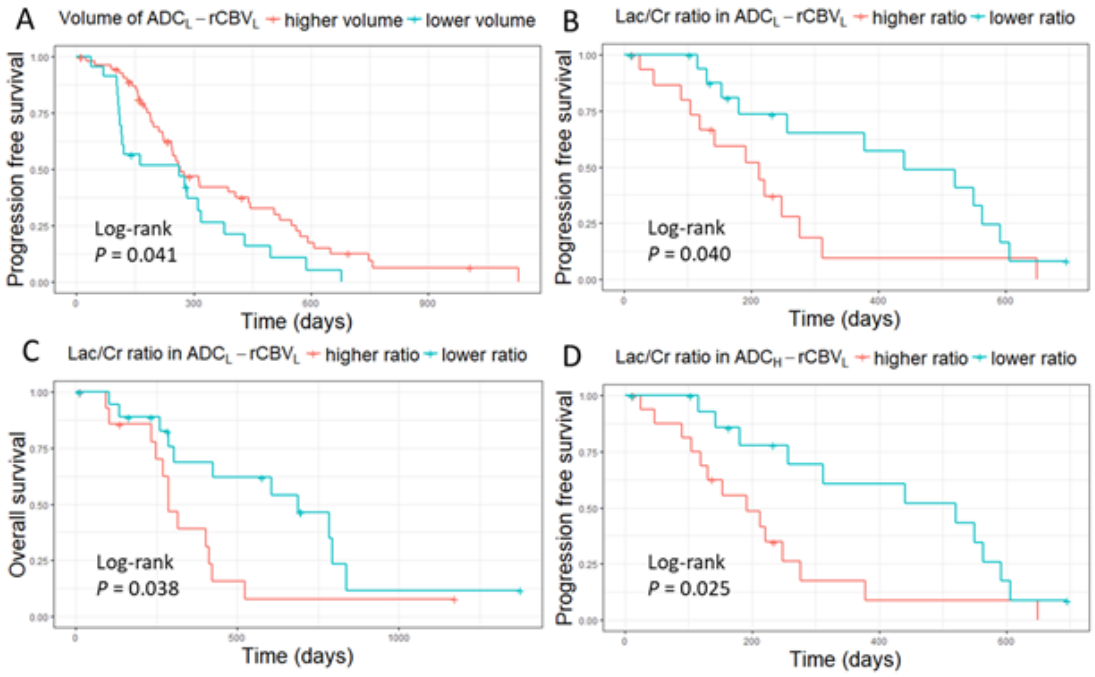

Figure 5.6 Kaplan-Meier plots of survival analysis. Log-rank tests show larger proportional volume of ADC_L-$rCBV_L$ compartment is associated with better PFS (P = 0.041) (A), while higher Lac/Cr ratio in this compartment is associated with worse PFS (P =0.040) (B) and OS (P = 0.038) (C). Higher Lac/Cr ratio in the ADC_H-$rCBV_L$ compartment is associated with worse PFS (P = 0.025) (D).

Table 5.4 Univariate and multivariate modelling of survivals

Factor	PFS						OS					
	Multivariate			Stepwise			Multivariate			Stepwise		
	HR	95%CI	*P*	HR	95%CI	*P*	HR	95%CI	*P*	HR	95%CI	*P*
Age	1.007	0.979-1.035	0.645				1.002	0.971-1.033	0.911	0.927	0.860-0.998	**0.045**
Sex (M)	1.499	0.838-2.681	0.172	5.043	1.063-23.91	**0.042**	1.252	0.662-2.365	0.490			
extent of resection (partial)	2.825	1.417-5.635	**0.003**	4.531	1.002-20.49	**0.050**	2.063	1.099-3.874	**0.024**	12.18	2.701-54.91	**0.001**
MGMT methylation status*	0.624	0.366-1.063	0.083	0.392	0.125-1.233	0.109	0.647	0.358-1.167	0.148	0.231	0.070-0.762	**0.016**
IDH mutation status	0.902	0.278-2.926	0.864				0.900	0.256-3.170	0.870			
CE volume	1.291	0.861-1.935	0.216	6.760	0.696-65.63	0.099	2.311	1.527-3.499	**<0.001**	3.080	1.487-6.383	**0.002**
Flair volume	0.775	0.519-1.157	0.212	2.008	0.818-4.926	0.128	0.653	0.444-0.961	**0.031**			
ADC_L-$rCBV_L$ volume				0.184	0.039-0.874	**0.033**						
ADC_H-$rCBV_L$ volume				0.102	0.011-0.992	**0.049**						
Lac/Cr in ADC_H-$rCBV_L$				6.562	2.023-21.29	**0.002**				2.367	0.825-6.790	0.109
Lac/Cr in ADC_L-$rCBV_L$				2.995	1.012-8.861	**0.047**				4.974	1.608-15.39	**0.005**
Lac/Cr in CEC				0.053	0.010-0.295	**0.001**				0.090	0.016-0.520	**0.007**

*MGMT-methylation status unavailable for 4 patients. PFS: progression-free survival; OS: overall survival; HR: hazard ratio; CI: confidence interval; IDH-1: Isocitrate dehydrogenase1; MGMT: O-6-methylguanine-DNA methyltransferase; CE: Contrast-enhancing; FLAIR: fluid attenuated inversion recovery; Lac: lactate; ADC_L-$rCBV_L$: region of low-ADC and low-rCBV; ADC_H-$rCBV_L$: region of high-ADC and low-rCBV; CEC: contrast enhanced control.

5.5 Discussion

This study combined perfusion and diffusion parameters to quantify low perfusion compartments that may be responsible for treatment resistance. The non-invasive approach using physiological imaging may potentially improve on the commonly-used weighted structural imaging.

The clinical values of the individual markers have been assessed previously. Among them, rCBV is reported to indicate IDH mutation status and associated with hypoxia-initiated angiogenesis (Kickingereder et al., 2015). Decreased ADC is considered to represent higher tumour cellularity/cell packing (Chen et al., 2013b) and associated with shorter survival (Shiroishi et al., 2016). Here we integrated the two markers to identify two low perfusion compartments with hypoxic stress. With similar perfusion levels in these two compartments, the higher cellularity (ADC_L) in the ADC_L-$rCBV_L$ compartment suggests it may display a higher degree of mismatch between supply and demand of nutrients.

We measured the lactate, macromolecule and lipid levels at 0.9 ppm (ML9) in the spectra, as increased lactate indicates hypoxia, while ML9 is associated with pro-inflammatory microglial response (Pardon et al., 2016). The elevated ML9/Cr ratios may suggest both compartments displayed elevated inflammation response (Pardon et al., 2016), potentially due to the recruitment of inflammatory cells by necrosis (Galluzzi and Kroemer, 2008), The positive correlation between tumour volume and lactate levels in the ADC_L-$rCBV_L$ compartment could indicate the acquired hypoxia as the tumour grows. When evaluating the non-enhancing peritumoural regions, we found that tumours with large infiltration tended to have smaller ADC_H-$rCBV_L$ and larger ADC_L-$rCBV_L$ compartments, suggesting the latter might be more responsible for infiltration. This was supported by our findings that minimally invasive phenotypes displayed significantly lower lactate levels in the ADC_L-$rCBV_L$ compartment.

We further investigated the effects of two compartments to patient survivals. Interestingly, a higher Lac/Cr ratio in the two compartments was related to worse outcomes ($HR > 1$) while this ratio in other tumour regions showed a reduced hazard ($HR < 1$). This suggests that the

resistant phenotypes induced by hypoxia mainly reside in the two compartments. As the ADC_L-$rCBV_L$ compartment was associated with tumour infiltration area, diffusion invasiveness, and significantly affected both PFS and OS, this compartment may be more responsible for treatment resistance.

We found that the higher volume of both compartments was significantly associated with better survivals, while higher Lac/Cr ratios were associated with worse survivals. These results suggested that the extent of low perfusion, indicated by volume, and the intensity of hypoxia, indicated by lactate level, have different clinical implications. Specifically, the higher proportion of the low perfusion compartments may represent a relatively lower proliferative phenotype, while the more intensive hypoxia in these compartments may represent a more aggressive phenotype.

Our findings have clinical significance. Our identification of possibly resistant regions could inform the choice of treatment target. Additionally, recent studies postulated that antiangiogenic agents failed to demonstrate consistent response because they can induce the adaptive clones and thus cause treatment resistance (Liu et al., 2016, Hu et al., 2012). Our findings may provide indications for antiangiogenic therapy. Particularly, more attention might be needed for patients with larger volumes of the ADC_L-$rCBV_L$ compartment when considering antiangiogenic agents.

There are limitations in our study. Due to the MRS spatial resolution, the multivariate analysis was based on a subset of patients. Similarly, survival analyses were performed on patients who received post-operative chemoradiotherapy. The cut-off values defining the two compartments were based on the quartiles of rCBV and ADC distributions, rather than optimizing for threshold specifically. Lastly, although the imaging markers are validated histologically from other studies (Price et al., 2006), a full biological validation can only be achieved with a multi-region sampling of each tumour.

5.6 Conclusion

We showed that multi-parametric imaging could identify two low perfusion compartments. This approach may help optimize the current clinical routine which is mainly based on non-specific conventional imaging. The compartment demonstrating both low perfusion and restricted diffusion may indicate a habitat resistant to adjuvant therapies. This could provide crucial information for treatment choice in personalized treatment. As our analyses were based on clinically available imaging modalities, this approach could easily be implemented, and potentially extended to other system.

Chapter 6 Multi-parametric and Multi-regional Histogram Analysis of MRI: Modality Integration Reveals Imaging Phenotypes of Glioblastoma

6.1 Abstract

Purpose

Integrating multiple imaging modalities is crucial for MRI data interpretation. The purpose of this study is to determine whether the proposed multi-view approach can effectively integrate histogram features from multimodal MRI and whether selected features can offer incremental prognostic values.

Methods

Eighty primary glioblastoma patients underwent surgery and chemoradiotherapy. Histogram features of diffusion and perfusion imaging were extracted from contrast-enhancing (CE) and non-enhancing (NE) regions independently. Unsupervised patient clustering was performed by the proposed multi-view approach. Kaplan-Meier and Cox proportional hazards regression analyses were performed to evaluate the relevance of clustering to survival. The metabolic signatures of patient clusters were analysed by multi-voxel spectroscopy. The prognostic values of histogram features were evaluated by survival and receiver operator characteristics curve analyses.

Results

Two patient clusters were generated, consisting of 53 and 27 patients respectively. Cluster 2 demonstrated better overall survival (OS) ($P = 0.007$) and progression-free survival (PFS) ($P < 0.001$) than Cluster 1. Cluster 2 displayed lower N-acetylaspartate/creatine ratio ($P = 0.013$), and higher glutamate + glutamine/Cr (Glx/Cr) ratio ($P = 0.027$) in NE region. Higher mean value of anisotropic diffusion in NE region was associated with worse OS (HR = 1.40, $P = 0.020$) and PFS (HR = 1.36, $P = 0.031$). Seven features selected by this approach showed significantly incremental value in predicting 12-month OS ($P = 0.020$) and PFS ($P = 0.022$).

Conclusions

The multi-view clustering method can provide an effective integration of multimodal MRI. The histogram features selected may be used as potential prognostic markers.

6.2 Introduction

As shown in Chapter 4 & 5, integrating multi-parametric MRI can reveal the *intra-tumoural* habitats, which suggests that advanced MRI may confer physiological information and compensate for the non-specificity of structural imaging. In this chapter, we will investigate if integrating multi-parametric MRI reflects the *inter-tumoural* heterogeneity.

As shown in Chapter 4, histogram features can characterize tumour heterogeneity by measuring the distribution of voxels within the tumour, and were reported to be related with tumour malignancy and patient survival (O'Connor et al., 2015). As emerging advanced MRI modalities, including diffusion and perfusion imaging markers, are developed to reflect tumour physiological properties, increasing numbers of features can be generated. It remains a challenge to effectively incorporate the physiological information to reflect the multifaceted characteristics of the tumour. Further, selecting optimal features for clinical decision making is crucial.

Although machine learning algorithms have been successful in stratifying patients (Parmar et al., 2015), classical machine learning techniques may not be effective in integrating the complementary information that multimodal advanced MRI confers, with all imaging features merged at an early stage. The multi-view approach is a data integration method that was initially developed to jointly analyse multiple genomic data derived from different molecular experiments, i.e., gene expression, copy number variation. Given the success of this approach in integrating multiple omics data to understand the complex biological system (Serra et al., 2015), we hypothesized that it could be applied to multi-parametric advanced MRI for more stable clustering results and better insights into tumour characterization (Fratello et al., 2017, Sun et al., 2014). Therefore, the purpose of this current study was to determine whether the multi-view approach can effectively integrate histogram features of multiple quantitative advanced MRI, and whether the selected features can offer incremental values in survival prediction.

6.3 Methods

6.3.1 Patients

This study was approved by the local institutional review board. Signed informed consent was obtained from all patients. Patient inclusion and exclusion criteria are in Section 3.1.1. Patient treatment is detailed in Section 3.1.2.1. Assessment of IDH-1 R132H Mutation and MGMT Methylation Status are described in 3.2.

6.3.2 Pre-operative MRI acquisition

MRI sequences were acquired on a 3-Tesla MRI system (Magnetron Trio; Siemens Healthcare, Erlangen, Germany) with a standard 12-channel receive-head coil. MRI sequences included: post-contrast T1-weighted, T2-weighted FLAIR, DSC sequence, DTI, and multi-voxel 2D 1H-MRS. Sequence details are provided in 3.3.2.2.

6.3.3 Image processing

All images were co-registered to T2-weighted images, using FLIRT (Jenkinson et al., 2002). DTI was processed as described in Section 3.4.2. The decomposition into isotropic (p) and anisotropic (q) components was performed as previously described (Pena et al., 2006b). DSC was processed as described in Section 3.4.3. The relative cerebral blood volume (rCBV), mean transit time (MTT) and relative cerebral blood flow (rCBF) maps were calculated. CSI data were processed as described in 3.4.4. Only CSI voxels containing more than 50% tumour T2-voxels were included for further analysis. Tumour regions of interest (ROIs) were manually drawn as described in 3.4.6.1.

6.3.4 Histogram features

The study design is summarized in Figure 6.1. Histogram features were extracted using the Statistics and Machine Learning Toolbox of MATLAB (version 2016a). Perfusion images (rCBV, MTT and rCBF) and diffusion images (DTI-p and DTI-q) were analysed separately.

The CE and NE ROIs in each map were also analysed independently. Therefore, four categories of feature sets (CE-diffusion, NE-diffusion, CE-perfusion, NE-perfusion) can be obtained, considering features extracted from multiple modalities and regions. Intensity histograms were constructed using 100 bins. A total of 10 features were calculated, including mean, standard deviation (SD), median, mode, skewness, kurtosis, and 5th (Prc5), 25th (Prc25), 75th (Prc75), 95th (Prc95) percentiles of intensity histograms. Therefore, altogether 100 features were extracted from each subject.

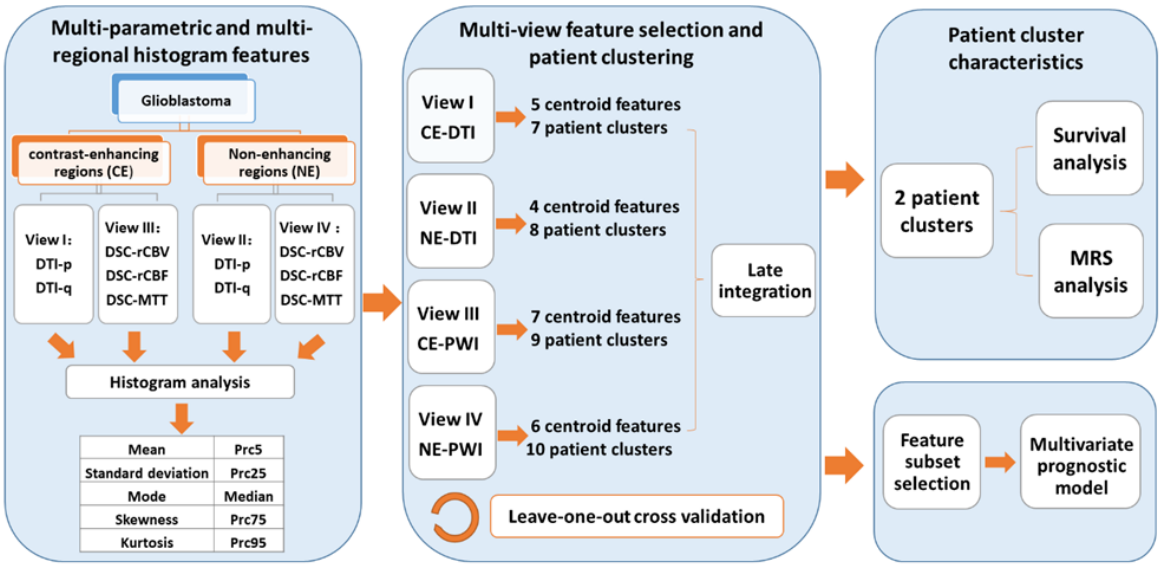

Figure 6.1 Study design. DTI-p and DTI-q maps are generated from diffusion tensor imaging (DTI). The relative cerebral blood volume (rCBV), mean transit time (MTT) and relative cerebral blood flow (rCBF) maps are generated from dynamic susceptibility contrast (DSC) imaging. Histogram features extracted from the multiple modalities and regions (contrast-enhancing and non-enhancing) are treated as four independent views. Each view is first clustered to select centroid features, which are later used to cluster patients. The resulting clusters from each view are integrated to yield two patient clusters. A leave-one-out cross-validation is performed. Patient clusters are assessed in survival analysis and their metabolic signatures are compared. The centroid features are ranked according to the importance in the clustering and selected features are used to build the multivariate prognostic model.

6.3.5 Multi-view feature selection and clustering

The analysis was performed using a multi-view late integration methodology called Multi-View Biological Data Analysis (MVDA), implemented in R and available from GitHub

(https://github.com/angy89/MVDA). As perfusion and diffusion characteristics were considered to bear different physiology information, and different tumour region may have different biological significance, we hypothesised that each feature set may represent a unique view in characterising tumour properties. Therefore, we treated four categories of feature sets as different views to maximize tumour characterization in each case. We applied this analytic tool into imaging analysis, considering that the multi-view approach allows analysing each view independently and then merging the results using a late integration methodologies (Pavlidis et al., 2001). This offer the advantage to avoid representing bias in feature selection compared to classical feature selection and machine learning methods.

The analysis was divided into multiple steps: I. To reduce the dimensionality and remove noisy information, the features were first clustered using the hierarchical ward clustering method for each view. The number of feature clusters was determined by the previously proposed VAL index (Serra et al., 2015). Clustering solutions with high correlation within each cluster and low correlation between the clusters were preferred. The number of features was reduced by selecting the centroids of the feature clusters which represent the features of each view. II. For each view, the patients were clustered by applying a hierarchical ward clustering method using the features selected from the previous step. The number of patient clusters was also determined by the VAL index (Serra et al., 2015). III. The clustering results of each view were integrated into a late integration method. The vector of clustering assignment of each view was transformed into a binary membership matrix, with patients on the rows and clustering on the columns. These matrices were transposed and stacked vertically to create a larger matrix X with L rows (the clusters) and N columns (the patients). This matrix was then factorized to obtain two matrices P (with L rows and k columns) and H (with k rows and N columns), minimizing the difference between X and PH. In this settings, H represented the membership matrices of the N patients to the final multi-view clusters. The number of multi-view clusters was set to 2 to dichotomize patients into two clusters with better or worse survivals respectively.

6.3.6 Leave-one-out cross validation of the clustering

To validate patient clustering was not obtained by random, a leave-one-out cross-validation (LOOCV) procedure was applied. Briefly, all steps of the MVDA approach were repeated by leaving one patient out of the cohort at each repetition. The consensus analysis was performed in the 80 clustering results obtained from the LOOCV approach. An 80 ×80 co-occurrence consensus clustering matrix M was created, where M (*i, j*) indicating percentage of times that the patients *i* and *j* were clustered together across the 80 dataset perturbations.

6.3.7 Feature ranking

To estimate the contribution of each centroid feature in the clustering, the variable importance evaluation function 'varImp' in the R package 'Caret' was used (Kuhn, 2008). The patient clustering result was firstly used to train a logistic regression model, which then was used to evaluate the importance of each feature, according to the model performance. The feature importance was scored and scaled by the function with a maximum value of 100.

6.3.8 Statistical analysis

All statistical analyses were performed in RStudio v3.2.3. CSI data were compared with the Wilcoxon rank sum test using the Benjamin-Hochberg procedure for controlling the false discovery rate in multiple comparisons. Kaplan-Meier and Cox proportional hazards regression analyses were performed to evaluate patient survival. For Cox proportional hazards regression, all relevant covariates, including IDH-1 mutation status, MGMT methylation status, sex, age, the extent of resection and contrast-enhancing tumour volume were considered. For Kaplan-Meier analysis using the Log-rank test, each feature was dichotomized using optimal cutoff values calculated by 'surv_cutpoint' function in the R Package "survminer". Patients who were alive at the last known follow-up were censored. Logistic regression was used to test prognostic values of covariates for 12-month overall survival (OS) and progression-free survival (PFS). The baseline models were constructed using all relevant clinical covariates, including IDH-1 mutation status, MGMT promoter methylation status, the extent of resection sex, age, contrast-enhancing tumour volume. Histogram features were subsequently added into baseline models

to construct OS and PFS models. The incremental prognostic values of imaging features were determined according to the area under the receiver operator characteristics curve (AUC), which was compared using one-way ANOVA. The hypothesis was accepted at a two-sided significance level of alpha = 0.05.

6.4 Results

6.4.1 Patients

We included 80 patients who received CCRT and had available survival data into the study. Patient characteristics and two patient clusters were summarized in Table 6.1.

Table 6.1 Clinical characteristics

Variables	**Patient Number**			***P* Value**
	Total (n = 80)	Cluster 1 (n = 53)	Cluster 2 (n = 27)	
Age at diagnosis				
<60	35	18	16	0.058
≥60	45	35	11	
Sex				
Male	58	41	17	0.201
Female	22	12	10	
Extent of resection (of enhancing tumour)				
Complete resection	56	35	21	0.267
Partial resection	22	17	5	
Biopsy	2	1	1	
MGMT-methylation status*				
Methylated	37	24	13	0.929
Unmethylated	41	27	14	
IDH-1 mutation status				
Mutant	7	4	3	0.622
Wild-type	73	49	24	
Pre-operative Tumour volumes(cm3) #				
Contrast-enhancing	49.7 ± 28.1	50.2 ± 28.4	50.4 ± 28.1	0.823
Non-enhancing	64.7 ± 48.3	48.7 ± 27.9	92.8 ± 53.5	0.007
Survival (days)				
Median OS (range)	461 (52-1259)	424 (52-839)	689 (109-1259)	0.020†
Median PFS (range)	264(25-1130)	248 (25-607)	318 (279-1130)	<0 .001†

*MGMT-methylation status unavailable for 2 patients; #mean ± SD of original data. †Log-Rank test; SD: standard deviation; MGMT: O-6-methylguanine-DNA methyltransferase; IDH-1: Isocitrate dehydrogenase 1; cm: centimeters; OS: overall survival; PFS: progression-free survival.

6.4.2 Identification of patient clusters

From the four views, 5, 4, 7 and 6 centroid features were respectively selected (Figure 6.2, Table 6.2). Using the centroid features and optimal cluster numbers determined in the algorithm, patients were firstly divided into 7, 8, 9 and 10 clusters in each view, using hierarchical ward clustering. Late integration of four views yielded a final clustering of two patient clusters, with 53 and 27 patients in each cluster respectively.

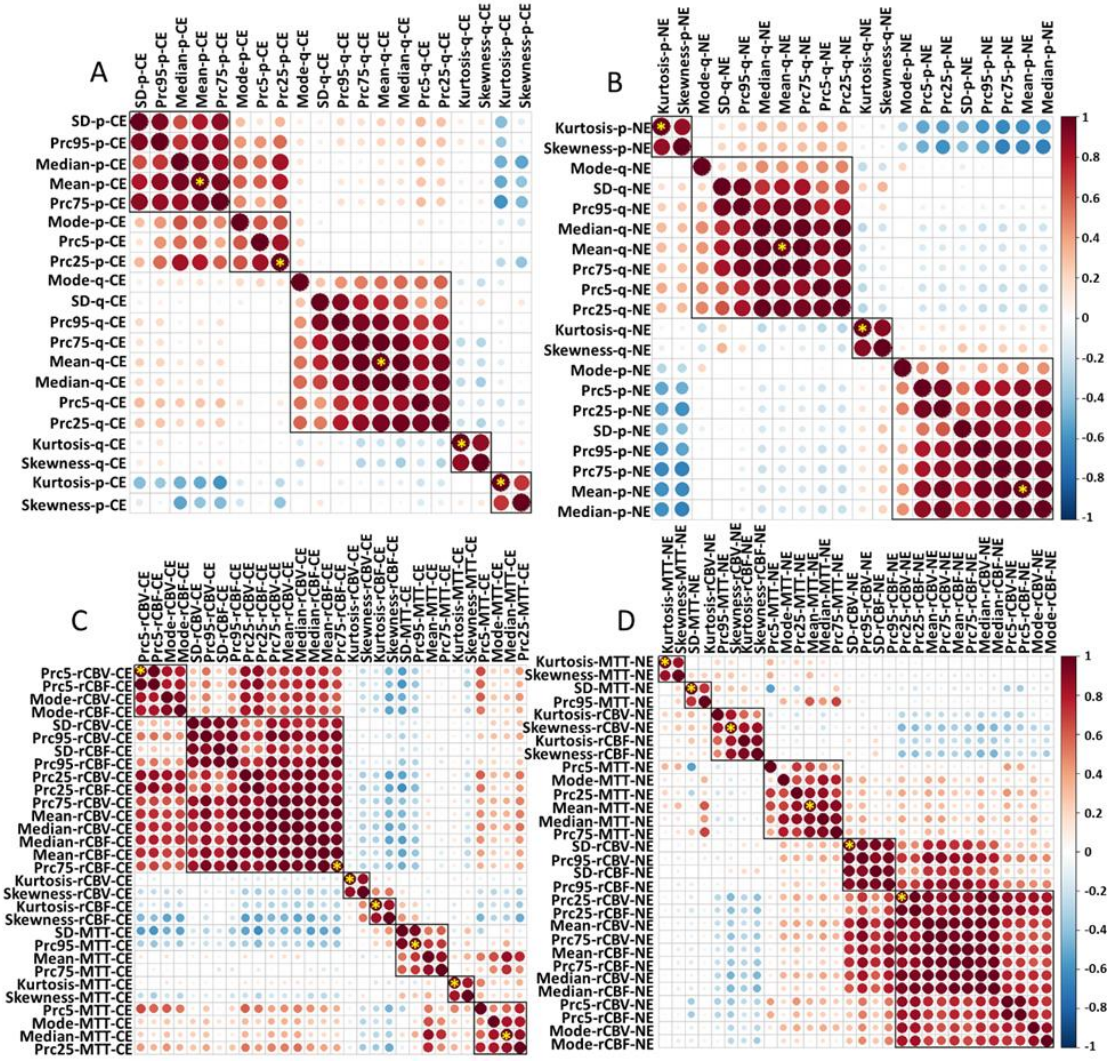

Figure 6.2 Multi-view feature selection In each view, all features are clustered using the hierarchical ward clustering method. The centroid features (marked by yellow stars) are selected to represent each view. A: view 1 (CE-DTI); B: view 2 (NE-DTI); C: view 3 (CE-PWI); D: view 4 (NE-PWI).

Table 6.2 Features selected from multi-view clustering

View	Features
View1: CE-diffusion	Mean-p-CE
	Prc25-p-CE
	Kurtosis -p-CE
	Mean-q-CE
	Kurtosis-q-CE
View2: NE-diffusion	Mean-p-NE
	Kurtosis-p-NE
	Mean-q-NE
	Kurtosis-q-NE
View3: CE-perfusion	Prc75-rCBF-CE
	Prc5-rCBV-CE
	Kurtosis-rCBV-CE
	Kurtosis-rCBF-CE
	Prc95-MTT-CE
	Median-MTT-CE
	Kurtosis-MTT-CE
View4: NE-perfusion	Prc25-rCBV-NE
	SD-rCBV-NE
	Skewness-rCBV-NE
	Median-MTT-NE
	SD-MTT-NE
	Kurtosis-MTT-NE

6.4.3 Leave-one-out cross-validation of patient clustering

After leave-one-out cross-validation, the co-occurrence consensus clustering matrix was computed. The result showed that the two patient clusters generated from the unsupervised clustering were stable. The mean values of the co-occurrence consensus clustering matrix were 0.79 for Cluster 1 and 0.68 for Cluster 2 (Figure 6.3).

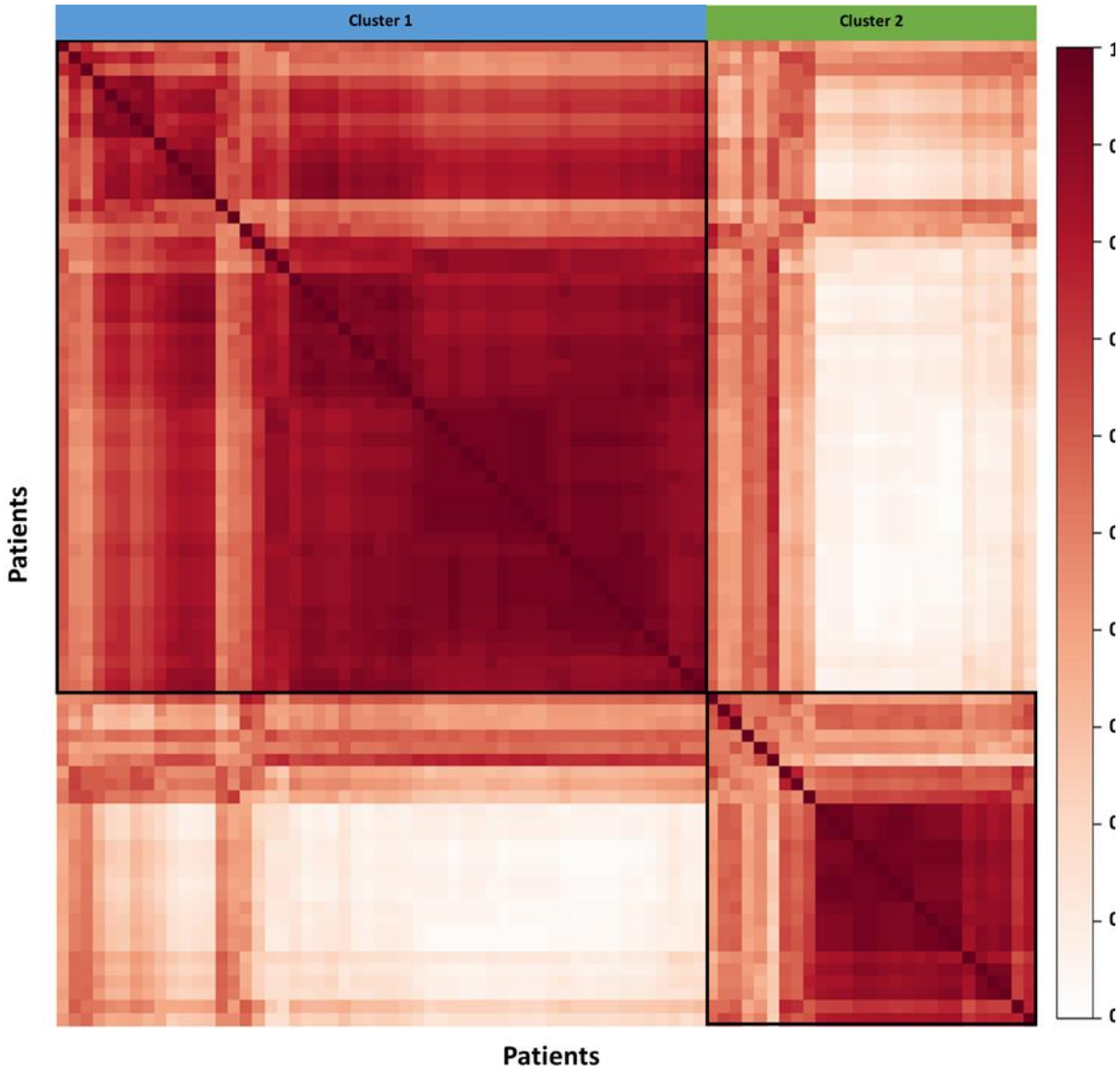

Figure 6.3 Leave-one-out cross-validation of patient clustering. After multi-view clustering, consensus analysis was performed based on the 80 clustering results obtained after the leave-one-out cross-validation. The mean value of the co-occurrence consensus clustering matrix was 0.79 for patient Cluster 1 and 0.68 for patient Cluster 2.

6.4.4 Clinical relevance of patient clusters

The two patient clusters showed no significant differences in clinical characteristics (Table 6.1). Interestingly, two clusters had similar contrast-enhancing tumour volume. Cluster 1, however, had significantly smaller non-enhancing tumour volume ($P = 0.007$) than Cluster 2.

Further, the two clusters showed a significant difference in survival. Specifically, Cluster 2 showed better OS (Log-rank test, $P = 0.020$) and better PFS (Log-rank test, $P < 0.001$) than Cluster 1 in Kaplan-Meier analysis (Table 6.1, Figure 6.4.A & 6.4.B).

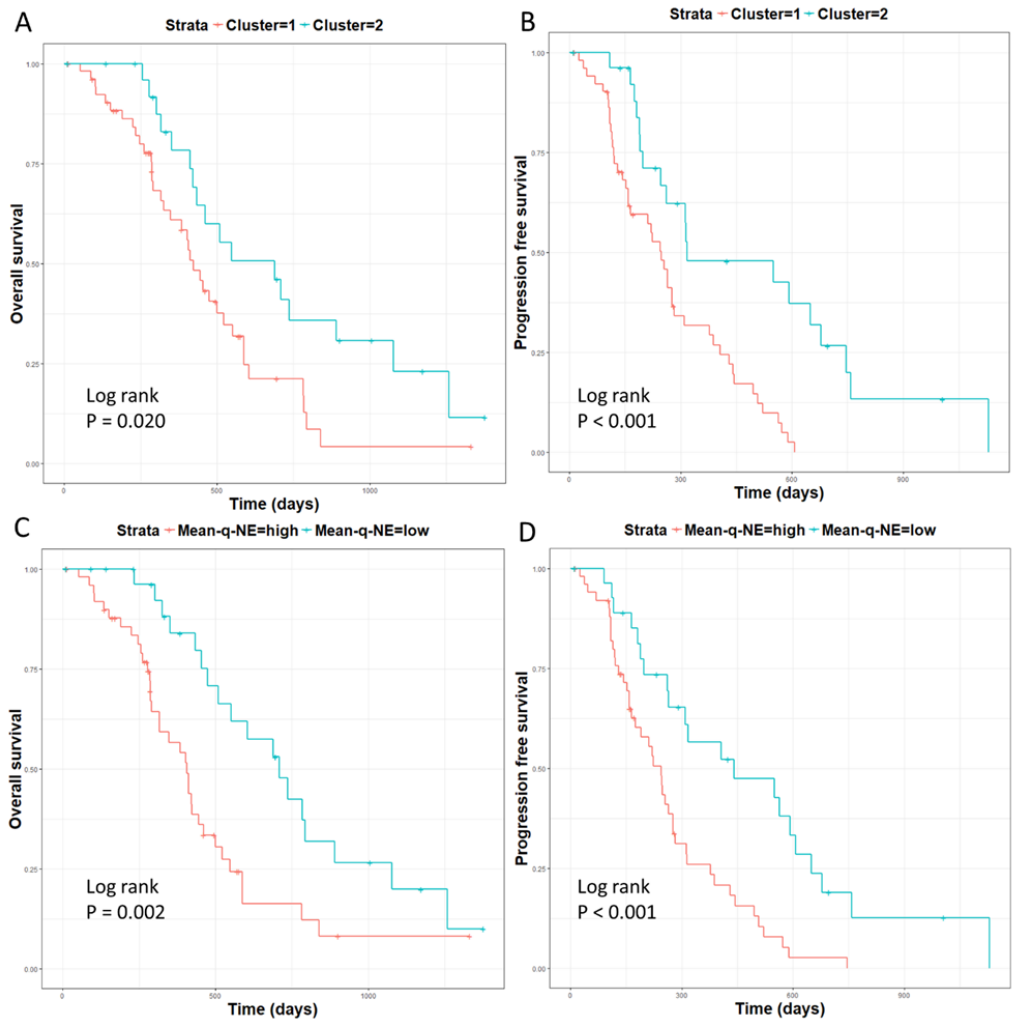

Figure 6.4 Survivals of patient clusters. Log-rank test showed patient Cluster 2 displayed better OS ($P = 0.020$) (A) and PFS ($P < 0.001$) (B). Higher man value of DTI-q in the non-enhancing region (Mean-q-NE) was associated with a worse OS ($P = 0.002$) (C) and PFS ($P < 0.001$) (D).

Since MGMT promoter methylation status was missing in two patients, the multivariate Cox proportional hazards regression modelling was tested in the remaining 78 patients. The results showed that Cluster 2 displayed significantly better OS ($P = 0.007$, HR = 0.32) and PFS ($P < 0.001$, HR = 0.33) than Cluster 1, considering relevant covariates. Among these covariates,

extent of resection ($P = 0.019$, HR = 2.20) and contrast-enhancing tumour volume ($P < 0.001$, HR = 1.02) significantly affected OS. Extent of resection ($P = 0.003$, HR = 2.84) significantly affected PFS. No significance was found in other clinical factors.

6.4.5 Metabolic signatures of patient clusters

Due to the abovementioned rules excluding CSI voxels containing less than 50% tumour, CSI data were missing in four patients. Our results showed N-acetylaspartate/creatine (NAA/Cr) ratio of Cluster 2 was significantly lower than in Cluster 1, both in the CE ($P < 0.001$) and NE region ($P = 0.013$). In NE region, glutamate + glutamine/Cr (Glx/Cr) ratio of Cluster 2 was significantly higher than Cluster 1 ($P = 0.027$ respectively). No other metabolites showed significant differences. The comparison of NAA/Cr and Glx/Cr of two patient clusters are detailed in Table 6.3 and demonstrated in Figure 6.5. Two example spectra are demonstrated by Figure 6.6.

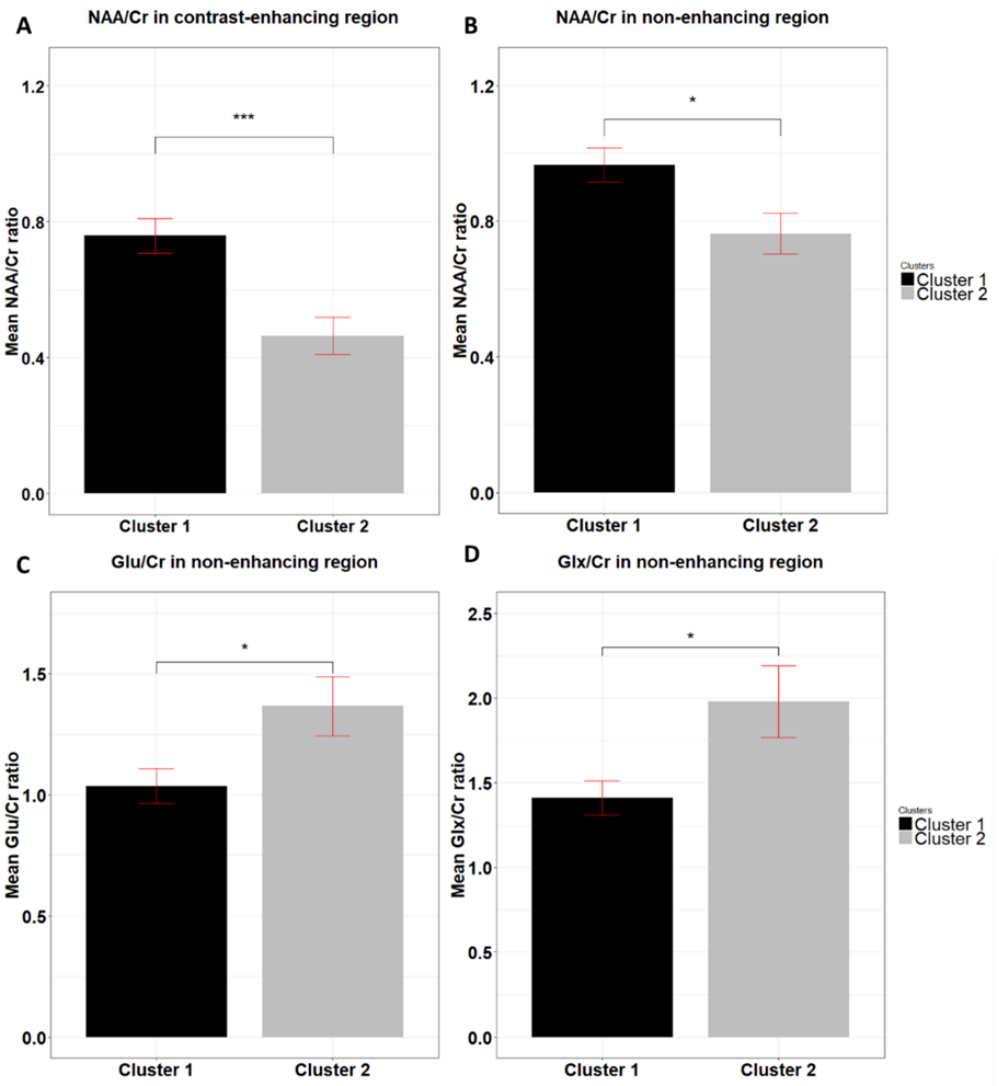

Figure 6.5 NAA/Cr and Glx/Cr of two patient clusters. N-acetylaspartate/creatine (NAA/Cr) ratio in Cluster 1 was significantly higher than in Cluster 2, both in the contrast-enhancing (CE) region ($P < 0.001$) (A) and non-enhancing (NE) region ($P = 0.013$) (B). In the NE region, Cluster 1showed significantly higher glutamate/Cr (Glu/Cr) ratio ($P = 0.037$) (C) and glutamate + glutamine/Cr (Glx/Cr) ratio ($P = 0.027$) (D) than Cluster 2.

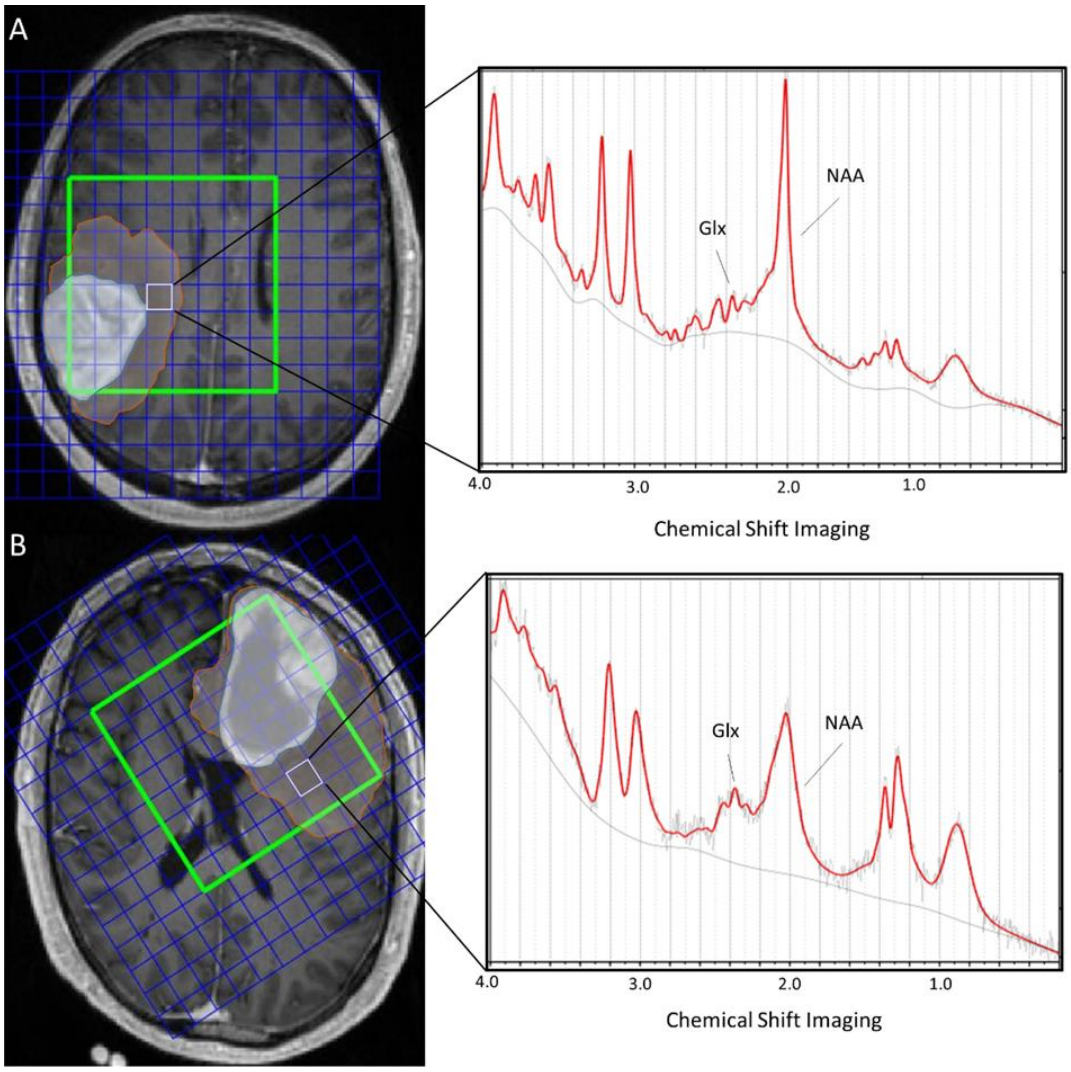

Figure 6.6 Example spectrum of patient clusters. T1-weighted contrast-enhanced MR images show contrast-enhancing (CE) (blue) and non-enhancing (NE) (orange) tumour regions, with two example spectra of NAA at 2.0 ppm and Glx at 2.05-2.50 ppm. One example from Cluster 1 (A) shows NAA/Cr ratio of 1.36 and Glx/Cr ratio of 1.54. The other example from Cluster 2 (B) shows NAA/Cr ratio of 0.58 and Glx/Cr ratio of 3.09.

Table 6.3 Metabolic statistics of patient clusters

Metabolite	Contrast-enhancing tumour region					Non-enhancing tumour region				
	Cluster 1		Cluster 2		*P* Value	Cluster 1		Cluster 2		*P* Value
	Mean ± SD	95% CI	Mean ± SD	95% CI		Mean ± SD	95% CI	Mean ± SD	95% CI	
Cho/NAA	0.60 ± 0.32	0.50-0.69	0.49 ± 0.26	0.38-0.60	0.091	0.54 ± 0.50	0.38-0.70	0.45 ± 0.19	0.37-0.53	0.689
Cho/Cr	0.70 ± 0.24	0.63-0.77	0.63 ± 0.17	0.55-0.70	0.244	0.44 ± 0.13	0.40-0.48	0.40 ± 0.14	0.34-0.46	0.149
NAA/Cr	0.76 ± 0.35	0.66-0.86	0.46 ± 0.27	0.35-0.58	<0.001	0.97 ± 0.32	0.86-1.07	0.76 ± 0.30	0.64-0.89	0.013
GSH/Cr	0.31 ± 0.28	0.23-0.40	0.40 ± 0.36	0.23-0.57	0.245	0.34 ± 0.19	0.27-0.41	0.39 ± 0.27	0.26-0.51	0.687
Glx/Cr	1.89 ± 1.11	1.56-2.23	1.85 ± 1.29	1.31-2.40	0.651	1.41 ± 0.58	1.20-1.62	1.98 ± 1.04	1.54-2.42	0.027
mIn/Cr	1.37 ± 0.88	1.12-1.62	1.28 ± 0.77	1.08-1.99	0.657	1.14 ± 0.41	1.00-1.27	1.16 ± 0.38	1.00-1.32	0.924
Lac/Cr	6.37 ± 5.73	4.67-8.07	4.81 ± 4.14	2.93-6.69	0.448	1.13 ± 0.98	0.75-1.52	1.45 ± 2.62	0.11-2.80	0.087

Cho: Choline; NAA: N-acetyl aspartate; GSH: glutathione; Glu: glutamate; Glx: glutamate + glutamine; mIn: myo-inositol; Lac: lactate; CI: confidence interval.

6.4.6 Feature ranking and feature subset selection

Seven features with a score over 50 were selected according to the importance of centroid features in the clustering (Figure 6.7): Mean-p-NE (mean value of DTI-p in the non-enhancing tumour regions, score: 100), Mean-q-NE (mean value of DTI-q in the non-enhancing tumour regions, score: 82.5), Prc25-rCBV-NE (twenty-fifth percentile of rCBV in the non-enhancing tumour regions, score: 74.7), Kurtosis-p-NE (kurtosis of DTI-p histogram in the non-enhancing tumour regions, score: 66.6), Mean-q-CE (mean value of DTI-q in the contrast-enhancing tumour regions, score: 63.9), Prc25-p-CE (twenty-fifth percentile of DTI-p in the contrast-enhancing tumour regions, score: 63.7), Prc95-rCBF-NE (ninety-fifth percentile of rCBF in the non-enhancing tumour regions, score: 61.7).

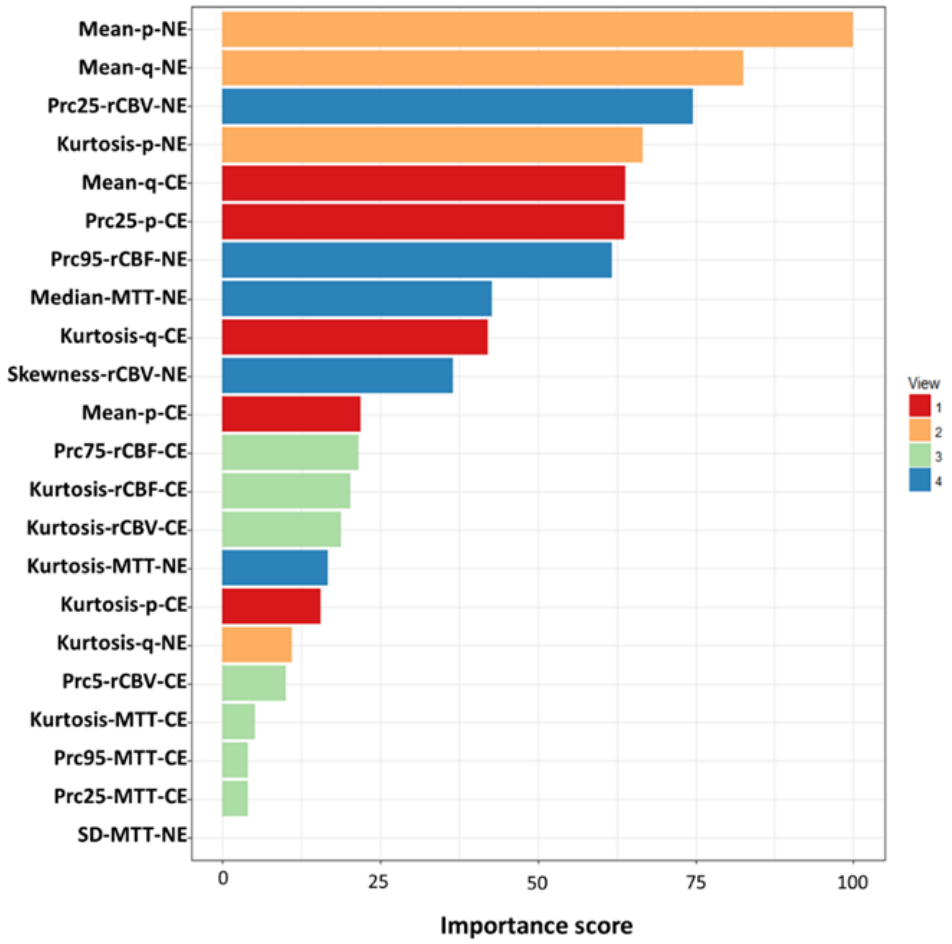

Figure 6.7 Feature ranking. The centroid features were ranked according to the importance in the clustering. The scores were scaled with a maximum value of 100.

6.4.7 Multivariate prognostic performance of selected features

The seven selected features all showed significance in survival analysis (Table 6.4). Particularly, higher Mean-q-NE was associated with worse OS (HR = 1.40, P = 0.020) and worse PFS (HR = 1.36, P = 0.031). The Kaplan-Meier curves showing the relevance of Mean-q-NE in OS and PFS are demonstrated by Figure 6.4 C & 6.4 D.

For prediction of 12-month OS and PFS, the AUC of baseline multivariate models were 0.81 (confidence interval [CI]: 0.70-0.93) and 0.77 (CI: 0.65-0.88) respectively. The results of model comparison showed that these seven features significantly improved both OS model (AUC: 0.91, CI: 0.84-0.99, P = 0.020) and PFS model (AUC: 0.89, CI: 0.81-0.97, P = 0.022) (Figure 6.8).

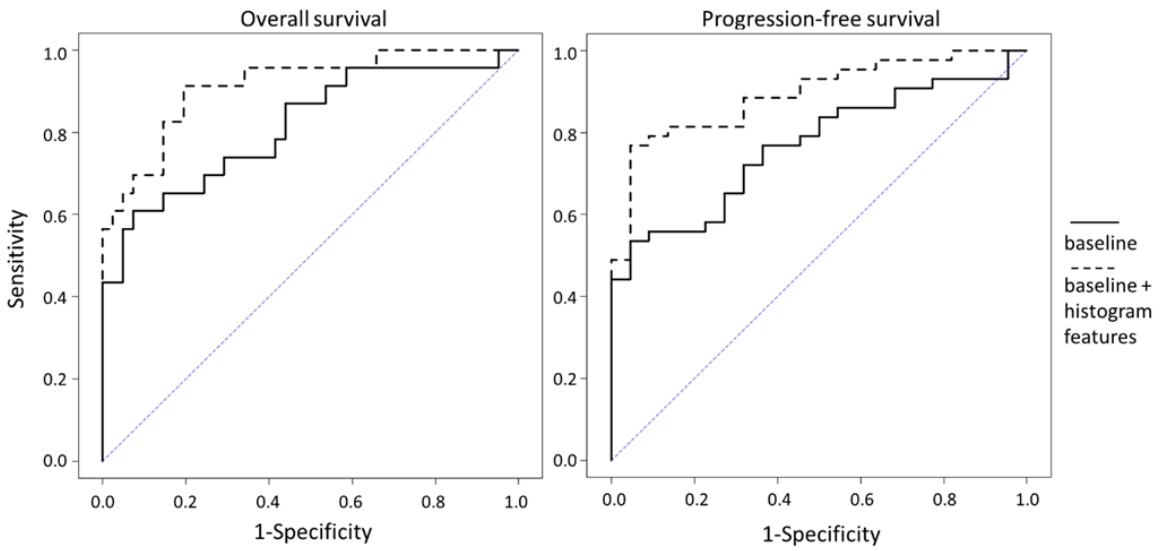

Figure 6.8 Receiver operating characteristic (ROC) curve analysis. Receiver operating characteristic (ROC) curves showed that the models of 12-month OS (left) and PFS (right) were significantly improved (P = 0.020, and P = 0.022 respectively) by adding the seven most important histogram features into the baseline models.

Table 6.4 Survival statistics of the selected features

Feature	Progression-free survival*				Overall survival*			
	HR	95%CI	*P* value (Cox regression)	*P* value (Log-rank)	HR	95%CI	*P* value (Cox regression)	*P* value (Log-rank)
Mean-p-NE	0.79	0.58-1.08	0.143	**< 0.001**	0.74	0.53-1.04	0.083	**0.015**
Mean-q-NE	1.40	1.05-1.86	**0.020**	**< 0.001**	1.36	1.03-1.79	**0.031**	**0.002**
Prc25-rCBV-NE	1.28	0.94-1.74	0.121	0.052	1.53	1.09-2.14	**0.014**	**0.019**
Kurtosis-p-NE	1.18	0.85-1.63	0.326	0.168	1.66	1.15-2.39	**0.007**	**0.048**
Mean-q-CE	1.17	0.90-1.51	0.245	**0.029**	1.17	0.89-1.55	0.268	0.197
Prc25-p-CE	0.88	0.66-1.17	0.369	**0.032**	0.79	0.56-1.10	0.165	**0.004**
Prc95-rCBF-NE	1.11	0.88-1.40	0.358	**0.049**	1.15	0.88-1.51	0.307	0.063

*Cox models accounted for IDH-1 mutation status, MGMT methylation status, sex, age, the extent of resection and contrast-enhancing tumour volume. HR: hazard ratio; CI: confidence interval; CE: contrast-enhancing region; NE: non-enhancing region.

6.5 Discussion

This study showed that integrating multi-parametric and multi-regional MRI histogram features may help to stratify patients and identify invasive tumour phenotype, using a multi-view integration approach. Seven histogram features extracted from diffusion and perfusion images were particularly useful for predicting patient outcomes, as demonstrated by multivariable Cox regression and receiver operating characteristic curve analysis.

Histogram analysis of quantitative MRI offers a method of characterizing tumour heterogeneity (O'Connor et al., 2008, Shiroishi et al., 2016). Evidence support the utility of MRI histogram features in heterogeneity evaluation and survival prediction (Choi et al., 2016, Andras et al., 2011, Santarosa et al., 2016). One recent study, however, showed that diffusion and perfusion histogram parameters only showed marginal prognostic values in multivariate models containing clinical factors (Burth et al., 2016). Here our results demonstrated that diffusion and perfusion histogram parameters carry prognostic values, even after accounting for relevant clinical covariates in the multivariate models. Moreover, features selected using the unsupervised algorithm can significantly improve the survival prediction performance of clinical models. Further studies using prospective design are needed for validating the prognostic value of imaging parameters.

Limited studies have investigated both perfusion and diffusion imaging parameters in one cohort (Coban et al., 2015, Burth et al., 2016, Hilario et al., 2014). Moreover, most studies analysed perfusion and diffusion parameters separately. As perfusion and diffusion imaging measure different facets of tumour physiology, we hypothesized that integrating them effectively may lead to better tumour characterization. The multi-view approach can offer the advantage of a parallelized selection of features from multiple modalities, and synthesize the complementary information at a late stage. By doing so, it can avoid representation bias, since the analyses on each view are independent and integrated for final clustering (Serra et al., 2015). With this unsupervised algorithm, we separated patients into two clusters with distinct survivals and metabolic signatures. Our results may suggest that appropriately integrating multiple modalities is crucial for tumour characterization.

The physiology of tumour core (CE) and peritumoural region (NE) are considered distinct, which is our motivation of differentiating tumour regions for feature extraction and treating them as independent views. Our results showed higher feature Mean-q-NE (mean value of DTI-q in NE region) was associated with worse survivals. Correspondingly, MRS results showed that higher NAA/Cr and lower Glx/Cr levels in the NE region were also associated with worse survivals. Glioblastoma is recognized to preferentially migrate along the white matter tracts, which may lead to increased anisotropic movement of water molecules. Further, NAA is known as a marker of neuronal integrity, and glutamate is a key neurotransmitter that maintains neuronal function. High extracellular glutamate may be caused by structural destruction in the tumour (Noch and Khalili, 2009). Since the patients in our cohort received maximal safe surgery with the aim to resect the CE region, one possible explanation for the above findings is that the worse survival group may have disrupted rather than destroyed neurons in the NE region, which may facilitate tumour infiltration and be responsible for treatment failure. However, this finding is different from the previous findings that a decreased NAA within the tumour may indicate a more aggressive phenotype. Here our results may indicate the NAA profile in the non-enhancing tumour is heterogeneous, which may confound our finding. The findings here merit a further investigation, especially using histological validation.

With the advances of imaging modality and computer vision, radiomics approach can extract high-throughput features from medical images, which are hypothesized to provide more comprehensive measures of tumour imaging phenotype (Itakura et al., 2015, Aerts et al., 2014b). The increasing number of features, however, may pose the challenges of effective feature selection and modality integration for robust phenotyping (Verma et al., 2017, Zhou et al., 2018). Currently, many techniques have been developed for this purpose (Larue et al., 2017). Considering the specific tumour biology information conferred by physiological imaging over structural imaging, new approaches with biological hypothesis might be needed to characterise the complex tumour system. Our current study investigated the feasibility of a genomic analytic tool in imaging studies, using histogram features considering the interpretability and robustness of features. Future work may potentially be extended to broader imaging feature sets and bioinformatics tools.

Our study has some limitations. Firstly, although we used a leave-one-out cross-validation, the patient population reported is from a single centre. Secondly, although previous studies have validated the histological correlation of the imaging markers, our current findings need further biological validation. Lastly, as the ^{1}H-MRS voxels were larger than T2 space voxels, we had fewer patients with CSI data available.

6.6 Conclusion

Our results showed that the multi-view clustering method can provide an effective approach of integrating multiple quantitative MRI features. The histogram features selected from the proposed approach may be used as potential imaging markers in personalized treatment strategy and response determination.

Chapter 7 Decoding the Inter-dependence of Multi-parametric Magnetic Resonance Imaging to Unravel Patient Subgroups Correlated with Survivals

7.1 Abstract

Objective

Glioblastoma is highly heterogeneous in microstructure and vasculature, creating various tumour microenvironments among patients, and could lead to different phenotypes. The purpose of this study was to interrogate the inter-dependence of microstructure and vasculature using perfusion and diffusion imaging, and to investigate the utility of this approach in tumour invasiveness assessment.

Methods

A total of 115 primary glioblastoma patients were prospectively recruited for surgery and pre-operative MRI scan. Apparent diffusion coefficient (ADC) was calculated from diffusion imaging, and relative cerebral blood volume (rCBV) was calculated from perfusion imaging. Empirical copula transform was applied to ADC and rCBV values in contrast-enhancing tumour region to obtain their joint distribution, which was then discretized to extract second-order features for hierarchical clustering. Clinical characteristics and lactate levels obtained

from MR spectroscopy were compared. Survivals were analyzed using Kaplan-Meier and multivariate Cox regression analyses.

Results

Three patient subgroups were identified by unsupervised clustering. These subtypes showed no significant differences in clinical characteristics but were significantly different in lactate level and patient survivals. Specifically, the subtype demonstrating high inter-dependence of ADC and rCBV displayed a higher lactate level than the other two subtypes ($P = 0.016$ and $P = 0.044$ respectively). Both subtypes of low and high inter-dependence showed worse progression-free survival compared to the intermediate subtype ($P = 0.046$ and $P = 0.009$ respectively).

Conclusions

The inter-dependence between perfusion and diffusion imaging may be useful in stratifying patients and evaluating tumour invasiveness. This approach provided overall measures of tumour microenvironment using multimodal MRI.

7.2 Introduction

As stated in Chapter 1, remarkable heterogeneity can be found in glioblastoma (Sottoriva et al., 2013b, Verhaak et al., 2010). Tumour habitats of high or low cell densities can exist in either sufficiently or poorly perfused sub-regions, causing spatial variation in the tumour microenvironment (Gatenby et al., 2013). As shown in Chapter 4 & 5, tumour habitats or sub-regions can be revealed using the combination of high/low intensities of multiple imaging modalities. It is shown in Chapter 6 that integrating the information of multiple MRI modalities is useful to identify invasive tumour phenotypes. These methods, however, tend to complement the information of a single modality with other modalities, providing limited information about the overall interaction between modalities. Validated surrogates to quantify the inter-dependence between perfusion and diffusion imaging remains scant.

Tumour imaging is central to depict the global prosperities of solid tumours. Multi-parametric imaging enables the incorporation of complementary imaging modalities. The relative cerebral blood volume (rCBV) calculated from perfusion weighted imaging can measure tumour vascularity and has been shown to correlate with cellular proliferation in high-grade gliomas (Price et al., 2011). The apparent diffusion coefficient (ADC) calculated from diffusion weighted imaging provides information about the tissue microstructure of different cellularity/cell packing (Kalpathy-Cranner et al., 2014), by measuring microscopic diffusivity of water molecules. Considering the complementary values of multi-parametric imaging, joint analysis of perfusion and diffusion has the potential to provide clinical insight by depicting the global variations of cellular structure and vasculature in solid tumours, which may potentially reflect tumour microenvironment.

Here we propose an approach to characterise the overall tumour microenvironment by investigating the inter-dependence between diffusion and perfusion MRIs using the copula transform (Nelsen, 2007), a multivariate probability distribution describing the inter-dependence of random variables. We leveraged empirical copula transform to solve the challenges of parametric model fitting posed by the distinct marginal distribution of different modalities and then extracted features from the discrete joint distribution matrix to quantify the inter-dependence between ADC and rCBV. Therefore, the purpose of this study was to

characterise the overall tumour microenvironment by quantifying the inter-dependence of ADC and rCBV using copula transform, and to investigate the utility of inter-dependence characteristics in patient stratification.

7.3 Theory

7.3.1 Challenges in analysing the inter-dependence of random variables

The existing literature involving analysis of inter-dependencies commonly originate from the probabilistic interpretation of Canonical Correlation Analysis (Bach and Jordan, 2005). To be precise, let $X = (x_1, \dots, x_{N_X})$and $Y = (y_1, \dots, y_{N_Y})$ be random variables with dimensions N_X and$N_Y \in \mathbb{N}$, respectively (i.e.,$X \in \mathbb{R}^{N_X}$), then the following inter-dependence model can be introduced:

$$Z \sim Mult(\theta), \text{where} (X, Y)|Z \sim \mathcal{N}_{N_X+N_Y}(\mu_z, \Phi),$$

where Φ represents the covariance matrix of variables X and Y.

The normal distribution assumption in the above model fitting, however, may be challenged by severe model mismatch if the variables are non-normally distributed. Later, it was proposed that normal distribution assumption on variables could be relaxed by applying exponential family transforms (Klami et al., 2012). However, since most exponential transforms are not available in multi-dimensional settings, such method is still impractical for multidimensional data.

One way to mitigate above limitations is to apply copula framework. The empirical copula can be used to prepare our data for later discrete feature extraction and clustering. Therefore we named our approach inter-dependence clustering via copula transform and discrete feature extraction.

7.3.2 Empirical copula

In probability theory, a copula is a normalized multivariate probability distribution that provides a framework to quantify the inter-dependence structure between random variables. This framework is particularly useful when the given random variables follow non-normal distributions. Moreover, it can be applied to higher dimensional data, which is difficult when using standard joint distributions.

We first recall the definition of the copula transform and Sklar's theorem which provides theoretical validation for the application of the copula transform (Sklar, 1973).

Definition. A function C: $[0,1]^N \rightarrow [0,1]$ is a N-dimensional copula if C is a joint cumulative distribution function (CDF) of a N-dimensional random vector on the unit cube $[0,1]^N$ with uniform marginal.

Sklar's Theorem. Let $F_i(x) := Pr[X_i \leq x]$ are continuous marginal CDFs. Then, every multivariate cumulative distribution function

$$H(x_1, \dots, x_N) = Pr[X_1 \leq x_1, \dots, X_N \leq x_N]$$

of a random vector $(X_1, \dots, X_N)$ can be expressed in terms of its marginal $F_i(x_i) = Pr[X_i \leq x_i]$ and a copula C, such that

$$H(x_1, \dots, x_N) = C(F_1(x_1), \dots, F_N(x_N)).$$

The copula C describes the dependence structure between the variables $X_1, \dots, X_N$.A wide range of marginal distributions, such as exponential, gamma, beta, and empirical, can be included in Sklar's theorem. However, since a standard joint distribution is challenging to be obtained from noisy MRI data, we used the empirical copula to estimate the distribution function, namely:

$$C(u_1, \dots, u_N) := \frac{1}{N} \sum_{i=1}^{N} \chi_{(U_1^i \leq u_1, \dots, U_N^i \leq u_N)}.$$

7.3.3 Clustering model specification

Copula examines the inter-dependence between random variables across the entire distribution. In particular, they capture the effects of higher-order moments, i.e., skewness or kurtosis. Although such effects might benefit the research in Geostatistical interpolation and spatial statistics, they may possibly cause issues of fat-tails and skewness of data distribution, and such effeteness may hence present unnecessary noises and cause a mismatch in clustering, including:

a) The weight of the data value at each point might be altered. That is, some data points might be given undesired priorities by the copula transform.
b) Spatial information of the data might be changed. The copula transform is not an isometric transform (Lindenstrauss and Tzafriri, 2013) and hence the data matrix may get deformed after the copula is applied.

7.3.4 Methodology design

Here we propose to use discrete feature extraction to reduce the above-mentioned noises elements as the spatial information is reduced in the discretization process (Wiatowski et al., 2016). Our cluster analysis consists of the following steps:

Step 1. By applying the empirical copula transform, we normalized the voxel values of ADC and rCBV to [0,1] and extracted the inter-dependence structure of the transformed ADC and rCBV values.

Step 2. We discretized the resulting copula into a 10×10 matrix, in which each element $p(i,j)$ represented the relative frequency of voxels within ROI falling into the corresponding discretized value range:

$$p(i,j) = \frac{P(i,j)}{\sum_{i=1}^{10} i \sum_{j=1}^{10} p(i,j)} \qquad (i,j = 1,2,\dots,10)$$

where $P(i,j)$ is the number of voxels whose normalized ADC and rCBV value falls into

$$\left[\frac{i-1}{10}, \frac{i}{10}\right] \text{ and } \left[\frac{j-1}{10}, \frac{j}{10}\right],$$

respectively.

The following quantities were also defined:

$$\mu_i = \sum_{i=1}^{10} i \sum_{j=1}^{10} p(i,j)\ , \quad \mu_j = \sum_{j=1}^{10} j \sum_{i=1}^{10} p(i,j)$$

$$\sigma_i = \sum_{i=1}^{10} (i-\mu_i)^2 \sum_{j=1}^{10} p(i,j)\ , \quad \sigma_j = \sum_{j=1}^{10} (j-\mu_j)^2 \sum_{i=1}^{10} p(i,j)$$

The characteristic metrics of the copula matrix were calculated as second-order features (Haralick et al., 1973), which included Energy, Contrast, Entropy, Homogeneity, Correlation, SumAverage, Variance, Dissimilarity, and AutoCorrelation:

$$Energy = \sum_{i=1}^{10}\sum_{j=1}^{10} p(i,j)^2$$

$$Contrast = \sum_{i=1}^{10}\sum_{j=1}^{10} (i-j)^2 p(i,j)$$

$$Correlation = \sum_{i=1}^{10}\sum_{j=1}^{10} \frac{(i-\mu_i)(j-\mu_j)p(i,j)}{\sigma_i \sigma_j}$$

$$Homogeneity = \sum_{i=1}^{10}\sum_{j=1}^{10} \frac{p(i,j)}{1+|i-j|}$$

$$Variance = \frac{1}{10 \times 10}\sum_{i=1}^{10}\sum_{j=1}^{10} \left[(i-\mu_i)^2 p(i,j) + \left(j-\mu_j\right)^2 p(i,j)\right]$$

$$SumAverage = \frac{1}{10 \times 10}\sum_{i=1}^{10}\sum_{j=1}^{10} [i\, p(i,j) + j\, p(i,j)]$$

$$Entropy = -\sum_{i=1}^{10}\sum_{j=1}^{10} p(i,j)\ log_2(p(i,j))$$

$$Dissimilarity = \sum_{i=1}^{10}\sum_{j=1}^{10} |i-j|\, p(i,j)$$

$$Autocorrelation = \sum_{i=1}^{10}\sum_{j=1}^{10} ij\, p(i,j)$$

Step 3. A hierarchical clustering of patients was then performed based on the above features.

7.3.5 Remark

We should point out that in Step 2, when performing discretization, we only counted the relative frequency. Firstly, as frequency counting is invariant regarding weight changes of the data value, the extracted matrix is not affected by the possible priority shifting of the copula transform. Secondly, since we only computed the relative frequency of required data points relative to the given regions of interest, the extracted matrix is again invariant regarding possible deformation of the data distribution through the copula transform.

7.4 Methods

7.4.1 Patients

The inclusion and exclusion criteria are in Section 3.1.1. This study was approved by the local institutional review board. Signed informed consent was obtained from all patients. Patient treatment is detailed in Section 3.2.2.1. Assessment of IDH-1 R132H Mutation and MGMT Methylation Status are described in 3.2.

7.4.2 MRI acquisition

MRI sequences in this study included: post-contrast T1-weighted, T2-weighted, dynamic susceptibility contrast-enhancement (DSC), diffusion tensor imaging (DTI) with inline ADC calculation, and multi-voxel 2D ^{1}H-MRS chemical shift imaging (CSI). Sequence details are

provided in 3.3.2.2. All patient underwent MRI within 72hrs postoperatively as a clinical routine scanning to evaluate the extent of resection.

7.4.3 Image processing

DSC data were processed and rCBV maps were generated after leakage correction using NordicICE (NordicNeuroLab, Bergen, Norway), during which an arterial input function was automatically defined. For each subject, all MRI images were co-registered to T2-weighted images with an affine transformation, using the linear image registration tool (FLIRT) functions in FSL (Jenkinson et al., 2002). CSI data were processed as described in 3.4.4. Only CSI voxels completely in tumour T2-voxels were included for further analysis.

7.4.4 Copula transform and patient clustering

We applied the copula transform to the ADC and rCBV maps on each patient individually, with no outliers removed, using the method we proposed the analysis in Section 7.2. The study design is illustrated in Figure 7.1.

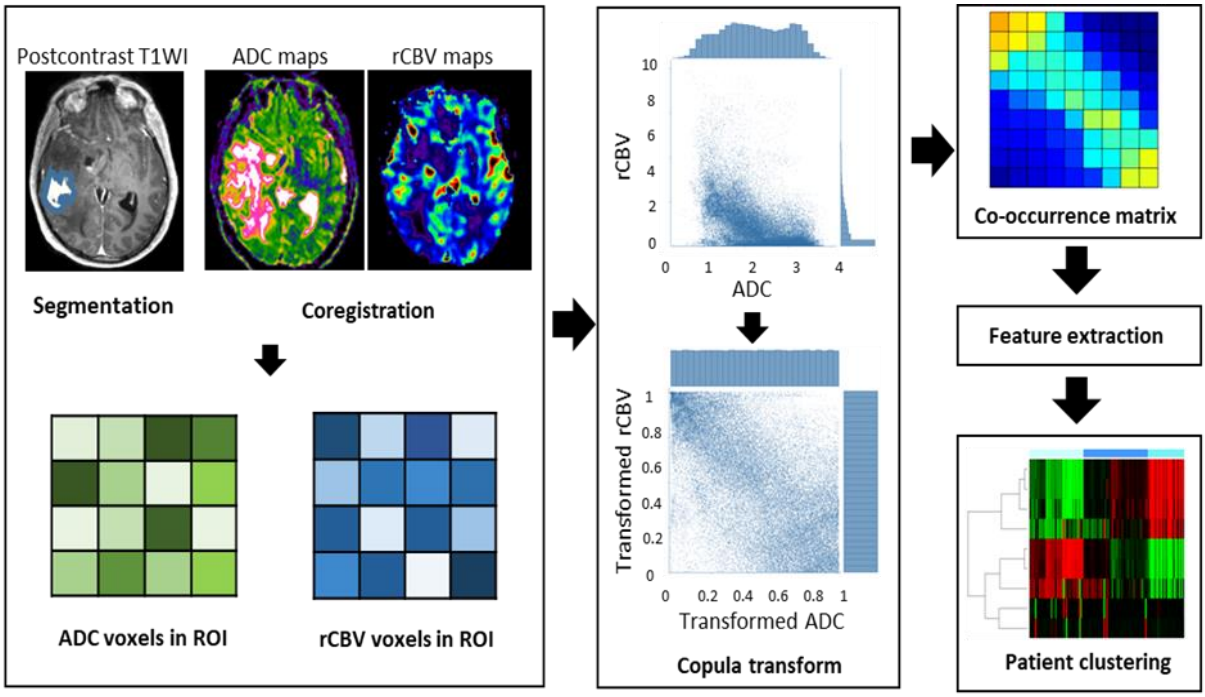

Figure 7.1 Study design. All images are co-registered before tumour regions are manually segmented from post-contrast T1-weighted images (T1WI). Voxels are then extracted from both ADC and rCBV maps. Empirical copula transform is performed on the joint distribution of ADC and rCBV voxels, which is then discretized before extracting second-order features from the matrix. These features are used in patient clustering to reveal subtypes.

To find the most stable and unambiguous patient clustering, we varied the number of clusters from 2 to 10. The optimal number of clusters was selected according to the majority vote among the 26 indices as implemented in the 'Nbclust' package in R (Charrad et al., 2014).

7.4.5 Leave-one-out cross-validation of the clustering

A leave-one-out cross-validation (LOOCV) procedure was applied for constructing and validating the patient clusters. The clustering steps were repeated by leaving one patient out of the cohort at each repetition. The consensus analysis was performed based on the clustering results obtained from the LOOCV approach. A consensus matrix M was calculated, where M (*i, j*) indicating percentage of times that the patients *i* and *j* were clustered together across the dataset perturbations.

7.4.6 Statistical analysis

All analyses were performed in RStudio v3.2.3 (Rstudio, Boston, MA, USA). The clinical characteristics and CSI data of the clusters were compared with Kruskal-Wallis rank sum test, using the Benjamini-Hochberg procedure for controlling the false discovery rate in multiple comparisons. Kaplan-Meier and Cox proportional hazards regression analyses were performed to evaluate patient overall survival and progression-free survival. Survival analysis was based on the subset of patients (n = 84) who received concurrent temozolomide (TMZ) chemoradiotherapy followed by adjuvant TMZ post-operatively. Cox proportional hazards regression was performed, accounting for relevant covariates, including IDH-1 mutation, MGMT methylation, sex, age, the extent of resection and contrast-enhancing tumour volume. Patients who were alive at the last known follow-up were censored. The hypothesis of no effect was rejected at a two-sided level of 0.05.

7.5 Results

7.5.1 Patient population

A total of 115 (84.6%) glioblastoma patients (mean age 59.3 years, range 22 - 76 years, 87 males) were included in this study.

7.5.2 Patient clustering

Based on the quantitative features characterising the joint distribution of ADC and rCBV, three patient clusters were identified through hierarchical clustering, containing 40 patients (35 %), 48 patients (42 %), and 27 patients (23 %) respectively (Figure 7.2). The average discretized matrix of ADC-rCBV joint distribution of three subtypes is demonstrated by Figure 7.3. Three subtypes showed no significant differences in clinical factors, as indicated in Table 7.1. The lactate levels of three subtypes were distinct (Table 7.2, Figure 7.4). Subtype III displayed a higher level of Lac/Cr ratio than Subtype II ($P = 0.016$) and Subtype I ($P = 0.044$).

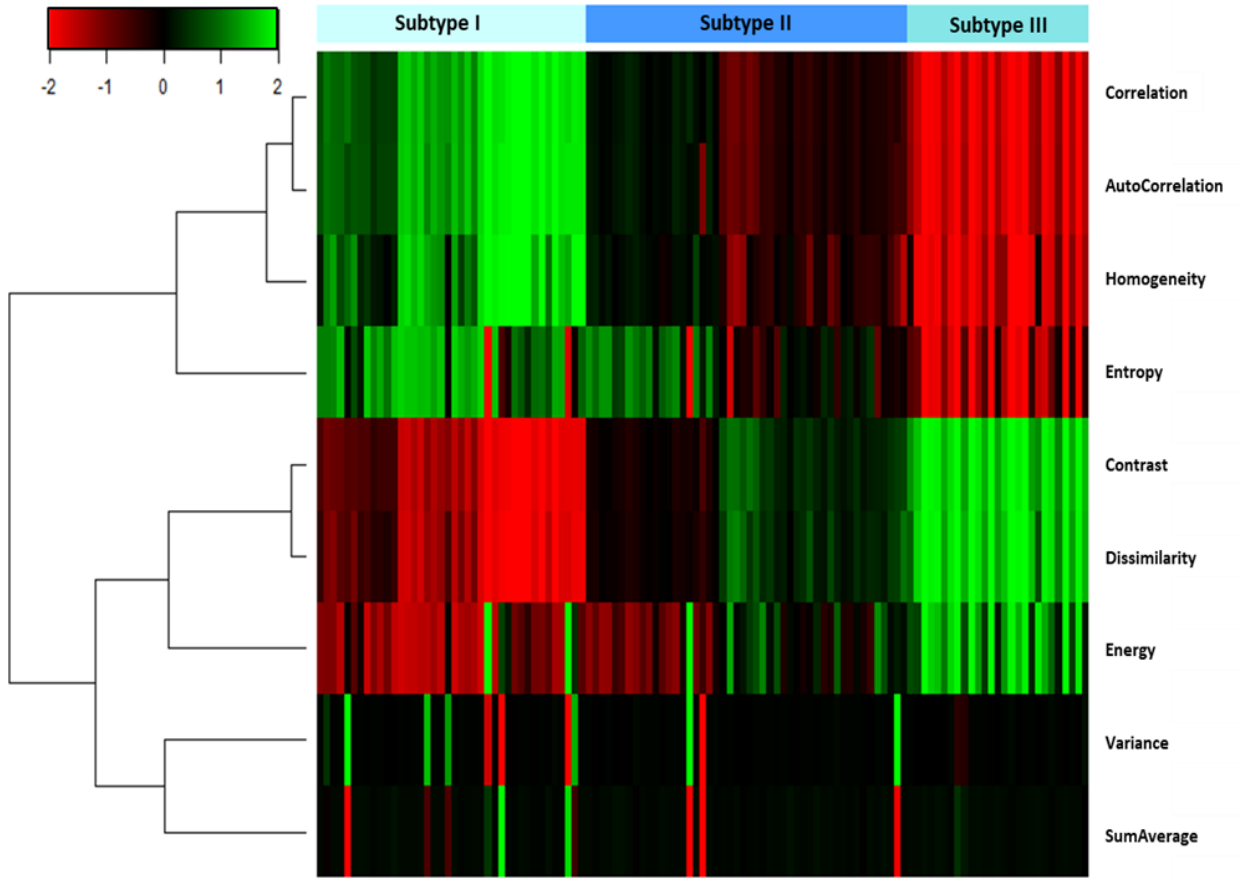

Figure 7.2 Patient clustering. Three patient clusters are identified using the features extracted from the joint matrix of copula-transformed ADC and rCBV.

Table 7.1 Clinical characteristics of subtypes

Variable	Subtype I (n = 40)	Subtype II (n = 48)	Subtype III (n = 27)	*P* value
Age at diagnosis (range, yrs.)	59 (33 -76)	62 (38 -75)	55 (22 -73)	0.261
Sex, number of patients				
Male	32	36	19	0.663
Female	8	12	8	
Extent of resection (of enhancing tumour), no. of patients				
Complete resection	30	30	17	0.208
Partial resection	7	16	9	
Biopsy	3	2	1	
MGMT promoter methylation status*				
Methylated	20	17	11	0.373
Unmethylated	19	30	14	
IDH-1 mutation status				
Mutant	1	3	3	0.354
Wild-type	39	45	24	
Tumour volumes(cm^3) [#]	48.6 ± 31.4	41.0 ± 25.1	55.9 ± 33.1	0.172
Survival (days)				
Median OS (range)	403 (163-1077)	551 (78-1376)	407 (52-1333)	**0.039**[†]
Median PFS (range)	262 (93-758)	389 (25-1130)	244 (37-589)	**0.025**[†]

*MGMT promoter methylation status unavailable for 4 patients; [#]mean ± SD of original data. [†]Log-Rank test; SD: standard deviation; MGMT: O-6-methylguanine-DNA methyltransferase; IDH-1: isocitrate dehydrogenase 1; cm: centimeter; OS: overall survival; PFS: progression-free survival. *P*-values indicate the significance of comparison across all three groups.

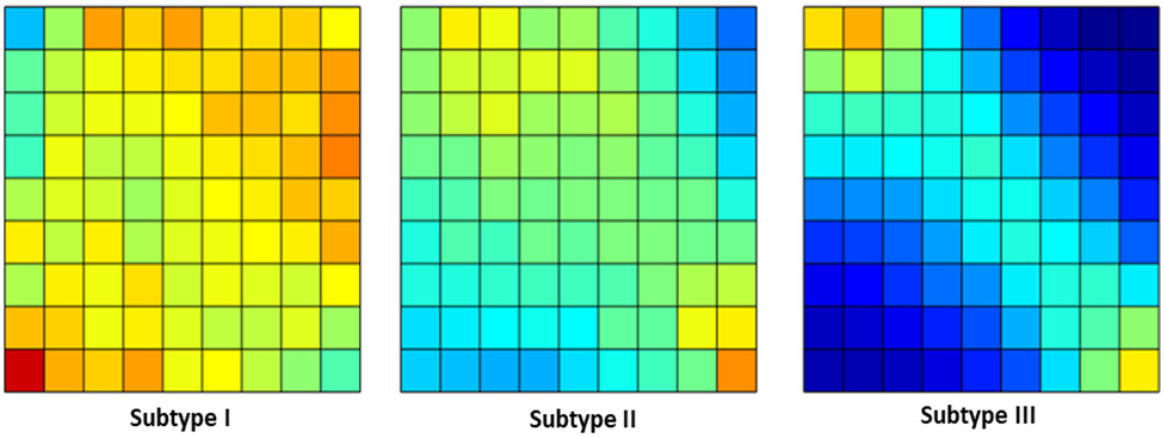

Figure 7.3 Average joint distribution matrices of three subtypes. The joint distribution of transformed ADC and rCBV values is discretized into a 10 × 10 joint distribution matrix for each patient. This figure shows the average matrix for each patient subgroup.

Table 7.2 Lac/Cr ratio of subtypes

	Descriptive	**Subtype II**	**Descriptive**	**Subtype II**
Subtype	Mean ± SD	95% CI	*P* value	*P* value
Subtype I	12.9 ± 2.7	7.2 ± 18.6	0.341	**0.030**
Subtype II	9.8 ± 5.8	5.8 ± 13.8	/	**0.006**
Subtype III	21.4 ± 3.4	14.3 ± 28.5	/	/
Lac: lactate; Cr: creatine; SD: standard deviation.				

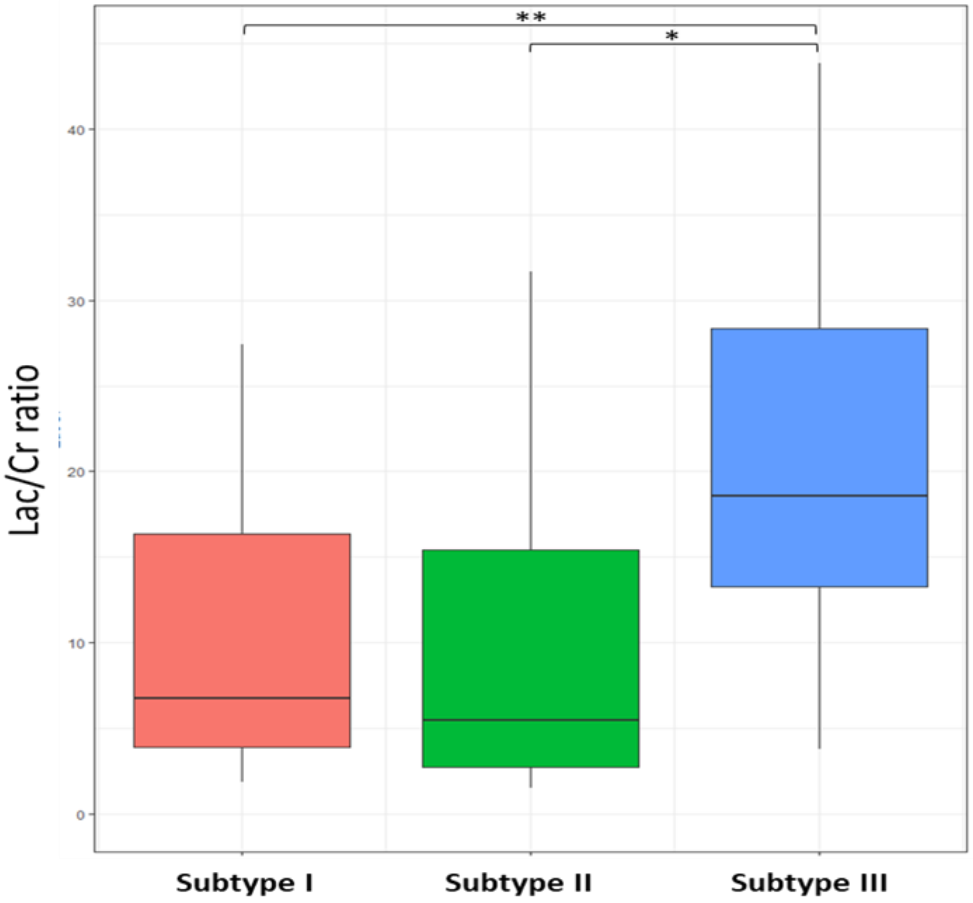

Figure 7.4 Lac/Cr of three patient clusters. Lac/Cr ratio in Subtype III is significant higher than Subtype I (P = 0.030) and Subtype II (P = 0.006). Lac: lactate; Cr: creatine; *: P <0.05; **: P < 0.01.

7.5.3 Leave-one-out cross-validation of patient subtypes

After the leave-one-out cross-validation, the co-occurrence consensus clustering matrix was computed. The results showed that three patient clusters generated from the unsupervised clustering were highly stable (Figure 7.5). The mean values of the co-occurrence consensus clustering matrix were 0.91 for Subtype I, 0.95 for Subtype II and 0.98 for Subtype III.

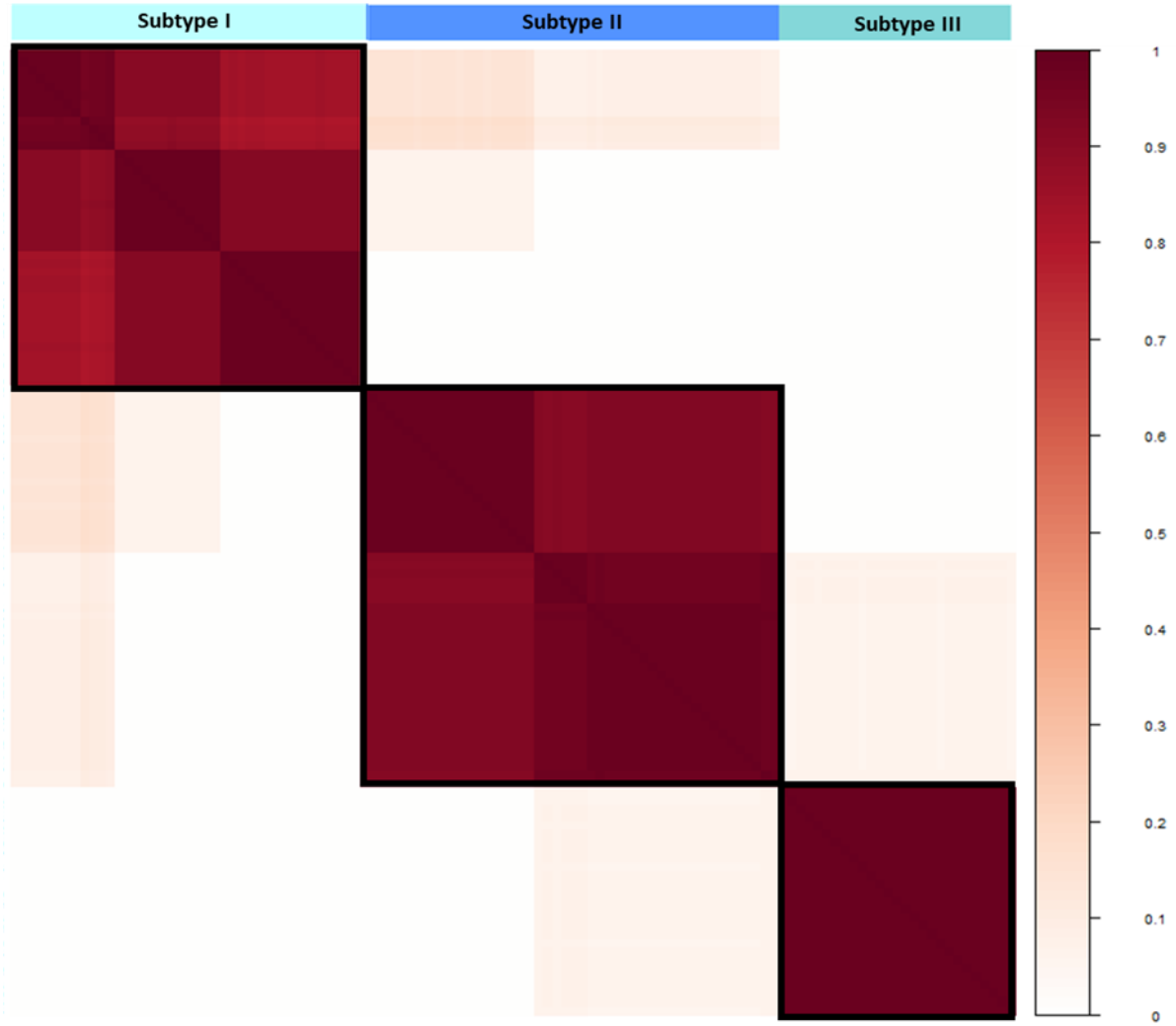

Figure 7.5 Leave-one-out cross-validation of patient clusters. Consensus analysis was performed based on the 115 clustering results obtained from the leave-one-out cross-validation. The mean value of the co-occurrence consensus clustering matrix is 0.91 for Subtype I, 0.95 for Subtype II and 0.98 for Subtype III.

7.5.4 Survivals of patient subtypes

Kaplan-Meier analysis using Log-rank test showed significantly different OS ($P = 0.039$) and PFS ($P = 0.025$) (Table 7.1, Figure 7.6) for the three identified subtypes. Cox regression models (Table 7.3) accounted for all relevant clinical covariates. In the multivariate model of OS, Subtype I showed significantly worse survival compared to Subtype II (HR = 3.042, $P = 0.003$). Extent of resection (HR = 2.691, $P = 0.011$) and tumour volume (HR = 1.019, $P = 0.001$) significantly affected OS. In multivariate modelling of PFS, Subtype I (HR = 1.992, $P = 0.046$)

and Subtype III (HR = 3.062, *P* = 0.009) showed significantly worse survival compared to Subtype II. Extent of resection (HR = 2.710, *P* = 0.007), and MGMT methylation status (HR = 0.532, *P* = 0.025) significantly affected PFS. Figure 7.7 demonstrates a case from Subtype II.

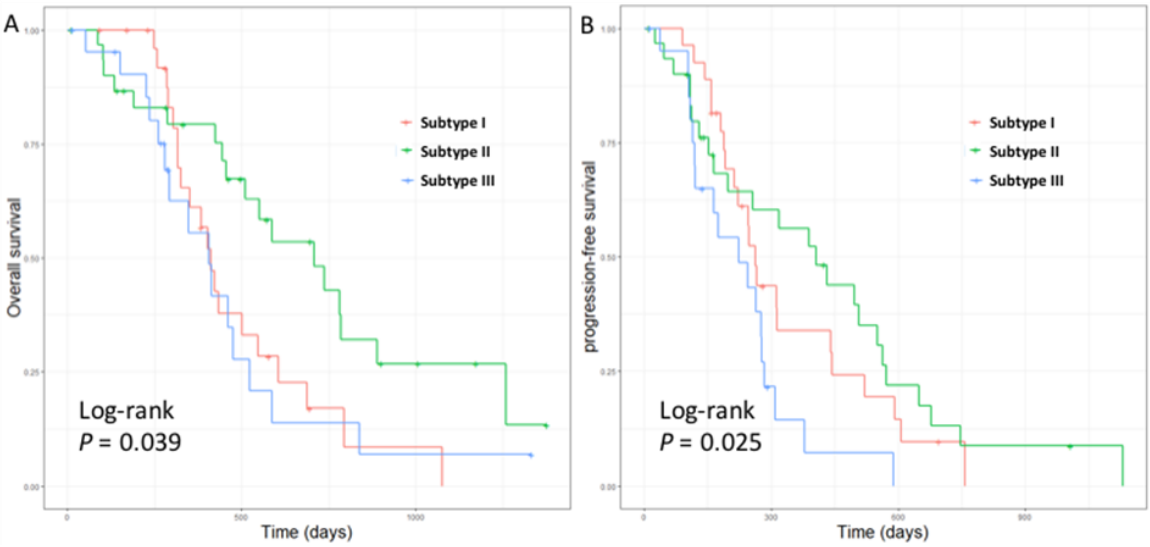

Figure 7.6 Survivals of patient clusters. Log-rank test shows that Subtype II displays better OS (P = 0.039) (A) and PFS (P = 0.025) (B) than Subtype I and Subtype III.

Table 7.3 Multivariate modelling of survivals

Factor	OS			PFS		
	HR	**95% CI**	***P* value**	**HR**	**95% CI**	***P* value**
Age	1.004	0.971-1.038	0.812	1.027	0.994-1.062	0.106
Sex (M)	1.242	0.624-2.471	0.537	1.807	0.976-3.346	0.060
Extent of resection	2.691	1.259-5.754	0.011	2.710	1.321-5.560	0.007
MGMT promoter methylation status*	0.565	0.307-1.040	0.067	0.532	0.306-0.924	0.025
IDH mutation status	1.066	0.286-3.973	0.925	0.936	0.270-3.246	0.917
Tumour volume#	1.019	1.008-1.030	0.001	1.002	0.991-1.012	0.742
Subtype I	3.042	1.453-6.367	0.003	1.992	1.011-3.925	0.046
Subtype III	1.857	0.790-4.367	0.156	3.062	1.327-7.062	0.009

*MGMT promoter methylation status unavailable for 2 patients; #contrast-enhancing tumour volume. HR: hazard ratio; MGMT: O-6-methylguanine-DNA methyltransferase; IDH-1: isocitrate dehydrogenase 1; OS: overall survival; PFS: progression-free survival.

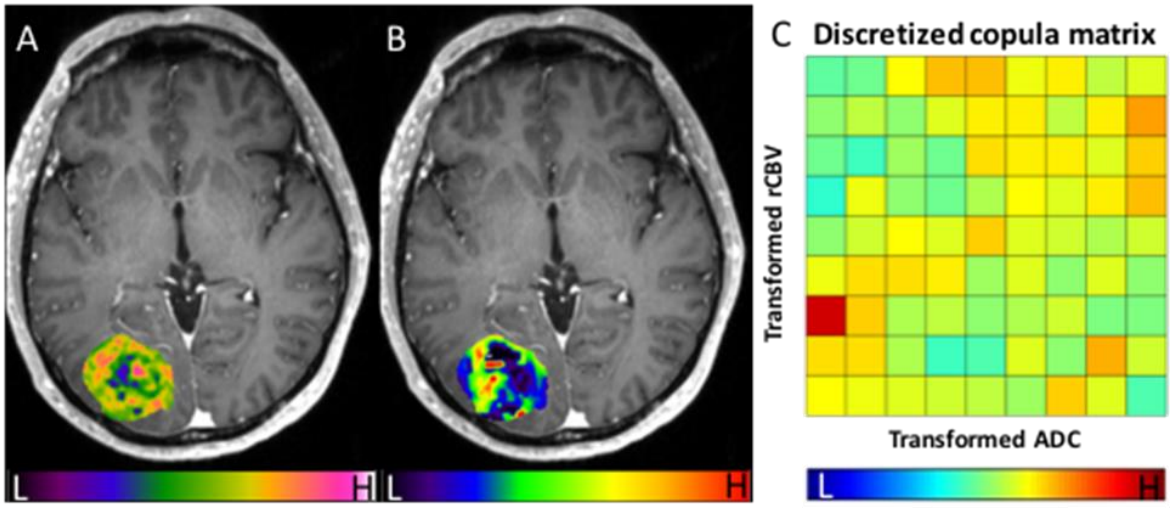

Figure 7.7 Case example of Subtype II. Pixel-wise ADC values (A) and rCBV values (B) are overlaid on post-contrast T1 weighted images. After the copula transform, the joint distribution are discretized (C). The matrix demonstrates a uniform distribution, which suggests a low inter-dependence of ADC and rCBV in this case.

7.6 Discussion

In this study, we characterized the inter-dependence of ADC and rCBV using copula transform and discrete feature extraction, and evaluated the clinical significance of the inter-dependence characteristics in patient outcomes. The results showed that the inter-dependence of perfusion and diffusion imaging can provide a useful tool for evaluating the variation of the tumour microenvironment. The inter-dependence between perfusion and diffusion imaging may offer useful information for patient stratification.

Tumour microstructure estimated from diffusion imaging and vascularity estimated from perfusion imaging can describe the key characteristics associated with tumour pathogenesis. Although existing evidence suggests benefits from combining imaging techniques to identify tumour sub-regions that are responsible for treatment failure (Boonzaier et al., 2017a), systematic measures to integrate perfusion and diffusion imaging are lacking. Previous studies have validated the robustness of copula transform in estimating non-linear correlation in multimodal neuroimaging data analysis (Ince et al., 2017). Here we leveraged the copula transform to extract the joint distribution matrix to investigate the interaction between

perfusion and diffusion imaging. The second-order statistics calculated from the joint distribution matrix of transformed ADC and rCBV can yield an array of measures that describe the overall heterogeneity of the joint distribution. To avoid the potential weight change during the copula transform, we used discretized features for characterization. The subtypes revealed by this approach demonstrated no significance in clinical factors, but were significantly different in patient outcomes. This finding may suggest that the interaction between perfusion and diffusion imaging offer information which is complementary to clinical factors for evaluating tumour aggressiveness.

The second-order features of ADC-rCBV joint distribution in Subtype III demonstrated diagonalised characteristics, as shown in Figure 3. This suggested high inter-dependence between microvasculature and microstructure in this subtype. Correspondingly, this subtype had a higher lactate level than the other two subtypes, indicating a more hypoxic microenvironment. Interestingly, although Subtype I showed the most uniform distribution characteristics among the three subtypes, and therefore demonstrated the less inter-dependent vasculature and microstructure, the survival of this subtype was worse than Subtype II. The higher lactate level of Subtype I implies more hypoxic microenvironment than Subtype II. This finding suggests that both high and low inter-dependence between vasculature and microstructure are associated with more hypoxic tumour microenvironment and more invasive phenotypes. A possible explanation for this association could be that Subtype III may represent a highly proliferative phenotype with an unmet oxygen demand leading to global hypoxia, while Subtype I may have a less coupled microvasculature and microstructure, leading to sub-regional hypoxia. Both could lead to treatment resistance and poorer outcomes, as demonstrated by our findings.

Our findings have clinical significance. The subtypes revealed by the inter-dependence between perfusion and diffusion may give insights potentially relevant for treatment selection. Our findings showed that both high and low inter-dependent tumour microvasculature and microstructure may be correlated with a higher degree of hypoxia, which may lead to resistance to radiation therapy. Cytoreductive surgery may be more crucial in these phenotypes. Future studies using a prospective cohort study design is needed to validate the clinical significance.

Our approach had limitations. Firstly, the resolution of CSI was lower than the resolution of the anatomical imaging and ^{1}H MR spectroscopy voxels were, therefore, larger than rCBV and ADC voxels. Secondly, our findings have not been validated in another independent validation cohort. Lastly, to reduce our cluster complexity, we applied discretization to the copula-transformed joint matrix in this study, our future work will focus on feature extraction technique that incorporates the weight and continuous information of copula matrix.

7.7 Conclusions

In conclusion, the inter-dependence between perfusion and diffusion imaging offer useful information that could potentially be used for glioblastoma patient stratification, by evaluating variation of the tumour microenvironment. This approach provides an overall measure of tumour microenvironment using multimodal MRI. This approach could be extended to include more imaging modalities in future studies, with the advantage of copula transform in multidimensional distributions.

Chapter 8 Radiomic Features from Multimodal MRI Show Improved Accuracy in Predicting MGMT Promoter Methylation in Glioblastoma

8.1 Abstract

Objectives

To determine whether physiological MRI can provide improved accuracy compared to structural MRI in predicting O6-methylguanine-DNA methyltransferase (MGMT) promoter methylation status in glioblastoma, using a radiomics approach.

Methods

A total of 115 primary glioblastoma patients were prospectively recruited for treatment. Pre-operative MRI included structural (T1-weighted, T2-weighted, post-contrast T1-weighted and FLAIR imaging) and physiological (diffusion tensor and dynamic susceptibility contrast imaging) sequences. Radiomic features were extracted from each modality separately. Feature ranking was performed on structural and physiological image features using an ensemble ranking method. Four supervised classifiers, including support vector machine, random forest, neural network and naïve Bayes, were compared. A ten-fold cross-validation was applied. An independent cohort including 15 primary glioblastomas was used to validate the predictive model. The prognostic values of MGMT methylation status and selected radiomics features were compared using survival models.

Results

The radiomics model based on physiological images showed better performance than structural images in all classifiers. Neural network achieved best prediction performance (structural model: AUC = 0.78, accuracy = 0.71; physiological model: AUC = 0.76, accuracy = 0.84) compared to other classifiers. The neural network predictive model obtained similar performance in the validation cohort. For predicting 12-month progression-free survival, the model of radiomic features and clinical factors outperformed and the model of MGMT methylation and clinical factors ($P = 0.010$).

Conclusions

Radiomic features can predict MGMT promoter methylation status of glioblastoma using supervised machine learning schemes. Models based on physiological image features provide increased performance compared to models based on structural image features.

8.2 Introduction

In previous chapters, we utilise multi-parametric MRIs to reveal the intra-tumoural and inter-tumoural heterogeneity of glioblastoma. As we discussed in Chapter 1, Radiomics is a quantitative approach of tumour characterisation, with a large number of features extracted from the images. These features have been shown to differentiate tumour phenotypes with different underlying molecular pathways and patient survival time (Itakura et al., 2015). Here we would investigate the role of radiomics in the study of tumour heterogeneity.

As we discussed in Chapter 1, glioblastoma is among the most lethal cancers. Concurrent TMZ chemoradiotherapy has considerably improved patient survival in newly diagnosed glioblastoma patients (Hegi et al., 2005b) and is recommended as standard of care (Stupp et al., 2010). Glioblastoma patients, however, display inconsistent response to TMZ. Better response to TMZ can be observed from a subgroup of patients with a methylated O6-methylguanine-DNA methyltransferase (MGMT) promoter (Stupp et al., 2009). MGMT is central in maintaining genomic integrity by encoding a DNA repair protein. MGMT, therefore, helps to reduce the tumour cell DNA damage caused by TMZ (Pegg, 1990). The methylation of MGMT promoter can lead to increased sensitivity to TMZ by silencing the MGMT expression (Hegi et al., 2008). As such, the promoter methylation of MGMT has been widely used as an independent favourable prognostic factor in glioblastoma patients (Dunn et al., 2009b). Pyrosequencing is reported to be reproducible and robust in assessing MGMT promoter methylation (Mikeska et al., 2007). This approach, however, relies on the tissue obtained via invasive methods.

Recently, radiomic features were reported to reflect MGMT promoter methylation status (Korfiatis et al., 2016, Xi et al., 2017, Li et al., 2018). However, the features used in these studies were extracted from structural images only, which may be prone to be non-specific (O'Connor et al., 2008). The purpose of this current study is to determine whether physiological MRIs can provide improved accuracy in predicting MGMT promoter methylation status. We utilized two sets of radiomic features extracted from structural and physiological MRIs respectively. These radiomic features, which describe the tumour shape, margin, intensity histogram and texture, were used to build predictive models of MGMT promoter methylation

status, in which multiple classifiers were implemented. The predictive accuracies of the models were compared and features of particular importance in prediction were explored.

8.3 Methods

8.3.1 Development cohort

The inclusion and exclusion criteria are in Section 3.1.1. This study was approved by the local institutional review board. Signed informed consent was obtained from all patients. Patient treatment is detailed in Section 3.2.2.1. Assessment of IDH-1 R132H Mutation and MGMT Methylation Status are described in 3.2.

8.3.2 Pre-operative MRI acquisition

A 3-Tesla MRI system (Magnetron Trio; Siemens Healthcare, Erlangen, Germany) with a standard 12-channel receive-head coil was used for pre-operative MRI scan. MRI sequences included structural sequences (T1-weighted [T1W], T2-weighted [T2W], pre-contrast T1-weighted [T1C] and T2-weighted fluid attenuated inversion recovery [FLAIR]), dynamic susceptibility contrast (DSC) and diffusion tensor imaging (DTI). The complete scanning protocol is detailed in Section 3.3.2.2.

8.3.3 Image processing

All MRI images were co-registered to T2W images with an affine transformation, using the FSL linear image registration tool (FLIRT) (Jenkinson et al., 2002). Mean diffusivity (MD) and fractional anisotropy (FA) were obtained from DTI using FDT. The relative cerebral blood volume (rCBV), mean transit time (MTT) and relative cerebral blood flow (rCBF) maps were calculated from the DSC. Tumour ROIs were manually drawn as described in 3.4.6.1. The study design is summarized in Figure 8.1.

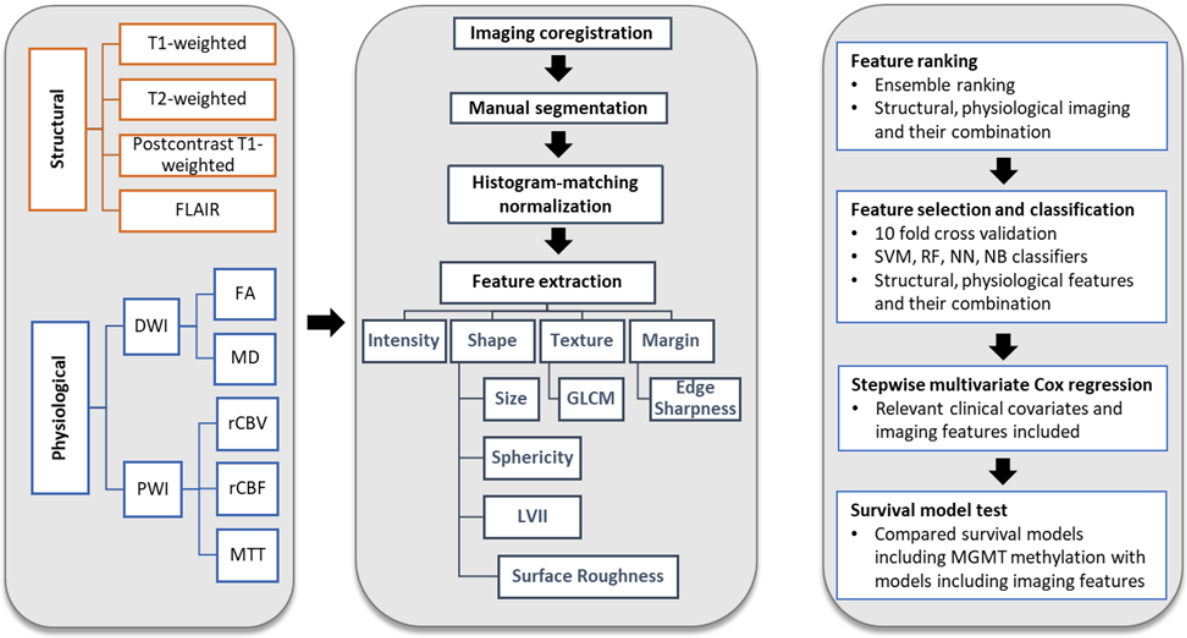

Figure 8.1 Study design. Structural sequences (T1-weighted, T2-weighted, post-contrast T1-weighted and FLAIR) and physiological sequences (MD and FA are calculated from DWI; rCBV, rCBF and MTT are calculated from PWI). All images are co-registered to T2-weighted images and then normalized using the histogram-matching method. Radiomics features are extracted from the manually segmented tumour regions. Features include intensity, shape, texture, and margin features. Feature ranking is performed on structural, physiological imaging and their combination, based on an ensemble importance score. Support vector machine, random forest, neural network and naïve Bayes are applied in classification using a ten-fold cross-validation. The optimal combination of hyperparameters in each classifier and the number of features used in the classifiers are tuned according to the prediction accuracy. A permutation test is performed to examine if the performance is achieved by chance. Prognostic value of MGMT methylation status and selected image features are compared in survival models.

8.3.4 Radiomic feature extraction

We defined 3D radiomic features to characterize the tumour. Features were extracted from structural images (T1W, T2W, FLAIR, and T1C) and physiological images (FA, MD, rCBV, rCBF, MTT). From each map, a total of 943 features were extracted automatically in MATLAB (MathWorks, Natick, MA) v2017b using open-source code available in Github (Echegaray et al., 2017). Image features include: (1) shape features (four Size features describing the tumour size; 39 Local Volume Invariant Integral [LVII] features describing the local curvature of the

tumour; 430 Surface Roughness features characterizing the surface of the tumour: and one Sphericity feature describing how similar the shape of the tumour is to a sphere); (2) margin features (25 Edge Sharpness features describing intensity changes between the interior and exterior of the tumour); (3) intensity features (12 features describing the statistics of pixel values within the tumour) (4) Grey-level co-occurrence matrix (GLCM) texture features (432 features measuring the spatial distribution of pixel intensities within the tumour).

8.3.5 Feature ranking

Feature ranking was performed using the R package 'EFS' (Neumann et al., 2017), an ensemble feature ranking method that incorporates eight feature selection methods for binary classifications. Each feature is given an importance score between 0 and 1, with 1 indicating high importance for classification. This method seeks to avoid the specific bias caused by one single feature selection method, reduce feature redundancy and improve the interpretability of feature reduction (Saeys et al., 2008).

8.3.6 Classification scheme

We implemented Support Vector Machines (SVM), Random Forest (RF), Naïve Bayes (NB) and Neural Network (NN) classifiers to predict MGMT methylation status. A detailed description of the four classifiers can be found in Section 3.4.7.3. All classifiers were trained and evaluated in RStudio with the package 'Caret' (Kuhn, 2008). The optimal combination of hyperparameters in each classifier and number of features selected in the classifiers were tuned according to prediction accuracy, with 10-fold cross validations repeated 200 times for each classifier. The performance of each classifier was evaluated according to the prediction accuracy, specificity, sensitivity and the area under the receiver operating characteristic curve (AUC). The performance results in the training set were reported as the average value across 200 times.

8.3.7 Permutation test

We performed a permutation test to evaluate the accuracy of the proposed methods. The test was performed using the R function 'sample' to permute the MGMT promoter methylation status of the entire cohort without replacement. The test was repeated 1000 times, with each classifier procedure running through in each repetition. The *P* values were calculated under the null hypothesis that the predicted results by the methods are random (Phipson and Smyth, 2010).

8.3.8 Independent validation cohort

To further evaluate the classifier performance, another patient cohort which included 15 glioblastoma patients were analysed using an identical pipeline for image processing, feature extraction and classification. A different 3T system (MR750, GE Healthcare, Waukesha, WI) and a different imaging protocol were used for the scanning. The imaging protocol is as follows: Axial T1W: TR/TE/TI: 8.2/3.2/450ms; slice thickness: 1mm; flip angle 12°; FOV 100 × 100 mm;), after intravenous injection of 9 mL gadobutrol (Gadovist,1.0 mmol/mL; Bayer, Leverkusen, Germany), T1C imaging was acquired; Axial T2W: TR/TE/TI: 5226/8ms; flip angle 111°; FOV 100 × 100 mm; slice thickness: 6mm; FLAIR: TR/TE/TI: 8000/125/2158 ms; flip angle 111°; FOV 80 × 80 mm; slice thickness: 7mm; DTI: TR/TE 8000/88ms; flip angle 90°; FOV 100 × 100 mm; slice thickness: 3mm; 64 directions; b values 1000 sec/mm^2; DSC: TR/TE 2000/17 ms; flip angle 60°; FOV 100 ×100 mm; slice thickness: 6mm, with 9 mL gadobutrol followed by a 20 mL saline flush.

8.3.9 Statistical analysis

All analyses were performed in RStudio v3.2.3. Patient characteristics of MGMT promoter methylated and unmethylated group were compared using Welch Two Sample t-test. Survival was tested on the patients who received concurrent temozolomide (TMZ) chemoradiotherapy followed by adjuvant TMZ post-operatively. Patients who were alive at the last known follow-up were censored.

To further reduce the number of features and identify the optimal survival models, multivariate Cox regression with forward and backward stepwise selection procedures was performed, considering other relevant clinical covariates. Model performance for predicting 12-month overall survival (OS) and progression-free survival (PFS) were evaluated using Akaike Information Criterion (AIC). Survival models were constructed firstly using all clinical covariates including MGMT promoter methylation status, and then using the selected image features to replace MGMT promoter methylation status. The performance of the models was compared using the area under the receiver operator characteristics curve (AUC). The hypothesis of no difference was rejected at a two-sided level of 0.05. Mean values of variables are presented ± standard deviation [SD].

8.4 Results

8.4.1 Patients and regions of interest

A total of 136 patients were recruited for pre-operative MRI scans. After surgery, 21 of 136 (15.4 %) patients were excluded due to non-glioblastoma pathology diagnosis. Another four patients were excluded due to missing MGMT promoter methylation status. Thus, altogether 111 of 115 (96.5 %) patients (mean age 59 years, range 22-75 years, 83 males) were included, and 82 of 111 (73.9 %) patients received concurrent TMZ chemoradiotherapy followed by adjuvant TMZ post-operatively. Other patients received short-course radiotherapy (16.2 %, 18/111) or best supportive care (9.9 %, 11/111), due to poor post-operative status. Four of 82 patients (4.9 %) were lost to follow up. Clinical characteristics of all patients, and methylated/unmethylated subgroups are summarized in Table 8.1.

The contrast-enhancing volume of the methylated tumours was 48.4 ± 32.7 cm^3 and 56.8 ± 33.8 cm^3 for unmethylated tumours ($P = 0.185$). The non-enhancing volume of the two groups were 58.9 ± 47.4 cm^3 and 67.2 ± 41.9 cm^3 ($P = 0.341$). A full comparison of the two groups was detailed in Table 8.1.

Table 8.1 Clinical characteristics of development cohort

Variables	Patient Number			*P* value
	Total (n = 111)	Methylated* (n = 48)	Unmethylated* (n = 63)	
Age at diagnosis				
<60	39	32	40	0.446
≥60	72	16	23	
Sex				
Male	83	34	49	0.415
Female	28	14	14	
Extent of resection (of enhancing tumour)				
Complete resection	76	34	42	0.642
Partial resection	31	13	18	
Biopsy	4	1	3	
IDH-1 mutation status				
Mutant	7	4	3	0.464
Wild-type	104	44	60	
Pre-operative Tumour volumes(cm3) #				
Contrast-enhancing	53.2 ± 33.3	48.4 ± 32.7	56.8 ± 33.8	0.185
Non-enhancing	63.6 ± 44.3	58.9 ± 47.4	67.2 ± 41.9	0.341
Survival (days)				
Median OS (range)	424 (52-1259)	475 (52-1259)	422 (78-890)	0.059†
Median PFS (range)	262 (25-1130)	318 (25-1130)	246 (47-747)	0.067†

*Patients were subgrouped according to MGMT promoter methylation status. #mean ± SD of original data. †Log-Rank test. SD: standard deviation; MGMT: O-6-methylguanine-DNA methyltransferase; IDH-1: Isocitrate dehydrogenase 1; cm: centimeters; OS: overall survival; PFS: progression-free survival.

8.4.2 Feature Ranking and Classification Performance

Both structural and physiological image features were ranked according to the ensemble importance score. All classifiers showed fair performance in predicting MGMT methylation status (Table 8.2). The results showed that physiological image features resulted in higher prediction accuracy than the structural image features in four classifiers. A combination of physiological and structural features showed further improvement in accuracy. The

permutation test indicated that prediction accuracy obtained from the four classifiers were all significantly higher than by chance (all $P < 0.001$).

Table 8.2 Structural features selected in neural network classifier in development cohort (n = 111)

	SVM			RF			NN			NB		
	STR	**PHY**	**Hybrid**	**STR**	**PHY**	**Hybrid**	**STR**	**PHY**	**Hybrid**	**STR**	**PHY**	**Hybrid**
Feature number	8	5	10	6	10	15	5	6	14	5	5	14
Accuracy	0.71	0.74	0.78	0.68	0.74	0.77	0.71	0.76	0.84	0.69	0.74	0.75
Sensitivity	0.74	0.79	0.82	0.74	0.83	0.83	0.72	0.80	0.83	0.65	0.79	0.77
Specificity	0.67	0.69	0.74	0.60	0.62	0.69	0.71	0.71	0.86	0.75	0.68	0.73
PPV	0.75	0.77	0.80	0.71	0.74	0.78	0.76	0.78	0.89	0.77	0.76	0.79
NPV	0.67	0.71	0.76	0.64	0.73	0.76	0.66	0.73	0.80	0.62	0.71	0.70
AUC	0.74	0.81	0.84	0.74	0.81	0.83	0.78	0.84	0.87	0.76	0.78	0.84

STR: structural imaging; PHY: physiological imaging; Hybrid: a combination of structural and physiological imaging. PPV: positive predictive value; NPV: negative predictive value; AUC: area under the receiver operating characteristic (ROC) curve; SVM: support vector machine; RF: random forest; NN: neural network; NB: Naïve Bayes.

The performance comparison of four classifiers, based on AUC and accuracy, shows that NN had a higher prediction performance than other classifiers. The structural, physiological image features and their combination selected by the ensemble ranking and the NN classifier are presented in Table 8.3 - 8.5.

Table 8.3 Structural features selected in neural network classifier in development cohort (n = 111)

	Importance score	**Feature**
1	1.00	LVII _Radius_3mm_range
2	0.89	T2_glcm_distance_1mm_energy_interquartileRange
3	0.88	T2_glcm_distance_1mm_contrast_median
4	0.86	T1_glcm_distance_3mm_sumMean_min
5	0.84	T2_glcm_distance_1mm_sumMean_mean

Table 8.4 Physiological features selected in neural network classifier in development cohort (n = 111)

	Importance score	**Feature**
1	0.73	LVII_Radius_3mm_range
2	0.69	FA_glcm_distance_1mm_contrast_min
3	0.67	rCBF_edgeSigmoidFitting_window_median
4	0.65	MD_glcm_distance_1mm_contrast_kurtosis
5	0.64	MTT_glcm_distance_3mm_clusterShade_skewness
6	0.64	MTT_glcm_distance_1mm_entropy_median

Table 8.5 Hybrid feature ranking in neural network classifier in development cohort (n = 111)

	Importance score	Feature
1	0.73	LVII_Radius_3mm_range
2	0.69	FA_glcm_distance_1mm_contrast_min
3	0.67	rCBF_edgeSigmoidFitting_window_median
4	0.65	MD_glcm_distance_1mm_contrast_kurtosis
5	0.65	T2_glcm_distance_1mm_energy_interquartileRange
6	0.64	MTT_glcm_distance_3mm_clusterShade_skewness
7	0.64	MTT_glcm_distance_1mm_entropy_median
8	0.64	T2_glcm_distance_1mm_contrast_median
9	0.64	MD_glcm_distance_1mm_clusterTendency_skewness
10	0.62	T1_glcm_distance_3mm_sumMean_min
11	0.62	MTT_glcm_distance_3mm_inverseVariance_skewness
12	0.61	T2_glcm_distance_1mm_sumMean_mean
13	0.60	rCBV_glcm_distance_3mm_maxProbability_kurtosis
14	0.60	MTT_glcm_distance_2mm_maxProbability_skewness

8.4.3 Diagnostic Validation of Radiomics Features

Using the above selected features and NN classifier, the validation cohort achieved an AUC of 0.73 and 0.82 respectively. The combination of structural and physiological image features achieved an AUC of 0.96 (Table 8.6).

Table 8.6 Performance of NN in validation cohort(n = 15)

	STR	PHY	Hybrid
Accuracy	0.67	0.73	0.87
Sensitivity	0.50	0.75	0.75
Specificity	0.86	0.71	1.00
PPV	0.80	0.75	1.00
NPV	0.60	0.71	0.78
AUC	0.73	0.82	0.96

STR: structural imaging; PHY: physiological imaging; Hybrid: a combination of structural and physiological imaging. PPV: positive predictive value; NPV: negative predictive value.

8.4.4 Prognostic Values of Radiomic Features

The stepwise procedure based on AIC selected four and one image features for the PFS model and OS model respectively (Table 8.7), from the combination of structural and physiological image features selected by the NN classifier. For the prediction of 12-month PFS and OS, AUC of the model based on image features and clinical factors was higher than the model based on MGMT methylation status and clinical factors (PFS: $P = 0.010$; OS: not significant, Figure 8.2).

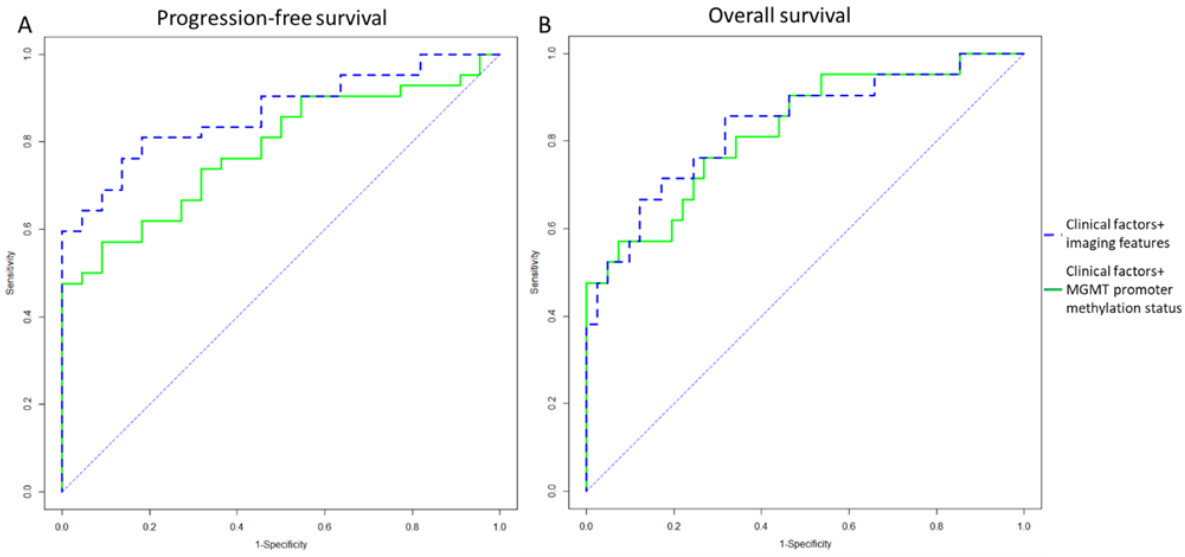

Figure 8.2 Comparison of survival models based on MGMT promoter methylation status and imaging features. For the prediction of 12-month PFS and OS, AUC of the model based on image features and other clinical factors was significantly higher (0.87, confidence interval [CI]: 0.78-0.95) than the model with MGMT and other clinical factors (0.78, CI: 0.67-0.89, P = 0.010). For the prediction of 12-month PFS, AUC of the model with image features and other clinical factors was higher (0.84, CI: 0.72-0.95) than the model with MGMT and other clinical factors (0.82, CI: 0.71-0.94, not significant).

Table 8.7 Stepwise multivariate Cox regression in development cohort (n = 111)

Variables	Progression-free survival*			Overall survival*		
	HR	95% CI	*P*	HR	95% CI	*P*
Extent of resection	4.07	2.088-7.941	< 0.001	2.41	1.282-4.511	0.006
Contrast-enhancing volume	/	/	/	1.02	1.006-1.029	0.002
LVII_Radius_3mm_range	1.21	0.939-1.549	0.142	1.23	0.967-1.569	0.091
FA_glcm_distance_1mm_contrast_min	0.99	0.974-1.000	0.058	/	/	/
ADC_glcm_distance_1mm_contrast_kurtosis	1.48	1.191-10.15	0.023	/	/	/
T1_glcm_distance_3mm_sumMean_min	0.96	0.934-0.995	0.023	/	/	/

*Multivariate Cox models accounted for IDH-1 mutation status, MGMT methylation status, sex, age, the extent of resection and contrast-enhancing tumour volume. A stepwise procedure was performed to select optimal models. HR: hazard ratio; CI: confidence interval.

8.5 Discussion

In this study, we sought to explore the radiomic features that could predict MGMT promoter methylation status of glioblastoma, and compare the predictive values of radiomic features extracted from structural or physiological images. Our results showed that physiological imaging can provide more accurate prediction compared to structural imaging; neural network classifier may potentially offer a reliable classification scheme for MGMT promoter methylation prediction.

Previously, several studies reported the relevance of structural imaging markers in predicting MGMT methylation status (Romano et al., 2013, Moon et al., 2012, Li et al., 2018). One study, however, reported a poor correlation between imaging features with MGMT promoter methylation status (Carrillo et al., 2012). Since only semantic features from the radiology lexicon were used, the authors suggested advanced imaging post-processing techniques may be needed to extract more useful features, for example, textural features. Another study reported that ring enhancement and structural texture features were associated with MGMT methylation status with an accuracy of 71% in classification, and that unmethylated tumours had larger tumour volume than methylated tumour (Drabycz et al., 2010). Consistent with this

study, our structural features yielded similar accuracies, although the difference in tumour volume was not confirmed.

Inconsistent results were reported regarding the usefulness of diffusion and perfusion parameters in MGMT methylation status prediction. The apparent diffusion coefficient (ADC) and rCBF were reported to achieve high accuracies in various studies (Romano et al., 2013, Han et al., 2018). Another study, however, showed that ADC and FA were not useful in differentiating methylated and unmethylated glioblastoma, whereas K^{trans} values of methylated cases were significantly higher than in unmethylated cases (Ahn et al., 2014). In our study, we leveraged the radiomics approach to integrate physiological modalities. The results showed that physiological imaging offers higher accuracy and sensitivity in four classifiers, and higher specificity in two classifiers (SVM and RF), compared to structural imaging. This finding supports the utility of physiological imaging for predicting MGMT methylation.

In accordance with several studies (Drabycz et al., 2010, Korfiatis et al., 2016, Xi et al., 2017), our results showed that texture features provide the most valuable feature set for prediction. Texture features can measure the tumour heterogeneity by quantifying spatial complexity in images (O'Connor et al., 2015). The usefulness of texture features for predicting molecular subtypes (Yang et al., 2015), IDH mutation status (Jakola et al., 2018) and 1p/19q co-deletion (Brown et al., 2008) were reported previously, suggesting the potential of texture features in bridging imaging phenotypes and genetic/epigenetic signatures. Further, we found that one tumour shape-based feature (Local Volume Invariant Integral) ranked the highest importance. As this feature quantifies the local curvature of the tumour, our finding implies that methylated and unmethylated glioblastomas may be different in tumour morphology.

There are limitations in our study. Firstly, high numbers of radiomic features may require larger datasets to fully test the robustness of feature selection and classification scheme, ideally from multiple centres. Secondly, in the determination of MGMT promoter methylation status, we used a 10% threshold of four CpG islands in the MGMT promoter, which may be optimized by further studies. This may possibly explain the OS and PFS of the MGMT-methylated subgroup only showed marginally significant better OS and PFS than MGMT-unmethylated subgroup. Future studies will need to investigate the potential of radiomics features in prediction the continuous MGMT methylation percentage. Thirdly, one of the principal

challenges in radiomics is the robustness of predictive features. In our study, we used an ensemble feature selection to avoid the specific bias from any single algorithm. Many other efforts have been made, including a recent study using all-relevant feature selection (Li et al., 2018). Future efforts are needed to test algorithms for clinically reproducible and applicable features.

8.6 Conclusion

Radiomic features can predict MGMT promoter methylation status of glioblastoma using supervised machine learning schemes. Physiological image features demonstrated higher prediction accuracies than structural image features. Features that measure tumour image texture were the most useful features in prediction.

Chapter 9 General Conclusions and Limitations

9.1 Summary of findings

The aim of this thesis was to investigate the utility of multi-parametric MRI, explored by habitat imaging, imaging integration techniques and radiomics approach, in patient prognosis determination and epigenetic prediction. The main hypotheses tested are:

1. **Joint histogram analysis of isotropic and anisotropic diffusion components could differentiate tumour regions into sub-regions with different diffusion patterns, which may be useful for a better understanding of the intra-tumoural heterogeneity of tumour infiltration. (Chapter 4)**

   In Chapter 4, we proposed a method of joint histogram analysis, using DTI decomposition, to explore the heterogeneity of tumour infiltration. The intra-tumoural habitats revealed by this approach can provide incremental prognostic values for patients. A non-enhancing sub-region with decreased isotropic diffusion and increased anisotropic diffusion was associated with worse patient outcomes (for PFS, HR = 1.08, $P < 0.001$; for OS, HR = 1.36, $P < 0.001$) and could possibly be a sub-region for targeted therapy. The findings of this study support the usefulness of DTI in revealing *intra-tumoural* invasive tumour habitats.

2. **Low perfusion compartments could be visualized and quantified using multi-parametric quantitative MRI. The tumour habitats identified using this approach could correlate with patient prognosis. (Chapter 5)**

In Chapter 5, we integrated ADC and rCBV for the identification of low perfused tumour habitats with different diffusivity. Higher lactate in the low perfused habitat with restricted diffusivity was associated with worse survivals (PFS: HR = 2.995, P = 0.047; OS: HR = 4.974, P = 0.005). The findings of this study support the usefulness of habitat imaging using multi-parametric MRI for the identification of *intra-tumoural* invasive sub-regions.

3. **A multi-view feature selection and machine learning approach could effectively integrate histogram features from quantitative multi-parametric MRI. The selected imaging features using this approach may offer incremental values in survival prediction. (Chapter 6)**

   In Chapter 6, we applied a multi-view feature selection and clustering method, which can provide an effective integration of multi-parametric MRI for patient prognosis determination (for OS: P = 0.007; for PFS: P < 0.001). The histogram features selected can be used as potential prognostic markers. The findings of this study suggest the importance of integrating multiple imaging modalities for MRI interpretation in the study of *inter-tumoural* heterogeneity.

4. **The inter-dependence of perfusion and diffusion imaging can be characterised, which would provide useful information for evaluating tumour microenvironment. The imaging phenotypes revealed by this approach could be of prognostic value (Chapter 7)**

   In Chapter 7, we investigated the inter-dependence of microstructure and vasculature for glioblastoma characterisation, using perfusion and diffusion imaging. The patient subtypes revealed by this approach showed significant differences in patient survival (PFS: P = 0.046 and P = 0.009, respectively). The findings of this study suggest that the interaction of imaging modalities provides crucial information for understanding *inter-tumoural* heterogeneity.

5. **Using radiomics approach, advanced physiological MRIs may provide improved accuracy than conventional structural MRIs, for the prediction of O^6-methylguanine-DNA methyltransferase (MGMT) promoter methylation status. The predictive models constructed using the selected radiomic features could improve the prognostic performance. (Chapter 8)**

   In Chapter 8, we compared the values of advanced physiological MRI with structural MRI, in predicting MGMT promoter methylation status of glioblastoma, using a radiomics approach. Advanced physiological images showed better performance than structural images in the prediction of MGMT methylation status. The findings of this study suggest that physiological MRI provides more specific information for predicting epigenetic markers than structural MRI.

9.2 Limitations of studies

The limitations of experimental chapters (Chapter 4-8) have been described in each individual chapter. The general limitations of the project are described below.

9.2.1 Patient inclusion criteria

To target the patient with a diagnosis of supratentorial glioblastoma, a radiological diagnosis of glioblastoma was used, based on the contrast enhancement on post-contrast T1-weighted imaging. This may cause a bias by excluding those glioblastoma patients with non-enhancing lesions, although most glioblastoma is contrast-enhancing. We do exclude those non-glioblastoma patients according to their post-operative pathology diagnosis. The generalisation of the findings of the thesis is therefore limited to the contrast-enhancing glioblastomas.

9.2.2 Single centre cohort

As we discussed in Section 1.10.2.4, to validate the imaging findings, an optimal validation cohort is from another independent centre, preferably from multiple centres. This purpose of

this procedure is not only to reduce systematic bias, but also to reduce the variance caused by different manufacturer/models of MRI scanners. The latter has long been known to significantly affect the reproducibility of imaging findings. This limitation could be improved by the future study using multiple centre cohorts.

9.2.3 Sample size

As discussed in 1.10.2.3, radiomics approach can generate a large amount of imaging feature for tumour characterisation. The relatively large numbers of features compared to the patient number may cause overfitting. The sample size of glioblastoma cohort, however, is limited by its relatively low incidence. To relieve this limitation, we have applied the various type of feature selection techniques, including the multi-view feature selection method (Chapter 6), ensemble feature ranking and selection method (Chapter 8) and the stepwise procedure (Chapter 5, 6, 8). In the future studies, multiple centre cohort may help to increase the sample size and improve robustness.

9.2.4 Effects of dexamethasone

Vasogenic oedema caused by the glioblastoma can be significantly relieved by the use of dexamethasone and improve patient outcomes. Therefore, it is unethical to withhold dexamethasone. Previous studies reported the effects of dexamethasone on rCBV (Bastin et al., 2006), rCBF (Kirton et al., 2006), MTT (Bastin et al., 2006), MD (Sinha et al., 2004), FA (Sinha et al., 2004) and ADC (Minamikawa et al., 2004). A systematic literature review of 24 articles showed that the use of dexamethasone may cause a decrease in tumour perfusion, and diffusion (Kotsarini et al., 2010). The patients in this thesis, however, were all in a steady dose of dexamethasone, which reflects the standard of patient care.

9.2.5 Pseudoprogression

As discussed in Section 1.9.2., the incidence of pseudoprogression is increasing since TMZ chemoradiotherapy was widely used. In this study, treatment response and tumour progression

were evaluated according to RANO criteria, which incorporates clinical and radiological changes. Pseudoprogression was suspected where new contrast enhancement appeared within first 12 weeks after completing chemoradiotherapy. In such cases, treatment was continued and pseudoprogression was identified where later response occurred. As a result, in some cases, true progression was determined retrospectively.

9.2.6 Lack of histological validation

Previously biopsies have been taken from the tumour, which helps to validate the correlation between DTI abnormalities with histological changes. The imaging findings of this thesis, however, still needs an image-guided biopsy. Although we included molecular biomarkers in Chapter 8 to show the usefulness of imaging marking in reflecting tumour biology, the validation of intra-tumoural habitats needs multiple biopsy and further evidence. We would argue that the advantage of imaging studies is to provide a non-invasive tool for clinical patient management. Further, we believe the findings of this study will provide a reference for targeting.

9.3 Future directions

This thesis aims to investigate the role of multi-parametric MRI and radiomics approach in the study of tumour heterogeneity. The work described here can be developed in the following directions:

9.3.1 Image-guided biopsy to validate imaging biomarkers

As discussed above, a lack of histological validation is one of the limitations of this thesis. Therefore, future work using image-guided multiple biopsies is a crucial step in future studies. This involves the improvement of the neuro-navigation system and clinical surgical procedure. To reduce the influence of brain shift during the craniotomy, a needle biopsy can be applied before durotomy. Using the multiple samples obtained through image-guided needle biopsy, genomic profiling can be applied, with the aim of 1) validating the imaging markers using

genomic profiling; 2) revealing intra-tumoural heterogeneity using tumour phylogenetic analysis; 3) investigating the integration of tumour cells with tumour microenvironment.

9.3.2 Improving the reproducibility and robustness of the radiomics approach

As we discussed in Section 1.10.4, the standardisation in radiomics workflow design is of crucial importance to the reproducibility of radiomics approach. The standardisation involves multiple processes in the radiomics approach, including imaging acquisition and reconstruction, data annotation, feature extraction and machine learning scheme. Particularly, the feature set identification has not reached consensus in the community. Different feature sets are being used in multiple laboratories, which may significantly influence the reproducibility of the radiomics approach. In future work, we aim to investigate the impact of feature definition in radiomics, by applying multiple feature extraction and model selection techniques. The robustness of feature sets will be compared for clinical validation. We have been prospectively recruiting an independent multi-centre cohort in a recent clinical trial called "Predicting sites of tumour progression in the invasive margin of glioblastomas (PRaM)", which aims to investigate the robustness of imaging biomarkers from mixed scanners and imaging protocols, which would potentially bring benefits to the testing of reproducibility and robustness of radiomics.

9.3.3 Incorporating radiomics and habitat imaging into prospective and longitudinal cohort study

As we discussed in Section 1.10.4, for the clinical validation of the imaging markers identified using radiomics, it is crucial to involve multiple research centres and interdisciplinary collaboration. Our imaging study revealing invasive phenotypes showed clinical significance. These studies, however, were using a retrospective design, which may need further rigorous validation. Prospective study design, using the paradigm of clinical efficacy investigation, will be of importance to the clinical validation of imaging markers and habitats. Our future work will include a validation process incorporating the clinical and biological knowledge into

model testing. Longitudinal study design may also help the clinical validation of imaging findings, as one of the advantages of the imaging approach, which may provide more promising findings.

Chapter 10 List of Publications

The work presented in or related to this thesis has contributed to following papers or conference presentations that have been published or submitted for publication.

Original articles

1. **Li, C.**, Wang, S., Yan, JL, Piper, R., Liu, H., Torheim, T., Kim, H., Boonzaier, NR., Sinha, R., Matys, T., Markowetz, F. & Price, SJ. (2018). Intratumoral Heterogeneity of Tumor Infiltration of Glioblastoma Revealed by Joint Histogram Analysis of Diffusion Tensor Imaging. *Neurosurgery*. doi: 10.1093/neuros/nyy388
2. **Li, C.,** Yan JL., Torheim T., McLean, MA., Boonzaier, NR., Huang, Y., Yuan J., van Dijken BRJ., Matys, T., Markowetz, F., & Price, SJ. (2017). Low perfusion compartments in glioblastoma quantified by advanced magnetic resonance imaging and correlated with patient Survival. *(Under review)*.
3. **Li, C.**, Wang, S., Serra, A., Torheim, T., Yan, JL., Boonzaier, NR., Matys, T., McLean, MA., Markowetz, F. & Price, SJ. (2017). Multi-Parametric and Multi-Regional Histogram Analysis of MRI: Revealing Imaging Phenotypes of Glioblastoma Correlated with Patient Survival. *(Under review)*.
4. **Li, C.**, Wang, S., Liu, P, Torheim, T, Boonzaier, NR., Schönlieb, CB., Markowetz, F. & Price, SJ. (2018). Decoding the interdependence of multiparametric magnetic resonance imaging to unravel patient subgroups correlated with outcomes. (S*ubmitted)*.
5. **Li, C.**, Wang, S., Zou, J., Torheim, T., Boonzaier, NR., Liu, H., Markowetz, F. & Price, S. J. (2018). Radiomic Features from Multimodal MRI Show Improved Accuracy in Predicting MGMT Promoter Methylation in Glioblastoma. *(In preparation)*.

6. **Li, C.,** Wang, S., Yan, JL., Torheim, T., Sinha, R, Boonzaier, NR., Matys, T., Markowetz, F. & Price, S. J. (2018). Characterizing Tumor Invasiveness of Glioblastoma Using Multiparametric Magnetic Resonance Imaging. *(Under review)*.
7. Yan, JL., **Li, C.**, Boonzaier, NR., Matys, T, van der Hoorn, A. & Price, SJ. (2018). Characterising the peritumoral areas in glioblastomas on preoperative multimodal MRI to predict the area of tumor progression using radiomics. *(Submitted)*.
8. Yan, JL., **Li, C.**, Boonzaier, NR., Fountain, DM., Larkin TJ., Matys, T. & Price, SJ. (2017). Characterizing Tissue Anisotropy of the Peritumoral Region in Glioblastoma Using Diffusion Tensor Imaging. (*Under review*)
9. van Dijken, BRJ., van Laar, PJ., **Li, C.**, Yan, JL., Boonzaier, NR., Price, SJ., & van der Hoorn, A. (2018). Ventricle contact is associated with lower survival and increased peritumoral perfusion in glioblastoma. Journal of Neurosurgery. doi: https:// 10.3171/2018.5.JNS18340.
10. van Dijken, BRJ., Yan, JL., Boonzaier, NR., **Li, C.,** van der Hoorn, A. & Price, SJ (2017). Subventricular Zone Involvement Characterized by Diffusion Tensor Imaging in Glioblastoma. doi: 10.1016/j.wneu.2017.06.075.

Conferences

1. **Li, C.,** Wang, S., Torheim, T., Markowetz, F. and Price, SJ. Radiomic Features from Physiological MRI Shows Improved Accuracy over Structural MRI in Predicting MGMT Promoter Methylation in Glioblastoma. British Neuro-Oncology Society Annual Meeting, Winchester, July 2018. Oral presentation.
2. **Li, C.,** Wang, S., Serra, A., Torheim, T., Markowetz, F. and Price, SJ. Multi-parametric and multi-regional histogram analysis of MRI: revealing imaging phenotypes of glioblastoma correlated with patient survival. ISMRM Annual Meeting, Paris, June 2018. Oral presentation.
3. **Li, C.,** Wang, S., Torheim, T., Markowetz, F. and Price, SJ. Mutual information: depicting the interdependence of perfusion and diffusion magnetic resonance imaging in glioblastoma patients. ISMRM Annual Meeting, Paris, June 2018. E-Poster presentation.

4. **Li, C.,** Yan JL., Boonzaier, NR., Huang, Y., Yuan J. & Price, SJ. Multiparametric magnetic resonance imaging revealed tumour niches in glioblastoma patients. WFNOS Meeting, Zurich, May 2015. Poster presentation.

References

AERTS, H. J. W. L., VELAZQUEZ, E. R., LEIJENAAR, R. T. H., PARMAR, C., GROSSMANN, P., CAVALHO, S., BUSSINK, J., MONSHOUWER, R., HAIBE-KAINS, B., RIETVELD, D., HOEBERS, F., RIETBERGEN, M. M., LEEMANS, C. R., DEKKER, A., QUACKENBUSH, J., GILLIES, R. J. & LAMBIN, P. 2014b. Decoding tumour phenotype by noninvasive imaging using a quantitative radiomics approach. *Nature Communications,* 5.

AHN, S. S., SHIN, N. Y., CHANG, J. H., KIM, S. H., KIM, E. H., KIM, D. W. & LEE, S. K. 2014. Prediction of methylguanine methyltransferase promoter methylation in glioblastoma using dynamic contrast-enhanced magnetic resonance and diffusion tensor imaging Clinical article. *Journal of Neurosurgery,* 121**,** 367-373.

ANDRAS, J., PETER, M., MIKLOS, E. & ERVIN, B. 2011. Glioma grade assessment by using histogram analysis of diffusion tensor imaging-derived maps. *Neuroradiology,* 53**,** 483-491.

ASSELIN, M. C., O'CONNOR, J. P. B., BOELLAARD, R., THACKER, N. A. & JACKSON, A. 2012. Quantifying heterogeneity in human tumours using MRI and PET. *European Journal of Cancer,* 48**,** 447-455.

BACH, F. R. & JORDAN, M. I. 2005. A probabilistic interpretation of canonical correlation analysis.

BALDOCK, A. L., AHN, S., ROCKNE, R., JOHNSTON, S., NEAL, M., CORWIN, D., CLARK-SWANSON, K., STERIN, G., TRISTER, A. D., MALONE, H., EBIANA, V., SONABEND, A. M., MRUGALA, M., ROCKHILL, J. K., SILBERGELD, D. L., LAI, A., CLOUGHESY, T., MCKHANN, G. M., BRUCE, J. N., ROSTOMILY, R. C., CANOLL, P. & SWANSON, K. R. 2014. Patient-Specific Metrics of Invasiveness Reveal Significant Prognostic Benefit of Resection in a Predictable Subset of Gliomas. *Plos One,* 9.

BAMMER, R. 2003. Basic principles of diffusion-weighted imaging. *European Journal of Radiology,* 45**,** 169-184.

BARCELLOS-HOFF, M. H., LYDEN, D. & WANG, T. C. 2013. The evolution of the cancer niche during multistage carcinogenesis. *Nature Reviews Cancer,* 13**,** 511-518.

BASTIN, M. E., CARPENTER, T. K., ARMITAGE, P. A., SINHA, S., WARDLAW, J. M. & WHITTLE, I. R. 2006. Effects of dexamethasone on cerebral perfusion and water diffusion in patients with high-grade glioma. *American Journal of Neuroradiology,* 27**,** 402-408.

BEHRENS, T. E. J., WOOLRICH, M. W., JENKINSON, M., JOHANSEN-BERG, H., NUNES, R. G., CLARE, S., MATTHEWS, P. M., BRADY, J. M. & SMITH, S. M. 2003. Characterization and propagation of uncertainty in diffusion-weighted MR imaging. *Magnetic Resonance in Medicine,* 50**,** 1077-1088.

BERTHOLDO, D., WATCHARAKORN, A. & CASTILLO, M. 2013. Brain proton magnetic resonance spectroscopy: introduction and overview. *Neuroimaging Clin N Am,* 23**,** 359-80.

BHAT, K. P. L., BALASUBRAMANIYAN, V., VAILLANT, B., EZHILARASAN, R., HUMMELINK, K., HOLLINGSWORTH, F., WANI, K., HEATHCOCK, L., JAMES, J. D., GOODMAN, L. D., CONROY, S., LONG, L. H., LELIC, N., WANG, S. Z., GUMIN, J., RAJ, D., KODAMA, Y., RAGHUNATHAN, A., OLAR, A., JOSHI, K., PELLOSKI, C. E., HEIMBERGER, A., KIM, S. H., CAHILL, D. P., RAO, G., DEN DUNNEN, W. F. A., BODDEKE, H. W. G. M., PHILLIPS, H. S., NAKANO, L., LANG, F. F., COLMAN, H., SULMAN, E. P. & ALDAPE, K. 2013. Mesenchymal Differentiation Mediated by NF-kappa B Promotes Radiation Resistance in Glioblastoma. *Cancer Cell,* 24**,** 331-346.

BLÜML, S. 2013. Magnetic resonance spectroscopy: basics. *MR spectroscopy of pediatric brain disorders.* Springer.

BODAMMER, N., KAUFMANN, J., KANOWSKI, M. & TEMPELMANN, C. 2004. Eddy current correction in diffusion-weighted imaging using pairs of images acquired with opposite diffusion gradient polarity. *Magnetic Resonance in Medicine,* 51**,** 188-193.

BOONZAIER, N. R., LARKIN, T. J., MATYS, T., VAN DER HOORN, A., YAN, J. L. & PRICE, S. J. 2017b. Multiparametric MR Imaging of Diffusion and Perfusion in Contrast-enhancing and Nonenhancing Components in Patients with Glioblastoma. *Radiology,* 284**,** 180-190.

BOOTS-SPRENGER, S. H., SIJBEN, A., RIJNTJES, J., TOPS, B. B., IDEMA, A. J., RIVERA, A. L., BLEEKER, F. E., GIJTENBEEK, A. M., DIEFES, K., HEATHCOCK, L., ALDAPE, K. D., JEUKEN, J. W. & WESSELING, P. 2013. Significance of complete 1p/19q co-deletion, IDH1 mutation and MGMT promoter methylation in gliomas: use with caution. *Mod Pathol,* 26**,** 922-9.

BRANDES, A. A., FRANCESCHI, E., TOSONI, A., BLATT, V., PESSION, A., TALLINI, G., BERTORELLE, R., BARTOLINI, S., CALBUCCI, F. & ANDREOLI, A. 2008. MGMT promoter methylation status can predict the incidence and outcome of pseudoprogression after concomitant radiochemotherapy in newly diagnosed glioblastoma patients. *Journal of Clinical Oncology,* 26**,** 2192-2197.

BRENNAN, C. W., VERHAAK, R. G., MCKENNA, A., CAMPOS, B., NOUSHMEHR, H., SALAMA, S. R., ZHENG, S., CHAKRAVARTY, D., SANBORN, J. Z., BERMAN, S. H., BEROUKHIM, R., BERNARD, B., WU, C. J., GENOVESE, G., SHMULEVICH, I., BARNHOLTZ-SLOAN, J., ZOU, L., VEGESNA, R., SHUKLA,

S. A., CIRIELLO, G., YUNG, W. K., ZHANG, W., SOUGNEZ, C., MIKKELSEN, T., ALDAPE, K., BIGNER, D. D., VAN MEIR, E. G., PRADOS, M., SLOAN, A., BLACK, K. L., ESCHBACHER, J., FINOCCHIARO, G., FRIEDMAN, W., ANDREWS, D. W., GUHA, A., IACOCCA, M., O'NEILL, B. P., FOLTZ, G., MYERS, J., WEISENBERGER, D. J., PENNY, R., KUCHERLAPATI, R., PEROU, C. M., HAYES, D. N., GIBBS, R., MARRA, M., MILLS, G. B., LANDER, E., SPELLMAN, P., WILSON, R., SANDER, C., WEINSTEIN, J., MEYERSON, M., GABRIEL, S., LAIRD, P. W., HAUSSLER, D., GETZ, G., CHIN, L. & NETWORK, T. R. 2013. The somatic genomic landscape of glioblastoma. *Cell,* 155**,** 462-77.

BRODBELT, A., GREENBERG, D., WINTERS, T., WILLIAMS, M., VERNON, S., COLLINS, V. P. & NATIONAL CANCER INFORMATION NETWORK BRAIN TUMOUR, G. 2015. Glioblastoma in England: 2007-2011. *Eur J Cancer,* 51**,** 533-42.

BROWN, R., ZLATESCU, M., SIJBEN, A., ROLDAN, G., EASAW, J., FORSYTH, P., PARNEY, I., SEVICK, R., YAN, E., DEMETRICK, D., SCHIFF, D., CAIRNCROSS, G. & MITCHEL, R. 2008. The use of magnetic resonance imaging to noninvasively detect genetic signatures in oligodendroglioma. *Clinical Cancer Research,* 14**,** 2357-2362.

BULIK, M., JANCALEK, R., VANICEK, J., SKOCH, A. & MECHL, M. 2013a. Potential of MR spectroscopy for assessment of glioma grading. *Clinical Neurology and Neurosurgery,* 115**,** 146-153.

BURRELL, R. A., MCGRANAHAN, N., BARTEK, J. & SWANTON, C. 2013. The causes and consequences of genetic heterogeneity in cancer evolution. *Nature,* 501**,** 338-45.

BURTH, S., KICKINGEREDER, P., TICHY, D., BONEKAMP, D., WICK, A., LOW, S., NOWOSIELSKI, M., WICK, W., BENDSZUS, M. & RADBRUCH, A. 2016. Clinical Parameters Outweigh Diffusion- and Perfusion-Derived Mri Parameters in Predicting Survival in Newly-Diagnosed Glioblastoma. *Neuro-Oncology,* 18**,** 34-34.

CARRILLO, J. A., LAI, A., NGHIEMPHU, P. L., KIM, H. J., PHILLIPS, H. S., KHARBANDA, S., MOFTAKHAR, P., LALAEZARI, S., YONG, W., ELLINGSON, B. M., CLOUGHESY, T. F. & POPE, W. B. 2012. Relationship between Tumor Enhancement, Edema, IDH1 Mutational Status, MGMT Promoter Methylation, and Survival in Glioblastoma. *American Journal of Neuroradiology,* 33**,** 1349-1355.

CHARRAD, M., GHAZZALI, N., BOITEAU, V. & NIKNAFS, A. 2014. Nbclust: An R Package for Determining the Relevant Number of Clusters in a Data Set. *Journal of Statistical Software,* 61**,** 1-36.

CHAWLA, S., WANG, S., WOLF, R. L., WOO, J. H., WANG, J., O'ROURKE, D. M., JUDY, K. D., GRADY, M. S., MELHEM, E. R. & POPTANI, H. 2007. Arterial spin-labeling and MR spectroscopy in the differentiation of gliomas. *American Journal of Neuroradiology,* 28**,** 1683-1689.

CHEN, L. H., LIU, M., BAO, J., XIA, Y. B., ZHANG, J. Q., ZHANG, L., HUANG, X. Q. & WANG, J. 2013b. The Correlation between Apparent Diffusion Coefficient and Tumor Cellularity in Patients: A Meta-Analysis. *Plos One,* 8.

CHINOT, O. L., WICK, W., MASON, W., HENRIKSSON, R., SARAN, F., NISHIKAWA, R., CARPENTIER, A. F., HOANG-XUAN, K., KAVAN, P., CERNEA, D., BRANDES, A. A., HILTON, M., ABREY, L. & CLOUGHESY, T. 2014. Bevacizumab plus Radiotherapy-Temozolomide for Newly Diagnosed Glioblastoma. *New England Journal of Medicine,* 370**,** 709-722.

CHOI, Y. S., AHN, S. S., KIM, D. W., CHANG, J. H., KANG, S. G., KIM, E. H., KIM, S. H., RIM, T. H. & LEE, S. K. 2016. Incremental Prognostic Value of ADC Histogram Analysis over MGMT Promoter Methylation Status in Patients with Glioblastoma. *Radiology,* 281**,** 175-184.

COBAN, G., MOHAN, S., KURAL, F., WANG, S., O'ROURKE, D. M. & POPTANI, H. 2015. Prognostic Value of Dynamic Susceptibility Contrast-Enhanced and Diffusion-Weighted MR Imaging in Patients with Glioblastomas. *American Journal of Neuroradiology,* 36**,** 1247-1252.

COHEN, A. L., HOLMEN, S. L. & COLMAN, H. 2013. IDH1 and IDH2 Mutations in Gliomas. *Current Neurology and Neuroscience Reports,* 13.

COLLINS, V. P., ICHIMURA, K., DI, Y., PEARSON, D., CHAN, R., THOMPSON, L. C., GABE, R., BRADA, M., STENNING, S. P. & COLLABORATORS, B. 2014. Prognostic and predictive markers in recurrent high grade glioma; results from the BR12 randomised trial. *Acta Neuropathologica Communications,* 2.

DAVNALL, F., YIP, C. S., LJUNGQVIST, G., SELMI, M., NG, F., SANGHERA, B., GANESHAN, B., MILES, K. A., COOK, G. J. & GOH, V. 2012. Assessment of tumor heterogeneity: an emerging imaging tool for clinical practice? *Insights Imaging,* 3**,** 573-89.

DETRE, J. A., LEIGH, J. S., WILLIAMS, D. S. & KORETSKY, A. P. 1992. Perfusion Imaging. *Magnetic Resonance in Medicine,* 23**,** 37-45.

DEXTRAZE, K., SAHA, A., KIM, D., NARANG, S., LEHRER, M., RAO, A., NARANG, S., RAO, D., AHMED, S., MADHUGIRI, V., FULLER, C. D., KIM, M. M., KRISHNAN, S., RAO, G. & RAO, A. 2017. Spatial habitats from multiparametric MR imaging are associated with signaling pathway activities and survival in glioblastoma. *Oncotarget,* 8**,** 112992-113001.

DRABYCZ, S., ROLDAN, G., DE ROBLES, P., ADLER, D., MCINTYRE, J. B., MAGLIOCCO, A. M., CAIRNCROSS, J. G. & MITCHELL, J. R. 2010. An analysis of image texture, tumor location, and MGMT promoter methylation in glioblastoma using magnetic resonance imaging. *Neuroimage,* 49**,** 1398-1405.

DUNN, J., BABORIE, A., ALAM, F., JOYCE, K., MOXHAM, M., SIBSON, R., CROOKS, D., HUSBAND, D., SHENOY, A., BRODBELT, A., WONG, H., LILOGLOU, T., HAYLOCK, B. & WALKER, C. 2009a. Extent of MGMT promoter methylation correlates with outcome in glioblastomas given temozolomide and radiotherapy. *British Journal of Cancer,* 101**,** 124-131.

ECHEGARAY, S., BAKR, S., RUBIN, D. L. & NAPEL, S. 2017. Quantitative Image Feature Engine (QIFE): an Open-Source, Modular Engine for 3D Quantitative Feature Extraction from Volumetric Medical Images. *J Digit Imaging*.

EMBLEM, K. E., NEDREGAARD, B., NOME, T., DUE-TONNESSEN, P., HALD, J. K., SCHEIE, D., BOROTA, O. C., CVANCAROVA, M. & BJORNERUD, A. 2008. Glioma grading by using histogram analysis of blood volume heterogeneity from MR-derived cerebral blood volume maps. *Radiology,* 247**,** 808-817.

ESSIG, M., SHIROISHI, M. S., NGUYEN, T. B., SAAKE, M., PROVENZALE, J. M., ENTERLINE, D., ANZALONE, N., DORFLER, A., ROVIRA, A., WINTERMARK, M. & LAW, M. 2013. Perfusion MRI: The Five Most Frequently Asked Technical Questions. *American Journal of Roentgenology,* 200**,** 24-34.

FEDOROV, A., BEICHEL, R., KALPATHY-CRAMER, J., FINET, J., FILLION-ROBIN, J. C., PUJOL, S., BAUER, C., JENNINGS, D., FENNESSY, F., SONKA, M., BUATTI, J., AYLWARD, S., MILLER, J. V., PIEPER, S. & KIKINIS, R. 2012. 3D Slicer as an image computing platform for the Quantitative Imaging Network. *Magnetic Resonance Imaging,* 30**,** 1323-1341.

FRATELLO, M., CAIAZZO, G., TROJSI, F., RUSSO, A., TEDESCHI, G., TAGLIAFERRI, R. & ESPOSITO, F. 2017. Multi-View Ensemble Classification of Brain Connectivity Images for Neurodegeneration Type Discrimination. *Neuroinformatics,* 15**,** 199-213.

FRIEBOES, H. B., ZHENG, X., SUN, C. H., TROMBERG, B., GATENBY, R. & CRISTINI, V. 2006. An integrated computational/experimental model of tumor invasion. *Cancer Research,* 66**,** 1597-1604.

GADDA, D., MAZZONI, L. N., PASQUINI, L., BUSONI, S., SIMONELLI, P. & GIORDANO, G. P. 2017. Relationship between Apparent Diffusion Coefficients and MR Spectroscopy Findings in High-Grade Gliomas. *J Neuroimaging,* 27**,** 128-134.

GALLUZZI, L. & KROEMER, G. 2008. Necroptosis: a specialized pathway of programmed necrosis. *Cell,* 135**,** 1161-3.

GATENBY, R. A., GROVE, O. & GILLIES, R. J. 2013. Quantitative imaging in cancer evolution and ecology. *Radiology,* 269**,** 8-15.

GEVAERT, O., MITCHELL, L. A., ACHROL, A. S., XU, J. J., ECHEGARAY, S., STEINBERG, G. K., CHESHIER, S. H., NAPEL, S., ZAHARCHUK, G. & PLEVRITIS, S. K. 2014. Glioblastoma Multiforme: Exploratory Radiogenomic Analysis by Using Quantitative Image Features. *Radiology,* 273**,** 168-174.

GIESE, A., BJERKVIG, R., BERENS, M. E. & WESTPHAL, M. 2003. Cost of migration: invasion of malignant gliomas and implications for treatment. *J Clin Oncol,* 21**,** 1624-36.

GILLIES, R. J., KINAHAN, P. E. & HRICAK, H. 2016. Radiomics: Images Are More than Pictures, They Are Data. *Radiology,* 278**,** 563-577.

GILLIES, R. J., SCHORNACK, P. A., SECOMB, T. W. & RAGHUNAND, N. 1999. Causes and effects of heterogeneous perfusion in tumors. *Neoplasia,* 1**,** 197-207.

GOO, H. W. & RA, Y. S. 2017. Advanced MRI for Pediatric Brain Tumors with Emphasis on Clinical Benefits. *Korean Journal of Radiology,* 18**,** 194-207.

GREAVES, M. & MALEY, C. C. 2012. Clonal evolution in cancer. *Nature,* 481**,** 306-13.

GREEN, H. A. L., PENA, A., PRICE, C. J., WARBURTON, E. A., PICKARD, J. D., CARPENTER, T. A. & GILLARD, J. H. 2002. Increased anisotropy in acute stroke - A possible explanation. *Stroke,* 33**,** 1517-1521.

GROSSMANN, P., STRINGFIELD, O., EL-HACHEM, N., BUI, M. M., VELAZQUEZ, E. R., PARMAR, C., LEIJENAAR, R. T. H., HAIBE-KAINS, B., LAMBIN, P., GILLES, R. J. & AERTS, H. J. W. L. 2017. Defining the biological basis of radiomic phenotypes in lung cancer. *Elife,* 6.

HABBERSTAD, A., LIND-LANDSTÖM, T. & TORP, S. 2012. The histopathological spectrum of primary human glioblastomas with relations to tumour biology. *J Clinic Experiment Pathol,* 2**,** 2161-0681.10001.

HAGMANN, P., JONASSON, L., MAEDER, P., THIRAN, J. P., WEDEEN, V. J. & MEULI, R. 2006. Understanding diffusion MR imaging techniques: from scalar diffusion-weighted imaging to diffusion tensor imaging and beyond. *Radiographics,* 26 Suppl 1**,** S205-23.

HAMBARDZUMYAN, D. & BERGERS, G. 2015a. Glioblastoma: Defining Tumor Niches. *Trends in Cancer,* 1**,** 252-265.

HAN, Y., YAN, L. F., WANG, X. B., SUN, Y. Z., ZHANG, X., LIU, Z. C., NAN, H. Y., HU, Y. C., YANG, Y., ZHANG, J., YU, Y., SUN, Q., TIAN, Q., HU, B., XIAO, G., WANG, W. & CUI, G. B. 2018. Structural and advanced imaging in predicting MGMT promoter methylation of primary glioblastoma: a region of interest based analysis. *Bmc Cancer,* 18.

HANAHAN, D. & WEINBERG, ROBERT A. 2011a. Hallmarks of Cancer: The Next Generation. *Cell,* 144**,** 646-674.

HARALICK, R. M., SHANMUGAM, K. & DINSTEIN, I. 1973. Textural Features for Image Classification. *Ieee Transactions on Systems Man and Cybernetics,* Smc3**,** 610-621.

HEGI, M. E., DISERENS, A. C., GORLIA, T., HAMOU, M. F., DE TRIBOLET, N., WELLER, M., KROS, J. M., HAINFELLNER, J. A., MASON, W., MARIANI, L., BROMBERG, J. E., HAU, P., MIRIMANOFF, R. O., CAIRNCROSS, J. G., JANZER, R. C. & STUPP, R. 2005a. MGMT gene silencing and benefit from temozolomide in glioblastoma. *New England Journal of Medicine,* 352**,** 997-1003.

HEGI, M. E., LIU, L., HERMAN, J. G., STUPP, R., WICK, W., WELLER, M., MEHTA, M. P. & GILBERT, M. R. 2008. Correlation of O6-methylguanine methyltransferase (MGMT) promoter methylation with clinical outcomes in glioblastoma and clinical strategies to modulate MGMT activity. *J Clin Oncol,* 26**,** 4189-99.

HILARIO, A., SEPULVEDA, J. M., PEREZ-NUNEZ, A., SALVADOR, E., MILLAN, J. M., HERNANDEZ-LAIN, A., RODRIGUEZ-GONZALEZ, V., LAGARES, A. & RAMOS, A. 2014. A Prognostic Model Based on Preoperative MRI Predicts Overall Survival in Patients with Diffuse Gliomas. *American Journal of Neuroradiology,* 35**,** 1096-1102.

HORMUTH, D. A., WEIS, J. A., BARNES, S. L., MIGA, M. I., RERICHA, E. C., QUARANTA, V. & YANKEELOV, T. E. 2015. Predicting in vivo glioma growth

with the reaction diffusion equation constrained by quantitative magnetic resonance imaging data. *Physical Biology,* 12.

HOWE, F. A., BARTON, S. J., CUDLIP, S. A., STUBBS, M., SAUNDERS, D. E., MURPHY, M., WILKINS, P., OPSTAD, K. S., DOYLE, V. L., MCLEAN, M. A., BELL, B. A. & GRIFFITHS, J. R. 2003. Metabolic profiles of human brain tumors using quantitative in vivo H-1 magnetic resonance spectroscopy. *Magnetic Resonance in Medicine,* 49**,** 223-232.

HU, L. S., KELM, Z., KORFIATIS, P., DUECK, A. C., ELROD, C., ELLINGSON, B. M., KAUFMANN, T. J., ESCHBACHER, J. M., KARIS, J. P., SMITH, K., NAKAJI, P., BRINKMAN, D., PAFUNDI, D., BAXTER, L. C. & ERICKSON, B. J. 2015. Impact of Software Modeling on the Accuracy of Perfusion MRI in Glioma. *American Journal of Neuroradiology,* 36**,** 2242-2249.

HU, Y. L., DELAY, M., JAHANGIRI, A., MOLINARO, A. M., ROSE, S. D., CARBONELL, W. S. & AGHI, M. K. 2012. Hypoxia-Induced Autophagy Promotes Tumor Cell Survival and Adaptation to Antiangiogenic Treatment in Glioblastoma. *Cancer Research,* 72**,** 1773-1783.

HUISMAN, T. 2010. Diffusion-weighted and diffusion tensor imaging of the brain, made easy. *Cancer Imaging,* 10**,** S163.

INCE, R. A., GIORDANO, B. L., KAYSER, C., ROUSSELET, G. A., GROSS, J. & SCHYNS, P. G. 2017. A statistical framework for neuroimaging data analysis based on mutual information estimated via a gaussian copula. *Hum Brain Mapp,* 38**,** 1541-1573.

ITAKURA, H., ACHROL, A. S., MITCHELL, L. A., LOYA, J. J., LIU, T., WESTBROEK, E. M., FEROZE, A. H., RODRIGUEZ, S., ECHEGARAY, S., AZAD, T. D., YEOM, K. W., NAPEL, S., RUBIN, D. L., CHANG, S. D., HARSH, G. R. T. & GEVAERT, O. 2015. Magnetic resonance image features identify glioblastoma phenotypic subtypes with distinct molecular pathway activities. *Sci Transl Med,* 7**,** 303ra138.

JAIN, A. K. 2010. Data clustering: 50 years beyond K-means. *Pattern recognition letters,* 31**,** 651-666.

JAKOLA, A. S., ZHANG, Y. H., SKJULSVIK, A. J., SOLHEIM, O., BO, H. K., BERNTSEN, E. M., REINERTSEN, I., GULATI, S., FORANDER, P. & BRISMAR, T. B. 2018. Quantitative texture analysis in the prediction of IDH status in low-grade gliomas. *Clin Neurol Neurosurg,* 164**,** 114-120.

JBABDI, S., MANDONNET, E., DUFFAU, H., CAPELLE, L., SWANSON, K. R., PELEGRINI-ISSAC, M., GUILLEVIN, R. & BENALI, H. 2005. Simulation of anisotropic growth of low-grade gliomas using diffusion tensor imaging. *Magnetic Resonance in Medicine,* 54**,** 616-624.

JELLISON, B. J., FIELD, A. S., MEDOW, J., LAZAR, M., SALAMAT, M. S. & ALEXANDER, A. L. 2004. Diffusion tensor imaging of cerebral white matter: a pictorial review of physics, fiber tract anatomy, and tumor imaging patterns. *AJNR Am J Neuroradiol,* 25**,** 356-69.

JENKINSON, M., BANNISTER, P., BRADY, M. & SMITH, S. 2002. Improved optimization for the robust and accurate linear registration and motion correction of brain images. *Neuroimage,* 17**,** 825-841.

JENKINSON, M., BECKMANN, C. F., BEHRENS, T. E., WOOLRICH, M. W. & SMITH, S. M. 2012. Fsl. *Neuroimage,* 62**,** 782-790.

JOHNSON, D. R. 2012. Rising incidence of glioblastoma and meningioma in the United States: Projections through 2050. *Journal of Clinical Oncology,* 30.

JONES, T. L., BYRNES, T. J., YANG, G., HOWE, F. A., BELL, B. A. & BARRICK, T. R. 2015b. Brain tumor classification using the diffusion tensor image segmentation (D-SEG) technique. *Neuro-Oncology,* 17**,** 466-476.

JULIA-SAPE, M., GRIFFITHS, J. R., TATE, A. R., HOWE, F. A., ACOSTA, D., POSTMA, G., UNDERWOOD, J., MAJOS, C. & ARUS, C. 2015. Classification of brain tumours from MR spectra: the INTERPRET collaboration and its outcomes. *Nmr in Biomedicine,* 28**,** 1772-1787.

KALPATHY-CRANNER, J., GERSTNER, E. R., EMBLEN, K. E., ANDRONESI, O. C. & ROSEN, B. 2014. Advanced Magnetic Resonance Imaging of the Physical Processes in Human Glioblastoma. *Cancer Research,* 74**,** 4622-4637.

KATHLEEN M SCHMAINDA, M. A. P., ROBERT T WUJEK, AND JENNIFER M CONNELLY 2018. Moving Towards A DSC-MRI Consensus: A new single dose option for standardized rCBV. *Joint Annual Meeting ISMRM-ESMRMB 2018.*

KICKINGEREDER, P., SAHM, F., RADBRUCH, A., WICK, W., HEILAND, S., VON DEIMLING, A., BENDSZUS, M. & WIESTLER, B. 2015. IDH mutation status is associated with a distinct hypoxia/angiogenesis transcriptome signature which is non-invasively predictable with rCBV imaging in human glioma. *Scientific Reports,* 5.

KIRTON, J. P., WILKINSON, F. L., CANFIELD, A. E. & ALEXANDER, M. Y. 2006. In vitro mineralization of pericytes is accelerated by glucocorticoid treatment. *International Journal of Experimental Pathology,* 87**,** A26-A27.

KLAMI, A., VIRTANEN, S. & KASKI, S. 2012. Bayesian exponential family projections for coupled data sources. *arXiv preprint arXiv:1203.3489*.

KOMAR, G., KAUHANEN, S., LIUKKO, K., SEPPANEN, M., KAJANDER, S., OVASKA, J., NUUTILA, P. & MINN, H. 2009. Decreased blood flow with increased metabolic activity: a novel sign of pancreatic tumor aggressiveness. *Clin Cancer Res,* 15**,** 5511-7.

KORFIATIS, P., KLINE, T. L., COUFALOVA, L., LACHANCE, D. H., PARNEY, I. F., CARTER, R. E., BUCKNER, J. C. & ERICKSON, B. J. 2016. MRI texture features as biomarkers to predict MGMT methylation status in glioblastomas. *Medical Physics,* 43**,** 2835-2844.

KOTSARINI, C., GRIFFITHS, P. D., WILKINSON, I. D. & HOGGARD, N. 2010. A Systematic Review of the Literature on the Effects of Dexamethasone on the Brain From In Vivo Human-Based Studies: Implications for Physiological Brain Imaging of Patients With Intracranial Tumors. *Neurosurgery,* 67**,** 1799-1815.

KREIS, R. 2004. Issues of spectral quality in clinical H-1-magnetic resonance spectroscopy and a gallery of artifacts. *Nmr in Biomedicine,* 17**,** 361-381.

KUHN, M. 2008. Building Predictive Models in R Using the caret Package. *Journal of Statistical Software,* 28**,** 1-26.

KUO, M. D. & JAMSHIDI, N. 2014. Behind the numbers: Decoding molecular phenotypes with radiogenomics--guiding principles and technical considerations. *Radiology,* 270**,** 320-5.

KUZUCAN, A., CHEN, J. H., BAHRI, S., MEHTA, R. S., CARPENTER, P. M., FWU, P. T., YU, H. J., HSIANG, D. J., LANE, K. T., BUTLER, J. A., FEIG, S. A. & SU, M. Y. 2012. Diagnostic performance of magnetic resonance imaging for assessing tumor response in patients with HER2-negative breast cancer receiving neoadjuvant chemotherapy is associated with molecular biomarker profile. *Clin Breast Cancer,* 12**,** 110-8.

LAMBIN, P., LEIJENAAR, R. T. H., DEIST, T. M., PEERLINGS, J., DE JONG, E. E. C., VAN TIMMEREN, J., SANDULEANU, S., LARUE, R. T. H. M., EVEN, A. J. G., JOCHEMS, A., VAN WIJK, Y., WOODRUFF, H., VAN SOEST, J., LUSTBERG, T., ROELOFS, E., VAN ELMPT, W., DEKKER, A., MOTTAGHY, F. M., WILDBERGER, J. E. & WALSH, S. 2017. Radiomics: the bridge between medical imaging and personalized medicine. *Nature Reviews Clinical Oncology,* 14**,** 749-762.

LAO, J. W., CHEN, Y. S., LI, Z. C., LI, Q. H., ZHANG, J., LIU, J. & ZHAI, G. T. 2017. A Deep Learning-Based Radiomics Model for Prediction of Survival in Glioblastoma Multiforme. *Scientific Reports,* 7.

LARUE, R. T. H. M., DEFRAENE, G., DE RUYSSCHER, D., LAMBIN, P. & VAN ELMPT, W. 2017. Quantitative radiomics studies for tissue characterization: a review of technology and methodological procedures. *British Journal of Radiology,* 90.

LATHIA, J. D., HEDDLESTON, J. M., VENERE, M. & RICH, J. N. 2011. Deadly Teamwork: Neural Cancer Stem Cells and the Tumor Microenvironment. *Cell Stem Cell,* 8**,** 482-485.

LAVIOLETTE, P. S., MICKEVICIUS, N. J., COCHRAN, E. J., RAND, S. D., CONNELLY, J., BOVI, J. A., MALKIN, M. G., MUELLER, W. M. & SCHMAINDA, K. M. 2014. Precise ex vivo histological validation of heightened cellularity and diffusion-restricted necrosis in regions of dark apparent diffusion coefficient in 7 cases of high-grade glioma. *Neuro Oncol,* 16**,** 1599-606.

LAW, M., YOUNG, R. J., BABB, J. S., PECCERELLI, N., CHHEANG, S., GRUBER, M. L., MILLER, D. C., GOLFINOS, J. G., ZAGZAG, D. & JOHNSON, G. 2008. Gliomas: Predicting time to progression or survival with cerebral blood volume measurements at dynamic susceptibility-weighted contrast-enhanced perfusion MR imaging. *Radiology,* 247**,** 490-498.

LE BIHAN, D. 2013. Apparent diffusion coefficient and beyond: what diffusion MR imaging can tell us about tissue structure. *Radiology,* 268**,** 318-22.

LE BIHAN, D., BRETON, E., LALLEMAND, D., AUBIN, M. L., VIGNAUD, J. & LAVAL-JEANTET, M. 1988. Separation of diffusion and perfusion in intravoxel incoherent motion MR imaging. *Radiology,* 168**,** 497-505.

LE BIHAN, D., MANGIN, J. F., POUPON, C., CLARK, C. A., PAPPATA, S., MOLKO, N. & CHABRIAT, H. 2001. Diffusion tensor imaging: concepts and applications. *J Magn Reson Imaging,* 13**,** 534-46.

LEE, J., NARANG, S., MARTINEZ, J., RAO, G. & RAO, A. 2015. Spatial Habitat Features Derived from Multiparametric Magnetic Resonance Imaging Data Are Associated with Molecular Subtype and 12-Month Survival Status in Glioblastoma Multiforme. *Plos One,* 10.

LEOW, A. D., ZHU, S., ZHAN, L., MCMAHON, K., DE ZUBICARAY, G. I., MEREDITH, M., WRIGHT, M. J., TOGA, A. W. & THOMPSON, P. M. 2009. The tensor distribution function. *Magn Reson Med,* 61**,** 205-14.

LI, H., ZHU, Y. T., BURNSIDE, E. S., DRUKKER, K., HOADLEY, K. A., FAN, C., CONZEN, S. D., WHITMAN, G. J., SUTTON, E. J., NET, J. M., GANOTT, M., HUANG, E., MORRIS, E. A., PEROU, C. M., JI, Y. & GIGER, M. L. 2016. MR Imaging Radiomics Signatures for Predicting the Risk of Breast Cancer Recurrence as Given by Research Versions of MammaPrint, Oncotype DX, and PAM50 Gene Assays. *Radiology,* 281**,** 382-391.

LI, Z. C., BAI, H., SUN, Q., LI, Q., LIU, L., ZOU, Y., CHEN, Y., LIANG, C. & ZHENG, H. 2018. Multiregional radiomics features from multiparametric MRI for prediction of MGMT methylation status in glioblastoma multiforme: A multicentre study. *Eur Radiol*.

LIMKIN, E. J., SUN, R., DERCLE, L., ZACHARAKI, E. I., ROBERT, C., REUZE, S., SCHERNBERG, A., PARAGIOS, N., DEUTSCH, E. & FERTE, C. 2017. Promises and challenges for the implementation of computational medical imaging (radiomics) in oncology. *Annals of Oncology,* 28**,** 1191-1206.

LINDENSTRAUSS, J. & TZAFRIRI, L. 2013. *Classical Banach spaces II: function spaces*, Springer Science & Business Media.

LIU, T. T., ACHROL, A. S., MITCHELL, L. A., RODRIGUEZ, S. A., FEROZE, A., MICHAEL, I., KIM, C., CHAUDHARY, N., GEVAERT, O., STUART, J. M., HARSH, G. R., CHANG, S. D. & RUBIN, D. L. 2016. Magnetic resonance perfusion image features uncover an angiogenic subgroup of glioblastoma patients with poor survival and better response to antiangiogenic treatment. *Neuro Oncol*.

LOUIS, D. N., PERRY, A., REIFENBERGER, G., VON DEIMLING, A., FIGARELLA-BRANGER, D., CAVENEE, W. K., OHGAKI, H., WIESTLER, O. D., KLEIHUES, P. & ELLISON, D. W. 2016. The 2016 World Health Organization Classification of Tumors of the Central Nervous System: a summary. *Acta Neuropathol,* 131**,** 803-20.

LOWRY, O. H., BERGER, S. J., CARTER, J. G., CHI, M. M. Y., MANCHESTER, J. K., KNOR, J. & PUSATERI, M. E. 1983. Diversity of Metabolic Patterns in Human-Brain Tumors - Enzymes of Energy-Metabolism and Related Metabolites and Cofactors. *Journal of Neurochemistry,* 41**,** 994-1010.

LU, S., AHN, D., JOHNSON, G. & CHA, S. 2003. Peritumoral diffusion tensor imaging of high-grade gliomas and metastatic brain tumors. *American Journal of Neuroradiology,* 24**,** 937-941.

LUPO, J. M., CHA, S. M., CHANG, S. M. & NELSON, S. J. 2005. Dynamic susceptibility-weighted perfusion Imaging of high-grade gliomas: Characterization of spatial heterogeneity. *American Journal of Neuroradiology,* 26**,** 1446-1454.

MAZUROWSKI, M. A., DESJARDINS, A. & MALOF, J. M. 2013. Imaging descriptors improve the predictive power of survival models for glioblastoma patients. *Neuro-Oncology,* 15**,** 1389-1394.

MCDOUGALL, S. R., ANDERSON, A. R. A. & CHAPLAIN, M. A. J. 2006. Mathematical modelling of dynamic adaptive tumour-induced angiogenesis: Clinical implications and therapeutic targeting strategies. *Journal of Theoretical Biology,* 241**,** 564-589.

MCKNIGHT, T. R., NOWOROLSKI, S. M., VIGNERON, D. B. & NELSON, S. J. 2001. An automated technique for the quantitative assessment of 3D-MRSI data from patients with glioma. *J Magn Reson Imaging,* 13**,** 167-77.

MCKNIGHT, T. R., VON DEM BUSSCHE, M. H., VIGNERON, D. B., LU, Y., BERGER, M. S., MCDERMOTT, M. W., DILLON, W. P., GRAVES, E. E., PIRZKALL, A. & NELSON, S. J. 2002. Histopathological validation of a three-dimensional magnetic resonance spectroscopy index as a predictor of tumor presence. *J Neurosurg,* 97**,** 794-802.

MIKESKA, T., BOCK, C., EL-MAARRI, O., HUBNER, A., EHRENTRAUT, D., SCHRAMM, J., FELSBERG, J., KAHL, P., BUTTNER, R., PIETSCH, T. & WAHA, A. 2007. Optimization of quantitative MGMT promoter methylation analysis using pyrosequencing and combined bisulfite restriction analysis. *Journal of Molecular Diagnostics,* 9**,** 368-381.

MINAMIKAWA, S., KONO, K., NAKAYAMA, K., YOKOTE, H., TASHIRO, T., NISHIO, A., HARA, M. & INOUE, Y. 2004. Glucocorticoid treatment of brain tumor patients: changes of apparent diffusion coefficient values measured by MR diffusion imaging. *Neuroradiology,* 46**,** 805-811.

MOHSEN, L. A., SHI, V., JENA, R., GILLARD, J. H. & PRICE, S. J. 2013. Diffusion tensor invasive phenotypes can predict progression-free survival in glioblastomas. *British Journal of Neurosurgery,* 27**,** 436-441.

MOLINA, D., PEREZ-BETETA, J., LUQUE, B., ARREGUI, E., CALVO, M., BORRAS, J. M., LOPEZ, C., MARTINO, J., VELASQUEZ, C., ASENJO, B., BENAVIDES, M., HERRUZO, I., MARTINEZ-GONZALEZ, A., PEREZ-ROMASANTA, L., ARANA, E. & PEREZ-GARCIA, V. M. 2016. Tumour heterogeneity in glioblastoma assessed by MRI texture analysis: a potential marker of survival. *British Journal of Radiology,* 89.

MOLLER-HARTMANN, W., HERMINGHAUS, S., KRINGS, T., MARQUARDT, G., LANFERMANN, H., PILATUS, U. & ZANELLA, F. E. 2002. Clinical application of proton magnetic resonance spectroscopy in the diagnosis of intracranial mass lesions. *Neuroradiology,* 44**,** 371-381.

MOON, W. J., CHOI, J. W., ROH, H. G., LIM, S. D. & KOH, Y. C. 2012. Imaging parameters of high grade gliomas in relation to the MGMT promoter methylation status: the CT, diffusion tensor imaging, and perfusion MR imaging. *Neuroradiology,* 54**,** 555-563.

NEIRA, J. A., UNG, T. H., SIMS, J. S., MALONE, H. R., CHOW, D. S., SAMANAMUD, J. L., ZANAZZI, G. J., GUO, X. T., BOWDEN, S. G., ZHAO, B. S., SHETH, S. A., MCKHANN, G. M., SISTI, M. B., CANOLL, P., D'AMICO, R. S. & BRUCE, J. N. 2017. Aggressive resection at the infiltrative margins of glioblastoma facilitated by intraoperative fluorescein guidance. *Journal of Neurosurgery,* 127**,** 111-122.

NELSEN, R. B. 2007. *An introduction to copulas*, Springer Science & Business Media.

NEUMANN, U., GENZE, N. & HEIDER, D. 2017. EFS: an ensemble feature selection tool implemented as R-package and web-application. *Biodata Mining,* 10.

NICOLASJILWAN, M., HU, Y., YAN, C. H., MEERZAMAN, D., HOLDER, C. A., GUTMAN, D., JAIN, R., COLEN, R., RUBIN, D. L., ZINN, P. O., HWANG, S. N., RAGHAVAN, P., HAMMOUD, D. A., SCARPACE, L. M., MIKKELSEN, T., CHEN, J., GEVAERT, O., BUETOW, K., FREYMANN, J., KIRBY, J., FLANDERS, A. E., WINTERMARK, M. & GRP, T. G. P. R. 2015. Addition of MR imaging features and genetic biomarkers strengthens glioblastoma survival prediction in TCGA patients. *Journal of Neuroradiology,* 42**,** 212-221.

NIR, T. M., JAHANSHAD, N., VILLALON-REINA, J. E., ISAEV, D., ZAVALIANGOS-PETROPULU, A., ZHAN, L., LEOW, A. D., JACK, C. R., JR., WEINER, M. W., THOMPSON, P. M. & ALZHEIMER'S DISEAASE NEUROIMAGINNG, I. 2017. Fractional anisotropy derived from the diffusion tensor distribution function boosts power to detect Alzheimer's disease deficits. *Magn Reson Med,* 78**,** 2322-2333.

NOCH, E. & KHALILI, K. 2009. Molecular mechanisms of necrosis in glioblastoma The role of glutamate excitotoxicity. *Cancer Biology & Therapy,* 8**,** 1791-1797.

NORSKA, A. & BARKER, P. B. 2010. Imaging of Brain Tumors: MR Spectroscopy and Metabolic Imaging. *Neuroimaging Clinics of North America,* 20**,** 293-+.

O'CONNOR, J. P. B., JACKSON, A., ASSELIN, M. C., BUCKLEY, D. L., PARKER, G. J. M. & JAYSON, G. C. 2008. Quantitative imaging biomarkers in the clinical development of targeted therapeutics: current and future perspectives. *Lancet Oncology,* 9**,** 766-776.

O'CONNOR, J. P. B., ROSE, C. J., WATERTON, J. C., CARANO, R. A. D., PARKER, G. J. M. & JACKSON, A. 2015. Imaging Intratumor Heterogeneity: Role in Therapy Response, Resistance, and Clinical Outcome. *Clinical Cancer Research,* 21**,** 249-257.

OPSTAD, K. S., GRIFFITHS, J. R., BELL, B. A. & HOWE, F. A. 2008. Apparent T-2 relaxation times of lipid and macromolecules: A study of high-grade tumor spectra. *Journal of Magnetic Resonance Imaging,* 27**,** 178-184.

OPSTAD, K. S., MURPHY, M. M., WILKINS, P. R., BELL, B. A., GRIFFITHS, J. R. & HOWE, F. A. 2004. Differentiation of metastases from high-grade gliomas using short echo time H-1 spectroscopy. *Journal of Magnetic Resonance Imaging,* 20**,** 187-192.

PADHANI, A. R. & MILES, K. A. 2010. Multiparametric Imaging of Tumor Response to Therapy. *Radiology,* 256**,** 348-364.

PARDON, M. C., YANEZ LOPEZ, M., YUCHUN, D., MARJANSKA, M., PRIOR, M., BRIGNELL, C., PARHIZKAR, S., AGOSTINI, A., BAI, L., AUER, D. P. & FAAS, H. M. 2016. Magnetic Resonance Spectroscopy discriminates the response to microglial stimulation of wild type and Alzheimer's disease models. *Sci Rep,* 6**,** 19880.

PARMAR, C., GROSSMANN, P., BUSSINK, J., LAMBIN, P. & AERTS, H. J. W. L. 2015. Machine Learning methods for Quantitative Radiomic Biomarkers. *Scientific Reports,* 5.

PARSONS, D. W., JONES, S., ZHANG, X., LIN, J. C., LEARY, R. J., ANGENENDT, P., MANKOO, P., CARTER, H., SIU, I. M., GALLIA, G. L., OLIVI, A., MCLENDON, R., RASHEED, B. A., KEIR, S., NIKOLSKAYA, T., NIKOLSKY, Y., BUSAM, D. A., TEKLEAB, H., DIAZ, L. A., JR., HARTIGAN, J., SMITH, D. R., STRAUSBERG, R. L., MARIE, S. K., SHINJO, S. M., YAN, H., RIGGINS, G. J., BIGNER, D. D., KARCHIN, R., PAPADOPOULOS, N., PARMIGIANI, G., VOGELSTEIN, B., VELCULESCU, V. E. & KINZLER, K. W. 2008a. An integrated genomic analysis of human glioblastoma multiforme. *Science,* 321**,** 1807-12.

PAULSON, E. S. & SCHMAINDA, K. M. 2008. Comparison of Dynamic Susceptibility-weighted Contrast-enhanced MR Methods: Recommendations for Measuring Relative Cerebral Blood Volume in Brain Tumors. *Radiology,* 249**,** 601-613.

PAVLIDIS, P., WESTON, J., CAI, J. & GRUNDY, W. N. 2001. Gene functional classification from heterogeneous data. *Proceedings of the fifth annual international conference on Computational biology.* Montreal, Quebec, Canada: ACM.

PEGG, A. E. 1990. Mammalian O-6-Alkylguanine-DNA Alkyltransferase - Regulation and Importance in Response to Alkylating Carcinogenic and Therapeutic Agents. *Cancer Research,* 50**,** 6119-6129.

PENA, A., GREEN, H. A. L., CARPENTER, T. A., PRICE, S. J., PICKARD, J. D. & GILLARD, J. H. 2006a. Enhanced visualization and quantification of magnetic resonance diffusion tensor imaging using the p : q tensor decomposition. *British Journal of Radiology,* 79**,** 101-109.

PERKUHN, M., STAVRINOU, P., THIELE, F., SHAKIRIN, G., MOHAN, M., GARMPIS, D., KABBASCH, C. & BORGGREFE, J. 2018. Clinical Evaluation of a Multiparametric Deep Learning Model for Glioblastoma Segmentation Using Heterogeneous Magnetic Resonance Imaging Data From Clinical Routine. *Invest Radiol*.

PETERSEN, J., BENDSZUS, M., DEBUS, J., HEILAND, S. & MAIER-HEIN, K. H. 2017. Effective user interaction in online interactive semantic segmentation of glioblastoma magnetic resonance imaging. *J Med Imaging (Bellingham),* 4**,** 034001.

PETRELLA, J. R. & PROVENZALE, J. M. 2000. MR perfusion imaging of the Brain: Techniques and applications. *American Journal of Roentgenology,* 175**,** 207-219.

PHIPSON, B. & SMYTH, G. K. 2010. Permutation P-values Should Never Be Zero: Calculating Exact P-values When Permutations Are Randomly Drawn. *Statistical Applications in Genetics and Molecular Biology,* 9.

PISTOLLATO, F., ABBADI, S., RAMPAZZO, E., PERSANO, L., DELLA PUPPA, A., FRASSON, C., SARTO, E., SCIENZA, R., D'AVELLA, D. & BASSO, G. 2010. Intratumoral Hypoxic Gradient Drives Stem Cells Distribution and MGMT Expression in Glioblastoma. *Stem Cells,* 28**,** 851-862.

PLAKS, V., KONG, N. W. & WERB, Z. 2015. The Cancer Stem Cell Niche: How Essential Is the Niche in Regulating Stemness of Tumor Cells? *Cell Stem Cell,* 16**,** 225-238.

PLAZA, M. J., BORJA, M. J., ALTMAN, N. & SAIGAL, G. 2013. Conventional and Advanced MRI Features of Pediatric Intracranial Tumors: Posterior Fossa and Suprasellar Tumors. *American Journal of Roentgenology,* 200**,** 1115-1124.

POPE, W. B., KIM, H. J., HUO, J., ALGER, J., BROWN, M. S., GJERTSON, D., SAI, V., YOUNG, J. R., TEKCHANDANI, L., CLOUGHESY, T., MISCHEL, P. S., LAI, A., NGHIEMPHU, P., RAHMANUDDIN, S. & GOLDIN, J. 2009. Recurrent Glioblastoma Multiforme: ADC Histogram Analysis Predicts Response to Bevacizumab Treatment. *Radiology,* 252**,** 182-189.

POPE, W. B., MIRSADRAEI, L., LAI, A., ESKIN, A., QIAO, J., KIM, H. J., ELLINGSON, B., NGHIEMPHU, P. L., KHARBANDA, S., SORIANO, R. H., NELSON, S. F., YONG, W., PHILLIPS, H. S. & CLOUGHESY, T. F. 2012. Differential Gene Expression in Glioblastoma Defined by ADC Histogram Analysis: Relationship to Extracellular Matrix Molecules and Survival. *American Journal of Neuroradiology,* 33**,** 1059-1064.

POTGIESER, A. R. E., WAGEMAKERS, M., VAN HULZEN, A. L. J., DE JONG, B. M., HOVING, E. W. & GROEN, R. J. M. 2014. The role of diffusion tensor imaging in brain tumor surgery: A review of the literature. *Clinical Neurology and Neurosurgery,* 124**,** 51-58.

POURATIAN, N., ASTHAGIRI, A., JAGANNATHAN, J., SHAFFREY, M. E. & SCHIFF, D. 2007. Surgery insight: the role of surgery in the management of low-grade gliomas. *Nature Clinical Practice Neurology,* 3**,** 628-639.

POVAZAN, M., HANGEL, G., STRASSER, B., GRUBER, S., CHMELIK, M., TRATTNIG, S. & BOGNER, W. 2015. Mapping of brain macromolecules and their use for spectral processing of H-1-MRSI data with an ultra-short acquisition delay at 7 T. *Neuroimage,* 121**,** 126-135.

PRICE, S. J., ALLINSON, K., LIU, H. X., BOONZAIER, N. R., YAN, J. L., LUPSON, V. C. & LARKIN, T. J. 2017. Less Invasive Phenotype Found in Isocitrate Dehydrogenase-mutated Glioblastomas than in Isocitrate Dehydrogenase Wild-Type Glioblastomas: A Diffusion-Tensor Imaging Study. *Radiology,* 283**,** 215-221.

PRICE, S. J., GREEN, H. A. L., DEAN, A. F., JOSEPH, J., HUTCHINSON, P. J. & GILLARD, J. H. 2011. Correlation of MR Relative Cerebral Blood Volume Measurements with Cellular Density and Proliferation in High-Grade Gliomas: An Image-Guided Biopsy Study. *American Journal of Neuroradiology,* 32**,** 501-506.

PRICE, S. J., JENA, R., BURNET, N. G., CARPENTER, T. A., PICKARD, J. D. & GILLARD, J. H. 2007. Predicting patterns of glioma recurrence using diffusion tensor imaging. *European Radiology,* 17**,** 1675-1684.

PRICE, S. J., JENA, R., BURNET, N. G., HUTCHINSON, P. J., DEAN, A. F., PENA, A., PICKARD, J. D., CARPENTER, T. A. & GILLARD, J. H. 2006. Improved delineation of glioma margins and regions of infiltration with the use of diffusion tensor imaging: An image-guided biopsy study. *American Journal of Neuroradiology,* 27**,** 1969-1974.

PRICE, S. J., PENA, A., BURNET, N. G., JENA, R., GREEN, H. A. L., CARPENTER, T. A., PICKARD, J. D. & GILLARD, J. H. 2004. Tissue signature characterisation of diffusion tensor abnormalities in cerebral gliomas. *European Radiology,* 14**,** 1909-1917.

PRICE, S. J., YOUNG, A. M. H., SCOTTON, W. J., CHING, J., MOHSEN, L. A., BOONZAIER, N. R., LUPSON, V. C., GRIFFITHS, J. R., MCLEAN, M. A. & LARKIN, T. J. 2016. Multimodal MRI Can Identify Perfusion and Metabolic Changes in the Invasive Margin of Glioblastomas. *Journal of Magnetic Resonance Imaging,* 43**,** 487-494.

PROVENCHER, S. W. 2001. Automatic quantitation of localized in vivo 1H spectra with LCModel. *NMR Biomed,* 14**,** 260-4.

RASCHKE, F., FELLOWS, G. A., WRIGHT, A. J. & HOWE, F. A. 2015b. H-1 2D MRSI Tissue Type Analysis of Gliomas. *Magnetic Resonance in Medicine,* 73**,** 1381-1389.

RICARD, D., IDBAIH, A., DUCRAY, F., LAHUTTE, M., HOANG-XUAN, K. & DELATTRE, J. Y. 2012. Primary brain tumours in adults. *Lancet,* 379**,** 1984-96.

RIEMENSCHNEIDER, M. J., HEGI, M. E. & REIFENBERGER, G. 2010. MGMT promoter methylation in malignant gliomas. *Target Oncol,* 5**,** 161-5.

ROMANO, A., CALABRIA, L. F., TAVANTI, F., MINNITI, G., ROSSI-ESPAGNET, M. C., COPPOLA, V., PUGLIESE, S., GUIDA, D., FRANCIONE, G., COLONNESE, C., FANTOZZI, L. M. & BOZZAO, A. 2013. Apparent diffusion coefficient obtained by magnetic resonance imaging as a prognostic marker in glioblastomas: correlation with MGMT promoter methylation status. *European Radiology,* 23**,** 513-520.

ROSEN, B. R., BELLIVEAU, J. W., VEVEA, J. M. & BRADY, T. J. 1990. Perfusion Imaging with Nmr Contrast Agents. *Magnetic Resonance in Medicine,* 14**,** 249-265.

RYU, Y. J., CHOI, S. H., PARK, S. J., YUN, T. J., KIM, J. H. & SOHN, C. H. 2014. Glioma: application of whole-tumor texture analysis of diffusion-weighted imaging for the evaluation of tumor heterogeneity. *PLoS One,* 9**,** e108335.

SABATKE, E. M. & BURGE, J. H. 2002. Basic principles in the optical design of imaging multiple aperture systems. *International Optical Design Conference 2002,* 4832**,** 236-248.

SAEYS, Y., ABEEL, T. & DE PEER, Y. V. 2008. Robust Feature Selection Using Ensemble Feature Selection Techniques. *Machine Learning and Knowledge Discovery in Databases, Part Ii, Proceedings,* 5212**,** 313-+.

SANSON, M., MARIE, Y., PARIS, S., IDBAIH, A., LAFFAIRE, J., DUCRAY, F., EL HALLANI, S., BOISSELIER, B., MOKHTARI, K., HOANG-XUAN, K. & DELATTRE, J. Y. 2009. Isocitrate Dehydrogenase 1 Codon 132 Mutation Is an Important Prognostic Biomarker in Gliomas. *Journal of Clinical Oncology,* 27**,** 4150-4154.

SANTAROSA, C., CASTELLANO, A., CONTE, G. M., CADIOLI, M., IADANZA, A., TERRENI, M. R., FRANZIN, A., BELLO, L., CAULO, M., FALINI, A. & ANZALONE, N. 2016. Dynamic contrast-enhanced and dynamic susceptibility contrast perfusion MR imaging for glioma grading: Preliminary comparison of vessel compartment and permeability parameters using hotspot and histogram analysis. *European Journal of Radiology,* 85**,** 1147-1156.

SAWLANI, R. N., RAIZER, J., HOROWITZ, S. W., SHIN, W., GRIMM, S. A., CHANDLER, J. P., LEVY, R., GETCH, C. & CARROLL, T. J. 2010. Glioblastoma: A Method for Predicting Response to Antiangiogenic Chemotherapy by Using MR Perfusion Imaging-Pilot Study. *Radiology,* 255**,** 622-628.

SERRA, A., FRATELLO, M., FORTINO, V., RAICONI, G., TAGLIAFERRI, R. & GRECO, D. 2015. MVDA: a multi-view genomic data integration methodology. *Bmc Bioinformatics,* 16.

SHAH, M., XIAO, Y. M., SUBBANNA, N., FRANCIS, S., ARNOLD, D. L., COLLINS, D. L. & ARBEL, T. 2011. Evaluating intensity normalization on MRIs of human brain with multiple sclerosis. *Medical Image Analysis,* 15**,** 267-282.

SHINOHARA, R. T., SWEENEY, E. M., GOLDSMITH, J., SHIEE, N., MATEEN, F. J., CALABRESI, P. A., JARSO, S., PHAM, D. L., REICH, D. S., CRAINICEANU, C. M., LIFE, A. I. B. & INITIA, A. D. N. 2014. Statistical normalization techniques for magnetic resonance imaging. *Neuroimage-Clinical,* 6**,** 9-19.

SHIROISHI, M. S., BOXERMAN, J. L. & POPE, W. B. 2016. Physiologic MRI for assessment of response to therapy and prognosis in glioblastoma. *Neuro Oncol,* 18**,** 467-78.

SINHA, S., BASTIN, M. E., WARDLAW, J. M., ARMITAGE, P. A. & WHITTLE, I. R. 2004. Effects of dexamethasone on peritumoural oedematous brain: a DT-MRI study. *Journal of Neurology Neurosurgery and Psychiatry,* 75**,** 1632-1635.

SKLAR, A. 1973. Random variables, joint distribution functions, and copulas. *Kybernetika,* 9**,** (449)-460.

SMITH, C. L., KILIC, O., SCHIAPPARELLI, P., GUERRERO-CAZARES, H., KIM, D. H., SEDORA-ROMAN, N. I., GUPTA, S., O'DONNELL, T., CHAICHANA, K. L., RODRIGUEZ, F. J., ABBADI, S., PARK, J., QUINONES-HINOJOSA, A. & LEVCHENKO, A. 2016. Migration Phenotype of Brain-Cancer Cells Predicts Patient Outcomes. *Cell Reports,* 15**,** 2616-2624.

SMITH, S. M., JENKINSON, M., WOOLRICH, M. W., BECKMANN, C. F., BEHRENS, T. E. J., JOHANSEN-BERG, H., BANNISTER, P. R., DE LUCA, M., DROBNJAK, I., FLITNEY, D. E., NIAZY, R. K., SAUNDERS, J., VICKERS, J., ZHANG, Y. Y., DE STEFANO, N., BRADY, J. M. & MATTHEWS, P. M. 2004. Advances in functional

and structural MR image analysis and implementation as FSL. *Neuroimage,* 23**,** S208-S219.

SOARES, D. P. & LAW, M. 2009b. Magnetic resonance spectroscopy of the brain: review of metabolites and clinical applications. *Clinical Radiology,* 64**,** 12-21.

SORENSEN, A. G. 2006. Magnetic resonance as a cancer imaging biomarker. *J Clin Oncol,* 24**,** 3274-81.

SORENSEN, A. G., BATCHELOR, T. T., ZHANG, W. T., CHEN, P. J., YEO, P., WANG, M. Y., JENNINGS, D., WEN, P. Y., LAHDENRANTA, J., ANCUKIEWICZ, M., DI TOMASO, E., DUDA, D. G. & JAIN, R. K. 2009. A "Vascular Normalization Index" as Potential Mechanistic Biomarker to Predict Survival after a Single Dose of Cediranib in Recurrent Glioblastoma Patients. *Cancer Research,* 69**,** 5296-5300.

SOTTORIVA, A., SPITERI, I., PICCIRILLO, S. G. M., TOULOUMIS, A., COLLINS, V. P., MARIONI, J. C., CURTIS, C., WATTS, C. & TAVARE, S. 2013b. Intratumor heterogeneity in human glioblastoma reflects cancer evolutionary dynamics. *Proceedings of the National Academy of Sciences of the United States of America,* 110**,** 4009-4014.

STATNIKOV, A., WANG, L. & ALIFERIS, C. F. 2008. A comprehensive comparison of random forests and support vector machines for microarray-based cancer classification. *Bmc Bioinformatics,* 9.

STERNBERG, E. J., LIPTON, M. L. & BURNS, J. 2014. Utility of Diffusion Tensor Imaging in Evaluation of the Peritumoral Region in Patients with Primary and Metastatic Brain Tumors. *American Journal of Neuroradiology,* 35**,** 439-444.

STUPP, R., HEGI, M. E., MASON, W. P., VAN DEN BENT, M. J., TAPHOORN, M. J. B., JANZER, R. C., LUDWIN, S. K., ALLGEIER, A., FISHER, B., BELANGER, K., HAU, P., BRANDES, A. A., GIJTENBEEK, J., MAROSI, C., VECHT, C. J., MOKHTARI, K., WESSELING, P., VILLA, S., EISENHAUER, E., GORLIA, T., WELLER, M., LACOMBE, D., CAIRNCROSS, J. G., MIRIMANOFF, R. O., TREATMENT, E. O. R., GRP, C. B. T., GRP, R. O. & TRIALS, N. C. I. C. C. 2009. Effects of radiotherapy with concomitant and adjuvant temozolomide versus radiotherapy alone on survival in glioblastoma in a randomised phase III study: 5-year analysis of the EORTC-NCIC trial. *Lancet Oncology,* 10**,** 459-466.

STUPP, R., TONN, J. C., BRADA, M., PENTHEROUDAKIS, G. & GRP, E. G. W. 2010. High-grade malignant glioma: ESMO Clinical Practice Guidelines for diagnosis, treatment and follow-up. *Annals of Oncology,* 21**,** v190-v193.

SUN, J., BI, J. & KRANZLER, H. R. 2014. Multi-view singular value decomposition for disease subtyping and genetic associations. *BMC Genet,* 15**,** 73.

SWANSON, K. R., BRIDGE, C., MURRAY, J. D. & ALVORD, E. C. 2003. Virtual and real brain tumors: using mathematical modeling' to quantify glioma growth and invasion. *Journal of the Neurological Sciences,* 216**,** 1-10.

SWANSON, K. R., ROSTOMILY, R. C. & ALVORD, E. C. 2008. A mathematical modelling tool for predicting survival of individual patients following resection of glioblastoma: a proof of principle. *British Journal of Cancer,* 98**,** 113-119.

TOFTS, P. S. & KERMODE, A. G. 1991. Measurement of the Blood-Brain-Barrier Permeability and Leakage Space Using Dynamic Mr Imaging .1. Fundamental-Concepts. *Magnetic Resonance in Medicine,* 17**,** 357-367.

VAN DER HOORN, A., YAN, J. L., LARKIN, T. J., BOONZAIER, N. R., MATYS, T. & PRICE, S. J. 2016. Validation of a semi-automatic co-registration of MRI scans in patients with brain tumors during treatment follow-up. *Nmr in Biomedicine,* 29**,** 882-889.

VAN DIJKEN, B. R. J., VAN LAAR, P. J., HOLTMAN, G. A. & VAN DER HOORN, A. 2017. Diagnostic accuracy of magnetic resonance imaging techniques for treatment response evaluation in patients with high-grade glioma, a systematic review and meta-analysis. *European Radiology,* 27**,** 4129-4144.

VERHAAK, R. G. W., HOADLEY, K. A., PURDOM, E., WANG, V., QI, Y., WILKERSON, M. D., MILLER, C. R., DING, L., GOLUB, T., MESIROV, J. P., ALEXE, G., LAWRENCE, M., O'KELLY, M., TAMAYO, P., WEIR, B. A., GABRIEL, S., WINCKLER, W., GUPTA, S., JAKKULA, L., FEILER, H. S., HODGSON, J. G., JAMES, C. D., SARKARIA, J. N., BRENNAN, C., KAHN, A., SPELLMAN, P. T., WILSON, R. K., SPEED, T. P., GRAY, J. W., MEYERSON, M., GETZ, G., PEROU, C. M., HAYES, D. N. & NETWORK, C. G. A. R. 2010. Integrated genomic analysis identifies clinically relevant subtypes of glioblastoma characterized by abnormalities in PDGFRA, IDH1, EGFR, and NF1. *Cancer Cell,* 17**,** 98-110.

VERMA, V., SIMONE, C. B., KRISHNAN, S., LIN, S. H., YANG, J. Z. & HAHN, S. M. 2017. The Rise of Radiomics and Implications for Oncologic Management. *Jnci-Journal of the National Cancer Institute,* 109.

VILLANUEVA-MEYER, J. E., MABRAY, M. C. & CHA, S. 2017. Current Clinical Brain Tumor Imaging. *Neurosurgery,* 81**,** 397-415.

VORONA, G. A. & BERMAN, J. I. 2015. Review of diffusion tensor imaging and its application in children. *Pediatric Radiology,* 45**,** 375-381.

WACLAW, B., BOZIC, I., PITTMAN, M. E., HRUBAN, R. H., VOGELSTEIN, B. & NOWAK, M. A. 2015. A spatial model predicts that dispersal and cell turnover limit intratumour heterogeneity. *Nature,* 525**,** 261-+.

WAGNER, M. W., NARAYAN, A. K., BOSEMANI, T., HUISMAN, T. A. G. M. & PORETTI, A. 2016. Histogram Analysis of Diffusion Tensor Imaging Parameters in Pediatric Cerebellar Tumors. *Journal of Neuroimaging,* 26**,** 360-365.

WANG, Q., HU, B., HU, X., KIM, H., SQUATRITO, M., SCARPACE, L., DECARVALHO, A. C., LYU, S., LI, P., LI, Y., BARTHEL, F., CHO, H. J., LIN, Y. H., SATANI, N., MARTINEZ-LEDESMA, E., ZHENG, S., CHANG, E., SAUVE, C. G., OLAR, A., LAN, Z. D., FINOCCHIARO, G., PHILLIPS, J. J., BERGER, M. S., GABRUSIEWICZ, K. R., WANG, G., ESKILSSON, E., HU, J., MIKKELSEN, T., DEPINHO, R. A., MULLER, F., HEIMBERGER, A. B., SULMAN, E. P., NAM, D. H. & VERHAAK, R. G. W. 2017. Tumor Evolution of Glioma-Intrinsic Gene Expression Subtypes Associates with Immunological Changes in the Microenvironment. *Cancer Cell,* 32**,** 42-56 e6.

WANG, S. J. & SUMMERS, R. M. 2012. Machine learning and radiology. *Medical Image Analysis,* 16**,** 933-951.

WELLER, M., STUPP, R., REIFENBERGER, G., BRANDES, A. A., VAN DEN BENT, M. J., WICK, W. & HEGI, M. E. 2010. MGMT promoter methylation in malignant gliomas: ready for personalized medicine? *Nat Rev Neurol,* 6**,** 39-51.

WEN, P. Y., MACDONALD, D. R., REARDON, D. A., CLOUGHESY, T. F., SORENSEN, A. G., GALANIS, E., DEGROOT, J., WICK, W., GILBERT, M. R., LASSMAN, A. B., TSIEN, C., MIKKELSEN, T., WONG, E. T., CHAMBERLAIN, M. C., STUPP, R., LAMBORN, K. R., VOGELBAUM, M. A., VAN DEN BENT, M. J. & CHANG, S. M. 2010. Updated Response Assessment Criteria for High-Grade Gliomas: Response Assessment in Neuro-Oncology Working Group. *Journal of Clinical Oncology,* 28**,** 1963-1972.

WESSELING, P., RUITER, D. J. & BURGER, P. C. 1997. Angiogenesis in brain tumors; Pathobiological and clinical aspects. *Journal of Neuro-Oncology,* 32**,** 253-265.

WHITE, M. L., ZHANG, Y., KIRBY, P. & RYKEN, T. C. 2005. Can tumor contrast enhancement be used as a criterion for differentiating tumor grades of oligodendrogliomas? *American Journal of Neuroradiology,* 26**,** 784-790.

WIATOWSKI, T., TSCHANNEN, M., STANIC, A., GROHS, P. & BÖLCSKEI, H. Discrete deep feature extraction: A theory and new architectures. International Conference on Machine Learning, 2016. 2149-2158.

WIJNEN, J. P., IDEMA, A. J. S., STAWICKI, M., LAGEMAAT, M. W., WESSELING, P., WRIGHT, A. J., SCHEENEN, T. W. J. & HEERSCHAP, A. 2012. Quantitative short echo time 1H MRSI of the peripheral edematous region of human brain tumors in the differentiation between glioblastoma, metastasis, and meningioma. *Journal of Magnetic Resonance Imaging,* 36**,** 1072-1082.

XI, Y. B., GUO, F., XU, Z. L., LI, C., WEI, W., TIAN, P., LIU, T. T., LIU, L., CHEN, G., YE, J., CHENG, G., CUI, L. B., ZHANG, H. J., QIN, W. & YIN, H. 2017. Radiomics signature: A potential biomarker for the prediction of MGMT promoter methylation in glioblastoma. *J Magn Reson Imaging*.

XU, J., FARUQUE, J., BEAULIEU, C. F., RUBIN, D. & NAPEL, S. 2012. A comprehensive descriptor of shape: method and application to content-based retrieval of similar appearing lesions in medical images. *J Digit Imaging,* 25**,** 121-8.

YAHYA, A., MADLER, B. & FALLONE, B. G. 2008. Exploiting the chemical shift displacement effect in the detection of glutamate and glutamine (Glx) with PRESS. *Journal of Magnetic Resonance,* 191**,** 120-127.

YAN, J. L., VAN DER HOORN, A., LARKIN, T. J., BOONZAIER, N. R., MATYS, T. & PRICE, S. J. 2017. Extent of resection of peritumoral diffusion tensor imaging-detected abnormality as a predictor of survival in adult glioblastoma patients. *Journal of Neurosurgery,* 126**,** 234-241.

YAN, Y. R., XIE, Q., LI, F., ZHANG, Y., MA, J. W., XIE, S. M., LI, H. Y. & ZHONG, X. Y. 2014. Epithelial-to-mesenchymal transition is involved in BCNU resistance in human glioma cells. *Neuropathology,* 34**,** 128-34.

YANG, D., RAO, G., MARTINEZ, J., VEERARAGHAVAN, A. & RAO, A. 2015. Evaluation of tumor-derived MRI-texture features for discrimination of molecular subtypes and prediction of 12-month survival status in glioblastoma. *Med Phys,* 42**,** 6725-35.

YAP, F. Y., BUI, J. T., KNUTTINEN, M. G., WALZER, N. M., COTLER, S. J., OWENS, C. A., BERKES, J. L. & GABA, R. C. 2013. Quantitative morphometric analysis of hepatocellular carcinoma: development of a programmed algorithm and preliminary application. *Diagn Interv Radiol,* 19**,** 97-105.

YE, D., MA, S. H., XIONG, Y. & GUAN, K. L. 2013. R-2-Hydroxyglutarate as the Key Effector of IDH Mutations Promoting Oncogenesis. *Cancer Cell,* 23**,** 274-276.

YE, X. Z., XU, S. L., XIN, Y. H., YU, S. C., PING, Y. F., CHEN, L., XIAO, H. L., WANG, B., YI, L., WANG, Q. L., JIANG, X. F., YANG, L., ZHANG, P., QIAN, C., CUI, Y. H., ZHANG, X. & BIAN, X. W. 2012. Tumor-associated microglia/macrophages enhance the invasion of glioma stem-like cells via TGF-beta1 signaling pathway. *J Immunol,* 189**,** 444-53.

YEN, K. E., BITTINGER, M. A., SU, S. M. & FANTIN, V. R. 2010. Cancer-associated IDH mutations: biomarker and therapeutic opportunities. *Oncogene,* 29**,** 6409-17.

ZHAN, L., LEOW, A. D., ZHU, S., BARYSHEV, M., TOGA, A. W., MCMAHON, K. L., DE ZUBICARAY, G. I., WRIGHT, M. J. & THOMPSON, P. M. 2009. A novel measure of fractional anisotropy based on the tensor distribution function. *Med Image Comput Comput Assist Interv,* 12**,** 845-52.

ZHANG, B., HE, X., OUYANG, F. S., GU, D. S., DONG, Y. H., ZHANG, L., MO, X. K., HUANG, W. H., TIAN, J. & ZHANG, S. X. 2017. Radiomic machine-learning classifiers for prognostic biomarkers of advanced nasopharyngeal carcinoma. *Cancer Letters,* 403**,** 21-27.

ZHANG, J. 2010. Diffusion tensor imaging of white matter pathology in the mouse brain. *Imaging Med,* 2**,** 623-632.

ZHOU, M., HALL, L., GOLDGOF, D., RUSSO, R., BALAGURUNATHAN, Y., GILLIES, R. & GATENBY, R. 2014. Radiologically defined ecological dynamics and clinical outcomes in glioblastoma multiforme: preliminary results. *Transl Oncol,* 7**,** 5-13.

ZHOU, M., SCOTT, J., CHAUDHURY, B., HALL, L., GOLDGOF, D., YEOM, K. W., IV, M., OU, Y., KALPATHY-CRAMER, J., NAPEL, S., GILLIES, R., GEVAERT, O. & GATENBY, R. 2018. Radiomics in Brain Tumor: Image Assessment, Quantitative Feature Descriptors, and Machine-Learning Approaches. *American Journal of Neuroradiology,* 39**,** 208-216.